Assessment and quantification of the forest foliar mercury uptake flux across Europe

Inauguraldissertation

zur

Erlangung der Würde eines Doktors der Philosophie

vorgelegt der

Philosophisch-Naturwissenschaftlichen Fakultät

der Universität Basel

von

Lena Wohlgemuth

Basel, 2023

Genehmigt von der Philosophisch-Naturwissenschaftlichen Fakultät
auf Antrag von

Erstbetreuerin: Prof. Dr. Christine Alewell
Zweitbetreuer: PD Dr. Günter Hoch
Externer Experte: Prof. Dr. Daniel Obrist

Basel, den 22.02.2022

Prof. Dr. Marcel Mayor
Dekan

Abstract

Mercury (Hg) is a pollutant of great concern for human and ecosystem health. Centuries of anthropogenic Hg emissions to the atmosphere from e.g. gold mines and coal power plants have increased Hg deposition to land and oceans. Human Hg exposure occurs primarily via the consumption of fish and marine mammals due to the large bioaccumulation potential of highly neurotoxic methyl-Hg along marine and freshwater food webs. In the atmosphere, Hg is mainly present as gaseous elemental Hg(0) (> 95%). As Hg(0) is subject to long-range atmospheric transport around the globe, it is essential to identify and constrain major environmental deposition pathways in order to inform Hg mitigation policies and reduce harmful human Hg intake.

Until recent years, it had been unclear, whether forest ecosystems represent a net source or a net sink for atmospheric Hg(0). However, novel studies on stable Hg isotopes have since identified vegetation biomass, including forest foliage, as the major vector for atmospheric Hg deposition to soils. Forest foliage takes up and accumulates atmospheric Hg(0) in foliage tissues throughout the growing season. Atmospheric Hg(0) sequestered by forest foliage is deposited to soils via e.g. litterfall, biomass die-off and throughfall. Soils are a net sink for atmospheric Hg(0), but also re-emit Hg(0) back to the atmosphere. From soils, Hg can be transported to aquatic biota via runoff.

Despite the importance of Hg deposition to forest ecosystems, net foliar Hg(0) fluxes have not been well constrained. Adding to this, the mechanism of foliar Hg(0) uptake is not yet fully understood. The goals of this thesis was to establish a method to measure and investigate net foliar Hg(0) uptake fluxes on a whole forest scale with a focus on i) environmental controls; ii) its magnitude to the European forested area, and iii) projection pathways under climate change. For measuring the net forest foliar Hg(0) uptake flux, a novel bottom-up method was developed and applied. This method scales measured foliar Hg concentrations per foliage surface area with forest leaf area indices to obtain a foliar Hg flux in units of foliar Hg per unit ground area. A prerequisite for this bottom-up method was to systematically assess variations in foliar Hg(0) uptake rates within the forest canopy, in order to take variations into account for scaling up foliar Hg(0) uptake rates to the whole forest. At a research site in Switzerland, vertical variations in foliar Hg(0) uptake rates within tree canopies were systematically assessed through seasonal analysis of foliage samples for Hg. Foliar Hg concentrations increased linearly throughout the growing season. Sun-exposed leaves growing at the top of canopies took up more Hg over the same time span than shade leaves of the lower canopy, which can probably ascribed to higher physiological activity of sunleaves compared to shade leaves. Therefore, a correction factor for the bottom-up method was derived in order to use foliage Hg(0) uptake rates by sunleaves for the whole tree canopy. Foliar Hg concentrations increased with age in multi-year old coniferous needles, but relative Hg(0) uptake rates decreased in older needles over two years old. Taking

relative biomass proportions of differently aged needles into account, age correction factors of foliar Hg(0) uptake by whole coniferous trees were determined for the bottom-up method.
Using the bottom-up method, foliage Hg(0) uptake fluxes were calculated from foliar Hg(0) uptake rates measured at multiple forest sites in Central and Northern Europe. Foliar Hg(0) uptake fluxes were extrapolated to the forested area of Europe. The total amount of Hg taken up by European forest foliage was calculated to be 20 - 30 Mg Hg growing season^{-1}, representing around a third of the annual anthropogenic Hg emissions of the European Union.
A large European dataset of foliage Hg(0) uptake rates was created by measuring Hg concentrations in > 3500 European foliage samples collected by partners of the ICP Forests biomonitoring network. This dataset allowed for empirical investigations of foliage Hg(0) uptake rates with available foliage- and site-specific meta data. Four major relationships were observed: 1) broadleaves display higher Hg(0) uptake rates per gram dry weight than coniferous needles of the same age; 2) foliage Hg(0) uptake rates correlate with foliage nitrogen concentrations, which is a proxy for foliage physiological activity; 3) foliage Hg(0) uptake rates in pine needles are lower at forest sites, where extended time periods of relatively high ambient vapor pressure deficit prevail during the growing season; and 4) foliage Hg(0) uptake rates in beech, oak and pine are lower at forest sites, where soil water content fell below a soil texture-specific critical soil water content over a relatively long time period during the growing season. The first two relationships suggest, that foliar Hg(0) uptake is positively correlated with the degree of foliage physiological activity, which is larger in broadleaves and in foliage of high nitrogen content compared to coniferous needles and low-nitrogen foliage. The second two relationships indicate, that drought stress owing to dry atmospheric/soil conditions impede foliar Hg(0) uptake in isohydric tree species like pine. All four observed relationships suggest that the foliar Hg(0) uptake occurs via a stomatal pathway and is therefore controlled by stomatal conductance for leaf diffusive gas exchange. Thus, foliar Hg(0) uptake is related to tree metabolic mechanisms of stomatal opening, which is controlled by physiological activity and meteorological parameters. This stomatal foliar Hg(0) uptake mechanism has implications for foliar Hg(0) uptake flux to European forests in the future. More frequents and severe summer droughts in Central and Southern Europe are projected under climate change. A simulation of the European pine forest foliar Hg(0) uptake flux derived from the water vapor pressure deficit under two different climate change scenarios in 2050 revealed only a slight decrease (3 – 4%) in the total seasonal flux. However, possible future meteorological summer conditions comparable to the European drought year of 2018 would result in a larger decrease of pine forest foliar Hg(0) uptake fluxes, which were calculated as 13% lower in 2018 compared to previous years.
The qualitative assessment and quantification of the forest foliar Hg(0) uptake flux provides new insights into the mechanism and relevance of this flux within the Hg cycle and bears the potential to learn more about stomatal conductance as an important ecophysiological parameter.

Acknowledgements

A great number of people have supported me during my PhD, for which I am truly grateful. Although it is impossible to name everyone, some people must be mentioned specifically:
First and foremost, I thank my PhD advisor Martin Jiskra, who employed me as part of his SNSF Ambizione grant. Martin is an excellent and dedicated researcher and has put a huge amount of effort into advising and teaching me for four years, which considerably advanced not only this thesis, but also my academic skills. Thank you, Martin for giving me the opportunity to do this PhD in such a dynamic and academically challenging project. I am very grateful for the support and encouragement I received throughout my PhD project.
Second, I would like to thank Stefan Osterwalder for a wonderful research trip to Sweden, a fun side-project involving mercury passive air samplers, and for his contagious and constant enthusiasm about mercury research. I benefited a lot from our discussions about mercury exchange processes. Thank you, Stefan.
Christine Alewell always patiently supported me throughout this thesis as my professor and supervisor. Particularly, I am grateful not only for her academic advice, but also for her encouragement and for sharing her broad experience related to presentation skills and professional communication, from which I benefited personally.
I would like to thank Günter Hoch for accepting to be my second PhD adviser and for our meetings, during which I got the opportunity to discuss tree physiological aspects of my project and learn how to measure stomatal conductance.
Another source of inspiration and knowledge about tree physiology was my email exchange with Christian Körner, for which I am grateful. Thank you, Christian for taking the time.
I would like to acknowledge Franz Conen for his open door, his scientific dedication and the opportunity to discuss any research questions. This was always helpful and stimulating.
A big thank you goes to Judith for her cheerful encouragement and our running trips, which I enjoyed a lot. I would like to thank Daniela for her commitment in the organisational aspects of my PhD. I am thankful for the opportunity to work with students from my institute, among them Fabienne Bracher, Carl Joseph, Remo Schweigler and Emanuel Glauser.
I am grateful for having met Chuxian Li during the last months of my PhD, who encouraged me with her enthusiasm about mercury research and with her kindness and openness.
I would like to thank all ICP Forests members, who contributed to my PhD by sharing samples and expertise. It was a good experience to getting to know the ICP Forests community. Particularly, Anne Thimonier, Pasi Rautio and Peter Waldner supported my work related to the European mercury foliage dataset.
Importantly, I thank my working group and members of the working group "Aquatic and Isotope Biogeochemistry" for four years of good exchange, support and friendship and for many fun lunch and coffee breaks.

Contents

Chapter 1

Introduction

1.1 The environmental mercury cycle

Mercury (Hg) is a toxic pollutant that is released into the environment primarily by human activities [1] and from geogenic sources like volcanoes and weathering rocks [2, 3]. Recent global inventories estimate annual anthropogenic Hg emissions to the atmosphere to $\sim$ 2000 - 3000 Mg Hg (Fig. 1.1), mostly as gaseous elemental Hg(0) from coal power plants and artisanal and small-scale gold mines [4]. On top of this input of previously immobile Hg into the active Hg cycle, there is a large Hg re-emission flux of approximately 2900 - 5000 Mg Hg yr^{-1} from the Earth surface to the atmosphere from legacy Hg [4] (Fig. 1.1). Once Hg enters the active environmental cycle with a turnover rates of months to decades, it can cause harm to humans and ecosystems mainly due to its bioaccumulation potential and its capacity to be methylated to highly toxic methyl-Hg by anaerobic bacteria [4]. In aquatic food webs, the biomagnification potential of methyl-Hg is particularly high [4, 5]. Thus, consumption of fish and marine mammals is the most common exposition pathway of human communities globally [4].
In the atmosphere, Hg is mainly present as Hg(0) (> 95%), which is chemically inert and can travel long distances, resulting in planet-wide Hg dispersion [6]. Transfer of atmospheric Hg to marine and terrestrial surfaces occurs via dry or wet deposition of inorganic Hg(0) and oxidized Hg(II) compounds. The tropospheric lifetime of total Hg (Hg(0) and Hg(II)) against deposition is estimated to be in the order of six months [7, 8]. Dry deposition of Hg(0) occurs by global vegetation uptake of Hg(0) (1300 - 2700 Mg Hg yr^{-1} [9, 10]), by direct Hg(0) attachment to land surfaces (420 - 500 Mg Hg yr^{-1} [9]) and by invasion of Hg(0) into the ocean (approximately 50% of 3800 - 4600 Mg Hg yr^{-1} [9, 11]) [1, 12–15] (Fig. 1.1). Wet Hg(II) deposition to terrestrial and marine surfaces happens after oxidation of atmospheric Hg(0) to particle-reactive and water-soluble Hg(II) compounds, which are effectively scavenged from the atmosphere via precipitation [13]. Wet Hg(II) deposition amounts to $\sim$ 1000 Mg Hg yr^{-1} on land (Fig. 1.1) [4, 9]. The extent and geographic pattern of Hg(II) wet deposition is mainly driven by tropospheric redox reaction rates between Hg(0) and Hg(II), precipitation regimes and local concentrations of relevant oxidants [16]. Major oxidants of Hg(0) to Hg(II) are considered to be bromine (Br), hydroxy radicals (OH), and ozone (O_3) [7]. The quantitative relevance of dry Hg(II) deposition

is uncertain due to analytical difficulties related to flux measurements [17, 18].
Atmospheric Hg deposition fluxes are simulated in Earth system models of Hg biogeochemical cycling like GEOS-Chem [8]. With the exception of rainfall Hg(II) fluxes to land, validation of modelled deposition against observations is challenging due to a lack of well constrained net Hg deposition fluxes. To date, comprehensive measurements of terrestrial net Hg(0) deposition fluxes on the level of a whole ecosystem or of net Hg(0)/Hg(II) fluxes to the open ocean are limited [11, 15]. In the past decade, fingerprinting studies of Hg stable isotope signatures in environmental samples have advanced knowledge on the relative contributions of different Hg deposition fluxes to environmental compartments. Vegetation uptake of atmospheric Hg(0) has been identified to be the most important atmospheric source to terrestrial surfaces, being attributed to 60% - 90% of Hg in soils [19–22]. Recent measurements and mass balances of Hg stable isotopes in seawater have estimated an approximately equal contribution of atmospheric Hg(0) and Hg(II) to ocean Hg uptake [11]. This evaluation diverges from previous simulations of atmospheric transport models, which ascribe $\sim$ 66% - 75% of ocean Hg to a Hg(II) deposition input [7, 8].

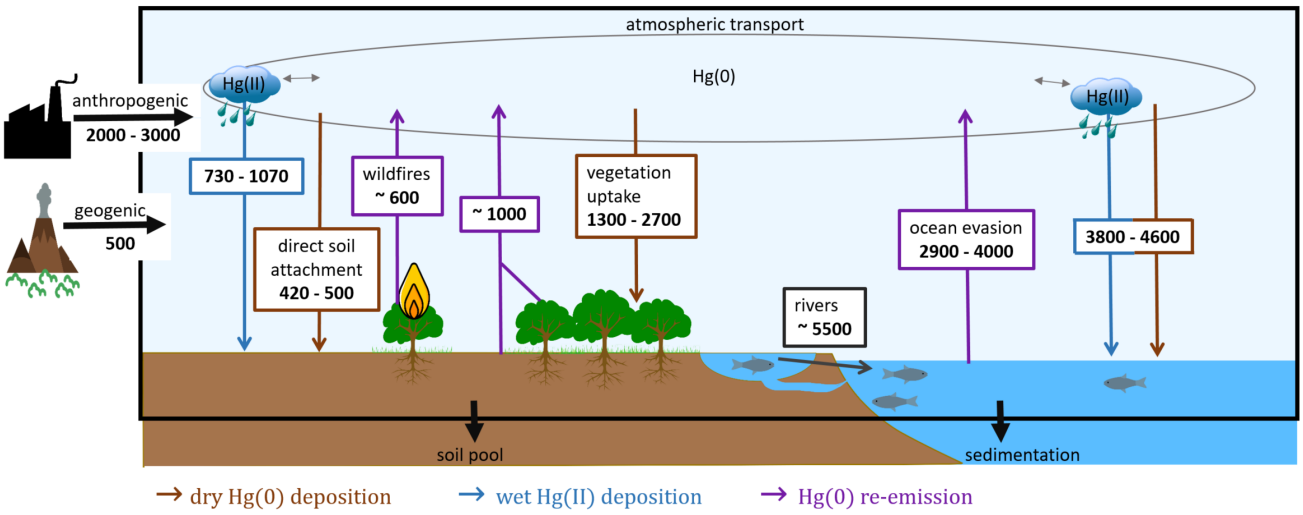

FIGURE 1.1. Emission and deposition fluxes of the active global Hg cycle with turnover rates of months to decades [4, 9]. Units of flux values (in bold) are Mg Hg year^{-1}.

Inconsistencies between results from transport models and stable isotope fingerprinting studies highlight the need for reliable measurements of net Hg deposition fluxes. An estimated annual amount of approximately up to 5500 $\pm$ 2700 Mg of terrestrial Hg yr^{-1} [23] (Fig. 1.1) is discharged to ocean margins via streams and rivers, most of which is buried in coastal sediments [24], while only less than a third of riverine Hg reaches the open ocean [23–26]. Open oceans re-emit Hg from marine surfaces, but are overall perceived to be a net sink of Hg with respect to the atmosphere [11] and are therefore linked to Hg(0) emission and deposition rates on land via atmospheric Hg(0) transport. Consequently, model development and parameterization of Hg fluxes to food fish crucially requires quantification and a detailed understanding

of Hg cycling in the terrestrial environment. The most relevant deposition process from the atmosphere to land surfaces is vegetation Hg(0) uptake [4, 15]. In the absence of vegetation Hg(0) uptake, annual Hg deposition to global oceans could increase by as much as $\sim$ 1000 Mg Hg yr^{-1} [9]. Thus, studying terrestrial Hg deposition with a focus on vegetation Hg(0) uptake is particularly relevant for the evaluation of Hg emission reduction activities put forward by signatories of the UN Minamata Convention on Mercury in 2017 [27].

1.2 Vegetation as vector for Hg(0) deposition

Accumulation of Hg(0) by vegetation tissues and subsequent Hg transfer to soils is the dominant source of Hg to terrestrial ecosystems globally [9]. A strong indication of this relation is the co-variation of atmospheric Hg(0) and CO_2 in the Northern Hemisphere, exhibiting minima in summer during the peak of photosynthetic activity and maxima in winter [12, 28]. Vegetation-derived Hg deposition is associated with plant net primary productivity and is therefore higher in e.g. tropical forests than in boreal ecosystems [9, 29, 30]. After assimilation by vegetation biomass, Hg is transferred to soils either when trees shed their foliage (litterfall), by wash off (throughfall) or by vegetation die off. Annual global Hg deposition via litterfall and throughfall are each estimated in the magnitude of $\sim$ 1200 Mg yr^{-1} respectively [10, 30, 31]. Apart from foliage uptake and throughfall, atmospheric Hg(0) is also accumulated by mosses, lichen, woody tissues and by roots through internal plant transport of previously assimilated Hg(0) from aboveground biomass [10]. This non-foliage related vegetation Hg(0) flux has to be included in whole-ecosystem studies and assessments of total global vegetation Hg fluxes. A recent evaluation of global Hg deposition after Hg assimilation by multiple biomes and plant tissue types amounts to 2705 $\pm$ 504 Mg Hg yr^{-1} [10], which represents around 75% of the global estimate for Hg deposition to land of 3600 Mg Hg yr^{-1} [32].
Most of Earth's vegetation consists of forests, which cover approximately 30% of the global land area and account for 75% of terrestrial gross primary production [33]. Consequently, forests represent one of the most active terrestrial ecosystems for the biogeochemical Hg cycle on land (for an overview of Hg related processes in forests, see Fig. 1.2). Until recently, it was unresolved, whether forest ecosystems overall act as a net-source or net-sink of atmospheric Hg(0) [34], since there is also a Hg re-emission flux from forests [15, 35]. However, findings on Hg isotope signatures in forest soils [19, 20], as well as the quantitative relevance of the global Hg litterfall flux [30] and atmospheric Hg(0) seasonality [12] provide evidence that forests represent a strong sink within the global Hg cycle. The amount of net Hg deposition to forest soils by litterfall, throughfall or direct dry deposition impacts the contamination of methyl-Hg in aquatic food webs [36], because Hg can be transported from forest soils to freshwater lakes, rivers and streams via runoff [15, 37] (Fig. 1.2).

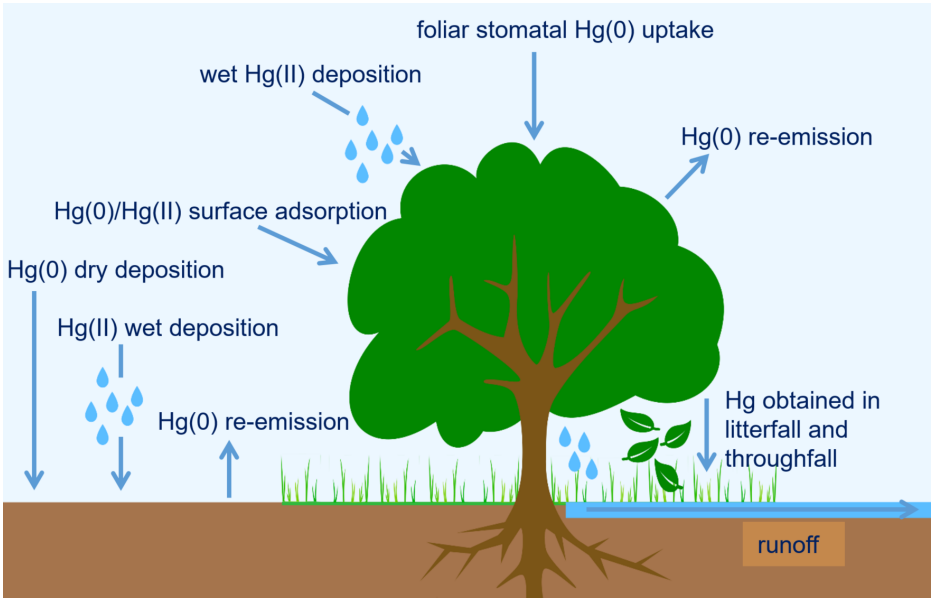

FIGURE 1.2. Overview of processes in terrestrial forest Hg cycling.

Forest foliage acts as a biologically active vector for the net deposition of atmospheric Hg(0) to forest ecosystems. Most of foliar Hg (> 90%) is accumulated in interior foliage tissues [38], making foliar uptake the dominant mechanism of Hg(0) accumulation rather than surface adsorption. The exchange of gases like H_2O vapor, O_2 or CO_2 between the atmosphere and foliage occurs via open stomata at the undersides of leaves [39]. Ambient Hg(0), which does not perform any tree biological function, is taken up inadvertently via this diffusive pathway of stomatal gas exchange [40–42]. To a lesser extent, non-stomatal uptake may occur by direct assimilation of Hg(0) vapor via foliage cuticles [43, 44]. Transfer of Hg from soils to foliage via roots and xylem sap is limited [45, 46], which was explained by biological barriers in roots [47–49]. Inside of foliar tissues, Hg(0) vapor is biochemically oxidized to bivalent Hg(II). Whereas the exact mechanism of Hg(0) oxidation remains to be demonstrated, H_2O_2, catalase and other reactive oxygen species have been suggested as potential oxidants [49]. The exact biochemical processes and cellular locations of foliar Hg(0) transformation have not yet been fully resolved [49]. By means of HR-XANES spectroscopy, Hg(II) has been identified to form Hg-biothiol complexes with thiol functional groups (-SH) and Hg sulfide nanoparticles (HgS_{NP}) inside of foliage [50]. The Hg-S bond is stable, therefore release of tightly bound Hg from foliage is restricted [49, 51]. However, there also exist a reversible component of leaf uptake [43], such that the foliar-atmosphere Hg(0) exchange is bi-directional [52]. Re-emission of Hg(0) from foliage occurs after photoreduction of previously metabolized Hg(II) to Hg(0) [35]. The Hg(0) re-emission flux depends on diurnal changes in stomatal conductance and meteorological conditions like sunlight, temperature and humidity as well as tree species and ambient Hg(0) [35, 53]. An isotopic mass balance model evaluated the foliar Hg(0) re-emission flux to around 30% of Hg(0) uptake in a subtropical beech forest in Yunnan (China) [35]. Over the course of

the growing season, however, the non-reversible component of stomatal foliage Hg(0) uptake increases foliar Hg concentrations continuously, such that there is a foliar Hg net deposition [38, 46, 54].

1.3 Regulation of foliar gas exchange through stomatal conductance

Trees regulate their foliage stomatal conductance to gas exchange, in order to control water transpiration rates and uptake of CO_2 for photosynthesis [55]. At any point in time, the stomatal conductance balances a trade-off between an optimal rate of photosynthesis and transpiration on the one hand and the necessity to avoid cavitation on the other hand [55]. In this way, stomatal conductance relates the diffusion of water vapor with the CO_2 exchange of forest foliage and represents an important process for global land-atmosphere biogeochemical cycles. The rate of tree transpiration is linearly proportional to leaf stomatal aperture [55]. The influx of CO_2 through open stomata is driven by a concentration gradient between ambient and intercellular CO_2 concentrations induced by the removal of intercellular CO_2 during photosynthesis according to Fick's First Law of Diffusion [55, 56]:

$$F_c = g_{sto,c} \cdot (c_{a,c} - c_{i,c}) \tag{1.1}$$

where F_c is the CO_2 flux (μmol m^{-2} s^{-1}), $c_{i,c}$ and $c_{a,c}$ are the CO_2 mole fractions (μmol mol^{-1}) in intercellular spaces and ambient air respectively, and $g_{sto,c}$ (mol m^{-2} s^{-1}) is the stomatal conductance to CO_2. At greater rates of photosynthesis, stomatal conductance to gas exchange has to increase as well, given a relatively constant CO_2 concentration gradient. Consequently, trees with a higher species-specific photosynthetic capacity have a higher maximum stomatal conductance for water vapor [57]. The relative stomatal conductance (actual stomatal conductance in proportion to tree species-specific maximum stomatal conductance) depends on current environmental conditions like atmospheric water vapor pressure deficit (VPD) and soil water availability (both related to transpiration rates) and ambient temperatures and radiation intensity (related to rates of photosynthesis) [58, 59]. Stomatal conductance (g_{sto}) for different gases A and B correspond to each other by their gas diffusion coefficients (D) [56]:

$$g_{sto,B} = g_{sto,A} \cdot \frac{D_B}{D_A} \tag{1.2}$$

By this theory, the diffusive stomatal flux of vapor Hg(0) should be subjected to the same tree stomatal regulation mechanism that adapts stomatal fluxes of water vapor and CO_2 to environmental parameters related to hydraulic (mainly soil water content, VPD) and photosynthetic conditions (temperature, radiation). Previous studies found a correlation between atmospheric

Hg(0) and CO_2 [12, 60]. However, this relationship of foliage influxes of Hg(0) with CO_2/water vapor under various environmental conditions has not yet been investigated. Therefore, large knowledge gaps remain in understanding physiological and environmental controls of foliage stomatal Hg(0) uptake flux [9]. Closing these knowledge gaps is particularly relevent for the parametrization of the foliage stomatal Hg(0) uptake flux in global Hg cycle models under climate change. The frequency and intensity of droughts in many global forest ecosystems is projected to increase in the next decades, which might cause a decrease in tree transpiration and stomatal conductance due to water scarcity [61]. In this scenario, stomatal Hg(0) uptake would decrease proportional to a decline in stomatal conductance of water vapor (Eq. 1.2), and thereby more Hg(0) could remain in the atmosphere during the growing season and potentially be a source for open oceans via atmospheric long-range transport [9]. On the other hand, foliage Hg(0) uptake was suggested to increase, owing to an increase in foliage net primary production associated with CO_2 fertilization [12, 62]. However, it is presently still unclear if the stomatal component of Hg(0) uptake will be enhanced with CO_2 fertilization, since trees might not respond with an increase of stomatal aperture under conditions of a higher gradient of intercellular to ambient CO_2 (Eq. 1.1) [61].

1.4 Objectives of this thesis

The goal of this thesis was to systemically investigate the forest foliar Hg(0) uptake flux. This goal is primarily motivated by i) the need for an improved quantification of this important net Hg flux from the atmosphere to forest ecosystems; and ii) knowledge gaps in our mechanistic understanding of foliar Hg(0) uptake, which impedes meaningful parametrization of this flux in global Hg cycle models and potentially our capacity for projecting this flux under climate change.
Specifically, the following research approaches were taken:

- Establishing and testing of a method to quantify the net foliage Hg(0) uptake flux (Chapter 2; Fig. 2.2).
- Systematic assessment of variations of foliar Hg(0) uptake rates within forest tree canopies and among tree species (Chapter 2; Fig. 2.4, 2.5, 2.7) as a prerequisite to quantify and assess the forest foliar Hg(0) uptake flux on an ecosystem scale.
- Extrapolation of the forest foliage Hg(0) uptake flux to the forested land area of Europe (Chapter 2.3.6; 4).
- Empirical evaluation of parameters impacting the forest foliar Hg(0) uptake flux by using a large European dataset on foliar Hg concentrations (Chapter 3). These parameters

involve proxies related to foliage physiological activity (Fig. 3.4) and meteorological conditions (Chapter 3.3.5 and 3.3.6).

- Modelling of the foliar Hg(0) uptake flux to European forests on a high spatial resolution taking differences among tree species and meteorological conditions into account (Fig. 4.1).
- Comparison of modelled European forest foliar Hg(0) uptake fluxes with respective Hg(0) flux outputs from a global chemical transport model (Chapter 4.3.2).
- Projection of the pine forest foliar Hg(0) uptake flux under different climate change scenarios (Chapter 4.3.4).

Chapter 2

A bottom-up quantification of foliar mercury uptake fluxes across Europe

This chapter has been published as an open access paper in the journal Biogeosciences (Copernicus Publications for the EGU) and can be found under DOI: 10.5194/bg-17-6441-2020.

This chapter was co-authored by:
Lena Wohlgemuth, Stefan Osterwalder, Carl Joseph,
Ansgar Kahmen, Günter Hoch, Christine Alewell,
Martin Jiskra

Abstract

The exchange of gaseous elemental mercury, Hg(0), between the atmosphere and terrestrial surfaces remains poorly understood mainly due to difficulties in measuring net Hg(0) fluxes on the ecosystem scale. Emerging evidence suggests foliar uptake of atmospheric Hg(0) to be a major deposition pathway to terrestrial surfaces. Here, we present a bottom-up approach to calculate Hg(0) uptake fluxes to aboveground foliage by combining foliar Hg uptake rates normalized to leaf area with species-specific leaf area indices. This bottom-up approach incorporates systematic variations in crown height and needle age. We analyzed Hg content in 583 foliage samples from six tree species at 10 European forested research sites along a latitudinal gradient from Switzerland to Northern Finland over the course of the 2018 growing season. Foliar Hg concentrations increased over time in all six tree species at all sites. We found that foliar Hg uptake rates normalized to leaf area were highest at the top of the tree crown. Foliar Hg uptake rates decreased with needle age of multi-year old conifers (spruce and pine). Average species-specific foliar Hg uptake fluxes during the 2018 growing season were 18 $\pm$ 3 μg Hg m^{-2} for beech, 26 $\pm$ 5 μg Hg m^{-2} for oak, 4 $\pm$ 1 μg Hg m^{-2} for pine and 11 $\pm$ 1 μg Hg m^{-2} for spruce. For comparison, the average Hg(II) wet deposition flux measured at 5 of the 10 research sites during the same period was 2.3 $\pm$ 0.3 μg Hg m^{-2}, which was four times lower than the site-averaged foliar uptake flux of 10 $\pm$ 3 μg Hg m^{-2}. Scaling up site-specific foliar uptake rates to the forested area of Europe resulted in a total foliar Hg uptake flux of approximately 20 $\pm$ 3 Mg during the 2018 growing season. Considering that the same flux applies to the global land area of temperate forests, we estimate a foliar Hg uptake flux of 108 $\pm$ 18 Mg. Our data indicate that foliar Hg uptake is a major deposition pathway to terrestrial surfaces in Europe. The bottom up approach provides a promising method to quantify foliar Hg uptake fluxes on an ecosystem scale.

2.1 Introduction

Mercury (Hg) is a toxic pollutant ubiquitous in the environment due to long-range atmospheric transport. Anthropogenic emissions of Hg into the atmosphere mainly originate from burning of coal, artisanal and small-scale gold mining and non-ferrous metal and cement production while geogenic emission occur from volcanoes and rock weathering [4]. Atmospheric Hg is deposited to terrestrial surfaces and the ocean and can be re-emitted back to the atmosphere [15, 63]. The residence time of Hg in the atmosphere and its transfer to land and ocean surfaces mainly depends on its speciation [1]. Gaseous elemental mercury Hg(0) is the dominant form (> 90%) of atmospheric Hg [6], exhibiting a residence time of several months to more than a year [64, 65]. Atmospheric Hg will ultimately be transferred to water and land surfaces by wet or dry deposition. In the wet deposition process, Hg(0) is oxidized in the atmosphere to water-soluble Hg(II) and washed down to the Earth surface by precipitation [1]. Wet deposition fluxes of Hg(II) to terrestrial surfaces are well constrained and direct measurements are

coordinated in regional and international atmospheric deposition monitoring programs (EMEP, NADP) [66–69].

Dry deposition fluxes of Hg(0) and Hg(II) to the Earth surface are less constrained owing to challenges in measuring net ecosystem exchange fluxes [1, 70] and atmospheric Hg(II) concentrations [17]. The dry deposition of Hg can occur by vegetation uptake and subsequent transfer to the ground via litterfall [30, 71], by wash-off from foliar surfaces via throughfall [72] or by direct deposition to terrestrial surfaces and soils [73]. Hg dry deposition is usually not routinely monitored, with the Hg litterfall monitoring network of NADP being a notable exception [71, 74]. Consequently, atmospheric mercury models inferring Hg dry deposition across Europe during summer months lack observational constraints [75]. Ecosystem scale mass balance studies, however, revealed that litterfall deposition to forest floors exceeds wet deposition [71, 74, 76–83]. Several lines of evidence suggest that uptake of atmospheric Hg(0) by vegetation represents an important process in terrestrial Hg cycling: i) isotopic fingerprinting studies revealed that approximately 90% of Hg in foliage and 60% – 90% of Hg in soils originate from atmospheric Hg(0) uptake by vegetation [19–22], ii) observations of foliar Hg concentrations increase with exposure time to atmospheric Hg(0) [38, 46, 80, 84–87] while Hg uptake via the root system was found to be minor [46, 86, 87], iii) atmospheric Hg(0) correlates with the photosynthetic activity of vegetation suggesting that summertime minima in atmospheric Hg(0) in the Northern hemisphere are controlled by vegetation uptake [12, 88].

The exact mechanism of the atmosphere-foliar Hg(0) exchange is not yet fully understood. Laacouri et al. [38] observed highest Hg concentrations in leaf tissues as opposed to leaf surfaces and cuticles, implying that Hg(0) diffuses into the leaves. Exposing plants to Hg(0) in form of enriched Hg isotope tracers, Rutter et al. [40] found that plant Hg uptake was mainly to the leaf interior. Leaf Hg content correlated with stomatal density [38] suggesting that stomatal uptake represents the main pathway. Nonstomatal uptake was observed by Stamenkovic and Gustin [43] under conditions of reduced stomatal aperture implying adsorption of atmospheric Hg to cuticles surfaces. Re-emission of Hg from foliage can occur by photoreduction of Hg(II) to Hg(0) and subsequent volatilization [78]. The re-emission potential of Hg previously taken up by foliage and strongly complexed in plant tissue [50] was suggested to be lower than the re-emission potential of surface-bound Hg [12, 35].

Hg contents in foliage were shown to be species-specific [38, 89–92]. It is currently unresolved if deciduous broad leaves accumulate higher Hg concentrations than needles [89, 90] or if it is the other way around [91, 93, 94]. Deciduous species shed their leaves at the end of the growing season, whereas most conifers grow needles over multiple years and continue to accumulate Hg, resulting in increasing Hg concentrations with needle age [95–97]. Furthermore, Hg concentrations in foliage have been shown to vary within the canopy [76]. Physiological differences between deciduous and coniferous tree species and inconsistent sampling of needle age and canopy height may have contributed to the uncertainty in literature whether deciduous

or coniferous species take up more Hg.
The goal of this study was to improve the understanding of foliar Hg(0) uptake and quantify foliar uptake fluxes at European forest research sites. The objectives were to: 1) determine the temporal evolution of Hg concentrations and the Hg pool in foliage of 6 tree species at 10 European research sites along a south-north transect from Switzerland to Finland over the 2018 growing season, 2) investigate the effect of needle age, crown height and tree functional group on foliar Hg uptake, 3) quantify foliar Hg uptake fluxes per m2 ground surface area based on the temporal evolution of the foliar Hg pool over the growing season. 4) estimate the foliar uptake fluxes for Europe and temperate forests globally by scaling up species-averaged foliar uptake rates determined in this study to respective forest areas.

2.2 Materials and Methods

2.2.1 Site description

Foliage samples were collected from 10 European research sites located along a south-north transect from Switzerland to Scandinavia (Fig. 2.1). The Hölstein site in Switzerland comprises the Swiss Canopy Crane II (SCCII) operated by the Physiological Plant Ecology Group of the University of Basel [98]. Our principal site Hölstein allowed to systematically access the entire canopy through the gondola of a crane. The research sites Schauinsland and Schmücke are part of the air monitoring network of the German Federal Environment Agency (UBA) [99]. Hyltemossa, Norunda, Svartberget and Pallas are Integrated Carbon Observation System (ICOS) sites operated by Lund University (LU), the Swedish University of Agricultural Sciences (SLU) and the Finnish Meteorological Institute (FMI) [100–102]. Hurdal is a prospective ICOS Ecosystem station, an ICP Forests Level II Plot and a European Monitoring and Evaluation Programme (EMEP) air measurement site operated by the Norwegian Institute of Bioeconomy Research (NIBIO) and the Norwegian Institute for Air Research (NILU) [103]. Bredkälen and Råö are Swedish EMEP air measurement sites operated by the Swedish Environmental Research Institute (IVL) [68, 104]. Tree species composition differed among sites. Hölstein, for instance, is a mixed forest harbouring 14 different tree species while Hyltemossa is an exclusive spruce stand (see Table A.5 for details).

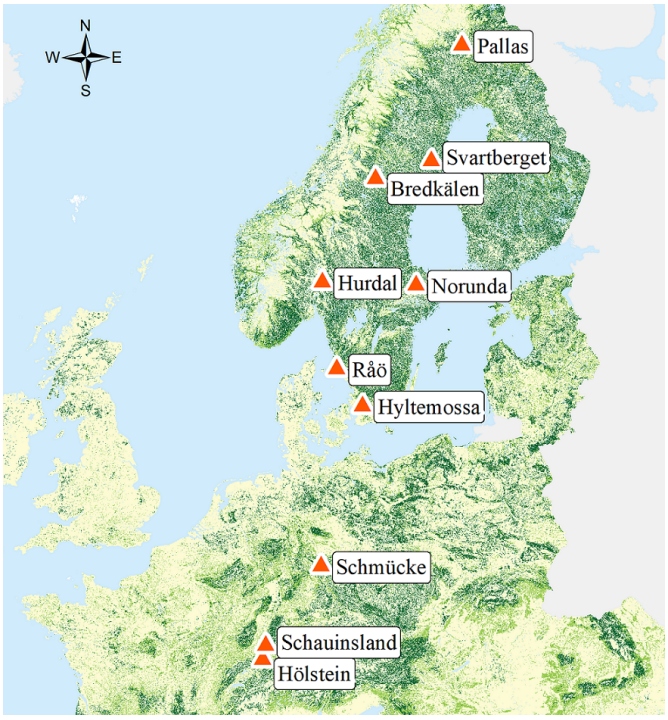

FIGURE 2.1. Research sites for foliage sampling during the 2018 growing season. Base map corresponds to the Joint Research Centre (JRC) Pan-European Forest Type Map 2006 [105, 106]. Reuse is authorized under reuse policy of the European Commission [107].

2.2.2 Sample collection

Foliage sampling strategy was guided by the ICP Forests Programme sampling manual [108], requesting to take samples that have developed under open sunlight from the top third of the crown canopy. At 4 sites (Svartberget, Hyltemossa, Norunda and Hölstein) we complied with the ICP Forest sampling protocol. At 6 sites (Pallas, Bredkälen, Hurdal, Råö, Schmücke and Schauinsland) we had to adapt the sampling strategy to local conditions and available equipment. At our focus research site in Hölstein, Switzerland a crane allowed access to the top of the crown and vertical sampling of beech, oak and spruce. Since pine did not grow needles at ground level we did not sample their vertical profiles. Vertical sampling of spruce needles in Hölstein during 2018 was repeated in 2019 with five spruce trees because only two spruce trees had been sampled during 2018 of which one died from drought induced stress by the end of the 2018 growing season [109]. The relative effect of height on Hg accumulation in Hölstein spruce needles is therefore investigated with data from the growing season 2019. Samples at Hyltemossa and Svartberget were cut from tree canopies using a 20 m telescopic scissors and at Hurdal using a 3 m telescopic scissors. At Norunda samples were shot from the tree canopies using a shotgun. At Schauinsland, Schmücke, Råö and Bredkälen we used a 5 m telescopic scissors for cutting the branches in the lower half of the crown. At Pallas and Råö branches were cut from low-growing trees at breast height. We collected intact leaves at three to six

time points during the 2018 growing season. Samples from at least three different branches of the same tree were pooled to a composite sample. We sampled at least three trees per species (one to four species) with the exception of Råö where only one oak and one spruce tree were available. Sampling and sample preparation was conducted using clean nitryl gloves. Leaves were cut from outermost branches. All samples were stored in Ziplock bags in the freezer until analysis. Sampling dates are reported in Table A.1 for each site. At Hölstein atmospheric Hg(0) was measured integrated over the whole sampling period by using passive air samplers (PAS) as described by McLagan et al. [286]. PAS were exposed at ground level (1.6 m) under the canopy at four locations on the plot and additionally at three heights of 10 m, 19 m and 35 m on the crane railing (details in A.7 and Fig. A.4) from 15 May 2018 to 18 October 2018. The PAS air measurement campaign at Hölstein was repeated in 2019 with PAS exposed at 1.5 m, 10 m, 19 m and 35 m height at the crane from 16 May 2019 to 12 September 2019. Measurement of one of the PAS installed at 10 m height in 2019 was excluded from further analysis because it produced an implausible high result which can probably be traced back to a measurement error. Under dry conditions at noon time on 17 July 2019 we measured stomatal conductance to water vapor of beech, pine and oak from the crane gondola at Hölstein using an SC-1 Leaf Porometer (Meter Group, Inc. USA). At 5 locations (Schauinsland, Schmücke, Råö, Bredkälen and Pallas) Hg(II) wet deposition measurements were performed by the operators of the research sites. At Schauinsland and Schmücke Eigenbrodt NSA 181/KD (Eigenbrodt GmbH, Königsmoor Germany) samplers were employed for collecting samples and total Hg was measured using atomic fluorescence spectroscopy (see UBA, 2004 for details on analysis). At Råö, Bredkälen and Pallas wet deposition was sampled according to EMEP protocol [110] (refer to Torseth et al. [111] for an overview of EMEP).

2.2.3 Sample preparation and measurements

In total 584 leaf samples were collected, weighted and analyzed for leaf mass per area (LMA) and subsequently dried and ground for Hg concentration analysis. The projected leaf area was measured using a LI3100 Area Meter (LI-COR Biosciences USA). We performed duplicate scans of 17% of foliage samples and obtained a mean per cent deviation between scans and respective duplicate scans of 3% ± 3%. For measuring projected needle area, we calibrated the LI3100 with rubberized wires of known length and a diameter of 1.74 ± 0.02 mm (see A.4 and Fig. A.2). For the two sites Hurdal and Pallas the performance and resolution of the LI3100 was insufficient and unrealistic results were discarded and median values from literature were used instead (see A.4 for details). For the three ICOS sites Hyltemossa, Norunda and Svartberget we obtained LMA values measured by research staff according to ICOS protocol [112] (Sect. A.4). Foliage samples were oven-dried at 60°C for 24 h. We did not observe any Hg losses irrespective of drying temperatures of 25°C, 60°C and 105°C (Fig. A.1). A similar result was

obtained by Yang et al. [113] for Hg in wood and by Lodenius et al. [114] for Hg in moss. Dried samples were weighted and homogenously grinded in an ordinary stainless steel coffee grinder. Total Hg concentrations were measured with atomic absorption spectrophotometry using a direct mercury analyzer (DMA-80 Hg, Heerbrugg, Switzerland). Standard Reference Materials (SRMs) used in this study were NIST-1515 apple leaves and spruce needle sample B from the 19th ICP Forests needle/leaf interlaboratory comparison. Standard measurement procedures included running a quality-control pre-sequence consisting of three method blanks, one process blank (wheat flour) and three liquid primary reference standards (PRS; 50 mg of 100 ng/g NIST-3133 in 1% BrCl). Daily performance of the instrument was assessed based on the three liquid PRS and all data were corrected accordingly if the measured PRS were within 90% to 110% of the expected value. If PRS were outside this acceptable range, the instrument was re-calibrated. Each sequence consisted of four SRMs, one process blank consisting of commercial wheat flour and 35 samples. Sequences were rejected if one SRM value was outside of the certified uncertainty range (NIST-1515) or 10% of the respective target concentration (ICP Forests spruce B) or if the absolute Hg content of the flour blank was > 0.3 ng. The average recovery for Hg during measurement of all samples in this study was 99.9% ± 4.0% (mean ± sd) (n = 15) for NIST-1515 and 101.6% ± 6.9% (mean ± sd) (n = 40) for ICP Forests spruce B. The process blanks exhibited an average Hg content of 0.10 ng ± 0.09 ng (mean ± sd) (n = 23). As an additional quality control, we passed the 21st and 22nd ICP Forests needle/leaf interlaboratory comparison test 2018/2019 and 2019/2020 for Hg.

2.2.4 Bottom-up calculation of foliar Hg uptake fluxes

Foliar Hg concentration (μg Hg $g_{d.w.}^{-1}$) of each leaf/needle sample was multiplied with the respective sample leaf mass per area (LMA; $g_{d.w.}$ m_{leaf}^{-2}) to obtain foliar Hg content normalized to leaf area (μg Hg m_{leaf}^{-2}). Foliar Hg uptake rates (uptakeRleaf area; μg Hg m_{leaf}^{-2} $month^{-1}$) for each tree species were derived from the change in Hg content normalized to leaf area over time (3 to 6 points in time) using a linear regression fit. Linear regression was performed applying an ordinary least square model in the Python module statsmodels (Python 3.7.0). Linear regression parameter (R2) of each site and tree species are summarized in Table A.1. Foliar Hg uptake fluxes (uptakeFground area; μg Hg m_{ground}^{-2} $month^{-1}$) per ground surface area were calculated by multiplying the foliar Hg uptake rates (uptakeRleaf area) with species-specific leaf area indices (LAIs; $m_{leafarea}^{2}$ m_{ground}^{-2}) in order to obtain foliar Hg uptake fluxes normalized to ground surface area:

$$uptakeF_{groundarea} = uptakeR_{leafarea} \cdot LAI \tag{2.1}$$

Fig. 2.2 illustrates this flux calculation schematically. We used species-specific LAIs retrieved from a global data base provided by Iio and Ito (2014) [115]. In total, 205 values of one-sided LAIs measured in Central Europe and Scandinavia between a latitude of 46° N and 63° N and

published in peer-reviewed journals were selected for calculating an average LAI value of each species. Species-specific average LAI values are displayed in Table A.2. All LAI values for each species are peak-season values. To calculate the foliar uptake flux over the growing season, the average daily uptake flux was multiplied by the length of the growing season in days. For each site, the growing season length in days, which depends on the latitude of the site, was obtained from Garonna et al. [116], Rötzer and Chmielewski [117] (Table A.1). The approximate relative abundance of sampled tree species (Table A.6) at the four research sites Hölstein, Hyltemossa, Norunda and Svartberget were obtained by research staff (pers. communication). We calculated the total foliar Hg uptake flux for these four research sites as the sum of species-specific foliar Hg uptake fluxes of all locally dominant tree species multiplied by their relative abundance (Table A.6).

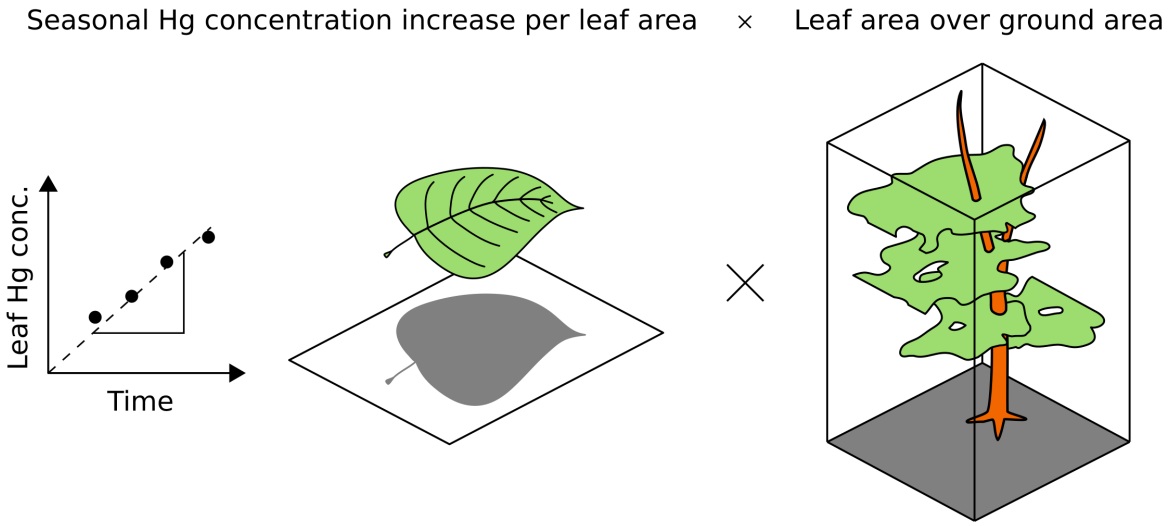

FIGURE 2.2. Bottom-up approach (Eq. 2.1) for calculating foliar Hg uptake flux per ground area (uptakeF; ng Hg m^{-2}_{ground} $month^{-1}$). The linear regression slope of leaf Hg concentration (ng Hg $g^{-1}_{d.w.}$) over time is multiplied with the respective sample leaf mass per area (LMA; $g_{d.w.}$ $m^{-2}_{leafarea}$). The resulting foliar Hg uptake rate per leaf area (uptake$R_{leafarea}$; ng Hg m^{-2}_{leaf} $month^{-1}$) is then multiplied with the species-specific leaf area index (LAI; $m^{2}_{leafarea}$ m^{-2}_{ground}).

2.2.5 Correction factor for needle Hg uptake flux as function of needle age

At all sites, we investigated Hg concentrations in multi-year pine and spruce needles from the current season (y_0, needles sprouting in spring of the sampling year) and in one-year old needles (y_1, needles sprouting in the year prior to the sampling year). At 5 sites (Bredkälen, Hölstein, Hyltemossa, Schauinsland and Schmücke) we additionally sampled two-year old (y_2) and three-year old (y_3) spruce needles. Sampling and measuring Hg uptake in all needle age classes of a conifer tree is time-consuming and costly. In standard forest monitoring programs young needles from age class y_0 or y_1 are usually sampled. We determined a species-specific

age correction factor (cf_{age}) to relate the needle uptake of an entire coniferous tree to the current season (y_0) needles. The factor cf_{age} was derived from Hg measurements of 316 needle samples of different age classes using i) the evaluated relative Hg accumulation rate (RAR; Eq. 2.2), which represents the Hg accumulation of each needle age class normalized to the Hg accumulation rate in current season (y_0), and ii) the respective relative biomass (RB) of each needle age class to the total needle biomass from literature determined by Matyssek et al. [118]. Needles used to determine the RAR were sampled by the Bavarian State Institute of Forestry at 11 ICP Forests plots in Bavaria, Germany in 2015 and 2017. Needle samples from 2015 consisted of 33 batches of spruce and 6 batches of pine samples. Needle samples from 2017 consisted of 32 batches of spruce and 6 batches of pine samples. For spruce needles, each batch was composed of samples of age class y_0 to age class y_3, of which 7 spruce needle batches were composed of samples of age class y_0 to y_5 and 6 spruce needle batches of age class y_0 to y_6. For pine needles, each batch of the two sampling years 2015 and 2017 was composed of samples of age class y_0 to y_1 and one pine needle batch was additionally composed of samples of age class y_2. The RAR of spruce and pine samples of different needle years (y_i, i = 1, 2, ..., n) in each sample batch of the sampling years 2015 and 2017 was calculated as follows:

$$RAR_{y_i} = \frac{c_{Hg}(y_i) - c_{Hg}(y_{i-1}))}{c_{Hg}(y_0)} \tag{2.2}$$

Resulting average RARs of the spruce and pine needle samples together with the RB are presented in Table A.3. For each needle age class the factor cf_{age} calculates as

$$cf_{age} = 1 \cdot RB_{y_0} + RAR_{y_1} \cdot RB_{y_1} + ... + RAR_{y_n} \cdot RB_{y_n} \tag{2.3}$$

In accordance to our bottom-up approach for calculating the foliar Hg uptake flux (Eq. 2.1) the modified flux calculation for conifers is:

$$uptakeF_{groundarea} = cf_{age} \cdot uptakeR_{y_{0;needlearea}} \cdot LAI \tag{2.4}$$

Final values of cf_{age} are summarized in Sect. A.6, Table A.3.

2.2.6 Correction factor for foliar Hg uptake flux as function of crown height

Standard foliage sampling in forest monitoring programs is from the top third of the crown [108]. We determined a species-specific height correction factor (cf_{height}) allowing to scale up the treetop foliar Hg uptake flux to whole-tree foliage. The species-specific height correction factor equals the multiplication of two ratios: i) the ratio $r_{conc.coeff.}$ of the linear regression coefficient (ng Hg $g_{d.w.}^{-1}$ $month^{-1}$) of Hg concentrations in foliar samples over the growing season at ground/mid canopy level to the equivalent coefficient at top canopy level and ii) the

ratio r_{LMA} of average LMA at ground/mid canopy level to the average LMA at top canopy level (Eq 2.5).

$$cf_{height} = r_{conc.coeff.} \cdot r_{LMA} \cdot \frac{conc.coeff._{ground}}{conc.coeff._{topcanopy}} \cdot \frac{LMA_{ground}}{LMA_{topcanopy}} \tag{2.5}$$

According to ecosystem models on light attenuation and photosynthesis in tree canopies [55, 119, 120] the 3 top canopy layers of leaf area intercept almost 90% of available sunlight leaving the lower leaf layers with reduced light. We thus assume that the top 3 canopy layers of leaf area index (LAI; $m^2_{leaf\,area}\ m^{-2}_{ground}$) mainly consist of sun-adapted foliage (i.e. sun-leaves) with Hg uptake rates corresponding to the uptake rates measured at top canopy. Leaf area indices and vertical foliar biomass distribution differ among tree species [121–125]. We did not apply a height correction for tree species with a LAI ≤ 3. For tree species with leaf area indices > 3 we assumed the following species-specific foliar Hg uptake flux of the whole tree foliage (uptakeF) in extension of Eq. 2.1:

$$uptakeF_{groundarea} = uptakeR_{topcanopy;leafarea} \cdot (3 + cf_{height} \cdot (LAI - 3)) \tag{2.6}$$

Final values of cf_{height} are summarized in Sect. A.11, Table A.5.

2.3 Results and Discussion

2.3.1 Effect of needle age on foliar Hg uptake

Spruce and pine revealed increasing Hg concentration with needle age at all sites (Fig. A.5). In order to demonstrate the increase in Hg concentration with needle age class, we display results from Hölstein, Hyltemossa and Schauinsland (Fig. 2.3). The average late season Hg concentration in one-year old (y_1) spruce needles was by a factor of 1.8 $\pm$ 0.4 (mean $\pm$ sd of all sites) times higher than the average late season Hg concentration in current season (y_0) spruce needles. From spruce needle age class y_2 to y_1 the ratio of average Hg concentrations was 1.3 $\pm$ 0.1 and from y_3 to y_2 1.4 $\pm$ 0.1. For pine the corresponding ratio was 1.9 $\pm$ 0.2 (mean $\pm$ sd of all sites) from y_1 to y_0 needles. Consequently, needle Hg concentrations in spruce and pine almost doubled from the season of sprouting to the subsequent growing season one year later. Needles older than one year (y_2, y_3) continue to accumulate Hg albeit at a slower rate than younger needles (y_0, y_1). This finding is in agreement with previous studies that reported positive trends of Hg concentration in spruce needles from age class y_1 to y_4 [95–97].

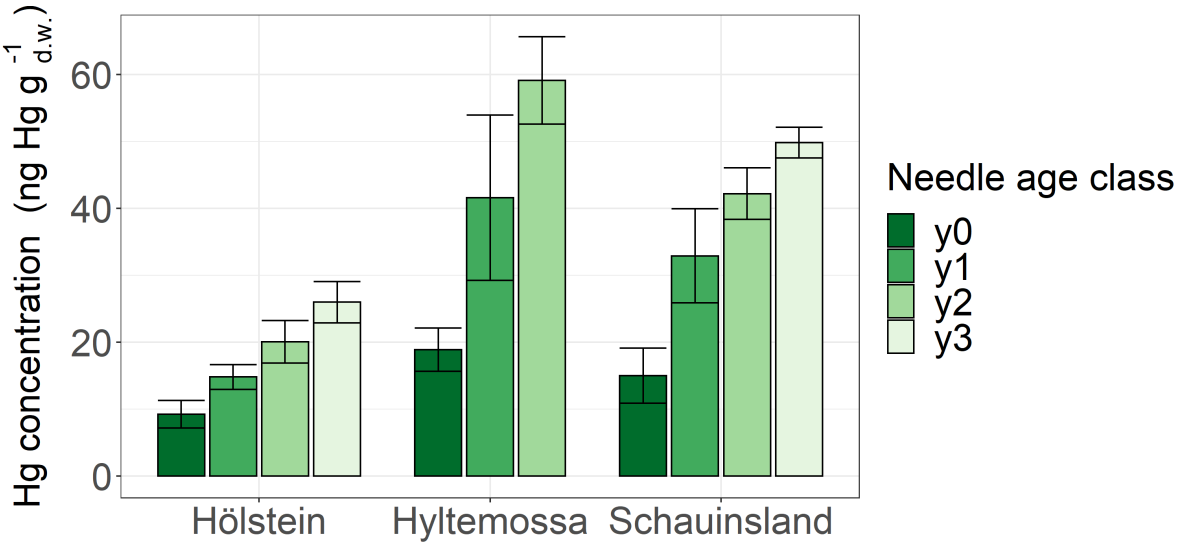

FIGURE 2.3. Hg concentrations (ng $g_{d.w.}^{-1}$) in spruce needles of four different age classes sampled at 3 research sites (Hölstein, Hyltemossa and Schauinsland) at the end of the 2018 growing season (October – November). Age class y_0 represents current season needles, age classes y_1, y_2 and y_3 one-, two- and three-year old needles, respectively. Error bars denote ± one standard deviation of samples taken from multiple trees at each site.

We systematically investigated age dependency of Hg accumulation rates using 292 spruce and 24 pine needle samples of age class y_0 to y_6 sampled by the Bavarian State Institute of Forestry in 2015 and 2017 (Sect. 2.2.5). The relative accumulation rate (RAR) represents the Hg accumulation of an individual needle age class normalized to the respective Hg accumulation rate in the current season y_0 needles (Eq. 2.2). Needles of all age classes continue to accumulate Hg, which is in concurrence with our 2018 Hg concentrations of needles y_0 to y_3 (Fig. 2.3). However, RAR decrease with needle age (Fig. 2.4). Assuming a linear decline in Hg uptake with spruce needle age, the mature needles (y_n) took up -0.17 ± 0.03 (linear regression coefficient ± se) in 2015 and -0.10 ± 0.02 (linear regression coefficient ± se) in 2017 than the previous age class y_{n-1}. The negative linear trend of pine needle Hg uptake was -0.18 ± 0.02 (linear regression coefficient ± se) in 2015 samples (from y_0 to y_2 Hg uptake) and -0.17 (linear regression coefficient) in 2017 samples (from y_0 to y_1 Hg uptake).

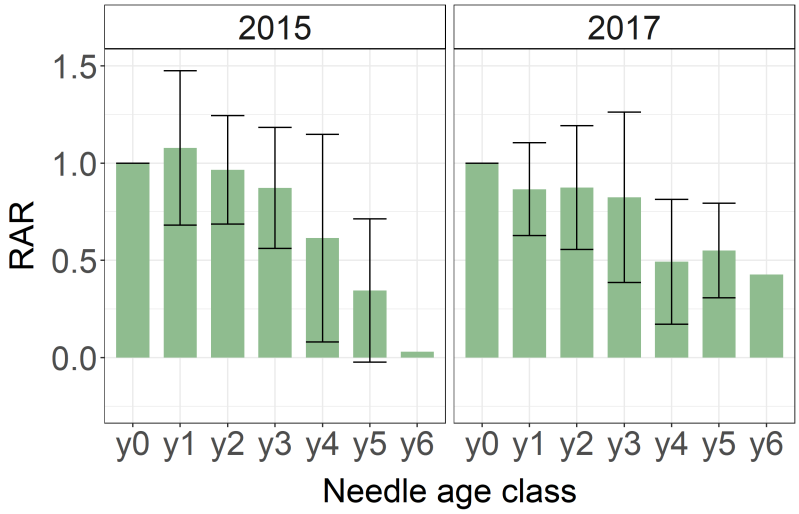

FIGURE 2.4. Average relative Hg accumulation rates (RAR) of 292 spruce needle samples of age class y_0 and y_6 taken by the Bavarian State Institute of Forestry in the two sampling years 2015 (left) and 2017 (right). The RAR represents the ratio of average Hg accumulation rate of the respective needle age class to the Hg accumulation of needle age class 0 (y_0). Error bars denote one standard deviation for RAR of needles sampled from multiple trees and sites.

The decline of Hg RAR with age could be related to a decrease in physiological activity with needle age. The rate of photosynthesis and stomatal conductance decreases in older needles [126–131]. Consequently, a physiologically less active older needle accumulates less Hg(0). Additionally, adsorption of Hg(0) to needle wax layers as a possible nonstomatal uptake pathway might be minimized in older needles because ageing needles suffer from cuticular wax degradation [132, 133]. As older needles exhibited higher Hg concentrations than younger needles, the Hg re-emission flux might increase with age. Differences of Hg RARs between sampling years 2015 and 2017 (Fig. 2.4) could be the result of climatic conditions during the two years like precipitation rates, temperature or vapor pressure deficit which impacts needle stomatal conductance and possibly stomatal Hg(0) uptake [134].

The continued Hg accumulation by needles over their entire life cycle has implications for the comparability of foliar Hg concentrations in needles and deciduous leaves. Deciduous leaves (beech and oak) exhibit higher average Hg concentrations than coniferous needles (pine and spruce) of the same age (y0) (see Table A.4 for data from Hölstein site). However, multi-year old pine and spruce needles can reach average Hg concentration values higher than leaves (A.8). We stress that needle age has to be reported in publications in order to avoid confusion when comparing foliar Hg concentrations of tree functional groups (deciduous vs. coniferous). Furthermore, Hg concentrations of all needle age classes have to be taken into account when calculating foliar Hg pools of coniferous forests (see A.9 for an exemplary needle Hg pool calculation).

From RAR values of our systematic needle analysis (Fig. 2.4) we calculated needle age correction factors (cf_{age}) according to Eq. 2.3 in order to scale up Hg uptake fluxes determined for y_0

needles to Hg uptake fluxes in needles of all age classes (Eq. 2.4). The correction factor cf_{age} was 0.79 $\pm$ 0.03 (factor according to Eq. 2.3 $\pm$ se) for spruce and 0.87 $\pm$ 0.06 (factor according to Eq. 2.3 $\pm$ se) for pine (see A.6 for details).

2.3.2 Effect of crown height on foliar Hg content

Foliar Hg concentration, leaf mass per area (LMA) and Hg content normalized to leaf area measured at Hölstein exhibited vertical variation with crown height (Fig. 2.5). In the following, we discuss all data relative to values measured at top canopy. Top canopy represents the foliage sampling height at the sun-exposed treetop, mid canopy describes the middle height range of sampled trees and ground level represents chest height (1.5 m).

Hg concentrations of beech (Fig. 2.5a), oak and spruce were lower in top canopy foliage than in foliage growing at ground level. By the end of the growing season (October), average Hg concentration in top canopy (33 – 38 m) beech leaves was 0.84 times and 0.72 times the average Hg concentration at mid canopy (18 – 21 m) and ground level (1.5 m) respectively. For oak, the ratio of average Hg concentrations in top canopy (28 – 38 m) leaves to mid canopy (19 – 22 m) leaves was 0.92 and for current season spruce needles the respective ratio was 0.85 from top canopy (43 - 47 m) to mid canopy (25 - 34 m) needles (spruce needles sampled in September 2019, see 2.2.2).

LMA of foliage samples from top canopies was higher than LMA of foliage samples from lower tree heights (Fig. 2.5b exemplary for beech). The season-averaged LMA ratio of top canopy foliar samples to ground foliar samples was 2.9 for beech, 1.3 for oak and 1.6 for spruce.

Because of the large vertical LMA gradient, foliar Hg content normalized to leaf area exhibited an opposite vertical gradient with tree height compared to Hg concentrations (Fig. 2.5c exemplary for beech). By the end of the growing season Hg content normalized to leaf area in top canopy (33 – 38 m) beech leaves was 1.17 times the Hg content per area in mid canopy (18 – 21 m) and 1.91 times in ground level (1.5 m) leaves. The equivalent ratio of Hg content per area in oak leaves was 1.13 from top canopy (28 – 38 m) to mid canopy (19 – 22 m) and 1.55 for spruce needles from top (43 - 47 m) to mid canopy (25 - 34 m).

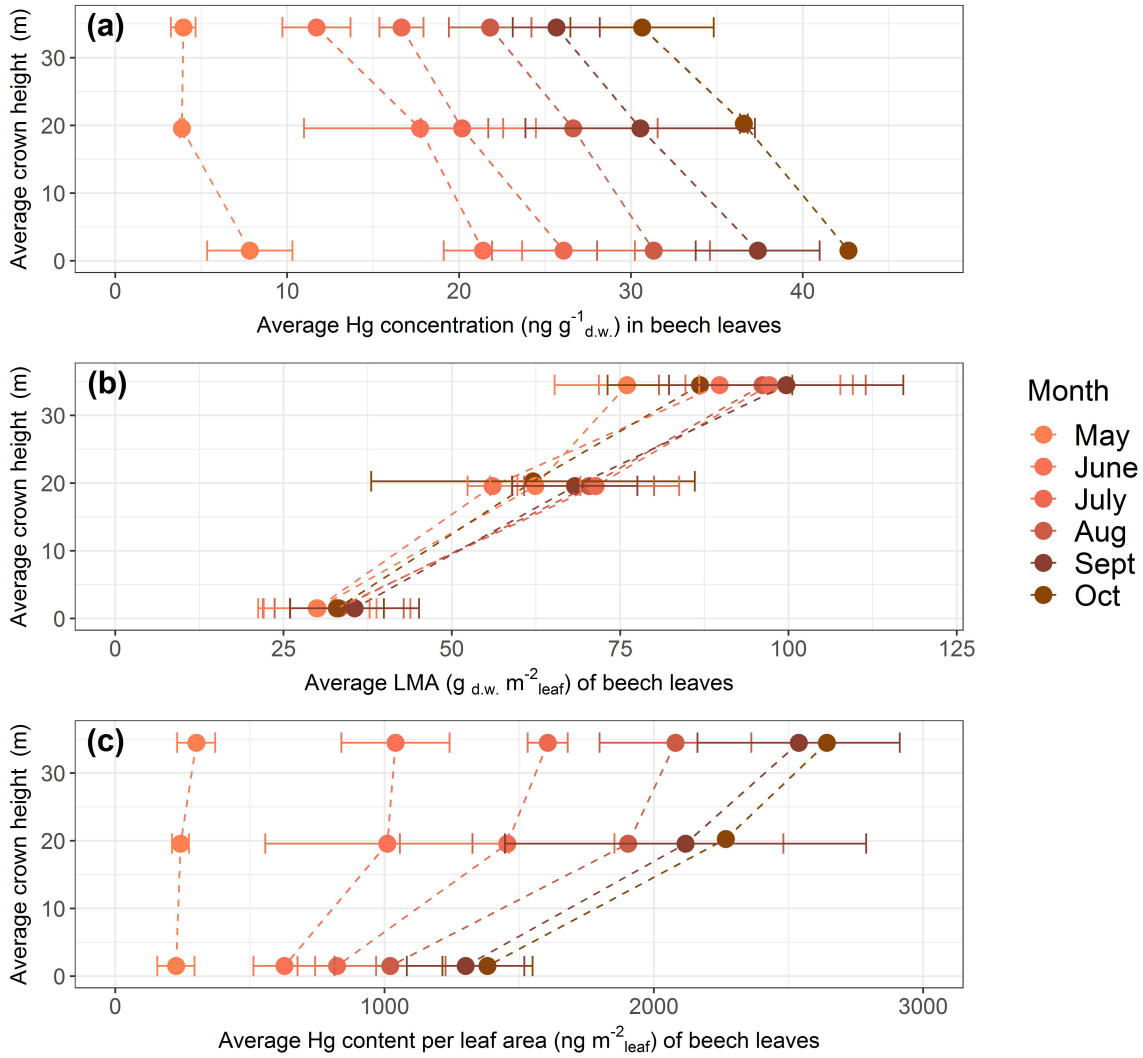

FIGURE 2.5. Average values of beech leaf parameters as a function of average tree crown height in meters above ground level at Hölstein, Switzerland over the course of the 2018 growing season: a) Hg concentrations (ng Hg $g_{d.w.}^{-1}$), b) leaf mass per area (LMA; $g_{d.w.}$ m_{leaf}^{-2}), c) Hg content normalized to projected leaf area (ng Hg m_{leaf}^{-2}). Error bars denote one standard deviation of leaf samples from multiple beech trees (n = 3 – 5).

Gradients of LMA with tree height are a result from leaf adaptation to changing light conditions and have previously been reported by multiple studies [135–140]. Leaves exposed to intense sunlight in tree canopies tend to grow thicker and denser thereby accumulate more photosynthesizing biomass per unit surface area [141, 142]. It is thus likely that foliar Hg content per gram dry weight is diluted in sun exposed canopy leaves relative to lower growing shade leaves explaining the observed gradient in foliar Hg concentrations with tree height (Fig. 2.5a). Foliar Hg content normalized to leaf area (ng Hg m_{leaf}^{-2}; Fig. 2.5c) is derived from the multiplication of Hg concentrations and respective LMA. As the gradient of LMA values with height (Fig. 2.5b) is reversed to and steeper than the gradient in Hg concentrations with height (Fig. 2.5a), foliar Hg content per leaf area (Fig. 2.5c) decreases from top to ground level. Therefore,

care has to be taken when comparing different data sets of foliar Hg concentrations, as foliar Hg concentrations depend on leaf morphology, which varies with height and tree species.

2.3.3 Effect of crown height on foliar Hg uptake rates per leaf area

Hg uptake rates per leaf area (upkate$R_{leaf\,area}$) were higher in top canopy compared to mid canopy/ground level by a ratio of 2.19 for beech, 1.22 for oak and 1.72 for spruce. Thus, foliage takes up more Hg per area at top canopy level than at ground level (Fig. 2.6a exemplary for beech). We propose two mechanisms that possibly explain increasing Hg uptake rates per leaf area with crown height: (1) Vertical variation in stomatal density and stomatal conductance: Leaves from the top of the canopy (sun leaves) have been reported to exhibit a significantly higher mean stomatal density than leaves within the canopy (shade leaves) [143]. A higher stomatal density (number of stomata pores per unit leaf area) is associated with a higher Hg content per leaf area [38]. The observed gradient of higher Hg uptake per leaf area towards the top canopy (Fig. 2.6a) possibly reflects higher stomatal density in sun leaves compared to shade leaves at ground level. Supplementary to stomatal density, we hypothesize that stomatal conductance to water vapor is a defining parameter for foliar Hg uptake per area. We measured stomatal conductance under dry conditions at Hölstein at noon on 17 July 2019 and observed higher average values in top canopy beech leaves than in ground level beech leaves (Fig. 2.6b). Stomatal conductance to water vapor is subject to temporal change depending on meteorological conditions and soil moisture content [55, 144]. Nevertheless, the observed gradient in stomatal conductance with tree height (Fig. 2.6b) conceivably indicates that foliar-atmosphere exchange of water vapor and Hg(0) are related. (2) Vertical air Hg(0) gradient: We observed a small gradient in atmospheric Hg(0) from 1.6 ng m^{-3} at the top (35 m a.g.l) to 1.4 $\pm$ 0.08 ng m^{-3} at ground level (1.6 m a.g.l.) integrated over the growing season 2018 (May – October) and from 1.7 ng m^{-3} (35 m a.g.l) to 1.4 ng m^{-3} (1.6 m a.g.l.) integrated over the growing season 2019 (May – September) (Fig. 2.6c). We hypothesize that depletion in atmospheric Hg(0) within the canopy was driven by foliar uptake of atmospheric Hg(0) [31, 145]. The vertical Hg(0) gradient in air possibly contributed to the gradient of Hg content per leaf area in beech, oak and spruce from top canopy to ground/mid canopy because ground level leaf area intercepts less air Hg(0) than canopy leaf area. A caveat to consider is that the Hg(0) concentration gradient measured depends on sampling rates of deployed passive samplers, which were considered to be constant with height (detailed discussion in A.7).

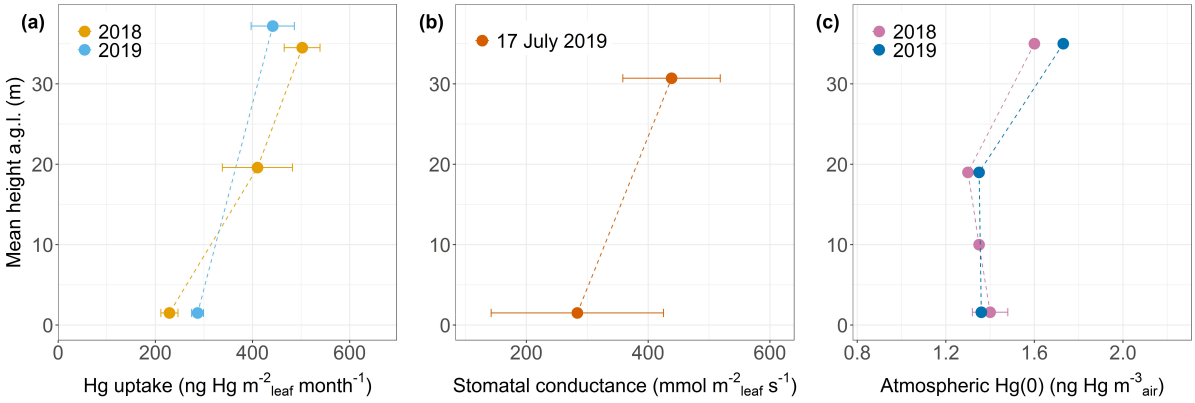

FIGURE 2.6. (a) foliar Hg uptake rate per leaf area (ng Hg m^{-2}_{leaf} $month^{-1}$; linear regression coefficient $\pm$ se) by beech leaves at various tree heights (m) at Hölstein during two growing seasons 2018 and 2019; (b) Stomatal conductance to water vapor (mmol m^{-2}_{leaf} s^{-1}; mean$\pm$ sd) measured in Hölstein beech leaves at top canopy and ground level under dry conditions at noon on 17 July 2019; (c) Atmospheric Hg(0) (ng Hg m^{-3} air) at various heights in Hölstein measured with passive air samplers and integrated over the 2018 and 2019 growing season respectively. Error bars at ground level height (1.6 m) of 2018 data denote $\pm$ one standard deviation for 4 passive samplers.

Re-emission of Hg(0) from foliage driven by photoreduction of Hg(II) to Hg(0) can counterbalance gross uptake of Hg(0) [35]. Re-emission rates will be enhanced in the top of the canopy due to higher light availability. However, re-emission rates were not large enough to compensate for higher Hg uptake per leaf area by top canopy leaves compared to ground level leaves (Fig. 2.6a).

2.3.4 Effect of tree functional group (deciduous vs. conifer) on foliar Hg uptake

Broad leaves of deciduous species (beech and oak) in Hölstein exhibited on average approximately five times higher Hg concentration increases (5.3 $\pm$ 0.6 ng Hg $g^{-1}_{d.w.}$ $month^{-1}$; mean $\pm$ se) compared to current-season pine and spruce needles (mean: 1.1 $\pm$ 0.4 ng Hg $g^{-1}_{d.w.}$ $month^{-1}$; mean $\pm$ se) (Fig. 2.7a). Higher Hg concentrations in broad leaves directly compared to conifer needles were also found by Blackwell and Driscoll [89], Navrátil et al. [90] but not by Obrist et al. [91], Hall and St. Louis [93], Obrist et al. [94]. Foliar Hg uptake rates normalized to leaf area in Hölstein were approximately 3 times higher in broad leaves (622 $\pm$ 84 ng Hg m^{-2}_{leaf} $month^{-1}$; mean $\pm$ se) than in conifer needles (222 $\pm$ 81 ng Hg m^{-2}_{leaf} $month^{-1}$; mean $\pm$ se) (Fig. 2.7b). Thus, our results exhibit higher foliar Hg uptake per leaf area in broad leaves than in current-season conifer needles.

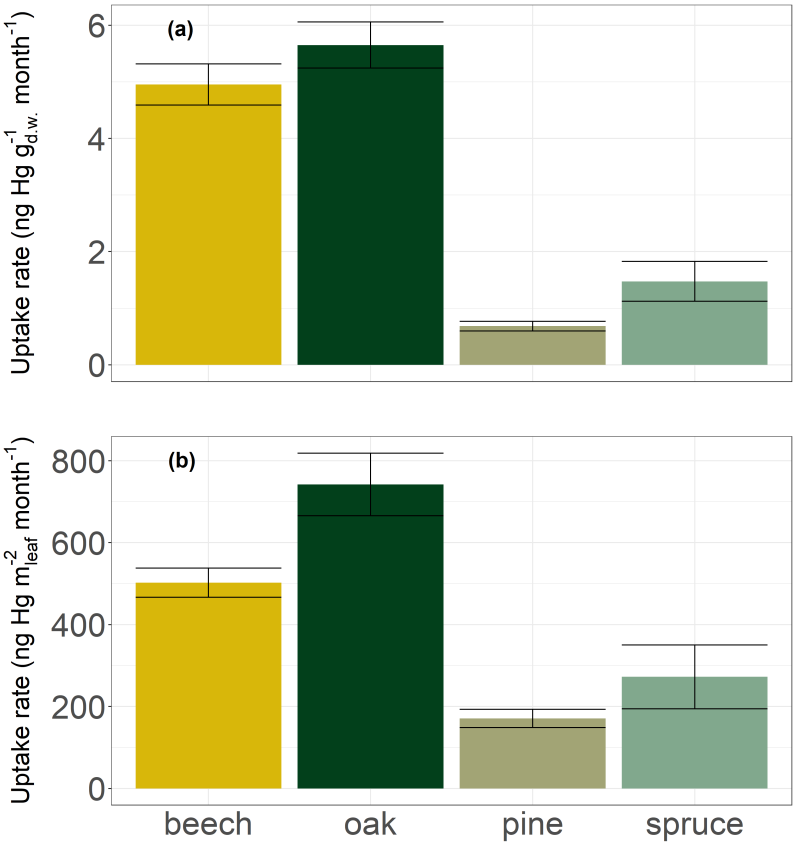

FIGURE 2.7. Uptake rates by leaves and current-season needles of 4 tree species at Hölstein (a) of ng Hg g^{-1} foliage dry weight and month; (b) of Hg uptake rate normalized to leaf area in ng Hg m^{-2}_{leaf} month^{-1}. Error bars denote standard errors of the linear regression of foliar Hg concentrations over the growing season.

We propose that Hg uptake rates have to be assessed in the context of different physiological characteristics of conifer needles and broad leaves. Needles generally have a larger LMA (245 $\pm$ 62 g m^{-2}_{leaf} in Hölstein) than broad leaves (79 $\pm$ 38 g m^{-2}_{leaf} in Hölstein). Plant tissues with large LMA such as needles are associated with low metabolic activity including photosynthesis and respiration [55, 146, 147]. Accordingly, the stomatal conductance to water vapor of canopy foliage in Hölstein on 17 July 2019 was lower for coniferous pine needles (289 $\pm$ 137 mmol m^{-2}_{leaf} s^{-1}; mean $\pm$ sd; n = 14) than for broad leaves of beech (438 $\pm$ 80 mmol m^{-2}_{leaf} s^{-1}; mean $\pm$ sd; n = 14) and oak (849 $\pm$ 221 mmol m^{-2}_{leaf} s^{-1}; mean $\pm$ sd; n = 15). The variation between foliage functional groups (conifer needles vs. broad leaves) indicates that foliar Hg uptake is related to stomatal conductance.

2.3.5 Foliar Hg uptake fluxes per ground area

We calculated foliar Hg uptake fluxes per ground area (m^2_{ground}) by multiplying foliar Hg uptake rates per leaf area (m^2_{leaf}) with species-specific LAI (Eq. 2.1). LAI values (mean $\pm$ sd) differed among tree species and were highest in spruce (7.3 $\pm$ 2.1) and beech (7.0 $\pm$ 1.6) and lowest in

pine (2.9 ± 1.4) and birch (2.6 ± 1.2) (Table A.2). In general, forests consisting of spruce trees with high LAI might therefore exhibit higher Hg uptake fluxes than deciduous forests with low average LAI even though Hg uptake rates per leaf area might be lower for conifer needles than for broad leaves (Sect. 2.3.4). We applied correction factors for needle age for conifer samples (Eq. 2.4) and crown height for sites where we collected top canopy samples (Hölstein, Hyltemossa, Norunda and Svartberget) (Eq. 2.6). The foliar Hg uptake flux showed a large variation ranging from 2 μg Hg m^{-2} (Pallas, pine) to 26 μg Hg m^{-2} (Schauinsland, beech) over the 2018 growing season (Fig. A.6). The 4 sites where samples were collected from top canopy exhibited a smaller range for spruce among sites from 7 to 15 μg Hg m^{-2} $season^{-1}$ (Fig. 2.8).

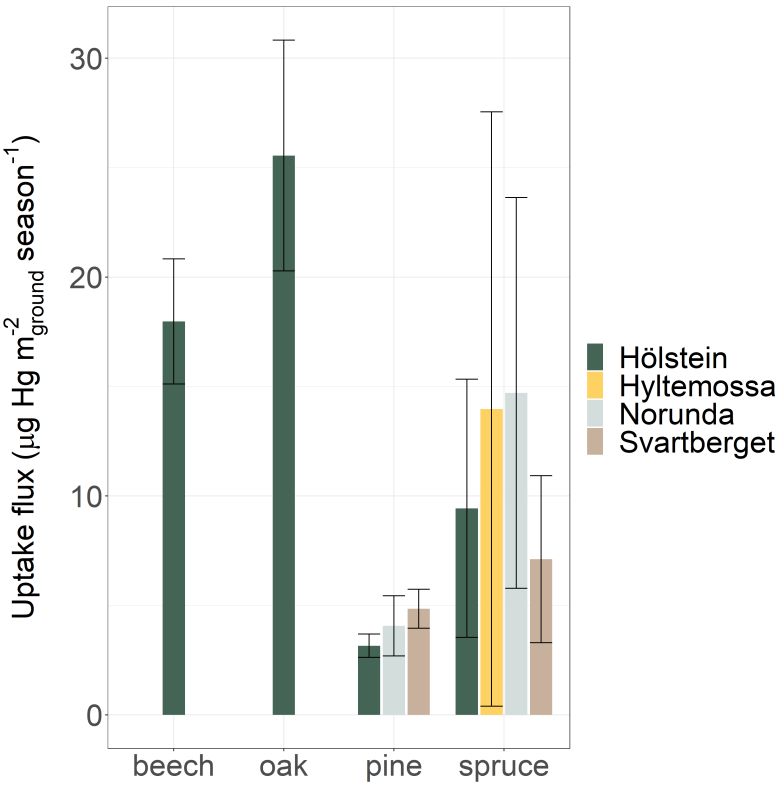

FIGURE 2.8. Foliar Hg uptake fluxes (μg Hg m^{-2} during the 2018 growing season) at four forested research sites where foliage samples were taken from crown height. Error bars indicate one standard error of the regression slope.

Given the systematic variation of Hg uptake rates with tree height (Fig. 2.5) we cannot exclude that the inconsistent sampling strategy might have influenced the observed Hg uptake fluxes among the 10 sampling sites. We will therefore not discuss further the observed variation among sites. To scale up site-based Hg uptake fluxes, we only consider sites where we consistently sampled the top third of the canopy (Hölstein, Hyltemossa, Norunda and Svartberget). The average foliar Hg uptake fluxes of each species at the four crown sampling sites (mean ± se of sites) during the 2018 growing season was 18 ± 3 μg Hg m^{-2} for beech, 26 ± 5 μg Hg m^{-2} for oak, 4 ± 1 μg Hg m^{-2} for pine and 11 ± 1 μg Hg m^{-2} for spruce (see A.15 for

standard errors of fluxes). Deciduous trees exhibited higher foliar uptake fluxes compared to coniferous trees resulting from generally higher uptake rates per leaf area (Fig. 2.7b) owing to higher physiological activity of deciduous trees.

2.3.6 Foliar Hg uptake fluxes along a latitudinal gradient in Europe

We calculated total Hg uptake fluxes at each research site as the sum of Hg uptake fluxes of each tree species and research site weighted by the relative abundance of the respective tree species to the other examined tree species at each site (Fig. 2.9a; Table A.6). The average foliar Hg uptake flux of the 4 research sites where foliage samples were obtained from tree crown heights over the 2018 growing season was 11 $\pm$ 3 μg Hg m^{-2} (mean $\pm$ sd). Spruce needle Hg uptake fluxes did not exhibit a clear trend with latitude (Fig. 2.9b with sites sorted for latitude). The aboveground foliar Hg uptake fluxes per site (range 6 - 14 μg Hg m^{-2} growing $season^{-1}$) are in the lower range of published Hg litterfall fluxes in Europe and North America measured for various years, which range from 9.7 to 28.5 μg Hg m^{-2} yr^{-1} [71, 74, 77, 80, 90, 148, 149]. The average wet Hg(II) deposition fluxes measured at Schauinsland, Schmücke, Råö, Bredkälen and Pallas over the course of the sampling period was 2.3 $\pm$ 0.3 μg Hg m^{-2} (mean $\pm$ sd). Wet Hg deposition fluxes were consistently lower than foliar Hg uptake fluxes. Our data constrain that foliar Hg uptake is a major deposition pathway to terrestrial surfaces in Europe, exceeding direct wet deposition of Hg(II) by a factor of four. Note that this assessment only compares Hg(0) uptake by foliage and does not take into account Hg incorporated into wood biomass [96] or Hg(0) adsorbed to leaf surfaces that is washed off between sampling events as throughfall [77, 149, 150]. Total Hg(0) deposition fluxes to terrestrial ecosystems, which also include Hg(0) deposition to soils and litter [70, 73, 151, 152] are therefore expected to be higher than foliar uptake fluxes quantified here.

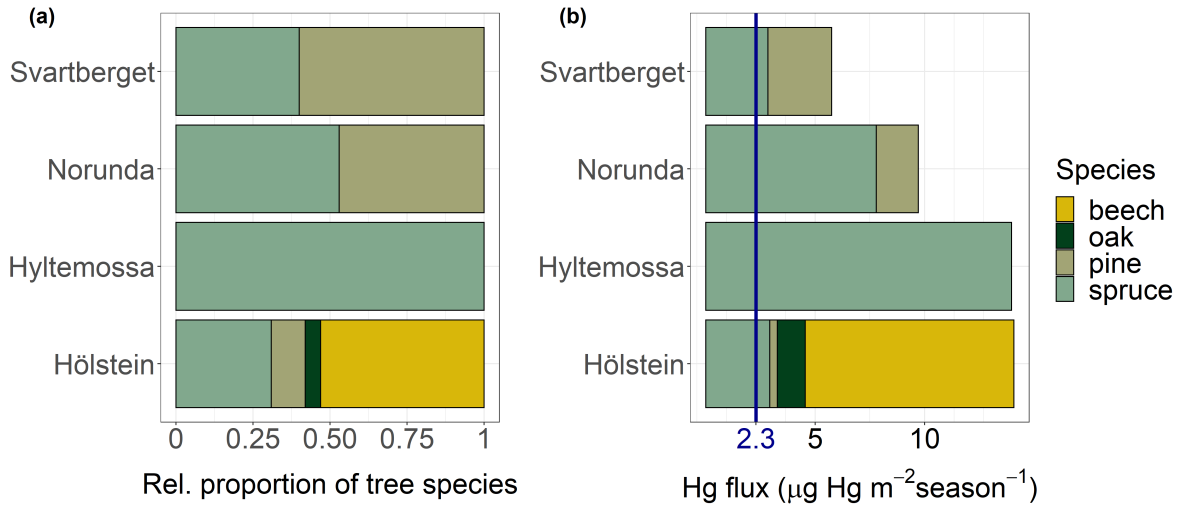

FIGURE 2.9. (a) Relative proportion of tree species to each other and (b) foliar Hg fluxes (μg Hg m^{-2} over the 2018 growing season) at 4 European research sites ordered by latitude from South (Hölstein at 47° N) to North (Svartberget at 64° N); blue label of 2.3 μg Hg m^{-2} season^{-1} corresponds to the average wet deposition flux measured at 5 sites over the course of the sampling period

Averaging species-specific foliar Hg uptake fluxes and weighting them with the tree species proportion in Europe derived from Brus et al. [153] yields an average foliar Hg uptake flux for Europe of 10.4 $\pm$ 2 μg Hg m^{-2} over the 2018 growing season (weighted mean $\pm$ se). Extrapolation of this weighted mean to the land area of European forests (192.672 $\cdot$ 10^6 hectares) results in a foliar flux of 20$\pm$ 3 Mg Hg during the 2018 growing season (see Sect. A.14 for details on flux extrapolation and Sect. A.15 for error propagation). Under the assumption that tree species in the global temperate zone are distributed equally to tree species in Europe we estimated an approximate foliar flux of 108 $\pm$ 18 Mg Hg to the area of global temperate forests (1.04 $\cdot$ 10^9 hectares) [154] during the 2018 growing season. This global extrapolation is at the lower end of global Hg litterfall deposition flux (163 Mg Hg yr^{-1}) estimated for temperate forests based on a Hg litterfall flux database of measurements between 1995 – 2015 [30]. In order to obtain a more precise foliar Hg uptake flux estimate to European and global forests, improved spatially resolved foliar Hg data and comprehensive ground-based forest statistics of tree species composition are needed.

2.3.7 Conclusions

We observed that Hg concentrations in foliage increased over the growing season in broadleaf and coniferous trees. Concentrations of Hg in multi-year needles increased with age. The foliar Hg uptake normalized to leaf area was higher on top of the canopy than at ground level. The temporal and vertical variation of foliar Hg uptake fluxes are consistent with the notion that stomatal uptake represents the main deposition pathway to atmospheric Hg(0). We emphasize that standardized sampling strategies and reporting of sampling height and needle age class is

essential to allow for comparison of foliar Hg results among different studies.
We developed a bottom-up approach to quantify foliar Hg(0) uptake fluxes on an ecosystem scale, considering the systematic variations in crown height, needle age and tree species. Our bottom-up approach integrates aboveground foliar Hg(0) uptake rates over the entire growing season and the whole tree level. We thus suggest that our approach provides a robust method to assess foliar Hg(0) uptake fluxes on a species level as well as on an ecosystem scale at a high temporal resolution. This approach is complementary to litterfall mass balances approaches, which provide Hg deposition estimates integrated over an entire year. We suspect that the foliar Hg uptake fluxes measured in this study represent net Hg(0) uptake fluxes as the increase of foliar Hg concentration was linear with time which would include possible Hg(0) re-emission from foliage [35]. With the bottom-up approach presented here, it is thus possible to obtain net foliar Hg(0) uptake fluxes that are temporally resolved over the growing season depending on the number of temporal foliar Hg measurements. The linear uptake of Hg(0) observed in this study across 10 European sites and for 6 different species suggests that forest foliage take up Hg(0) from the atmosphere over the entire growing season, supporting the notion that foliar uptake of Hg(0) drives the seasonal depletion in atmospheric Hg(0) in the Northern Hemisphere [12].
Our study demonstrates that foliar Hg uptake is an important deposition pathway to terrestrial surfaces and exceeds wet deposition by a factor of 4 on average. In contrast to Hg(II) in wet deposition, which is monitored in atmospheric deposition networks [66, 155], there is no standardized and established program to monitor Hg deposition in foliage or litterfall across Europe. We call for including foliar mercury deposition in monitoring networks on a country and international level. Robust and standardized data on the development of Hg deposition to foliage and forest ecosystems will allow to assess the effectiveness of the Minamata convention on mercury [27] and impact of climate change on mercury deposition to terrestrial ecosystems in the future.

Acknowledgments specific to this chapter

We are grateful to Fabienne Bracher, Emanuel Glauser and Judith Kobler Waldis for their help with foliage sample preparation and analysis. We acknowledge the Swiss Canopy Crane II (SCCII) Site at Hölstein operated by the Physiological Plant Ecology Research Group at the University of Basel and thank André Kühne and Matthias Arend for their on-site support. We thank Frank Wania from the University of Toronto for contributing valuable mercury passive air samplers and activated carbon. Hans-Peter Dietrich and Stephan Raspe from the Bavarian State Institute of Forestry thankfully provided us with multi-year foliage samples from Bavaria. We acknowledge ICOS Sweden for providing data from Hyltemossa, Norunda and Svartberget and we would like to thank Irene Lehner, Tobias Biermann, Michal Heliasz, Antonin Kusbach,

Johan Ahlgren, Ulla Nylander, Mikael Holmlund, Pernilla Löfvenius and Per Marklund for assistance in foliage sampling and experimental support. Volkmar Timmermann and Helge Meissner from NIBIO gratefully organized and performed foliage sampling at Hurdal. We thank Elke Bieber, Frank Meinhardt and Rita Junek from the German Federal Environment Agency for their support at Schauinsland and Schmücke air monitoring sites. We are grateful to Michelle Nerentorp Mastromonaco and Ingvar Wängberg from IVL and Eva-Britt Edin for foliage sampling support and site access at Råö and Bredkälen. We thank Katriina Kyllönen from FMI and Valtteri Hyöky for foliage sampling assistance and site access at Pallas. Special thanks go to Jann Launer for drawing Fig. 2.2. Finally, we thank Christian Körner for his helpful answers to questions on plant physiology.

Chapter 3

Physiological and climate controls on foliar mercury uptake by European tree species

This chapter has been published as an open access paper in the journal Biogeosciences (Copernicus Publications for the EGU) and can be found under DOI: 10.5194/bg-19-1335-2022.

This chapter was co-authored by:
Lena Wohlgemuth, Pasi Rautio, Bernd Ahrends, Alexander Russ, Lars Vesterdal, Peter Waldner, Volkmar Timmermann, Nadine Eickenscheidt, Alfred Fürst, Martin Greve, Peter Roskams, Anne Thimonier, Manuel Nicolas, Anna Kowalska, Morten Ingerslev, Päivi Merilä, Sue Benham, Carmen Iacoban, Günter Hoch, Christine Alewell, Martin Jiskra

Abstract

Despite the importance of vegetation uptake of atmospheric gaseous elemental mercury (Hg(0)) within the global Hg cycle, little knowledge exists on the physiological, climatic and geographic factors controlling stomatal uptake of atmospheric Hg(0) by tree foliage. We investigate controls on foliar stomatal Hg(0) uptake by combining Hg measurements of 3,569 foliage samples across Europe with data on tree species traits and environmental conditions. To account for foliar Hg accumulation over time, we normalized foliar Hg concentration over the foliar life period from the simulated start of the growing season to sample harvest. The most relevant parameter impacting daily foliar stomatal Hg uptake was tree functional group (deciduous versus coniferous trees). On average, we measured 3.2 times higher daily foliar stomatal Hg uptake rates in deciduous leaves than in coniferous needles of the same age. Across tree species, for foliage of beech and fir, and at two out of three forest plots with more than 20 samples, we found a significant ($p < 0.001$) increase in foliar Hg values with respective leaf nitrogen concentrations. We therefore suggest, that foliar stomatal Hg uptake is controlled by tree functional traits with uptake rates increasing from low to high nutrient content representing low to high physiological activity. For pine and spruce needles, we detected a significant linear decrease of daily foliar stomatal Hg uptake with the proportion of time during which water vapor pressure deficit (VPD) exceeded the species-specific threshold values of 1.2 kPa and 3 kPa, respectively. The proportion of time within the growing season during which surface soil water content (ERA5-Land) in the region of forest plots was low correlated negatively with foliar Hg uptake rates of beech and pine. These findings suggest that stomatal uptake of atmospheric Hg(0) is inhibited under high VPD conditions and/or low soil water content due to the regulation of stomatal conductance to reduce water loss under dry conditions. Other parameters associated with forest sampling sites (latitude and altitude), sampled trees (average age and diameter at breast height) or regional satellite observation-based transpiration product (GLEAM) did not significantly correlate with daily foliar Hg uptake rates. We conclude that tree physiological activity and stomatal response to VPD and soil water content should be implemented in a stomatal Hg model, to assess future Hg cycling under different anthropogenic emission scenarios and global warming.

3.1 Introduction

Mercury (Hg) is a toxic pollutant that is emitted by anthropogenic and geogenic activities into the atmosphere, where it can be transported over large distances and is eventually transferred to terrestrial and ocean surfaces by dry or wet deposition [15]. From a public health perspective, transfer rates of Hg to aquatic ecosystems are particularly relevant within this cycle, since Hg bioaccumulation in fish for consumption represents the most important Hg exposure pathway to many communities internationally [4]. In order to constrain future Hg levels in edible fish and to assess how Hg exposure responds to curbed anthropogenic Hg emissions under the

policies implemented by the 2017 UN Minamata convention on mercury, it is essential to understand and quantify all major net deposition fluxes within the global Hg cycle. Wet deposition occurs when water-soluble oxidized Hg(II) is washed out from the atmosphere with rainwater [1, 6] or by cloud water interception [156]. In a dry deposition process, gaseous elemental Hg(0) and Hg(II) directly bind to surfaces [15] or Hg(0) is taken up by plants [9]. For more than two decades, vegetation has been recognized as important vector for Hg(0) dry deposition within the terrestrial Hg cycle [80, 149, 157]. Based on this seminal work, researchers have since highlighted that vegetation impacts Hg levels of all other environmental compartments within the active Hg cycle [9, 15, 158]. Vegetation uptake of Hg(0) governs the seasonality of atmospheric Hg(0) in the Northern Hemisphere with concentration minima in summer at the end of the growing season [12]. Thus, vegetation has been suggested to operate like a global Hg pump [12, 88]. Atmospheric Hg(0) taken up by vegetation is oxidized to Hg(II) within the plant tissue [50] and transferred to soils via litterfall [20, 30, 71, 72, 74, 159–161]. Moreover, in forests, Hg deposition to the ground may occur by wash-off of Hg(0) from plant surfaces via throughfall and by Hg(0) uptake into woody tissues, lichen, mosses and soil litter [10, 60, 162]. Mercury sequestered by forest ecosystems accumulates in soil and may subsequently be transported from watersheds to streams, rivers and the ocean, where it can bioaccumulate in fish [36, 37, 163].
Concerning the mechanism of Hg accumulation in foliage, there are multiple lines of evidence that leaf stomata control the foliar Hg(0) uptake flux to terrestrial ecosystems: (i) Hg concentrations were found to be higher in internal foliar tissues than on leaf surfaces [38]; (ii) experiments revealed that isotopic Hg tracers are transferred from the air to the leaf interior [41]; (iii) foliar Hg concentrations are associated with leaf stomatal density and net photosynthesis [38, 42]; (iv) the isotopic composition of foliage is discriminated in heavy isotopes compared to atmospheric Hg(0) [19, 21, 145, 164]; (v) temporal and vertical variations of net foliar Hg(0) uptake fluxes in trees agree with the mechanism of stomatal Hg(0) uptake [165]. While there is increasing consensus that vegetation uptake of atmospheric Hg(0) occurs via the stomatal pathway, there remain research gaps regarding parameters regulating this stomatal Hg(0) uptake [9]. Consequently, the Hg(0) dry deposition flux to terrestrial surfaces in Hg Earth System Models is generally parametrized by static inferential or resistance-in-series approaches [166]. Ecosystem processes, including canopy gas exchange, are sensitive to climate conditions [167] and vary between different plant species [168]. Trees control leaf diffusive gas fluxes through their stomata in order to optimize the diffusive influx of carbon dioxide for photosynthesis, while averting excessive loss of water vapor to the atmosphere [55]. The regulation of stomata allows trees to dynamically adjust their metabolism to climatic conditions (temperature, atmospheric humidity, water vapor pressure deficit, solar radiation) and site-specific limitations (soil moisture, nutrient availability) under the constraints of tree-specific prerequisites (leaf structure, leaf life span, water use efficiency).
In this study we aim to improve the process understanding of the stomatal Hg(0) uptake with

the long-term goal to advance the parameterization of the foliar Hg(0) uptake in Hg Earth System Models. The objectives of the study were: (i) to investigate how foliar Hg(0) uptake depends on the physiological traits of tree species, and (ii) to study how stomatal response of trees to climate conditions control foliar Hg(0) uptake. We address these objectives by analyzing a large dataset of foliar Hg uptake rates, tree functional traits and climate conditions across natural gradients in European forests covering various tree species and climate conditions.

3.2 Materials and Methods

3.2.1 Foliage sampling and data set description

The final dataset for this study comprises Hg concentrations of 3,569 foliage samples from 2015 and 2017, of which 2,129 samples were provided by 17 participating countries of the UNECE International Co-operative Programme on Assessment and Monitoring of Air Pollution Effects on Forests (ICP Forests). The samples include sun exposed leaves and needles from the upper third of the tree canopy of 5 trees (Austrian Bio-Indicator Grid: 2 trees) of the main species on the plot taken during full development in summer (deciduous species) or at the onset of dormant season in autumn (evergreen species) using harmonized national methods according to the ICP Forests Manual [108] as described e.g. in Jonard et al. [169]. Around 10% of samples were taken during winter needle sampling campaigns (December until March). Sample preparation procedure typically includes separation of needle age classes, drying, milling and chemical analyses for macronutrients and further drying of a subsample at 105°C to constant weight for the determination of dry weight. The participating ICP Forests countries harvested and carried out these preprocessing steps and collected the associated metadata. Hg measurements of samples from ICP Forests Level II plots were performed at the University of Basel. Additional foliar Hg concentration data of 1440 samples from the Austrian Bio-Indicator Grid organized by the Austrian Federal Research Center for Forests (German acronym BFW) (Austrian Bio-Indicator Grid) were included in the analysis. The combined dataset consists of 3,569 foliage samples encompassing 23 species of coniferous and deciduous trees (Table B.1). The most frequent (number of samples > 100) species within the dataset are Norway spruce (Picea abies; n = 2073), Scots pine (Pinus sylvestris; n = 413), European beech (Fagus sylvatica; n = 372), silver fir (Abies alba; n = 162), sessile oak (Quercus petraea; n = 133), Austrian pine (Pinus nigra; n = 125) and common oak (Quercus robur; n = 101). We pooled individual tree species into groups of tree species genera (e.g. beech, oak, pine, spruce), see Table B.1. Coniferous samples consist of needles of different age classes: most of the needle samples (n = 1958) flushed in the sampling season (current season; y_0), 600 samples are one-year old (y_1), 121 samples are two-year old (y_2), 125 are three-year old (y_3), 22 samples are four-year old (y_4), 60 samples are five-year old (y_5) and 3 samples are six-year old (y_6) needles. All data analysis of this study

concerning tree species, foliage structure, nutrient contents and meteorological and site-specific parameters (Sect. 3.3.1 – 3.3.6) is based on Hg values of current-season (y_0) foliage. Foliage samples originate from 995 European sites: 232 sites are ICP Forests Level II forest monitoring plots, 737 locations are sampling sites of the Austrian Bio-Indicator grid and the remaining sites (26) are not classified within the ICP Forests program. See Figure 3.1 for a geographic overview of foliage sampling sites from the sampling year 2017.

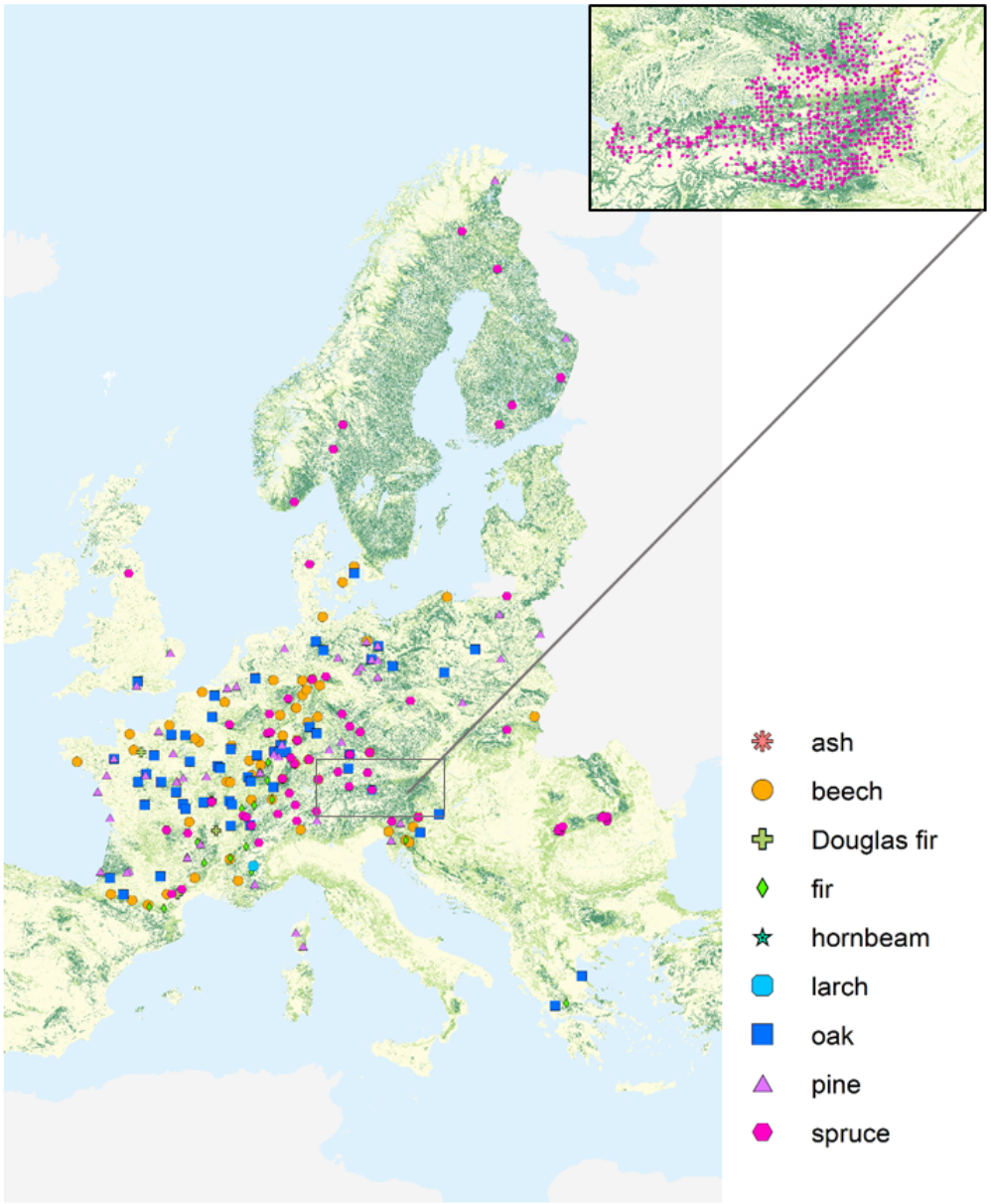

FIGURE 3.1. Overview of forest plots, at which Hg foliage samples were harvested from different tree species groups during the sampling year 2017. At around 12% of plots in 2017, foliage from more than one tree species group was sampled. Geographic distribution of sampling sites in 2015 is similar, except there were no samples from the ICP Forests partners Brandenburg (Germany), Baden-Württemberg (Germany) and Poland and there were samples from five additional plots in North Rhine-Westphalia (Germany), see Fig. B.1. The enlarged map view at the top right depicts sampling locations of the Bio-Indicator Grid in Austria in 2015 and 2017. Use of base map authorized under European Commission reuse policy [107].

We assembled the foliar Hg concentration dataset including the following metadata: sampling date, needle age class, leaf mass per area (LMA; 19% of samples), drying temperature, leaf nitrogen (N) and organic carbon (C_{org}) concentration. Foliage concentrations of N and Corg were measured in laboratories in respective ICP Forests countries following strict QA

procedures. The tolerable quality limit for N concentration measurements is ± 15% (for N concentration > 5 mg g^{-1}) of the mean inter-laboratory N concentration in foliar reference material distributed for ICP Forests laboratory comparison tests [108].
The measurements and observation from ICP Forests Level II forest plots additionally included the beginning of the growing season for the sampling years 2015 and 2017 (where available) [170], main tree species on the plot, mean age of trees on the plot (estimated during system installment), basal area and trees per hectare on the plot [171], soil texture of the upper soil layer (mineral soil between 0 – 5 cm or 0 – 10 cm from the survey years 2003 - 2019) [172, 173] as well as altitude and geographic coordinates. At the tree level, meta data consist of tree species, tree number and diameter at breast height [171]. Meteorological in-situ measurements of hourly temperature and relative humidity [174] were available for 82 forest Level II plots for both 2015 and 2017.
Furthermore, we amended the dataset with satellite-based values of transpiration from the Global Land Evaporation Amsterdam Model (GLEAM) [175, 176], of hourly soil water (layer 1, 0 – 7 cm) and surface air temperature (2 m height) from ERA5-Land [177] for the respective regions of every forest plot. GLEAM (v. 3.3a) data were available at daily resolution and on a 0.25° latitude-longitude regular grid. ERA5-Land values were available at hourly resolution and on a 0.1° latitude-longitude regular grid. For each forest plot, we calculated average daily GLEAM (v.3.3a) transpiration within the life period of foliage samples, from the beginning of the growing season to harvest. Similarly, from ERA5-Land values, we calculated the average 2 m air temperature within respective sample life periods. We detected outliers of time-normalized foliar Hg concentrations (see Sec. 3.2.3) within each tree species and needle age class by applying the modified Z score method according to Iglewicz and Hoaglin (1993) [178] using an absolute threshold value of 3.5, above which a modified Z score value was considered an outlier. As a result, 3.2% of values within the dataset were removed as outliers.

3.2.2 Correction of foliar Hg concentrations for drying temperature

Drying and grinding of foliage samples were carried out by ICP Forests laboratories and BFW. All foliar concentration values (Hg, N and Corg) within the dataset are normalized to dry weight for a sample drying temperature of 105 °C in order to make values internally consistent. The actual drying temperature differed between foliage samples (40 °C – 80 °C). In order to adjust for actual drying temperature, the laboratories determined the drying factor to correct for water content of each sample by drying an aliquot of foliage sample at actual drying temperature and subsequently at 105 °C. The drying factor was available for 62% of samples within the dataset. For the rest of the samples an average drying factors per tree species and needle age class was applied for drying temperature correction. Smallest average drying factor was 1.03 ± 0.003 (mean ± sd) for one-year old (y1) Pinus pinaster needles and biggest average drying factor was

1.07 ± 0.02 (mean ± sd) for Quercus robur leaves. Previous studies did not detect Hg losses with drying temperature in foliage [51, 165], wood [113] or moss [114].

3.2.3 Foliage Hg analysis

Total Hg concentrations in foliage samples from ICP Forests Level II plots were measured at the University of Basel using a direct mercury analyzer (Milestone DMA-80, Heerbrugg, Switzerland). Standard operation procedure involved measuring a pre-sequence of four blanks (three empty sample holders and wheat flour) and three liquid primary reference standards (50 mg of 100 ng g^{-1} NIST-3133 in 1% BrCl). If the three liquid primary reference standards were within 90% - 110% of expected value, we corrected all measurement results of the respective sequence accordingly. Otherwise, we discarded the sequence and re-calibrated the instrument. Standard reference materials (SRM) (NIST-1515 apple leaves and spruce needle sample B from the 19th ICP Forests needle/leaf interlaboratory comparison test) were measured in each sequence (4 SRM in a sequence of 40 samples) and the sequence was discarded, if the measured SRM value was outside the certified uncertainty range (NIST-1515) or outside ± 10% of the expected concentration (ICP Forests spruce B). Absolute Hg content in wheat blanks within the sequence had to be < 0.3 ng. We successfully participated in the 21st (2018/2019), 22nd (2019/2020) and 23rd (2020/2021) ICP Forests needle/leaf interlaboratory comparison (ILC) test. Total Hg concentrations in foliage samples from the Austrian Bio-Indicator Grid were measured using a Hg analyzer (Altec-AMA 254 HCS, Prague, Czech Republic). Standard operation procedure at BFW involved a pre-sequence of five blanks (empty nickel boats) and measurements of three samples of reference material (BCR-62 olive leaves or spruce needle samples from the 17th or 19th ICP Forests needle/leaf ILC test) after every 40th sample within a sequence. If the measurement results of the three reference samples were outside of 93% - 107% of expected value, a drift correction was performed. Final foliage Hg concentrations within the Bio-Indicator Grid represent average values of at least two replicates.

3.2.4 Determination of the beginning of the growing season for calculating daily foliage Hg uptake rates

Mercury concentrations in leaves and needles have been demonstrated to increase linearly over the course of the growing season [38, 80, 134, 165]. In this study, foliage samples within the data set were harvested at various points in time, making a direct comparison of measured Hg concentrations unfeasible. We therefore calculated foliar Hg uptake rates (in ng Hg $g_{d.w.}^{-1}$ d^{-1}) of current-season samples by normalizing foliar Hg concentrations to their respective life period in days from the beginning of the growing season (emergence of new foliage) to date of harvest. These resulting foliar Hg uptake rates are net Hg accumulation rates per gram dry weight on a

leaf basis and should not be confused with foliar Hg fluxes on a whole-tree basis. Please also note, that daily foliar Hg uptake rates in this study represent average values over the growing season. The actual daily foliar Hg uptake on a given day might differ from the average value depending on the time period within the growing season (e.g. early season vs. peak season) [38]. Needles of age 1 year or older were excluded from calculating daily foliage Hg uptake fluxes, since Hg uptake might slow down in physiologically less active older needles [165] and it is unclear, to which extend Hg uptake occurs in older needles in winter and in early spring before the emergence of new foliage. While dates of harvest were available for all samples, we determined the start of the growing season of current-season foliage by combining available data sources with start-of-season modelling. These data sources comprise in-situ phenological observations, which were available for 15% of samples, and observations of the emergence of current-season needles of coniferous tree species from the Pan European Phenological database PEP725 [179]. We assigned observations from PEP725 to the corresponding closest forest plot of the respective sampling year (2015 or 2017) by using the nearest neighbor function matchpt from the Biobase package in R [180], such that differences between PEP725 observation and forest plots did not exceed 3° in latitude, 30 m in altitude and closely matched longitude as possible. For details on the matching procedure and results see supplementary information, Sect. 3.3.1. To model the beginning of the growing season for deciduous trees, we utilized the leaf area index (LAI) product by Copernicus Global Land Service based on PROBA-V satellite imagery at a resolution of 300 m and 10 days [181, 182] following a recommendation by Bórnez et al. [183]. For information on the model and quality assurance, refer to supplementary information, Sect. 3.3.2.

3.2.5 Evaluation of data on water vapor pressure deficit (VPD)

At 82 ICP Forests Level II plots (in total from both years 2015 and 2017), in-situ meteorological data at an hourly resolution were recorded in 2015 and 2017, for which we calculated hourly water vapor pressure deficit (VPD) values at daytime (06:00 – 18:00 LT). The VPD represents the difference between the water vapor pressure at saturation and the actual water vapor pressure. We calculated saturated water vapor pressure from average hourly air temperature using the August-Roche-Magnus formula [184] and actual water vapor pressure as the saturation water vapor pressure multiplied by the average hourly relative humidity. These VPD values were calculated exclusively for daytime hours (06:00-18:00 LT), because both Hg(0) and photosynthetic CO2 uptake by trees are at maximum during the day [60]. From these daytime hourly VPD values at each forest plot, we calculated the proportion of hours within the daytime life period of the samples (from the beginning of the growing season to sampling day), during which VPD exceeded the four threshold values of 1.2 kPa, 1.6 kPa, 2 kPa and 3 kPa, respectively. We chose these four VPD thresholds as test values because they were reported in literature to

incrementally induce leaf stomatal closure of temperate forest trees, ranging from initial stomatal closure (around 0.8 kPa – 1 kPa [55]) to maximum stomatal closure (at around 3 kPa – 3.2 kPa [185]). We calculated the average proportion of daily daytime exceedance hours of VPD > respective threshold value by normalizing total number of respective daytime VPD exceedance hours with total number of daytime hours during the corresponding sample life period.

3.2.6 Evaluation of ERA5-Land volumetric soil water contents

We calculated the time proportion within sample life periods, during which the volumetric soil water content in the region of the respective forest plots fell below a soil texture dependent threshold value (PAW_{crit}) where plants are expected to close their stomata due to limited water availability. To this, we used the satellite-derived ERA5-Land data of hourly soil water in soil layer 1 (vertical resolution: 0 – 7 cm, horizontal resolution: 0.1° x 0.1°) [177] and data on soil texture of the respective forest plots, where available [172]. Field data from literature suggest, that plant stomata start to close, once the plant available water (PAW) in the soil falls below a critical value (PAW_{crit}) [186–188]. The soil PAW represents the difference between soil water at field capacity (SW_{FC}) and soil water at the permanent wilting point (SW_{PWP}). We calculated PAW_{crit} = 0.5 x PAW + SW_{PWP} following a recommendation by Büker et al. [189] and used PAW_{crit} as the threshold value to calculate the proportion of hours within the respective sample life periods, during which soil water < PAW_{crit}. See Figure B.11 for an exemplary time series of ERA5 soil water in the region of a forest plot in France in 2015. Soil texture specific values for SW_{FC} and SW_{PWP} (Table B.4) were obtained from Saxton and Rawls (2006) [190].

3.3 Results and Discussion

3.3.1 Variation of foliar Hg concentrations with foliar life period

Average foliar Hg concentrations (mean ± sd) differed between tree species groups (see Table B.1 for definition of tree species groups). Ash leaves exhibited highest Hg concentrations (32.2 ± 5.7 ng Hg $g_{d.w.}^{-1}$; n = 10), followed by beech leaves (25.5 ± 9.6 ng Hg $g_{d.w.}^{-1}$; n = 372), current-season Douglas fir needles (22.9 ± 6.7 ng Hg $g_{d.w.}^{-1}$; n = 27), hornbeam leaves (32.2 ± 5.7 ng Hg $g_{d.w.}^{-1}$; n = 10), oak leaves (20.8 ± 9.1 ng Hg $g_{d.w.}^{-1}$; n = 287), larch needles (13.4 ± 3.4 ng Hg $g_{d.w.}^{-1}$; n = 3), current-season spruce needles (11.8 ± 3.4 ng Hg $g_{d.w.}^{-1}$; n = 1509), current-season fir needles (11.4 ± 2.8 ng Hg $g_{d.w.}^{-1}$; n = 66) and current-season pine needles (11.0 ± 5.1 ng Hg $g_{d.w.}^{-1}$; n = 344). For all tree species sampled at more than 20 forest plots, we found significant ($p < 0.05$) positive trends of foliar Hg concentrations with respective sampling date within the growing season (see Figure 3.2 for beech and oak and Fig. B.4 for pine and spruce).

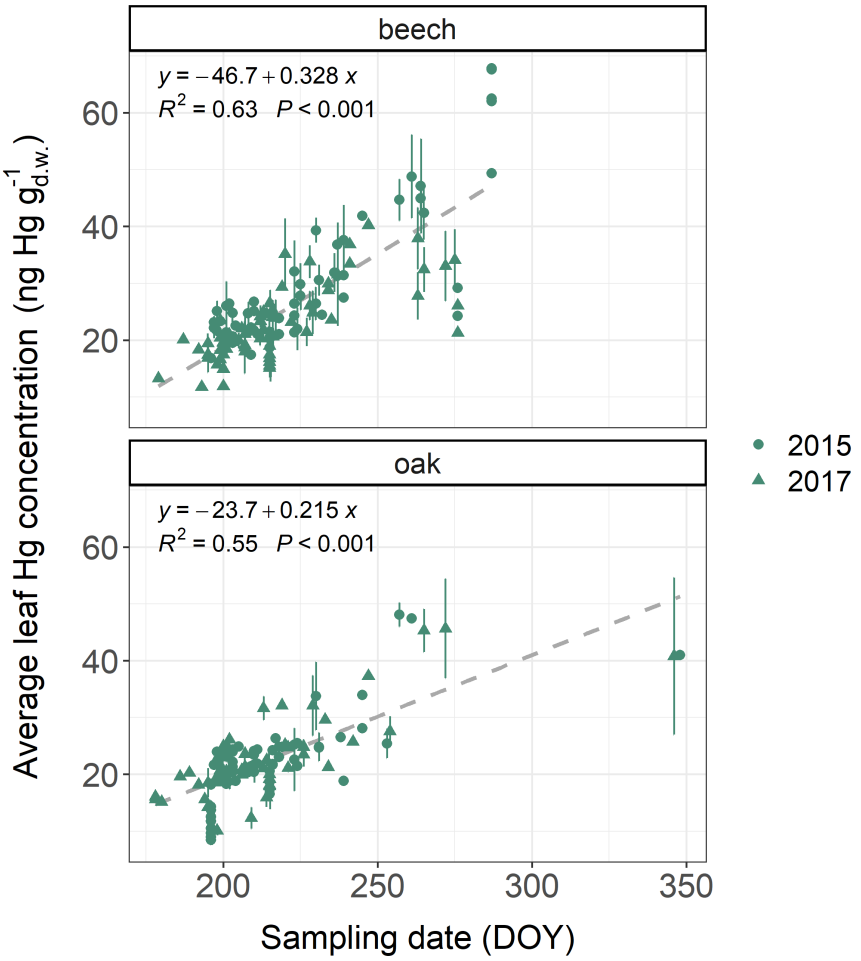

FIGURE 3.2. Average leaf Hg concentrations (ng Hg $g_{d.w.}^{-1}$) in beech and oak samples at multiple ICP Forests plots versus sampling dates (day of year; DOY) of respective samples. Sampling took place both in 2015 and 2017. Two plots of holm oak (Quercus ilex) are located in Greece and were sampled in December 2015 (DOY = 348) and December 2017 (DOY = 346). Error bars denote ± one standard deviation between multiple samples at each forest plot.

Increasing foliar Hg concentrations with progressing sampling date are in line with previous observations demonstrating that at individual sites Hg concentrations increased linearly over the growing season [38, 51, 80, 165]. To make Hg levels in foliage sampled at different times comparable, we calculated daily foliar Hg uptake rates by normalizing foliar Hg concentrations with the life period of samples. These daily foliar Hg uptake rates represent average values over the life period. The average life period (mean ± sd) of samples was 104 d ± 30 d for beech, 104 d ± 24 d for oak, 159 d ± 12 d for pine and 148 d ± 14 d for spruce. At five percent of spruce plots sampling took place in winter (December until March). Spruce and pine trees have been found to reduce their physiological activity (transpiration, net photosynthesis) at low soil temperatures (< 8 – 10 °C), potentially impacting stomatal Hg(0) uptake in winter [191, 192]. The average daily Hg uptake rates of current-season spruce needles sampled during peak season (0.084 ng Hg $g_{d.w.}^{-1}$ d^{-1}) and sampled during winter (0.067 ng Hg $g_{d.w.}^{-1}$ d^{-1}) were

significantly different (Welch two sample t-test; p = 0.015 at 95% confidence level). If spruce trees continue to accumulate Hg throughout the winter, Hg needle concentrations should be higher in winter samples than in samples harvested earlier during the growing season and Hg uptake rates per day should be comparable between winter and growing season samples. Thus, the difference of average daily Hg uptake between winter and growing season spruce needle samples indicates a decrease of Hg accumulation in spruce needles during winter. However, the potential of needle Hg uptake in winter needles requires further investigation, e.g. by performing a full winter sampling at multiple forest plots. For this study, we shortened the calculated life period of spruce needles from winter sampling plots to 15th November [117] to improve comparability of spruce needle Hg uptake rates within the dataset.

3.3.2 Variation of foliar Hg uptake rates with tree species groups

Median daily foliar Hg uptake rates (Fig. 3.3) in decreasing order are: ash (0.26 ng Hg $g_{d.w.}^{-1}$ d^{-1}), beech (0.25 ng Hg $g_{d.w.}^{-1}$ d^{-1}), oak (0.22 ng Hg $g_{d.w.}^{-1}$ d^{-1}), hornbeam (0.20 ng Hg $g_{d.w.}^{-1}$ d^{-1}), larch (0.14 ng Hg $g_{d.w.}^{-1}$ d^{-1}), current-season Douglas fir needles (0.13 ng Hg $g_{d.w.}^{-1}$ d^{-1}), current-season spruce needles (0.07 ng Hg $g_{d.w.}^{-1}$ d^{-1}), current-season fir needles (0.07 ng Hg $g_{d.w.}^{-1}$ d^{-1}) and current-season pine needles (0.05 ng Hg $g_{d.w.}^{-1}$ d^{-1}). The range of daily foliar Hg uptake of beech (0.12 – 0.42 ng Hg $g_{d.w.}^{-1}$ d^{-1}) is in agreement with the daily foliar Hg uptake rate of 0.35 ± 0.03 ng Hg $g_{d.w.}^{-1}$ d^{-1}, that Bushey et al. [76] had determined in beech leaves growing in New York State in 2005. There are distinct differences in median daily Hg uptake rates between current-season foliage of tree species groups (Fig. 3.3). The median daily foliar Hg uptake rate of deciduous leaf samples is 0.23 ng Hg $g_{d.w.}^{-1}$ d^{-1}, a factor of 3.2 larger than the median daily foliar Hg uptake rate of current-season conifer needle values (0.07 ng Hg $g_{d.w.}^{-1}$ d^{-1}). The difference between deciduous and coniferous leaves in the European dataset is smaller than a previous observation from a mixed forest site in Switzerland in 2018, where Hg uptake rates of coniferous species were reported to be 5 times lower than those of deciduous trees [165]. Similarly, Navrátil et al. [90] reported higher foliar Hg concentrations in beech leaves (36.3 ng Hg g^{-1}) than in current-season spruce needles (14.1 ng Hg g^{-1}) of two adjacent forest plots sampled during peak season (August). Higher Hg concentrations in deciduous leaves (median: 28 ng Hg g^{-1} from 341 remote sites) than in composite multi-age coniferous needles (median: 15 ng Hg g^{-1} from 535 remote sites) were also reported in a global literature compilation [9]. Differences in daily foliar Hg uptake between tree species within one genus (e.g. Quercus petraea and Quercus robur) were negligible (see Fig. B.5). We were not able to normalize daily foliar Hg uptake rates with atmospheric Hg(0) concentrations at each respective sampling site and sample life period, as air Hg(0) measurements were unavailable for our sampling sites. The relative standard deviation of average air Hg(0) concentrations at 6 European measurement sites within the EMEP network [111, 193] between May and Sept. 2015 and 2017 (see Table B.2

for details) was 0.06, which is lower than the relative standard deviation of the average daily Hg uptake rates between tree species and forest plots of 0.64 (Figure 3.3). We therefore argue, that the pronounced differences in median daily foliar Hg uptake rates between tree species cannot exclusively be explained by differences in atmospheric Hg(0) concentrations, but rather suggest a tree physiological cause. However, foliar Hg uptake rates should be normalized to ambient atmospheric Hg(0) concentrations, in particular when comparing foliar Hg observation between the northern and southern Hemisphere or over multi-decadal timescales.

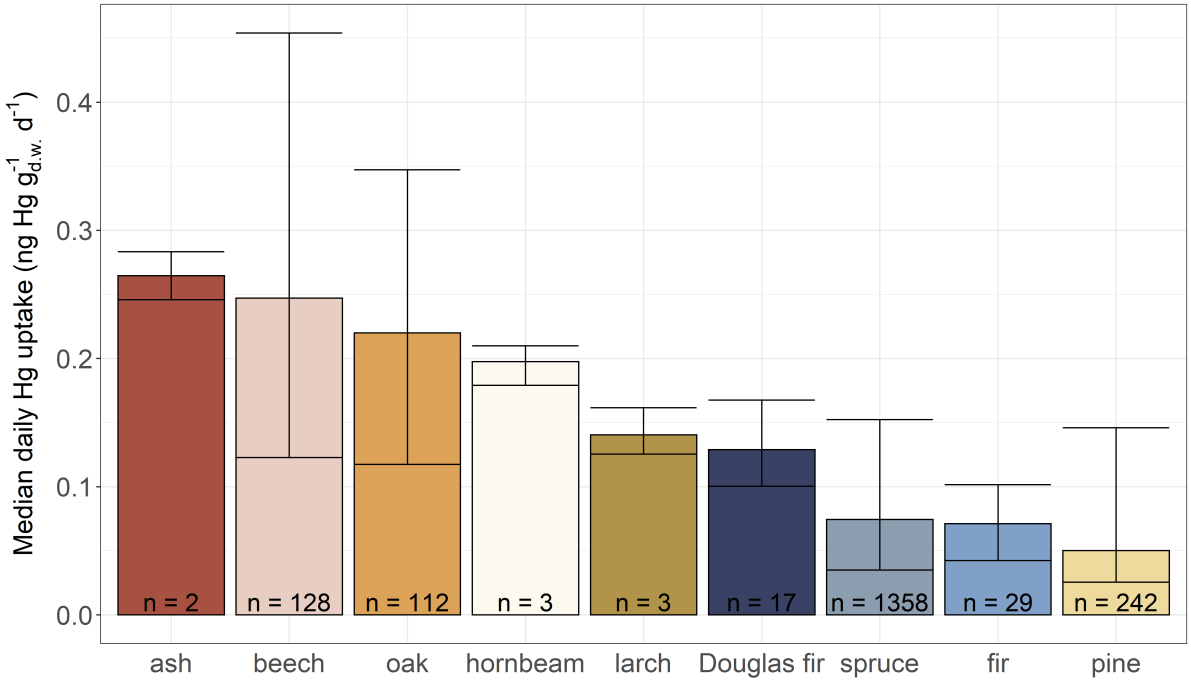

FIGURE 3.3. Median daily foliar Hg uptake (ng Hg $g^{-1}_{d.w.}$ d^{-1}) between different tree species groups (see Table B.1 for definition of tree species groups) arranged from highest to lowest value. Error bars give the value range within each tree species group and n indicates the number of sites at which the respective tree species were sampled in both the years 2015 and 2017. Foliar samples of evergreen coniferous tree species (Douglas fir, spruce, fir and pine) consist of needles of the current season.

3.3.3 Foliar Hg uptake and sample-specific N concentration

Foliar N concentration serves as a surrogate for the maximum photosynthetic capacity of foliage [194] as the bulk amount of foliar N is contained in the photosynthetic systems like chlorophylls, thylokoid proteins and rubisco [55, 195, 196]. Furthermore, foliar N represents an indirect proxy for foliar maximum stomatal diffusive conductance for water vapor, independent of tree species [55, 57, 197–201]. Note, that for this analysis we solely compared N and Hg concentrations for foliage samples harvested within a period of the growing season, during which leaf N concentrations are relatively stable (July – August for broadleaves [202, 203] and Sept – March for conifer needles [204, 205]). To assess the possibility of physiological factors controlling

the large variation of foliar Hg(0) uptake between different tree species groups (Fig. 3.3), we compared average daily foliar Hg uptake rates per tree species group with respective average foliar N concentrations. We found a positive linear correlation between foliar N concentration and Hg uptake rates as tree species groups with high average foliar N exhibited higher daily foliar Hg uptake rates (Table 3.1). This observation supports the notion, that the physiological activity of trees controls foliar Hg(0) uptake, thereby explaining the large variation among tree species groups [165]. We compared foliar Hg uptake rates and leaf N concentrations with values of median stomatal conductance for beech, oak, pine and spruce included in a global leaf-level gas exchange database compiled by Lin et al. [206] (see description of database calculation in Sect. B.7). Albeit stomatal conductance measurements for tree species of interest within the database [206] originated from one or only few sites (n = 1 – 5; Table 3.1), beech and oak exhibited higher median stomatal conductance values than spruce and pine, corresponding with higher daily Hg uptake rates and foliar N concentrations in beech and oak compared to spruce and pine. Thus, we observed a strong control of plant functional traits on foliar Hg(0) uptake with tree species of high photosynthetic activity (high N concentration) and stomatal conductance exhibiting the highest foliar Hg(0) uptake rates.

TABLE 3.1. Mean ± standard deviation of daily Hg uptake and foliar N concentration per tree species group from a subset of foliage samples harvested during July – Aug (broadleaf samples) or Sept – March (coniferous needle samples). Values are ordered from highest to lowest mean daily Hg uptake. All values from evergreen tree species groups (Douglas fir, fir, pine, spruce) were evaluated in current-season needles. Median stomatal conductance values (min – max) were calculated from a global database of leaf-level gas exchange parameters compiled by Lin et al. [206].

Tree species group	daily Hg uptake (ng Hg $g_{d.w.}^{-1}$ d^{-1})	foliar N conc. (mg N $g_{d.w.}^{-1}$)	n samples	median stomatal conductance (mol m^{-2} s^{-1}) Lin et al. [206]	n sites Lin et al. [206]
beech	0.25 ± 0.05	23.1 ± 2.9	312	0.10 (0.03 - 0.31)	2
oak	0.20 ± 0.05	25.1 ± 2.8	252	0.15 (0.01 - 0.35)	1
hornbeam	0.19 ± 0.03	19.4 ± 2.1	10		
Douglas fir	0.13 ± 0.02	17.0 ± 3.5	26		
spruce	0.08 ± 0.02	12.9 ± 1.7	1509	0.05 (0.01 - 0.16)	1
fir	0.07 ± 0.02	13.0 ± 1.7	66		
pine	0.06 ± 0.02	14.4 ± 3.0	355	0.06 (0.00 - 0.33)	5

Within tree species groups, linear regression coefficients of daily Hg uptake and foliar N concentration were significant ($p < 0.001$) for beech ($R^2 = 0.15$; n = 312) and fir ($R^2 = 0.27$; n = 66). Corresponding statistical significance for hornbeam, oak, pine and spruce could not be evaluated, since the respective data used for the linear regression was heteroscedastic. Blackwell and

Driscoll (2015) [207] found a significant relationship between foliar Hg concentration and foliar N% for yellow birch, sugar maple and American beech, but not for pine (red pine and white pine), red spruce or balsam fir. We examined whether unaccounted site-specific differences (e.g. soil N concentration) between forest plots could have caused the variability (low R^2) of daily Hg uptake versus foliar N concentration within tree species by individually analyzing foliar Hg concentration versus foliar N concentration at two oak and one beech forest plot, from which 20 or more foliage samples were available. Linear regression coefficients of foliar Hg concentrations versus foliar N concentrations were significant ($p < 0.001$) at two (oak and beech) of the three plots but not at the third plot ($p = 0.1$, oak) (see Fig. B.7). This finding suggests that foliar N concentrations represents an indicator of foliar Hg concentrations at individual forest sites, as it does for foliar Hg uptake of different tree species (Table 3.1). However, given the heterogeneity of nutrient availability between sites [208] and the complexity of internal foliar allocation of N to different parts of the photosynthetic apparatus [209], a generally valid correlation of foliar Hg uptake versus foliar N may not exist.

3.3.4 Foliar Hg uptake and Leaf Mass per Area

Within the whole dataset, leaf mass per area (LMA; $g_{d.w.}\ m^{-2}_{leaf}$) data were available in a subset of 349 foliage samples from 48 sites (from both 2015 and 2017). LMA is an important parameter in plant ecophysiology, because carbon gains of plants via photosynthetic activity and gas diffusion is optimized per unit of leaf area, as plants adapt their LMA, i.e. their foliage thickness and/or tissue density, to the availability of sunlight during growth [210–212]. This LMA adaptation of foliage to sunlight had been suggested to be more effective for optimizing photosynthetic capacity than within-leaf N partitioning of photosynthesizing biomass [213]. Therefore, we analyzed the connection of foliar Hg uptake to LMA across tree species. Figure 3.4 shows average LMA values (mean $\pm$ sd) of the subset of samples where LMA was reported, resolved by tree species, along with respective average daily Hg uptake rates and associated foliar N concentrations (all values displayed in Fig. 3.4 are listed in Table B.3; see Fig. B.8 for density plots of datasets from Table 3.1 and Fig. 3.4).

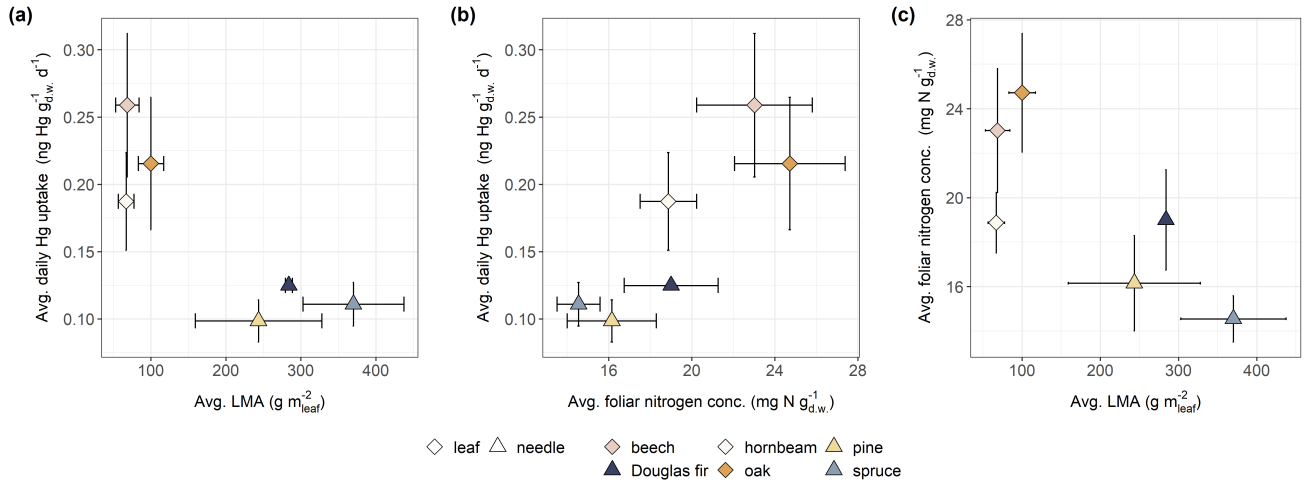

FIGURE 3.4. a) Average daily Hg uptake rates (ng Hg $g^{-1}_{d.w.}$ d^{-1}), b) average foliar nitrogen concentrations (mg N $g^{-1}_{d.w.}$) and c) average LMA ($g_{d.w.}$ m^{-2}_{leaf}) determined in 349 foliage samples and resolved by tree species group and foliage type (leaf/needle). Error bars denote ± one standard deviation. Number of samples (n) differs between tree species: beech (n = 164), Douglas fir (n = 2), hornbeam (n = 9), oak (n = 106), pine (n = 35) and spruce (n = 33).

Current-season needle samples of coniferous tree species groups (Douglas fir, pine, spruce) exhibited higher median LMA values (308 $g_{d.w.}$ m^{-2}_{leaf}), lower median daily Hg uptake rates (0.10 ng Hg $g^{-1}_{d.w.}$ d^{-1}) and lower median foliar N concentrations (15.4 mg N $g^{-1}_{d.w.}$) compared to leaf samples of deciduous tree species groups (beech, oak, hornbeam) (Fig. 3.4). Wright et al. [147] illustrated, that different evolutionary survival strategies of plant species are positioned along a single axis of foliage characteristics ranging from plant species with high photosynthetic capacity and respiration, high foliar N concentration, low LMA and short leaf life spans to plant species with the respective opposite attributes. Comparison of average daily foliar Hg uptake, LMA and foliar N concentrations (Fig. 3.4) across tree species in this study suggest, that foliar Hg(0) uptake aligns along this plant species economics spectrum, with deciduous leaves with high leaf N concentrations and thus high physiological capacity (photosynthesis, respiration) taking up more Hg(0) per gram dry weight over the same time span than coniferous needles with low leaf N concentrations and physiological capacity.

3.3.5 Foliar Hg uptake and water vapor pressure deficit (VPD)

Trees regulate their transpiration rates in response to temporary changes of water vapor pressure deficit (VPD) by controlling leaf stomatal aperture [214–216]. When a critical VPD threshold is exceeded, trees close their stomata to resist cavitation and excessive water loss in conditions of high atmospheric evaporative forcing (i.e. high VPD) [55, 216]. This decrease in leaf stomatal conductivity in response to high VPD suppresses stomatal uptake fluxes of gaseous pollutants like ozone [55, 217]. We investigated, whether VPD impacts foliar uptake of gaseous Hg(0) by relating species-specific average daily foliar Hg uptake rates to the proportion of

daytime (06:00 – 18:00 LT) hours of an average day within the respective sample life periods, during which hourly daytime VPD exceeded the threshold values of 1.2 kPa, 1.6 kPa, 2 kPa and 3 kPa, respectively at all forest plots with hourly meteorological data (n = 82 including both sampling years).

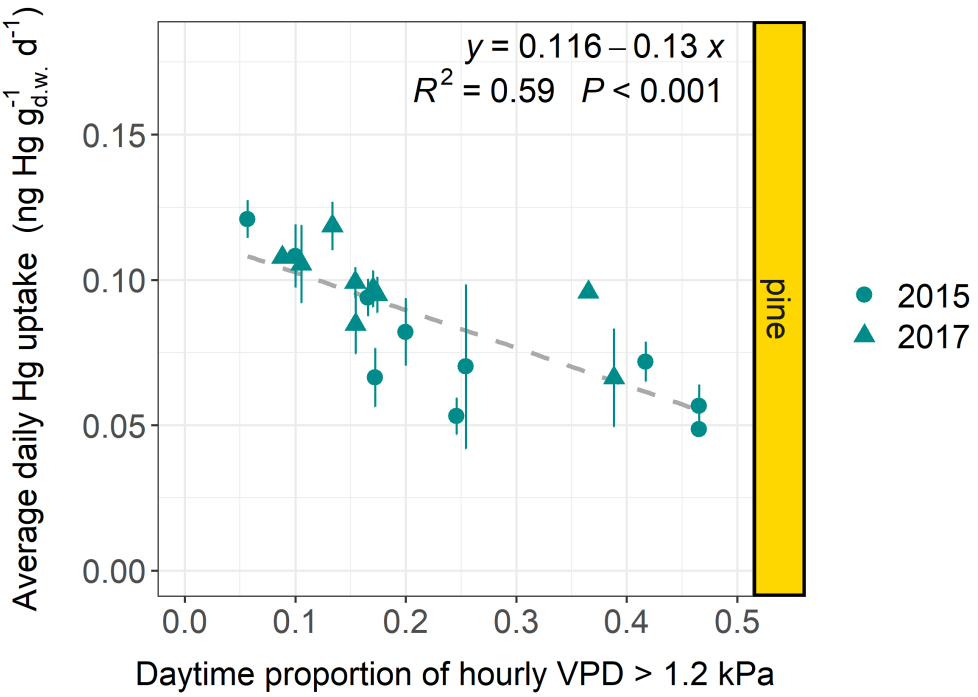

FIGURE 3.5. Average daily Hg uptake rates (ng Hg $g_{d.w.}^{-1}$ d^{-1}) of current-season pine needles from multiple forest plots (n plots = 19) versus the proportion of daytime hours (06:00 – 18:00 LT) within an average day of the respective sample life periods, during which the hourly daytime water vapor pressure deficit (VPD) exceeded a threshold value of 1.2 kPa. Data points originate from both sampling years 2015 and 2017. All forest plots are located in Central Europe (latitude 46° - 54°), for which ambient air Hg(0) concentrations are relatively constant (see Table B.2 and Fig. B.6). Error bars denote ± one standard deviation of daily needle Hg uptake rates between multiple samples at each forest plot.

The linear regression coefficients of average daily Hg uptake versus daily proportion of daytime hours, during which VPD exceeded a threshold value (1.2 kPa, 1.6 kPa, 2 kPa or 3 kPa) were significant ($p < 0.01$) for pine at all VPD threshold values (Fig. 3.5, Fig. B.9), for spruce at a VPD threshold value of 3 kPa ($R^2 = 0.44$; $p = 0.01$; $n = 14$) (Fig. B.9) and not significant for beech and oak at any VPD threshold value (Fig. B.10). Linear regression coefficients were negative for all species and VPD threshold values, i.e. by tendency, average daily foliar Hg uptake rates decreased with average proportion of daytime hours, during which VPD > respective threshold value (1.2 kPa, 1.6 kPa, 2 kPa or 3 kPa). We excluded Douglas fir, fir, hornbeam and larch from the regression analysis due to a low number of forest plots (n = 1 – 5). Average daily needle Hg uptake rates of spruce needles were clustered between two groups of forest plots with high and low daytime proportions of VPD > threshold (Fig. B.9) relative to each other. T-test revealed a significant ($p = 0.008$) difference in average daily spruce needle Hg uptake rates between the

two clusters for a VPD threshold value of 3 kPa and non-significant ($p > 0.05$) differences for all other VPD threshold values. The timing and degree of stomatal closure during dry conditions is tree species-specific [218, 219]. Tree species like pine and spruce are isohydric, i.e. they tend to respond to drought stress under high evaporative demand by closing their stomata earlier than anisohydric species like beech and oak [220–224]. Among isohydric species, pine has been discovered to reduce tree conductance and stomatal aperture during the onset of dry conditions earlier and at a greater rate than spruce [218, 225]. Spruce has been observed to keep stomata almost completely closed under drought stress, i.e. high VPD and/or soil water deficit [218]. We hypothesize, that the significantly decreasing average foliar stomatal Hg uptake rates with daytime proportion of VPD > 1.2 kPa for pine (Fig. 3.5) and of VPD > 3 kPa for spruce (Fig. B.9) possibly reflect the early physiological response of pine, and the high degree of stomatal closure under drought stress of spruce. Oak exhibits later stomatal closure at the onset of dry conditions and higher stomatal aperture under drought stress than e.g. pine [218, 221], which may be the reason why there was by tendency a negative, but not significant correlation coefficient of average foliar Hg uptake with daytime proportion of VPD > any threshold value for oak (Fig. B.10).

3.3.6 Foliar Hg uptake and soil water content

Linear regression coefficients of average daily foliar Hg uptake rates at each forest plot versus proportion of hours within sample life periods, during which ERA5-Land soil water fell below a soil texture specific threshold value (PAW_{crit}) (see Sect. 3.2.6), were negative for all tree species groups and significant for beech ($p = 0.036$) and pine ($p = 0.031$) (Fig. 3.6). The linear regression coefficient was not significant for oak ($p = 0.169$) and not available for spruce due to a low number of data points.

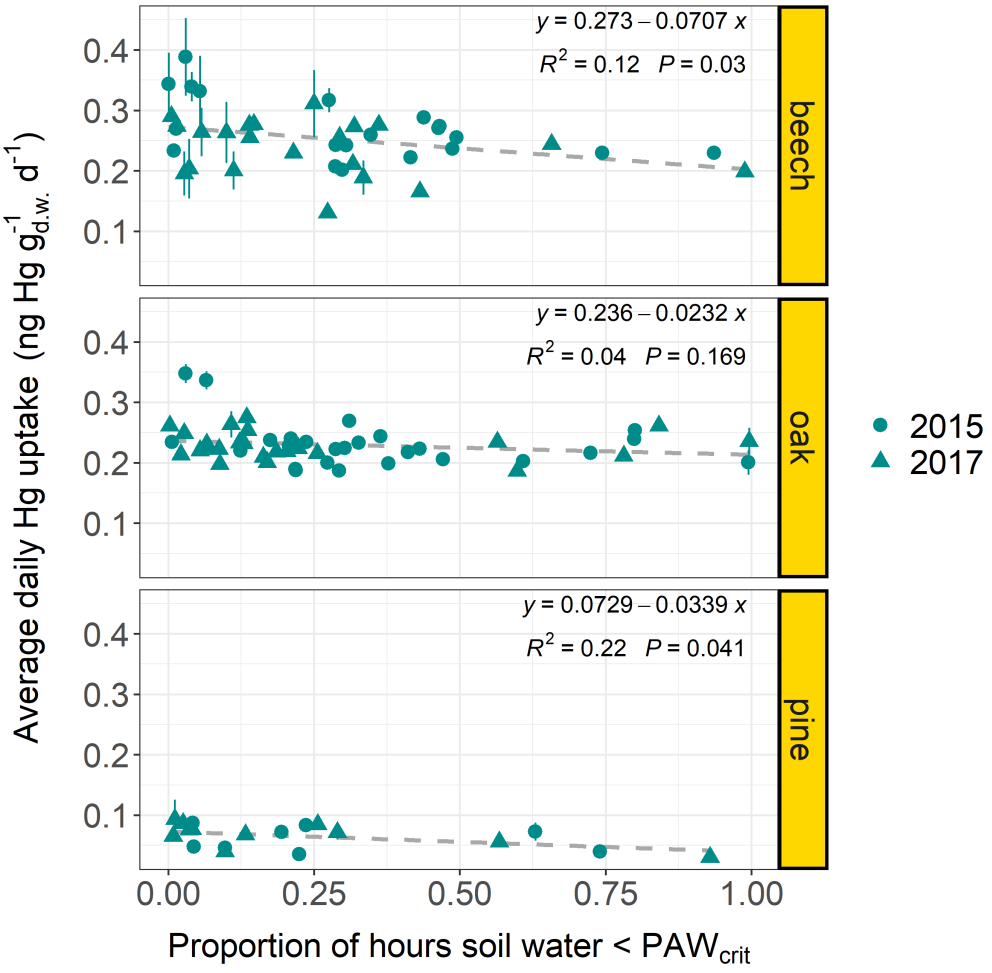

FIGURE 3.6. Average daily Hg uptake rates (ng Hg $g_{d.w.}^{-1}$ d^{-1}) of beech, oak and current-season pine foliage from multiple forest plots (beech plots n = 38; oak plots n = 45; pine plots n = 19; latitude: 41° - 55°) versus the proportion of hours within the respective sample life periods, during which the geographically associated hourly soil water from the ERA5-Land dataset [177] fell below a soil texture specific threshold value PAW_{crit} (see Sect. 3.2.6). Data points originate from both sampling years 2015 and 2017. Error bars denote ± one standard deviation of daily needle Hg uptake rates between multiple samples at each forest plot.

Linear regression results (Fig. 3.6) indicate, that foliar Hg uptake rates decrease at forest plots, where plant available water in the upper soil layer (0 – 7 cm) falls below specific thresholds (PAW_{crit}) for a relatively long time period over the growing season. Studies on the atmosphere-plant transport of ozone have highlighted, that plant stomatal ozone uptake declines with increasing soil water deficit, because drought prompts stomatal closure [226–228]. We hypothesize, that stomatal uptake of Hg(0) is impacted by soil conditions of low plant available water in a similar way to ozone. In the future, in-situ soil matrix potential measurements should be used to better quantify the response rate of foliar Hg(0) uptake to soil water content in order to overcome the limitations of the coarse satellite-derived soil water measurements used here. We also suggest determining the possible influence of additional parameters like

gravel content and density of soils, rooting depth of trees and atmospheric Hg(0), which could vary within the range of latitude (41° - 55°) of examined forest plots.

3.3.7 Foliar Hg uptake and geographic and tree-specific parameters

We performed linear regressions of average daily foliar Hg uptake rates per forest plot and tree species group (beech, oak, pine, spruce) versus geographic and tree-specific parameters. These parameters include altitude, latitude, average age of trees on plot, average tree diameter at breast height, average daily GLEAM transpiration values and average ERA5-Land 2 m air temperature over the course of the respective sample life periods (see Sect. 3.2.1). None of the resulting 54 linear regression coefficients were significant given a Bonferroni adjusted p-value = 0.000925. The differences between 2015 and 2017 species-specific averages of daily foliar Hg uptake rates from forest plots, at which foliage sampling took place during both sampling years, were small compared to the standard deviation of daily foliar Hg uptake rates within each sampling year and species (see Table B.5 for average and standard deviation values). From the sampling year 2015 to the sampling year 2017 this difference was 0.04 ng Hg $g_{d.w.}^{-1}$ d^{-1} for beech, 2 x 10^{-4} ng Hg $g_{d.w.}^{-1}$ d^{-1} for oak, 8 x 10^{-5} ng Hg $g_{d.w.}^{-1}$ d^{-1} for pine (current-season needles) and -3 x 10^{-3} ng Hg $g_{d.w.}^{-1}$ d^{-1} for spruce (current-season needles). We therefore suggest that differences in daily foliar Hg uptake rates between the sampling years 2015 and 2017 are negligible. In agreement with previous studies [51, 95–97, 165], we found a trend of Hg concentrations in differently aged spruce needles with older needles exhibiting higher Hg concentrations (Fig. 3.7), demonstrating that Hg accumulation continues in older needles. Annual Hg net accumulation seems to slow down in older spruce needles of age classes $y_3 - y_6$ in contrast to needles of age classes $y_0 - y_2$ (Fig. 3.7), albeit ranges of average Hg concentrations $\pm$ standard deviation overlap among older and younger spruce needles, which might be the result of relatively low sample numbers of older needles compared to younger needles (e.g. 3 samples for y_6 vs. 301 samples for y_1). A decline in foliar Hg uptake by older needles could be caused by lower physiological activity, cuticular wax degradation or an increase in Hg re-emission with needle age [165].

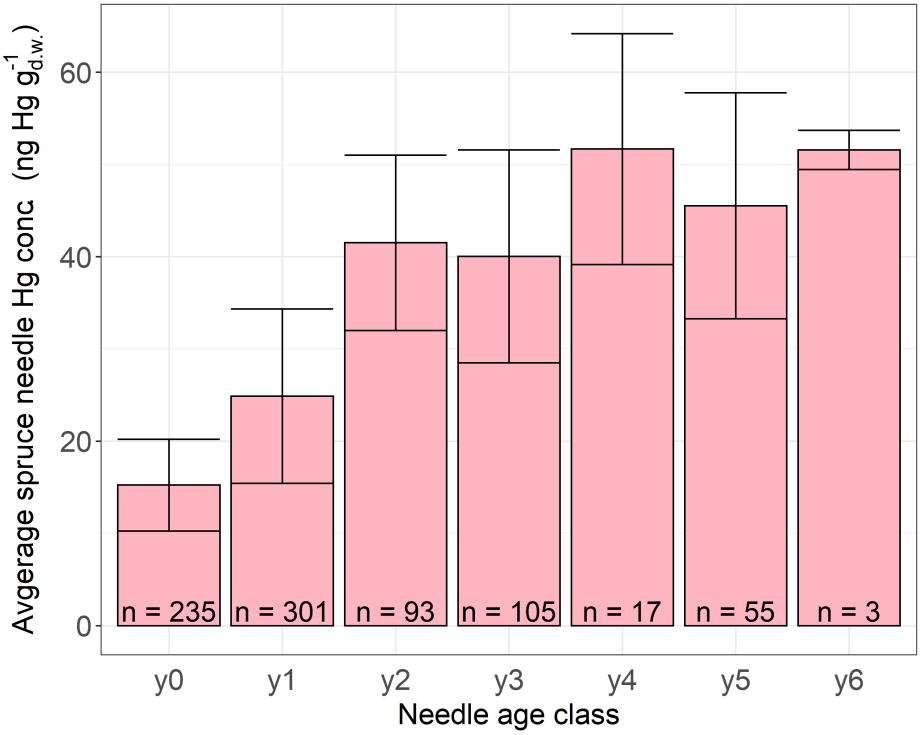

FIGURE 3.7. Average Hg concentrations (ng Hg $g_{d.w.}^{-1}$) in spruce needle samples of different ages. Needle age class y_0 corresponds to current-season needles flushed in the year of sampling, y_1 corresponds to one-year old needles, y_2 corresponds to two-year old needles etc. Error bars denote $\pm$ one standard deviation between multiple samples, n indicates number of samples.

3.3.8 Implications for Hg cycle modelling

Our findings suggest, that VPD impacts stomatal Hg(0) uptake by isohydric tree species due to stomatal closure during conditions of high VPD (Fig. 3.5). Similarly, elongated time periods of low soil water content within the growing season possibly result in a decrease of stomatal conductance to Hg(0) and thus in less foliar Hg(0) uptake by tree species such as beech and pine (Fig. 3.6). Other meteorological parameters such as temperature may also have an effect on stomatal closure and consequently stomatal Hg(0) uptake (Sect. 3.3.7). We therefore propose, to refine existing stomatal uptake models for the purpose of exploring the stomatal uptake flux of Hg(0) for common vegetation types across different global regions over the course of the growing season. For this, the sensitivity of species-specific foliar Hg uptake normalized to air Hg(0) concentrations have to be determined in laboratory experiments with regards to elevated VPD, low soil water content or temperature. Eventually, the effect of tree species, VPD, soil water and point in time within the growing season could be implemented in a stomatal Hg deposition model. We propose, that the stomatal flux module of the DO3SE (Deposition of Ozone for Stomatal Exchange) model could serve as a prototype for a stomatal Hg deposition model, because DO3SE provides estimates of stomatal ozone deposition based on plant phenological and meteorological conditions [217, 229]. Projections from stomatal Hg models are particularly

relevant for the evaluation of future global environmental Hg cycling, as the stomatal Hg(0) uptake flux exceeds direct Hg(II) wet deposition [60, 165], and quantitatively represents the most relevant deposition pathways to land surfaces, driving the seasonality of Hg(0) in the atmosphere [12, 88]. VPD is projected to increase with rising temperatures under global warming [184, 216], potentially causing a decrease in stomatal foliar Hg(0) uptake fluxes. A diminished global stomatal foliar Hg(0) uptake flux would result in higher Hg(0) concentrations in the atmosphere and higher Hg deposition fluxes to the ocean [9].

3.3.9 Conclusion

We created a large European forest dataset for investigating the control of tree physiology and climatic conditions on foliar stomatal Hg(0) uptake. We observed, that foliar Hg concentrations were highly correlated with foliage sampling date (Fig. 3.2), confirming the notion, that foliage takes up Hg(0) over the entire growing season and over multiple growing seasons in the case of coniferous needles (Fig. 3.7). Consequently, it is necessary to calculate foliar Hg uptake rates by normalizing foliar Hg concentrations by the time period of Hg(0) accumulation to make foliar Hg values from different sites comparable. For reasons of comparability, foliar Hg uptake rates should ideally be normalized to ambient air Hg(0) concentrations when large variation in atmospheric Hg(0) is expected (e.g. between northern and southern hemispheres, in polluted regions or over long timescales). We found notable differences of daily foliar Hg uptake rates between tree functional groups (broadleaves versus coniferous needles), i.e. Hg uptake rates of broadleaves were higher compared to coniferous needles of the same age by a factor of 3.2 (Fig. 3.3). Across tree species and within beech and fir, the linear regression coefficients of daily foliar Hg uptake rates versus foliar N concentration were significant (Sect. 3.3.3). Tree species groups with foliage of lower LMA exhibited higher daily rates of Hg uptake per dry weight of foliage (Sect. 3.3.4). We set these results within the context of stomatal foliar uptake of atmospheric Hg(0): Deciduous tree species like beech and oak, which exhibit functional traits of high physiological activity (photosynthesis, transpiration) over the time span of one growing season, as represented by high foliar N concentration and low LMA, retain a higher stomatal conductance for diffusive gas exchange. Thus, beech and oak leaves accumulate more Hg per unit dry weight over the same time span relative to needles of coniferous tree species. In addition to tree species-specific metabolism, climatic conditions like current VPD or soil water content, which impacts stomatal gas exchange, can affect foliar Hg uptake. For current-season pine needles, we found a significant negative linear regression coefficient of daily Hg uptake rates versus the average daily proportion of hours within sample life period, during which atmospheric evaporative forcing was high (VPD > 1.2 kPa) (Fig. 3.5), suggesting, that a reduction of stomatal conductance during conditions of high VPD suppresses foliar Hg(0) uptake. In a similar line of argument, low surface soil water content lowers stomatal

conductance and consequently foliar stomatal Hg(0) uptake (Fig. 3.6). We therefore suggest, that foliar Hg measurements bear the potential to serve as a proxy for stomatal conductance, providing a time-integrated measure for stomatal aperture when taking into account the spatial and temporal variation in atmospheric Hg(0). We call for the implementation of a stomatal Hg(0) deposition model, that takes tree physiology and environmental conditions like VPD or soil water content into account, in order to make projections about this important Hg deposition flux under climate change. The diminution of the vegetation mercury pump in response to drought stress as a result of climate change could result in elevated Hg concentration in the ocean and potentially in marine fish in future, a potential risk which warrants further quantitative studies.

Acknowledgments specific to this chapter

We thank Fabienne Bracher and Judith Kobler Waldis for assistance in foliage sample analysis. The evaluation was based on data that was collected by partners of the official UNECE ICP Forests Network (http://icp-forests.net/contributors). We are grateful to all ICP Forests participants who supported the project through foliage sampling, nutrient analysis and cooperation in the logistics of this project. In this context, we particularly thank Martin Maier, Andrea Hölscher and their team from the Department of Soil and Environment at FVA Baden-Württemberg; Daniel Žlindra from the Slovenian Forestry Institute; Nils König from Northwest German Forest Research Institute (NW-FVA); Hans-Peter Dietrich and Stephan Raspe from the Bavarian State Institute of Forestry (LWF Bayern); Michael Tatzber from the Austrian Research Centre for Forests (BFW); Arne Verstraeten and Luc De Geest from the Belgian Research Institute for Nature and Forest (INBO); Sébastien Macé from the French National Forest Office (ONF) and Panagiotis Michopoulos from the Forest Research Institute of Athens (FRIA). We are grateful to Samantha Wittke and Christian Körner for their helpful advice and support on leaf area indices and plant phenology. Special thanks go to Till Kirchner and Anne-Katrin Prescher from Thünen Institute for their assistance in accessing the ICP Forests Database.

Chapter 4

A spatial assessment of current and future foliar Hg uptake fluxes across Europe

This chapter has been published as an open access paper in the journal Global Biogeochemical Cycles and can be found under DOI: 10.1029/2023GB007833.

This chapter was co-authored by:
Lena Wohlgemuth, Aryeh Feinberg, Allan Buras, Martin Jiskra

Abstract

Atmospheric mercury (Hg) is deposited to land surfaces mainly through vegetation uptake. Foliage stomatal gas exchange plays an important role for net vegetation Hg uptake, because foliage assimilates Hg via the stomata. Here, we use empirical relationships of foliar Hg uptake by forest tree species to produce a spatially highly resolved (1 km^2) map of foliar Hg fluxes to European forests over one growing season. The modelled forest foliar Hg uptake flux is 23 $\pm$ 12 Mg Hg $season^{-1}$, which agrees with previous estimates from literature.

We spatially compared forest Hg fluxes with modelled fluxes of the chemistry-transport model GEOS-Chem and find a good overall agreement. For European pine forests, stomatal Hg uptake was shown to be sensitive to prevailing conditions of relatively high ambient water vapor pressure deficit (VPD). We tested a stomatal uptake model for the total pine needle Hg uptake flux during four previous growing seasons (1994, 2003, 2015/2017, 2018) and two climate change scenarios (RCP 4.5 and RCP 8.5). The resulting modelled total European pine needle Hg uptake fluxes are in a range of 8.0 - 9.3 Mg Hg $season^{-1}$ (min - max). The lowest pine forest needle Hg uptake flux to Europe (8 Mg Hg $season^{-1}$) among all investigated growing seasons was associated with unusually hot and dry ambient conditions in the European summer 2018, highlighting the sensitivity of the investigated flux to prolonged high VPD. We conclude, that stomatal modelling is particularly useful to investigate changes in Hg deposition in the context of extreme climate events.

4.1 Introduction

Mercury (Hg) is a toxic pollutant that is transported globally through the atmosphere and deposited from air to land surfaces mainly through vegetation uptake of ambient gaseous elemental Hg(0) [19–21, 151, 230]. Consequently, vegetation uptake has the potential to lower atmospheric Hg(0) transport and Hg deposition to oceans, where Hg can be methylated and bioaccumulated in marine seafood for human consumption [9]. In order to assess and improve the effectiveness of mitigation policies for human exposure, it is thus necessary to advance our understanding of environmental drivers of vegetation Hg(0) uptake, particularly in the context of global change [231].

Global vegetation and soil Hg(0) uptake is estimated at 2850 $\pm$ 500 Mg $year^{-1}$ and primarily driven by forests [9, 60, 230]. The amount of forest Hg(0) deposition exceeds approximate direct anthropogenic emissions to the air of 2200 Mg Hg $year^{-1}$ [231]. In forests, half of the total Hg(0) net deposition is estimated to be stored in tree foliage, while the other half is estimated to be transferred to vascular tissues (e.g. stem, branches, roots), taken up by understory vegetation (e.g. shrubs, grasses) and nonvascular plants (lichen and mosses) or Hg is directly transferred to the forest floor [9, 10, 60, 232]. In tree foliage, Hg concentrations increase linearly between foliage emergence and senescence [38, 51, 80, 134, 165] implying a net foliar Hg deposition flux, albeit Hg re-emission from foliar surfaces of up to 30% of gross foliage Hg(0) deposition had

been observed in a subtropical forest in China [35]. The bulk (90-96%) of Hg is stored in foliage tissues as opposed to leaf surfaces and correlates with leaf stomatal density [38]. Studies on Hg stable isotopes in foliage [9, 19], enriched isotope tracer experiments [41], the vertical variation of net foliar Hg uptake in forest canopies [165], and canopy Hg(0) fluxes, that correlate with CO_2 fluxes [232] strongly suggest a diffusive uptake pathway of atmospheric Hg(0) to foliage interiors via the stomata [49]. In this way, foliar Hg(0) uptake is linked to foliage stomatal aperture for atmospheric gas exchange [233].

Trees regulate foliage stomatal aperture to balance the inward diffusion of CO_2 for photosynthesis with the risk of desiccation caused by excessive outward diffusion of water vapor [55]. The degree of stomatal aperture depends on atmospheric CO_2 levels and hydrological conditions (soil water availability and atmospheric evaporative demand) and varies among foliage-specific traits (age, tree species-specific evolutionary metabolic strategy and water use efficiency) [55]. Pine, for instance, is an isohydric tree species capable of closing foliage stomata under warm and dry atmospheric conditions relatively early compared to tree species like oak and spruce [218, 221, 225], resulting in a reduced stomatal conductance for pine needle diffusive gas exchange [226]. Consistently, Hg(0) uptake rates by pine needles in Europe were found to be lower at forest sites across Europe, where prolonged warm and dry atmospheric conditions prevailed over a given growing season during daytime [233].

Species-specific stomatal response strategies to meteorological conditions are particularly relevant for projections of future foliar Hg uptake under climate change. Increasing global atmospheric temperatures driven by rising levels of greenhouse gases will result in an increased frequency of droughts [216] and higher soil moisture deficits [234, 235] in various regions of the world. These climatic conditions may decrease foliar Hg(0) uptake fluxes due to lower stomatal conductance [233]. A reduced plant Hg sink could further be amplified by deforestation and forest diebacks, particularly in the tropics [236–238]. Other regions of the world are projected to become wetter through an increase in precipitation rates under climate change [61], which might lead to higher foliage stomatal conductance relative to the present and thus higher foliar Hg uptake. With continuing anthropogenic carbon emissions, an elevated atmospheric CO_2 level might have an antagonizing effect on the foliar stomatal Hg(0) uptake flux: foliar Hg(0) uptake could decline with decreasing stomatal conductance under CO_2 fertilization [239], or, the opposite, the vegetation sink for Hg(0) could increase with intensified biomass growth and higher soil C contents [12, 62, 240]. In order to make projections of the foliar Hg uptake flux in the next decades, these climate change impacts need to be further investigated and potentially implemented into global and regional Hg cycle models.

Current and future Hg fluxes are modelled in Global Chemical Transport Models (CTMs). CTMs like GEOS-Chem [241] apply resistance-based algorithms [242] for modelling Hg(0) deposition fluxes from the atmosphere to vegetated ecosystems and are often based on parameters like leaf area indices (LAIs), temperature and wind speed. The resistance components for leaf

stomata within CTMs commonly represent consensus values optimized to fit observations of Hg deposition velocities over vegetated surfaces [62, 70, 241, 243], without taking stomatal feedback to environmental conditions into account [244, 245]. Consequently, forest tree species-specific stomatal responses to climate change at foliage level are not parameterized in CTMs. An additional problem related to CTMs is the uncertainty of modelled Hg(0) deposition fluxes due to insufficient model evaluation against dry deposition measurements [230]. This issue of model validation was highlighted in a recent revision of GEOS-Chem parameterization after matching the GEOS-Chem model design to various experimental Hg(0) deposition measurements, which resulted in a doubling of the modelled global flux of Hg(0) dry deposition to land compared to previous model outcomes [230].
The goal of this study is twofold. For one, we present a spatially highly resolved map of foliar Hg uptake fluxes to European forests using a bottom-up model, which we compare to mapped forest dry deposition fluxes modelled in the chemical transport model GEOS-Chem. Second, we focus our analysis on foliar Hg uptake fluxes to pine in order to investigate the sensitivity of an empirical stomatal response model to different climatic conditions during past growing seasons and for two climate change projections of the years 2068 - 2082, in order to outline the potential of incorporating a stomatal response function into CTMs.

4.2 Materials and Methods

4.2.1 Description of datasets

For creating maps of foliar and pine needle Hg uptake fluxes in Europe applying a bottom-up model (Sect. 4.2.2 and 4.2.3), we drew on multiple data sources:

- **Foliar Hg data**. A dataset of foliar Hg uptake rates was derived from Hg measurements in foliage of tree canopies at 272 forest sites of the UNECE International Co-operative Programme on Assessment and Monitoring of Air Pollution Effects on Forests (ICP Forests). Forest sites are mostly located in Central and Northern Europe (+ 737 sites in Austria from the Austrian Bio-Indicator Grid) and harmonized foliage sampling methods were employed. All foliage samples within this dataset were harvested at the end of the growing seasons 2015 or 2017. Therefore, average foliage values of 2015/2017 constitute reference values of forest foliar Hg uptake fluxes relative to respective fluxes during investigated years of this study. The dataset is publicly available and contains 3569 foliar Hg concentrations of 23 tree species and is described in detail in [233].

- **Meteorological data**. Values on ambient temperature and relative humidity at surface air pressure (1000 hPa) in Europe (spatial resolution: 0.25° x 0.25°) originate from ERA5 hourly reanalysis data and were downloaded from the Copernicus Climate Data Store

[246]. The applied time frame includes hourly daytime (07:00 - 18:00 LT) values during the respective growing seasons (April - October) of 1994, 2003, 2015, 2017, and 2018.

- **Climate change data**. Regional climate simulation data of air temperature and relative humidity at 2 m above surface level for the years 2068 - 2082 and two different climate change scenarios (Representative Concentration Pathway (RCP) 4.5 and RCP 8.5 [247]) were obtained from the Coordinated Regional Climate Downscaling Experiment (CORDEX) [248] framework for the European domain with a spatial resolution of 0.11° x 0.11° and a temporal resolution of 3hourly daytime (09:00 - 18:00 LT) values. For representing a range of different climate model outputs, we calculated average values from multiple regional climate models (RCMs) downscaled from global climate models (GCMs) depending on availability for download from the Copernicus Climate Data Store [249]. In total, we incorporated data of 15 combinations of 4 RCMs and 6 GCMs for RCP 4.5 and of 13 combinations of 6 RCMs and 8 GCMs for RCP 8.5 (see Table C.3) for an overview of models and ensemble members).

- **European tree species distribution**. We used a map of spatial proportions of tree species groups per km^2 land area from Brus et al. [153]. For use in calculating pine foliar Hg uptake fluxes (see Sect. 4.2.3), we summed up spatial relative abundance values of *Pinus sylvestris*, *Pinus pinaster*, *Pinus nigra* and *Pinus halepensis* from European forest inventories [250, 251] and multiplied these pine relative abundances with the respective total forest area per km^2 derived from Brus et al. [153] to obtain pine areal proportions (i.e., proportion of the surface area of a spatial tile, that is covered by pine forest). We performed the same calculation (sum of values of *Pinus sylvestris*, *Pinus pinaster*, *Pinus nigra* and *Pinus halepensis* and subsequent multiplication with respective total forest area) to estimate the distribution of pine in Europe under climate change using relative abundance probabilities projected from climate analogues for the time period 2061 - 2090 and RCP 4.5 and RCP 8.5 by Buras and Menzel [251].

- **Leaf Area Indices (LAIs) and Leaf Mass per Area (LMA) values**. We used the LAI satellite product (spatial resolution: 330 m) of PROBA-V [181, 182] to upscale foliar Hg uptake rates at each ICP Forests site to foliar Hg uptake fluxes (see Sect. 4.2.2), along with average LMA values per tree species from Forrester et al. [252].

4.2.2 Calculation of forest foliage Hg uptake fluxes

We determined forest foliar Hg uptake fluxes to European forests on a 1 km^2 spatial resolution applying three basic computational steps: 1) calculation of tree species-specific daily Hg uptake fluxes per m^2 ground area using a bottom-up model; 2) upscaling of respective foliar Hg fluxes per tree species to the European forested area using the areal distribution of corresponding

tree species; 3) multiplication of daily forest foliar Hg uptake fluxes per latitude with latitude-dependent growing season length in order to obtain the forest foliar Hg uptake fluxes over one growing season.

Computational step 1) is based on the premise, that foliar Hg uptake rates are tree species-specific [38, 51, 233]. For this reason, we calculated median daily foliar Hg uptake fluxes per tree species group (see Table C.2 for details) of all forest sites from the foliar Hg dataset (Sect. 4.2.1). The bottom-up modeling approach for calculating daily foliar Hg uptake fluxes from daily foliar Hg uptake rates is described in detail in Wohlgemuth et al. [165]. Briefly, daily foliar Hg uptake rates per gram foliage dry weight (units of ng Hg $g_{d.w.}^{-1}$ d^{-1}) were multiplied with tree species-specific LMA values (Sect. 4.2.1) to obtain daily foliar Hg uptake rates per foliage surface area (ng Hg m_{leaf}^{-2} d^{-1}). Subsequently, values of daily foliar Hg uptake rates per foliage surface area are multiplied with values of LAI (m_{leaf}^{2} m_{ground}^{-2}; Sect. 4.2.1), resulting in daily foliar Hg fluxes per unit ground area (ng Hg m_{ground}^{-2} d^{-1}). LAI values of coniferous forests are relatively constant during the active growing season after the initial growth phase of current-season needles [253], while LAI values of temperate deciduous forests increase rapidly at the beginning of the growing season (leaf flushing) and climax at peak season (June – August, northern hemisphere) [254]. For coniferous tree species, we used the maximum LAI value during the constant period at each forest site of the ICP Forests dataset to calculate needle foliar Hg uptake fluxes. For deciduous tree species, we calculated foliar Hg uptake fluxes as a temporal sequence at every LAI value available over the growing season and subsequently used median foliar Hg uptake flux values of the growing season. For LAI values larger than 3, we applied a species-specific tree height correction factor, to account for lower foliar Hg uptake fluxes of shaded leaves in the lower canopy [165] (refer to Table C.1 for utilized tree height correction factors). For coniferous species, we multiplied Hg uptake fluxes of current-season needles with a species-specific needle age correction factor to account for lower Hg uptake rates of older needle age classes [165] (refer to Table C.1 for utilized needle age correction factors).

Computational step 2) involves the multiplication of the proportion of each tree species per km^2 land area with the respective species-specific median daily foliar Hg uptake fluxes. We matched tree species-specific Hg data with the areal forest distribution of the respective tree species [153]. In the few cases of rare European tree species, where specific Hg data was lacking, we pooled Hg or forest distribution data by tree species group (see Table C.2 for an overview of matched tree species groups between the two datasets). Subsequently, we added up all tree species-specific daily foliar Hg uptake fluxes within each km^2 and obtained one forest foliar daily Hg uptake flux per km^2.

In computational step 3) we calculated forest foliar Hg uptake fluxes per km^2 and one growing season by multiplying each daily foliar Hg uptake flux per km^2 with the growing season length in days following a simple latitudinal model [185]. The latitudinal model of growing season determines a growing season length of 192 days at latitude 50° and decreases by 3.5 days per 1°

of latitude moving north and increases by 3.5 days per 1° of latitude moving south. We did not normalize forest foliar Hg uptake fluxes by different atmospheric Hg(0) levels, because ambient Hg(0) measured within the European monitoring programme EMEP [111] was evaluated to be relatively homogeneous in space in Europe and the growing seasons 2015 and 2017 [233].

4.2.3 Calculation of pine foliar Hg uptake fluxes

In previous research, the impact of relatively high atmospheric water VPD on foliar Hg uptake was assessed for pine, spruce, beech, and oak [233]. For pine, a significant empirical relation of pine needle Hg uptake fluxes with VPD was found: pine needle daily Hg uptake rates (upR_{pine}; ng Hg $g_{d.w.}^{-1}$ d^{-1}) were lower at forest sites, where pine trees experienced high hourly daytime VPD values $>$ 1.2 kPa over a relatively long time period during the growing season ($proportion_{dayVPD} > 1.2$kPa) [233]. The negative correlation of pine needle stomatal Hg uptake with timespan of elevated atmospheric VPD is explained by the hydraulic safety strategy of the isohydric tree species pine, which closes stomata relatively early in response to rising VPD (Sect. 4.1). We thus calculated daily foliar Hg uptake rates as a function of VPD exclusively for pine, which accounts for 36% of European forested area of our studied spatial domain. The linear regression of daily foliar Hg uptake rates with $proportion_{dayVPD} > 1.2$ kPa is: upR_{pine} = 0.116 – 0.13 x ($proportion_{dayVPD} > 1.2$ kPa) [233]. We applied this linear relationship to calculate the pine foliar Hg uptake rates of the forest area of Europe during four different growing seasons in 1994, 2003, an average of 2015 and 2017, 2018, and projected for the time period 2068 - 2082 under RCP 4.5 and RCP 8.5 [247]. Using the August-Roche-Magnus formula [184], we calculated ambient water VPD from daytime values of surface temperature and relative humidity, which are available on an hourly resolution from ERA5 [246] for past growing seasons and on a 3hourly resolution from EURO-CORDEX (Sect. 4.2.1) for simulated climate data. Subsequently, we determined the fraction of daytime hours, during which the VPD was above the threshold of 1.2 kPa during the respective latitudinal growing season length. All calculations involving climate data were performed at sciCORE scientific computing center at University of Basel. We defined growing season length per latitude using a latitudinal model ([185], see Sect. 4.2.2). In 2068 - 2082 we assumed the beginning of the growing season to be 3 days earlier and the end of the growing season to be 3 days later to take increases in growing season length under climate change into account [116, 255]. The underlying areal distribution of pine is based on European forest inventories and projections of pine abundances based on climate analogues under RCP 4.5 and RCP 8.5 by Buras and Menzel [251] (see Sect. 4.2.1).

4.2.4 GEOS-Chem forest deposition flux calculation

GEOS-Chem is a global 3-D chemistry transport model, which includes a comprehensive Hg cycle [241]. Table 4.1 gives an overview of the methodological approach and input parameters

for calculating the respective Hg fluxes of GEOS-Chem and the bottom-up model (Sect. 4.2.2), which we compared spatially in this study.

TABLE 4.1. Comparison of the bottom-up model and GEOS-Chem

	bottom-up model	**GEOS-Chem**
model input parameters	spatial forest distribution [153]; leaf area indices (LAIs) [181, 182]; leaf mass per area (LMA) [252]; meteorological parameter: daytime ambient water VPD [246]; foliar Hg uptake rates [233]	spatial forest distribution [256]; leaf area indices (LAIs) [257]; atmospheric Hg(0) levels (GEOS-Chem v12.8.1 simulation 2015); meteorological parameters: air temperature, pressure, solar radiation, cloud cover, wind speed (GEOS-FP) [258]
spatial resolution	1 km x 1 km	0.25 x 0.3125°
basic methodological approach for Hg flux calculation	spatial upscaling of measured foliar Hg uptake rates [165]	in-series calculation of Hg dry deposition velocity from parameterized resistance values [242]
foliage stomatal Hg uptake flux component	calculated for pine based on daytime vapor pressure deficit (VPD) values (Sect. 4.2.3)	calculated within the canopy resistance component as a function of land type, leaf area indices (LAIs), and solar radiation
model output compared in this study	tree-species specific forest foliar Hg(0) uptake fluxes	Hg(0) dry deposition fluxes to coniferous and deciduous forest land cover

We used an offline version of the GEOS-Chem dry deposition code [259] to be able to calculate dry deposition velocities at higher resolution and only for certain land use types (i.e., forest areas). The offline dry deposition code computes deposition velocities applying a resistance-based approach [242, 260]. Input variables (Table 4.1) are gridded hourly GEOS-FP meteorological data (e.g., air temperature, wind speed, solar radiation, and cloud cover) and

weekly LAI values based on MODIS [257] for the year 2015. The model calculates the Hg(0) dry deposition velocity based on species-specific parameters including its biological reactivity ($f_0 = 10^{-5}$) and Henry's Law Constant ($H^* = 0.11$ M atm^{-1}). To isolate the uptake of Hg(0) to forests, we calculated the dry deposition velocity only over coniferous and deciduous land cover types from the Olson land map [256]. The offline calculations output hourly dry deposition velocities over the European domain at 0.25 × 0.3125° resolution. We converted the calculated Hg(0) deposition velocities to fluxes by multiplying with hourly surface Hg(0) concentrations from a GEOS-Chem v12.8.1 simulation for 2015. For this study, we compared the GEOS-Chem Hg(0) dry deposition fluxes to forests with foliar Hg(0) uptake fluxes calculated using the bottom-up model. For both models, Hg fluxes were averaged over the latitude-dependent growing season length in days and cropped to the same spatial extent. As GEOS-Chem and the bottom-up model differ in their geographic resolution (GEOS-Chem: 0.25° x 0.31° $\sim$ 955 km^2 vs. bottom-up: 1 km^2), we downsampled daily forest foliar Hg uptake fluxes from the bottom-up model through bilinear interpolation.

4.2.5 Uncertainty analysis of foliar Hg uptake fluxes

The relative uncertainty value per tree species group depended on propagated uncertainties of calculation parameters used to derive the respective foliar Hg uptake flux per tree species group (see Table C.4 for details and values). Subsequently, we calculated one relative uncertainty value per geographic tile of our European flux map (Fig. 4.1) by summarizing the relative uncertainty of each foliar Hg uptake flux per tree species group within each tile according to error propagation principles [261, 262]. We obtained the relative uncertainty for the total foliar Hg uptake flux to European forests (Fig. 4.1) by propagating all relative uncertainty values per tile. The final relative uncertainty value of total foliar Hg uptake flux to European forests and the reference growing seasons 2015/2017 is 0.52.

4.3 Results and Discussion

4.3.1 Spatial distribution of forest foliar Hg uptake fluxes across Europe

Figure 4.1 visualizes forest foliar Hg uptake fluxes per growing season at a spatial resolution of 1 km^2 (g Hg km^{-2} season^{-1}) in Europe. Forest foliar Hg uptake fluxes generally follow a spatial distribution of European forests, because this map (Fig. 4.1) is based on the proportion of forest tree species per land area [153]. Consequently, the largest forest foliage Hg uptake fluxes in terms of area are in Fennoscandia (defined here as Norway, Sweden, and Finland) with dense forest land cover of mostly pine and spruce [153]. Outside of Fennoscandia, forest foliage Hg uptake fluxes fall along large contiguous forested areas, e.g. in the Carpathian

Mountains (located in most parts in Romania and Slovakia), the South-Eastern Alps (mostly in Austria, Slovenia, and Italy), the Balkans, or forested low mountain areas like the Black Forest (Germany). By magnitude, forest foliar Hg uptake fluxes (Fig. 4.1) agree well with annual canopy Hg(0) deposition of two temperate forests (14.3 and 15.4 μg m^{-2}) in North America, which were measured by applying a micrometeorological method [232].

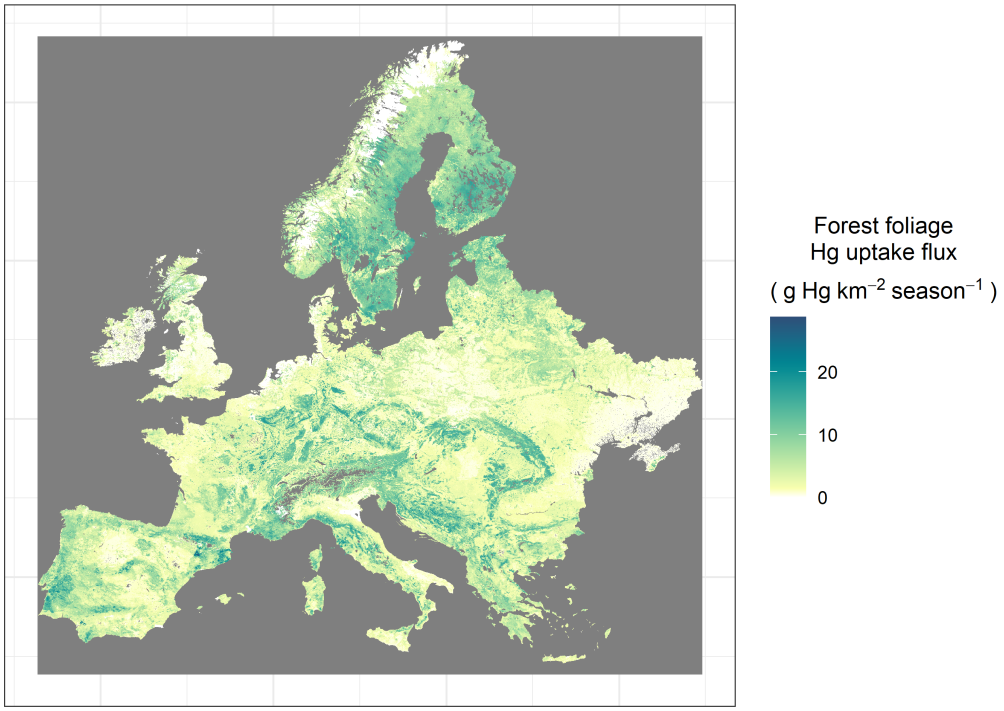

FIGURE 4.1. Spatial distribution of forest foliar Hg uptake fluxes (g Hg km^2 growing season^{-1}) to Europe based on a bottom-up extrapolation of foliar Hg concentrations, that were measured and averaged over the 2015 and 2017 growing seasons. Dark grey areas represent excluded non-forested areas (e.g. surface waters or mountain areas).

The sum of forest foliar Hg uptake fluxes over the land area of Europe (compare Fig. 4.1) equals 23 $\pm$ 12 Mg Hg season^{-1}. This total flux is in the same range as a previous estimate of the total foliar Hg uptake flux to Europe (20 $\pm$ 3 Mg Hg over the 2018 growing season) based on foliar Hg uptake fluxes at four forested sites [165]. Zhou and Obrist [10] evaluated a median global foliar Hg assimilation of 28 Mg yr^{-1} for deciduous broadleaf forests and 61 Mg yr^{-1} for evergreen needleleaf forests by combining foliar Hg concentrations with annual net foliar biomass production data of the respective forest types. From these global assimilation estimates by Zhou and Obrist [10], we calculated a total foliar Hg assimilation of 29 Mg yr^{-1} to the deciduous and coniferous forest land area of Europe (for details see Sect. C, Text S1), which is slightly higher but still within the uncertainty of the 23 $\pm$ 12 Mg Hg season^{-1} from this study. However, foliar Hg uptake fluxes based on net primary foliar biomass production by Zhou and Obrist [10] does not correct for lower foliar Hg uptake rates by shade leaves and multiyear old

needles (see Sect. 4.2.2) relative to sun leaves and younger needles [165], likely resulting in a systematic over-estimation. We assume, that the different time reference (seasonal vs. annual) of the flux from this study (23 $\pm$ 12 Mg Hg season^{-1}) and the flux derived from Zhou and Obrist [10] (29 Mg Hg yr^{-1}) only plays a minor role for explaining the difference between the two fluxes, since we expect a small net foliar biomass production in Europe in winter outside of the growing season. Results from micrometeorological Hg measurements in two temperate forests in North America show, that Hg(0) uptake during the active growing season dominates annual Hg(0) deposition [232]. Please note, that from a whole forest ecosystem perspective, fluxes displayed in Figure 4.1 are exclusively constrained to foliar Hg uptake and do not represent potential Hg fluxes to other ecosystem compartments like forest floor [232].

4.3.2 Comparison of bottom-up model with GEOS-Chem

Figure 4.2 depicts spatial ratios of daily forest Hg uptake fluxes of the bottom-up model to GEOS-Chem. Absolute difference values of the two model outputs are shown in Fig. C.2.

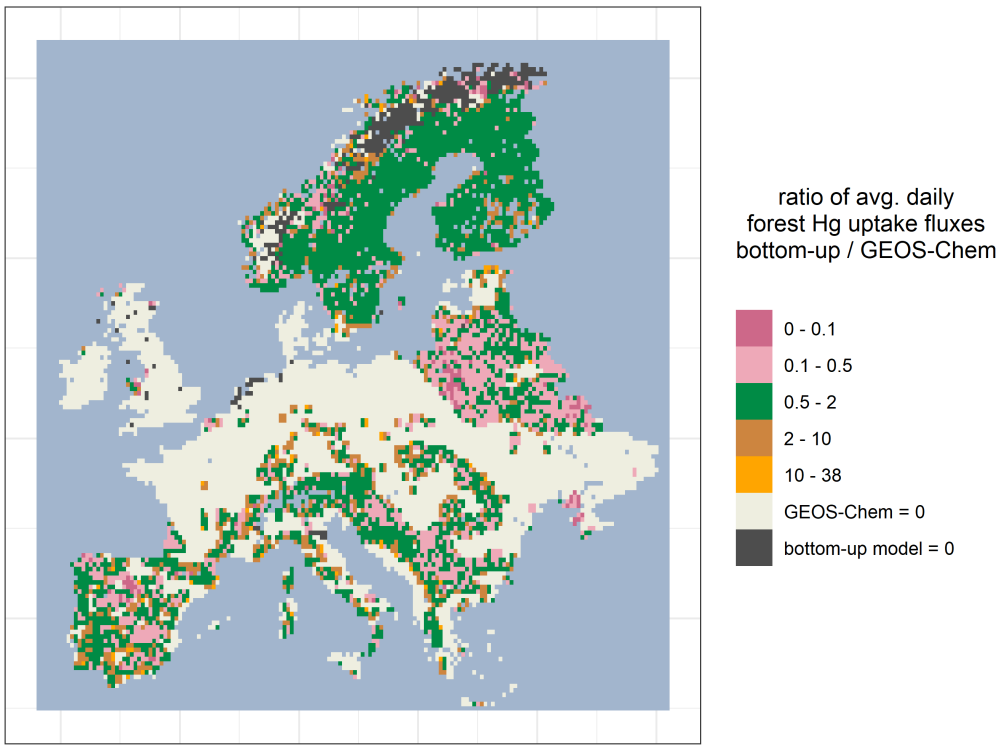

FIGURE 4.2. Ratios per spatial unit of daily forest Hg uptake fluxes averaged over the latitude-specific growing season length of the bottom-up model to GEOS-Chem.

The overall foliar Hg uptake flux to the total European forested area (Fig. 4.1 and 4.2) was 22 Mg Hg season^{-1} for GEOS-Chem, which almost equals the total flux of 23 $\pm$ 12 Mg Hg season^{-1} for the bottom-up model (Sect. 4.3.1). Results of average daily foliar Hg uptake fluxes

from GEOS-Chem and the bottom-up model were geographically comparable: In 59% of the spatial domain with values > 0, average daily foliar Hg uptake fluxes from the two models differed by factor of 1 - 2 from each other, in 37% of the domain, model values differed by a factor of 2 - 10 from each other, and in 4% of the domain respective values differed by a factor of > 10 from each other (Fig 4.2). We examined if differences in modelled average daily foliar Hg uptake fluxes at the same geographic location originate from differences in the underlying forest distribution maps of the two compared models. In 78% of spatial tiles with values > 0, the ratio of average daily foliar Hg uptake fluxes of the bottom-up model to GEOS-Chem agreed in range (Fig. 4.2) with the ratio of the forest fraction of the bottom-up model to GEOS-Chem per respective spatial tile. We thus find that the bottom-up model and GEOS-Chem generally produce similar forest Hg flux values per spatial unit given the same forest distribution. This spatial consistency of model outputs is surprising, as the bottom-up model is specific for foliar Hg(0) uptake fluxes based on a wide set of European field data, while GEOS-Chem broadly computes Hg(0) dry deposition fluxes to forests (Table 4.1). Reasons for minor differences in model outputs are challenging to identify, due to the different approaches, parameters and underlying maps of the two models (Sect. 4.2.4). For future assessment of model accuracy, we therefore suggest to compare model results to actual measurements of the forest foliar Hg uptake flux [60, 230, 232].

4.3.3 Pine foliar Hg uptake fluxes under different VPD scenarios

Figure 4.3 shows total pine forest foliar Hg uptake fluxes to Europe calculated under different conditions of atmospheric surface-level water VPD during four past growing seasons (1994, 2003, 2015/2017, 2018) and simulated for the years 2068 - 2082 as an average of multiple climate model outputs (see Sect. 4.2.2) under two different climate change scenarios (RCP 4.5 and RCP 8.5). The leftmost bar (Fig. 4.3) represents a theoretical baseline pine needle Hg uptake flux in absence of VPD induced stomatal control (potential maximum transpiration rates) on the pine needle Hg uptake flux. The total pine needle Hg uptake flux to Europe during the reference growing season 2015/2017 (Sect. 4.2.2) is 9.3 ± 3.7 Mg Hg representing 70% of the baseline flux of 13.3 ± 5.3 Mg Hg season^{-1}. Thus, based on the pine needle Hg uptake model used in this study (Sect. 4.2.3), the VPD effect reduces the total pine needle Hg uptake flux to Europe by approximately 30%.

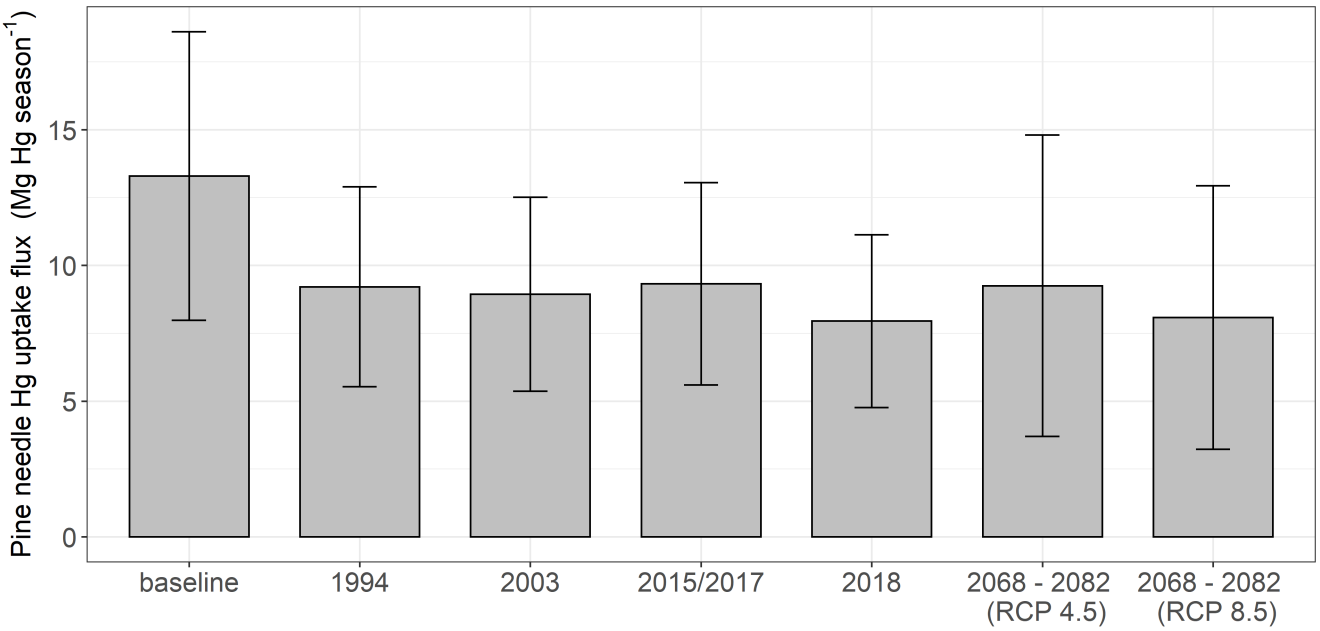

FIGURE 4.3. Pine needle Hg uptake flux to European pine forests (Mg Hg season^{-1}) calculated from atmospheric surface water vapor pressure deficit (VPD) conditions during the growing seasons 1994, 2003, 2015/2017, 2018 and projected for the years 2068 - 2082 under RCP 4.5 and RCP 8.5. Bar on the left represents a baseline pine forest needle Hg uptake flux with no VPD exceedance of 1.2 kPa throughout the growing season.

The relative standard deviation of modelled total pine needle Hg uptake fluxes for the investigated growing seasons (1994, 2003, 2015/2017, 2018, 2068 - 2082) was 0.07 Mg Hg season^{-1}. Consequently, modelled total European pine needle Hg uptake fluxes hardly differed from each other among growing seasons. The total pine needle Hg uptake flux in Europe depend on VPD conditions in areas where pine forests prevail. Pine forests are primarily located in Northern Europe (Fig. C.1). Pine forests located at latitudes $> 55.3°$N account for 21% of the total foliar Hg uptake flux to Europe during the reference growing season (Fig. 4.1). In Northern Europe, hourly ambient VPD was $>$ 1.2 kPa during 30% or less of daytime in the growing seasons 1994, 2003 and 2015/2017 due to relatively cool and moist ambient conditions as compared to Central and Southern Europe (see e.g. VPD conditions during reference time period 2015/2017 Fig. 4.4a). In contrast to previous years, the European summer hydrological condition of 2018 has been described as an intense hot drought, during which pronounced stomatal closure of coniferous forests in response to high VPD were recorded in Switzerland [263]. In Southern Fennoscandia, conditions of ambient hourly VPD $>$ 1.2 kPa prevailed over exceptionally long time proportions (around 40%) during the summer of 2018 (see Fig. 4.4b, [264]). As a result, the modelled total pine needle Hg uptake flux in Europe in 2015/2017 (9.3 Mg Hg season^{-1}) was by a factor of 1.16 higher than the respective flux in 2018 (8.0 Mg Hg season^{-1}). We conclude that hot and dry summer conditions (Fig. 4.3) in Fennoscandia crucially impact modelled past total pine needle Hg uptake fluxes in Europe. According to the model results, an average amount of

1.3 Mg Hg was not deposited via pine needle uptake in 2018 compared to 2015/17, potentially remaining in the atmosphere, where it can be long-range transported to the ocean [9]. These 1.3 Mg Hg are more than three times larger than the reported anthropogenic Hg emissions of Sweden in 2021 [265], highlighting the quantitative impact, that hot droughts can have on the pine needle Hg uptake flux.

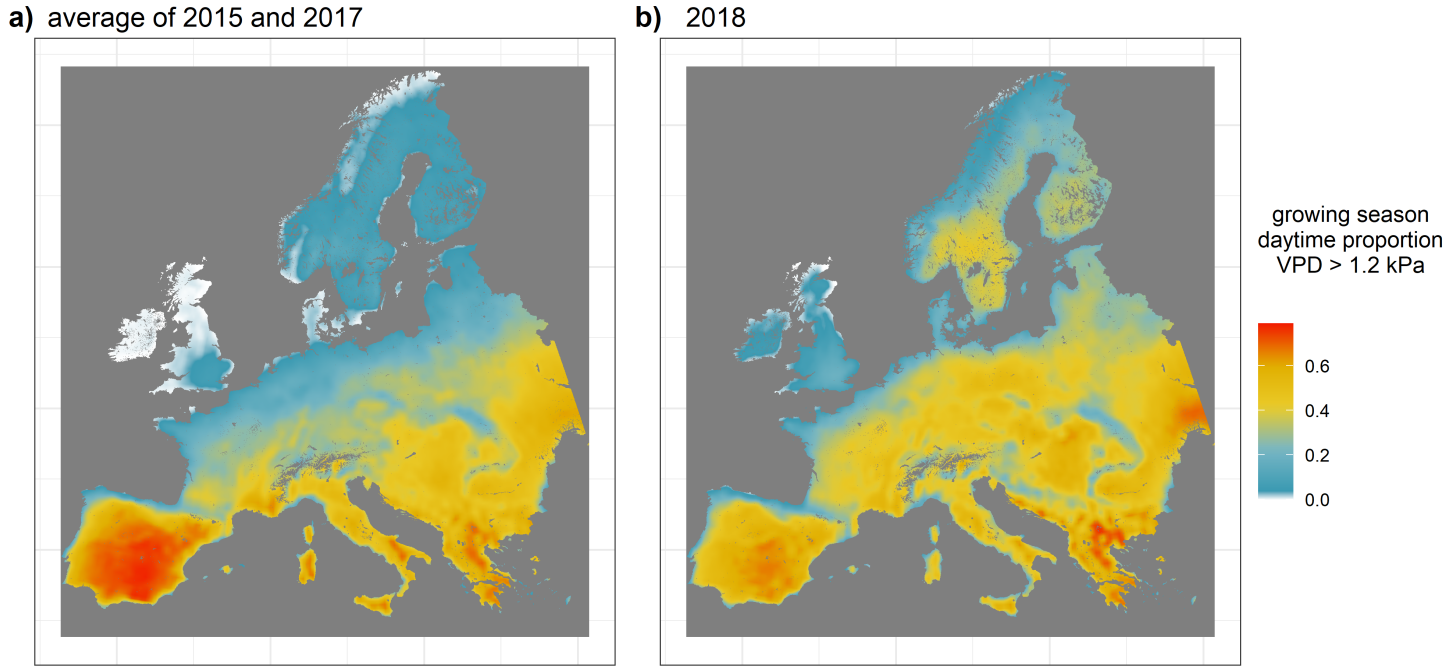

FIGURE 4.4. Average daytime proportion of surface level atmospheric water VPD > 1.2 kPa during a) the reference growing season 2015/2017, and b) the growing season 2018. All VPD values were calculated from hourly reanalysis data of ERA5 ambient air temperature and relative humidity (Sect. 4.2.1).

4.3.4 Projected pine forest needle Hg uptake fluxes under climate change scenarios

The projected total pine forest needle Hg uptake flux for 2068 - 2082 (RCP 4.5: 9.3 $\pm$ 5.5 Mg Hg season^{-1}; RCP 8.5: 8.1 $\pm$ 4.9 Mg Hg season^{-1}) was in the same range as the corresponding average flux for the years 1994, 2003, 2015 and 2017 of 9.1 $\pm$ 0.2 Mg Hg season^{-1} (mean $\pm$ sd), but slightly higher than the corresponding flux in the year of 2018 (8.0 $\pm$ 3.2 Mg Hg season^{-1}), during which Fennoscandia experienced a summer of relatively long hot and dry ambient conditions. Figure 4.5 maps the absolute deviation of the pine forest needle Hg uptake flux projected for 2068 - 2082 (simulated future flux) from the corresponding 2018 flux in Europe. Under RCP 4.5, the simulated future flux is higher (blue area in Fig. 4.5 a) than the 2018 flux in 65% of total area. Under RCP 8.5, the simulated future flux is higher (blue area in Fig. 4.5 b) than the 2018 flux in 43% of total area. In most area of Fennoscandia, where a majority of

pine forests in Europe are located (Fig. C.1), the future flux is projected to be larger than in 2018. For both climate change scenarios, the projection predicts lower pine needle Hg fluxes to the Balkans and to the Southern Iberian Peninsula than in 2018 (Fig. 4.5).

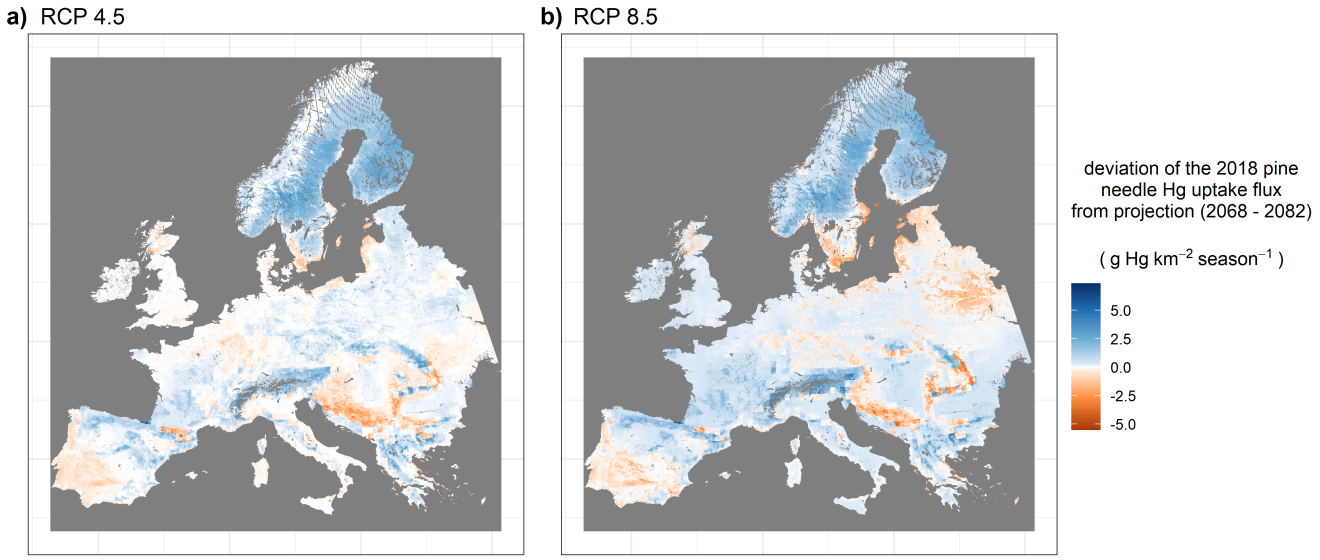

FIGURE 4.5. Absolute deviation of projected pine forest foliar Hg uptake fluxes for 2068 - 2082 (under RCP 4.5 (a) and RCP 8.5 (b)) from the corresponding flux modelled for 2018. In blue areas, the projected future flux under the two climate change scenarios is higher than the respective 2018 flux, in orange areas, this deviation is reversed.

The pine forest needle Hg uptake flux for 2068 - 2082 simulated here is a function of both modelled ambient VPD conditions during the growing season and the projected distribution of pine forests in Europe depending on climate analogs [251]. While the pine forest cover in Southern Sweden is projected to decrease under the climate change scenarios RCP 4.5 and RCP 8.5 from around 50% km^{-2} to around 25% km^{-2}, forest cover in Central and Northern Fennoscandia is projected to be relatively steady for climate analogs of both climate change scenarios (compare Fig. C.1 a - c). Average long-term precipitation rates are projected to increase in Scandinavia, along with a decrease of meteorological drought in the coming decades under different climate change scenarios [266–268], which could result in an increase of atmospheric humidity and a decrease of VPD in northern Europe [269]. Under this scenario of wetter forest environments, the Hg sink of Scandinavian pine forest needles would not be significantly diminished. However, drought trends in Fennoscandia are still inconsistent and extreme drought events like in 2018 might occur more frequently under the current rate of climate change [61]. The summer of 2018 was a record hot drought in Europe [264], while climate simulations for 2068 - 2082 are averaged over multiple climate models (Table C.3), possibly averaging out extreme events. In a scenario, where the maximum proportion of daytime VPD $>$ 1.2 kPA per growing season averaged over 2068 - 2082 prevails at each spatial unit, the total pine forest needle Hg uptake flux to Europe reduces to 6.9 Mg Hg season^{-1} for RCP 4.5 and 5.0 Mg Hg season^{-1} for

RCP 8.5, which corresponds to 74% and 62% of the respective flux derived from an average VPD daytime proportion. We therefore suggest that extreme climate events of extended time periods of ambient daytime VPD $>$ 1.2 kPa like during the growing season 2018 (Fig. 4.4b) could reduce the pine forest needle Hg uptake flux in Fennoscandia in future even compared to average long-term VPD projections (Fig. 4.5).

A source of model uncertainty of the future forest foliar Hg uptake flux under climate change arises from atmospheric Hg(0) concentrations that depend on anthropogenic emissions, re-emissions of mobilized legacy Hg and future global deposition fluxes under climate and land use change [231, 238], which we could not account for in this study. However, our model outputs call attention to the sensitivity of the pine needle Hg uptake flux to extreme hot and dry ambient conditions, which should be accounted for in chemistry-transport models under varying atmospheric Hg(0) levels. Going forward, the climate feedback of stomatal Hg(0) draw-down from the atmosphere should likewise be parameterized in CTMs for other tree species but pine. Temperate tree species like oak and beech also react to increasing VPD with stomatal closure [216, 233], albeit less instantaneously than pine [220, 221, 224], which merits further investigation in field and laboratory experiments in the context of foliar Hg uptake and climate change.

The impact of the hot and dry conditions on the pine Hg uptake fluxes might have implications for Hg inputs into aquatic ecosystems. In a recent review on Hg cycling in the context of global change, [231] highlighted the potential of legacy Hg (i.e. actively cycling Hg that was mobilized in the past) to cause contamination by mobilization of Hg from soils to wetlands and coastal ecosystems via riverine systems. While most soil Hg enters riverine systems by soil erosion from agricultural lands, contaminated sites, and deforested woodland [231, 270], a reduced forest foliar Hg uptake and subsequent deposition to forest soils may decrease the amount of runoff Hg from forest soils in the long-term, while long-range Hg transport to the open ocean via the atmosphere might be enhanced [9].

4.4 Conclusion

We created a highly resolved (1 km^2) map (Fig. 4.1), which visualizes the spatial variation of foliar Hg uptake fluxes to European forests. The highest foliar Hg uptake fluxes are in Fennoscandia, in densely forested areas of Central and Southern Europe, e.g. the Carpathian Mountains, the Balkans, or in multiple low mountain areas. We suggest, that this map (Fig. 4.1) can guide decisions on European background Hg monitoring of the terrestrial environment. The total forest foliar Hg uptake flux over the course of one growing season agrees well with Hg flux estimates derived from literature and from the chemical transport model GEOS-Chem for the same land area of Europe (Fig. 4.2). This precision among modelling results on a European scale using different approaches gives us confidence that the bottom-up model is overall able

to represent the seasonal forest foliar Hg uptake flux.
Using an empirical relationship between Hg needle uptake rates of pine trees and VPD threshold exceedance, we found a reduction in modelled pine forest needle Hg uptake flux during the relatively hot and dry growing season in Fennoscandia in 2018 compared to the growing seasons in 1994, 2003 and 2015/2017 (Fig. 4.3). The modelled average amount of Hg, that was not deposited via pine needle uptake in 2018 compared to the reference time period of 2015/17 exceeded the reported anthropogenic Hg emissions of Sweden in 2021, highlighting the quantitative significance of stomatal Hg uptake. If these hot summer droughts occurred more frequently in Fennoscandia under climate change, the pine forest needle Hg uptake flux would be diminished while these extreme conditions prevail, potentially increasing the Hg burden of the ocean via long-range atmospheric transport. In order to better represent the impact of extreme climate events on the pine forest needle Hg uptake flux, we therefore advise to incorporate a stomatal component of the pine needle Hg uptake flux into chemical transport models like GEOS-Chem.

Chapter 5

Conclusions and Outlook

5.1 Conclusion

5.1.1 Bottom-up modelling approach of the foliar Hg(0) flux

The bottom-up method developed during the project of this thesis aims to provide net foliage Hg(0) uptake fluxes on a whole forest ecosystem scale. It is based on the premise, that net foliar Hg(0) accumulation is to be normalized to surface area of foliage and that this foliage surface area is scaled up over forest ground area. Therefore, the bottom-up modelling approach is based on two scaling parameters: leaf mass per area (LMA) and leaf area index (LAI) (Chapter 2.2.4). Both parameters reflect the capacity of trees to flexibly adapt their foliage to environmental conditions during growth. This flexibility is essential for trees in order to optimize their photosynthetic capacity under the constrain of sunlight availability. Shade leaves, for example, grow at the lower part of tree canopies under reduced sunlight and are generally thinner and larger in area, i.e. have a lower LMA than sun leaves from the top of the canopy, allowing for optimal absorption of limited sunlight for photosynthesis [142]. Consequently, shade leaves have lower Hg concentrations per unit surface area than sun leaves (Fig. 2.5) and were also found to have lower Hg(0) uptake rates per surface area (Chapter 2.3.2). We therefore concluded, that scaling foliar Hg concentrations with respective LMA values provides a meaningful measure of net foliar Hg(0) uptake reflecting underlying foliage physiological uptake mechanisms per surface area on a small spatial scale (e.g. within a tree canopy) (Chapter 2.3.2). In order to account for systematic variation in foliar Hg(0) uptake rates between e.g. sun leaves vs. shade leaves or among coniferous needles of various age classes, this thesis derived correction factors for extrapolating foliar Hg(0) uptake rate to whole tree canopies or forests. The bottom-up method provides a straightforward way to obtain time integrated net foliage Hg(0) uptake fluxes, which can also be extrapolated to different forest sites. Another advantage is its easy applicability in the field, as it does not require on-site electricity. Furthermore, foliage sampling for the bottom-up method requires less expertise than measurements using e.g. dynamic flux bags [271] or single-plant environmental chambers [87]. The prerequisite of the bottom-up method are accurate LMA measurements of foliage samples for Hg analysis, which can be time-consuming

and have to be performed with care, particularly for determining the projected surface area of coniferous needles (Chapter A.4). Similarly, forest LAI has to be assessed accurately because small LAI and LMA measurement errors can propagate to large inaccuracies when foliar Hg concentrations are upscaled to foliar Hg(0) uptake fluxes from foliage to forest stands and to a larger spatial scale. As a prospective alternative for this kind of extrapolation, remotely sensed forest foliar biomass might be used in future derived from e.g. the Biomass satellite mission of the European Space Agency (Link: Biomass satellite). However, variation in foliage Hg(0) uptake within tree canopies (Chapter 2.2.6) and among needle age classes (Chapter 2.2.5) will still have to be accounted for (by e.g. a weighted average foliage Hg concentration) using such satellite products.

5.1.2 Biological processes of the forest foliar Hg(0) uptake flux

Vegetation Hg(0) uptake represents an atmospheric Hg deposition flux that is driven by ecological processes and therefore correlates with rates of biological activity (Chapter 3). Two controls of the foliar Hg(0) uptake by European forest trees were observed:

- Rate of foliage physiological activity: Tree species with a generally higher photosynthetic capacity and respiration rate assimilated more Hg(0) over the same time period than tree species with the opposite attributes (Chapter 3.3.4). The same premise was true for foliage growing at the same tree, i.e. sun leaves took up more Hg(0) per leaf surface area than shade leaves (Chapter 2.3.2).

- Drought: Forest sites, that experienced extended time periods of relatively dry atmospheric (Chapter 3.3.5) and/or soil (Chapter 3.3.6) conditions displayed lower foliar Hg(0) uptake rates of isohydric tree species like pine than wetter forest sites.

These two controls suggest, that the foliar Hg(0) uptake flux has to be understood in the context of foliage stomatal gas exchange processes. Exchange of water vapor and CO_2 by forest trees depends on tree species-specific foliar physiological processes like transpiration and photosynthesis and on climatic conditions. Trees open their stomata in order to transpire and to allow an influx of CO_2 [55]. Trees close their stomata in order to avoid cavitation under dry conditions [55]. Ambient Hg(0) can diffuse to foliage interior via open stomata, i.e. when stomatal conductance is high. Therefore, this thesis advances the notion, that foliar Hg(0) uptake is primarily controlled by foliage stomatal conductance as a key parameter to take into consideration when studying Hg(0) deposition to forests. If stomatal conductance is not accounted for in Hg cycle models, it will be difficult to accurately represent the forest foliar Hg(0) uptake flux, particularly under changing climate conditions.

5.1.3 The forest foliar Hg(0) uptake flux within the environmental Hg cycle

Assimilation of Hg(0) by vegetation is the most relevant (60% - 90%) atmospheric source to soil Hg [19–22]. Foliar Hg(0) uptake fluxes measured at 10 European forest sites were higher than comparable Hg(II) wet deposition fluxes by a factor of 5 on average (Chapter 2), confirming the quantitative relevance of foliar Hg(0) uptake compared to Hg(II) wet deposition. Foliar Hg(0) uptake represents an important contribution to total vegetation Hg input to forest ecosystems, which also comprises throughfall [77], Hg uptake by woody biomass [96] or by understory vegetation like mosses and lichen [10, 60]. Foliage was recently estimated to account for around 50% of global vegetation Hg assimilation [10]. Foliar Hg(0) uptake fluxes determined by the bottom-up method applied for this thesis (Chapter 2) are net fluxes, because foliar Hg concentrations, which increased linearly over the growing season, already include Hg(0) re-emission. In absence of net forest foliar Hg(0) uptake throughout the growing season, more Hg(0) would remain in the atmosphere [9]. On the European continent, a total amount of 20 - 30 Mg Hg(0) growing season^{-1} (Chapters 4.3.1, 2.3.6) is withdrawn from the atmosphere by forest foliage, representing approximately a third of anthropogenic Hg emissions of the European Union of around 77 Mg Hg in 2015 [4]. Any atmospheric Hg(0) taken up by forest foliage over the growing season reduces the potential of global Hg(0) distribution via long-range atmospheric transport to e.g. open oceans, where it can biomagnify as methyl-Hg in the local marine food web [11]. This thesis suggests, that the forest foliar Hg(0) uptake flux is of major importance for exploring these scenarios within the environmental Hg cycle like a repartitioning of deposition to land and to open oceans. Therefore, more research effort is needed to correctly parameterize the forest Hg(0) deposition flux in chemical Hg transport models, so projections of emission reduction can be assessed more meaningful with regard to aquatic ecosystems.

5.1.4 The forest foliar Hg(0) uptake flux under climate change

Global forests are challenged by a mix of emerging climate trends. Under the ongoing climate crisis, discrete forest disturbances like drought, insect/pathogen infestation, windthrow or wildfire are projected to increase in intensity and frequency, against a backdrop of gradual developments such as rising VPD, temperature and CO_2 [61]. Adding to these changes, forest logging has intensified over the past few decades as a result of land use change [272]. The forest Hg cycle is expected to change as a consequence of these climate-induced forest transformation processes [62, 273], yet the trend and magnitude of this change in the forest Hg cycle is still uncertain. Any disruption resulting in forest dieback through e.g. drought, wildfire or deforestation will reduce the capacity of forests to sequester atmospheric Hg(0). Changes in vegetation cover through biome shifts, on the other hand, might result in an increase of forest Hg(0) uptake, e.g. by an expansion of temperate broadleaf and boreal needleleaf forests to higher latitudes and thereby an increase in forested area accumulating atmospheric Hg(0) [62].

Since the industrialisation, atmospheric CO_2 concentrations have risen by more than 130 ppm to 412 ppm in 2021 [274, 275]. Higher net forest primary production as a result of CO_2 fertilization was proposed to increase vegetation Hg(0) assimilation [12, 62, 240]. However, the stomatal signal of foliage Hg(0) uptake investigated in this thesis suggests, that, a decrease in net foliar Hg(0) uptake flux under CO_2 fertilization is likely due to controls of foliage stomatal conductance. At elevated atmospheric CO_2 levels, plants tend to intensify net primary production but concurrently reduce their stomatal conductance to improve their water use efficiency [276, 277]. Given that foliar Hg(0) uptake mainly occurs via the stomatal pathway, the stomatal Hg(0) uptake rate could therefore be reduced with rising ambient CO_2. Under conditions of drought, the decline in stomatal conductance is exacerbated [276]. Experimental and modelling studies suggests that under continued climate change, forests might transition from CO_2 fertilization to a period dominated by drought [278]. Observations presented in this thesis conclude, that drought conditions like reduced soil moisture content (Chapter 3.3.6) and longer periods of elevated VPD (Chapter 3.3.5) reduce the forest foliar Hg(0) uptake flux, which, by extension, would result in more long-range transport of Hg(0) remaining in the atmosphere (Chapter 5.1.3). Therefore, this thesis recommends to put the focus for projections on the forest foliar Hg(0) uptake flux under climate change on stomatal conductance rather than on net primary production.

5.2 Outlook

5.2.1 Stomatal Hg(0) uptake modelling

The ultimate goal of testing and validating a stomatal Hg(0) model, which depends on environmental parameters, is to apply this model on a larger spatial scale by incorporating the stomatal component into a global chemical transport model (CTM) like GEOS-Chem. CTMs commonly do not incorporate stomatal feedback to plant-specific and meteorological parameters. By taking the stomatal Hg(0) component into account, a more meaningful model projection of the foliar stomatal Hg(0) uptake flux under climate change (Chapter 5.1.4) might be achieved. In order to implement a stomatal Hg(0) model, pre-existing stomatal models for other pollutants could serve as prototypes. A different gaseous pollutant, which diffuses into foliage via the stomatal pathway is tropospheric ozone (O_3) [279, 280]. A large amount of research efforts have been dedicated to implement and validate stomatal foliar O_3 uptake models, because O_3 uptake damages foliage interiors and metabolic processes, thereby jeopardizing e.g. agricultural crop yields [185]. DO3SE (Deposition of Ozone for Stomatal Exchange), for example, is a widely applied O_3 model, which evaluates the risk of O_3 damage to European vegetation types using a resistance in-series approach to O_3 deposition [185]. The stomatal resistance component within DO3SE represents the inverse foliage stomatal conductance to O_3 (g_{s,O_3}), which is computed

as a fraction of the plant-specific maximum stomatal conductance to O_3 (g_{max,O_3}) using relative functions (output values between 0 and 1), that scale g_{max,O_3} with plant phenology and environmental conditions of light, ambient temperature, VPD and soil water [217, 229, 281]. Consequently, meteorological input data for these scaling functions of the stomatal O_3 flux include air temperature, relative humidity, VPD, wind speed, radiation and soil water content [282]. In analogy to the conceptualization of the DO3SE model, the following steps towards a stomatal Hg(0) flux model have to be taken:

- Testing of the validity of the stomatal scaling functions within DO3SE for Hg(0) uptake fluxes on foliage level through targeted laboratory experiments by measuring foliar Hg(0) uptake and stomatal conductance under controlled parameters (temperature, humidity, soil moisture). Testing should also be extended to pre-existing datasets of environmental response values of g_{s,CO_2}, g_{s,H_2O} or g_{s,O_3}, that had been transformed to $g_{s,Hg(0)}$ according to Eq. 1.2.

- Validation of modelled stomatal Hg(0) flux values by comparison with measured field data using in-situ foliage parameters and meteorological input. A high time resolution (hourly) is needed for field foliar Hg(0) flux data, such that measurements using e.g. dynamic flux bags are required.

- Upscaling from foliage to canopy level using LAI values.

5.2.2 Using foliar Hg to constrain stomatal conductance

In this thesis, stomatal conductance was presented as crucial for understanding and modelling foliar Hg(0) uptake. In reverse, foliar Hg(0) uptake rates might serve as a proxy for stomatal conductance integrated over a time span of several weeks to one growing season. Comparibly easy-to-perform measurements of foliar Hg(0) uptake rates using e.g. the bottom-up method introduced in Chapter 2 could possibly provide a complementary approach to evaluating a time-integrated stomatal conductance without the need for continuous and labor-intensive stomatal conductance measurements over an entire growing season.
Additionally, foliar Hg analysis might provide clues on changes in foliar metabolic responses to climate change. Under global warming, plants are expected to increase their intrinsic water use efficiency, i.e. their ratio of photosynthesis to stomatal conductance [61, 283]. It is still uncertain, however, to which extent this increase in intrinsic water use efficiency is the result of rising rates of net photosynthesis due to CO_2 fertilization and/or of decreasing stomatal conductance due to drought conditions [277]. Stable carbon isotope ratios ($\delta^{13}C$) in foliage or wood represents a measure for intrinsic water use efficiency [284]. If foliar Hg(0) uptake can be established as a proxy for stomatal conductance, concurrent analysis of foliar Hg(0) accumulation and $\delta^{13}C$ in future over a longer time span or in retained foliage samples of the past decades will indirectly

provide a measure of the impact of net photosynthesis on water use efficiency. It has to be noted, though, that the effect of temporally changing ambient Hg(0) on foliar Hg(0) uptake has to be taken into account in such a analysis.
The prerequisite to establishing foliar Hg uptake as a proxy for stomatal conductance is an accurate parametrization of stomatal Hg(0) uptake by different plant species, under changing meteorological conditions and atmospheric Hg(0) concentrations. Ideally, research on foliar Hg(0) uptake can advanced a complementary tool to better constrain the hydrological status of trees.

Appendix A

Supporting Information: A bottom-up quantification of foliar mercury uptake fluxes across Europe

This Supporting Information has been published accompanying the research article with the title "A bottom-up quantification of foliar mercury uptake fluxes across Europe" (DOI: 10.5194/bg-17-6441-2020)

A.1 Overview of parameters associated with the ten forest research sites

TABLE A.1. Summary of exact location and associated parameters of the ten study sites.

Site	Longitude	Latitude	Growing season (d)	Species	R^2	Foliar Hg uptake flux ($\mu g\ m^{-2}_{ground}\ season^{-1}$)	Sampling dates (day.month.year)
Bredkälen	15°19′11"E	63°50′43"N	150	birch	0.94	2.6 ± 0.5	28.05.2018 04.10.2018
				pine	0.93	3.5 ± 0.6	
				spruce	0.50	14.2 ± 7.8	
Hölstein	7°46′33"E	47°26′19"N	220	beech	0.92	18.0 ± 2.9	15.05.2018 13.06.2018 11.07.2018 14.08.2018 13.09.2018 18.10.2018
				oak	0.92	25.6 ± 5.3	
				pine	0.84	3.2 ± 0.5	
				spruce	0.69	9.4 ± 5.9	
Hurdal	11°04′39"E	60°22′18"N	170	pine	0.86	5.1 ± 1.2	04.07.2018 13.09.2018 14.11.2018
				spruce	0.88	17.4 ± 2.6	
Hyltemossa	13°25′10"E	56°05′52"N	170	spruce	0.44	14.0 ± 13.6	28.05.2018 08.08.2018 06.11.2018
Norunda	17°29′00"E	60°05′00"N	170	pine	0.59	4.1 ± 1.4	28.05.2018 07.08.2018 08.10.2018
				spruce	0.75	14.7 ± 8.9	
Pallas	24°06′56"E	67°58′24"N	120	pine	0.86	2.3 ± 0.4	28.06.2018 29.08.2018 13.03.2019
				spruce	0.49	2.9 ± 0.9	
Råö	11°54′51"E	57°23′37"N	170	birch	0.96	3.3 ± 0.6	25.05.2018 30.07.2018 01.10.2018
				oak	1	9.1 ± 1.4	
				pine	0.77	3.3 ± 0.5	
				spruce	1	4.2 ± 2.2	
Schauinsland	7°54′28"E	47°54′48.7"N	200	beech	0.92	26.1 ± 4.5	12.06.2018 12.09.2018 06.11.2018
				spruce	0.89	25.8 ± 7.4	
Schmücke	10°46′08"E	50°39′15"N	190	ash	0.99	9.4 ± 1.8	31.05.2018 30.08.2018 11.10.2018
				spruce	0.64	8.3 ± 1.7	
Svartberget	19°45′55"E	64°14′41"N	190	pine	0.87	4.9 ± 0.9	14.06.2018 07.08.2018 01.10.2018
				spruce	0.82	7.1 ± 3.8	

A.2 Average LAI values for six tree species (birch, beech, ash, spruce, pine and oak)

TABLE A.2. Average LAI values ($m^2_{leaf}\ m^{-2}_{ground}$) derived from Iio and Ito [115] with standard deviation (sd.), standard error (se.) and number of values (n).

Species	avg. LAI value	sd. LAI value	rel. se. LAI value	n
birch	2.6	1.22	0.19	40
beech	7.0	1.57	0.19	70
ash	3.1	0.55	0.13	2
spruce	7.3	2.12	0.32	45
pine	2.9	1.37	0.25	31
oak	4.9	1.66	0.33	25

A.3 Foliar Hg concentration after drying at different temperatures

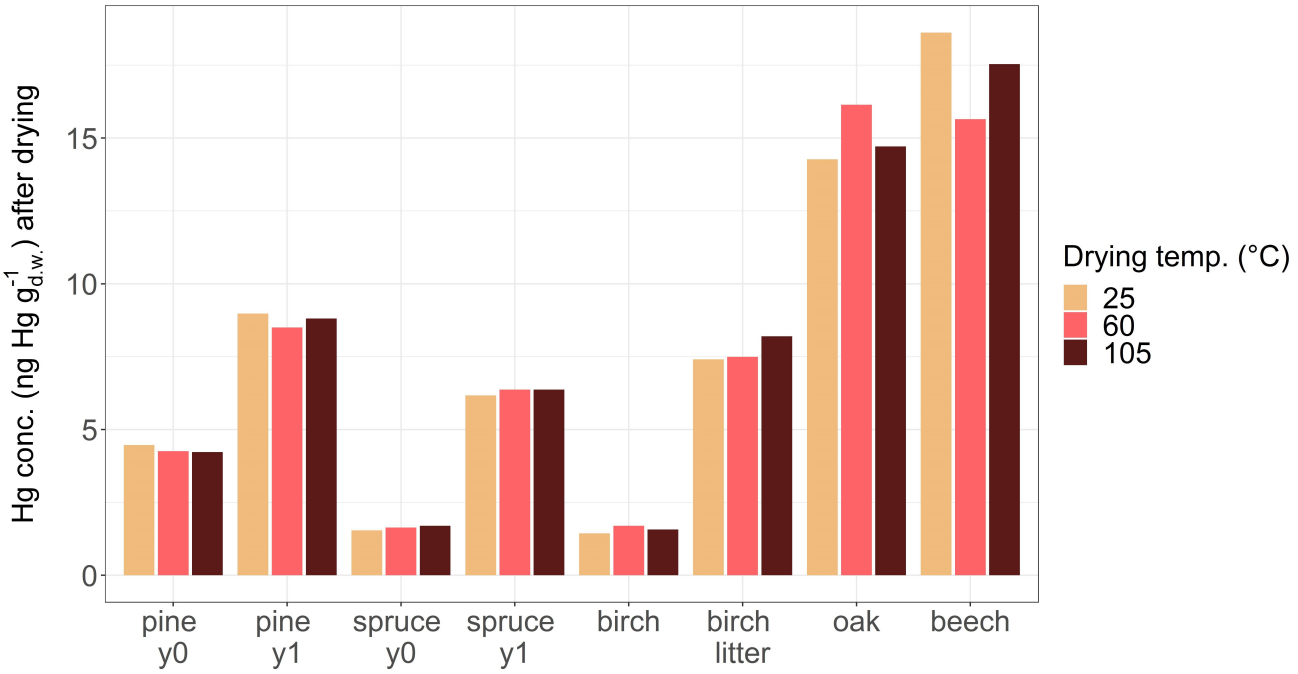

FIGURE A.1. Hg concentration (ng $g^{-1}_{d.w.}$) measured in 3 subsamples of 8 independent foliar samples of various tree species and needle age classes. Each respective subsample was dried at either 25°C, 60°C or 105°C for 24 hours prior to Hg measurement. Resulting Hg concentrations were all corrected for water content to make them comparable.

A.4 Details on measurements of needle area

A.4.1 Calibration of the LI3100 for needles

We used an LI3100 Area Meter (LI-COR Biosciences USA) for measuring projected areas of both leaf and needle samples. The per cent deviation between scans and duplicate scans was 3% ± 3%. Scans of projected leaf areas produced robust results. The accuracy of needle scans, however, proved challenging due to the high ratio of edge to area of needles. We thus calibrated the LI3100 applying round rubberized pieces of wires of known length and a diameter of 1.74 ± 0.02 mm as standard material to simulate needle phenology. Projected areas of the rubberized wires were verified by scanning the wires to a digital image and applying image recognition software to calculate the projected wire area. Calibration curves revealed that values for projected areas of standard material measured at the LI3100 met only 60% of respective target values (Fig. A.2). We suspect that the light sensor of the LI3100 is not able to fully resolve thin needles and thus recommend to use different area scanning devices with a higher accuracy for needle

geometry in future studies. In order to obtain needle area values as accurate as possible given the low resolution of needles at the LI3100, we replaced, where possible, needle area values with values determined by research staff (Hyltemossa, Norunda and Svartberget; see A.4.2) or with literature values at two sites (Hurdal and Pallas) where the LI3100 produced faulty and unrealistic results (A.4.3).

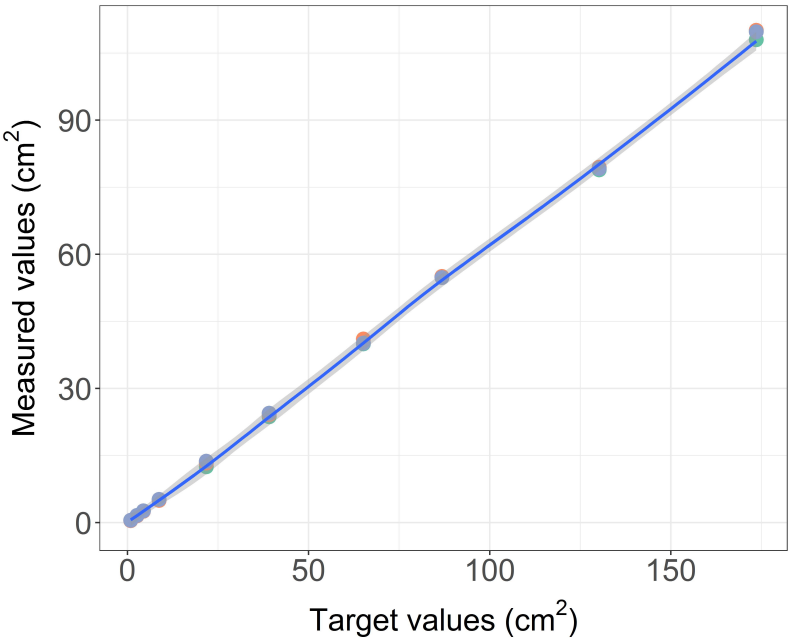

FIGURE A.2. Calibration curve of needle shaped rubberized standard materials of known projected area (cm^2) measured at a LI3100 Area Meter.

A.4.2 Projected needle area values from ICOS stations

At the Swedish ICOS stations Hyltemossa, Norunda and Svartberget projected areas and LMA of pine and spruce needles from the 2018 growing season were determined by research staff [112]. Given the low resolution of thin needles by the LI3100 (Sect. A.4.1) we suspected that the ICOS needle area values are closer to true values than our values. We thus multiplied the foliar Hg uptake rates (ng Hg $g_{d.w.}^{-1}$ month^{-1}) of tree species at Hyltemossa, Norunda and Svartberget with the average LMA values of tree species at the 3 sites respectively to obtain foliar Hg uptake rates normalized to projected needle area (ng Hg $m_{needle\ area}^{-2}$ month^{-1}). The average LMA of 2018 spruce needles at Hyltemossa was 331 $g_{d.w.}$ $m_{needle\ area}^{-2}$. The average LMA of pine and spruce needle areas at Norunda was 129 $g_{d.w.}$ $m_{needle\ area}^{-2}$ and 179 $g_{d.w.}$ $m_{needle\ area}^{-2}$ respectively. At average Svartberget the LMA of pine and spruce needle areas was 192 $g_{d.w.}$ $m_{needle\ area}^{-2}$ and 189 $g_{d.w.}$ $m_{needle\ area}^{-2}$ respectively.

A.4.3 Projected needle area values from samples of Hurdal and Pallas

Needle areas of needles collected at the research sites Hurdal and Pallas and measured at the LI3100 were exceptionally low resulting in relatively high average LMA values (mass over area) of 704 ± 144 $g_{d.w.}$ $m^{-2}_{needle\ area}$ and 680 ± 332 $g_{d.w.}$ $m^{-2}_{needle\ area}$ respectively. The average LMA value of needles of all other sites was 246 ± 74 $g_{d.w.}$ $m^{-2}_{needle\ area}$. We defined an acceptable LMA threshold value of 475 $g_{d.w.}$ $m^{-2}_{needle\ area}$ which corresponds to the 90th percentile value from 70 LMA values of evergreen gymnosperm foliage compiled by Poorter et al. [285]. We thus discarded needle areas of samples from Hurdal and Pallas due to faulty performance of the LI3100 at the particular measurement days which might be the result of unrecorded dirtying of the area meter conveyer belt but could not be reconstructed in retrospect. For the LMA values of needle samples from Hurdal and Pallas we thus used the median LMA value of 227 $g_{d.w.}$ $m^{-2}_{needle\ area}$ for evergreen gymnosperms following Poorter et al. [285].

A.5 Needle Hg concentrations of multiple needle age classes

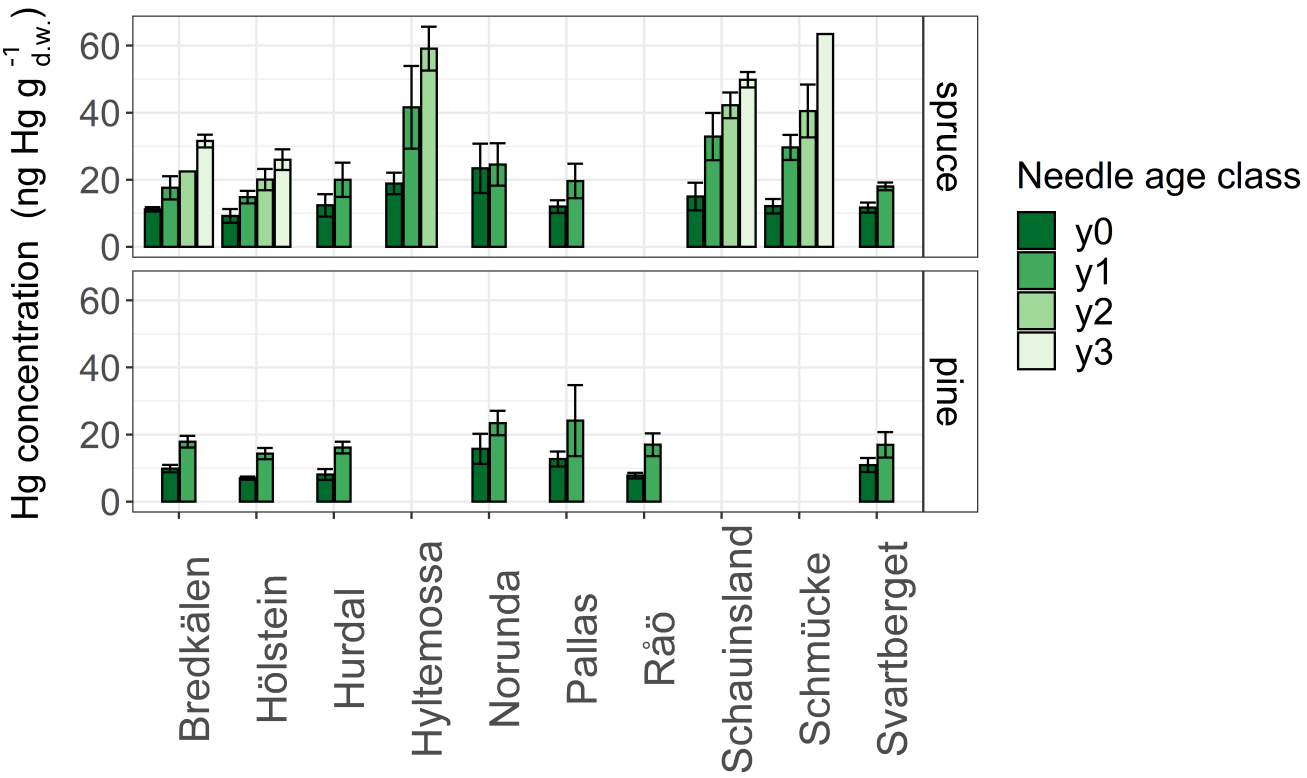

FIGURE A.3. Hg concentrations (ng $g^{-1}_{d.w.}$) in spruce and pine needles of various age classes sampled at the end of the 2018 growing season (October – November). Age class 0 represents current season needles, age classes 1, 2 and 3 one-, two- and three-year old needles respectively. Error bars denote one standard deviation between needle age samples of multiple trees at each site.

A.6 Details on analysis of needle age correction factors (cf_{age})

Cf_{age} allows to scale up Hg uptake flux determined in y_0 needles to Hg uptake flux in needles of all age classes (Eq. 2.4). For calculating needle age correction factors (cf_{age}) according to Eq. 2.3 we used i) RAR values averaged over Bavarian sampling sites and sampling years (spruce: 9 sampling sites in 2015 and 10 sampling sites in 2017; pine: 2 sampling sites in 2015 and 2017 respectively) determined in our systematic needle analysis (Fig 2.4) and ii) the relative biomass (RB) of each spruce needle age class from literature [118] (Table A.3). For pine we assumed that fully grown needle age classes (y_0 to y_2) exhibit equal RBs, thus RB for three pine needle age classes is 0.33 respectively (Table A.3). Standard error of cf_{age} was determined by error propagation of RAR standard errors, see Section A.15.

TABLE A.3. Species-specific correction factors for needle age (cf_{age}) allowing to scale up Hg uptake fluxes of current-season (y_0) needles to Hg uptake fluxes of needles of all age classes (Eq. 2.4). RAR is the relative Hg accumulation rate of respective needle age class normalized to Hg accumulation rate of y0 needles determined in our systematic needle analysis as average over sampling sites and sampling years. RB is the relative biomass of each needle age class to total biomass determined for spruces by Matyssek et al. [118]. Final needle age correction factor, cf_{age}, was calculated according to Eq. 2.3.

Tree species	**Needle age class**	**RAR** (mean ± se)	**RB**	**cf_{age}** (factor ± se)
spruce	y_0	1	0.195	0.79 ± 0.03
	y_1	0.95 ± 0.05	0.19	
	y_2	0.90 ± 0.05	0.18	
	y_3	0.84 ± 0.06	0.14	
	y_4	0.55 ± 0.11	0.17	
	y_5	0.45 ± 0.08	0.075	
	y_6	0.13 ± 0.14	0.05	
pine	y_0	1	0.33	0.86 ± 0.06
	y_1	0.99 ± 0.19	0.33	
	y_2	0.65	0.33	

A.7 Details on Hg(0) air measurements using passive air samplers (PAS)

We attached Hg passive air samplers (PAS) to the ceiling of the crane installed at Hölstein at heights of 35 m, 19 m, 10 m and to four trees at a height of 1.6 m respectively (Fig. S4). Each PAS comprised a sulfur-impregnated activated carbon (AC) sorbent with a white Radiello© diffusive housing inside a protective jar. The application of PAS is described in detail by McLagan et al. [286, 287]. We conducted two PAS campaigns. The PAS exposure period of the 2018 campaign was 156 days between 15 May to 18 October 2018 and the 2019 campaign lasted 119 days from 16 May to 12 September 2019. We calculated atmospheric Hg(0) concentrations by dividing the total Hg content measured in AC of each PAS respectively by the corresponding exposure period (156 days in 2018 or 119 days in 2019) and a sampling rate of 0.135 m^3 day^{-1} calibrated by McLagan et al. [288]. However, meteorological parameters like wind speed and temperature may slightly impact sampling rate. For every m s^{-1} increase in wind speed and every 1°C McLagan et al. [287] found an increase of sampling rate of 2.5% and 0.7% respectively. Higher wind speeds above canopy than at understory height level results in an increase of sampling rate of PAS at 35 m compared to PAS at 1.6 m and thus a decrease in gradient of atmospheric Hg(0) above canopy to understory.

Analysis of AC for total Hg content was performed using a DMA-80 (Milestone, Heerbrugg, Switzerland) according to sampling operation procedure described in section 2.2.3. Total AC of each PAS was analyzed for Hg at the DMA-80 in aliquots of two and Na_2CO_3 was added to each sampling boat following a recommendation by McLagan et al. [289]. Standard reference material of AC for the 2018 campaign was produced manually. For this purpose we extracted 280 μl of Hg vapor stabilized at 20°C (corresponding to 3.7 ng Hg) using a gas tight syringe (Hamilton Company) from a mercury vapor primary calibration unit (Tekran*SymbReg* Model 2505, Inc. Toronto, Canada). We injected the Hg vapor into an airtight Teflon tube attached to a glass tube filled with approximately 400 mg of AC. An attached pump drew the injected Hg vapor through the AC resulting in an adsorption of Hg to the AC. The average recovery of Hg in AC SRMs was 0.92 $\pm$ 0.13 (mean $\pm$ sd, n = 6). For measuring Hg in AC of our 2019 campaign we applied the bituminous coal standard NIST2685c and found an average recovery of 1.02 $\pm$ 0.08 (mean $\pm$ sd, n = 7). We were not able to perform a blank correction in 2018 as our field blanks got contaminated when accidentally storing them in a cupboard where Hg air concentrations were elevated probably due to legacy Hg which we confirmed by measuring air Hg using active instruments. In 2019 we analyzed a field blank which consisted of one PAS brought to the field at the beginning of the deployment period, opened, closed immediately again and stored until analysis together with deployed PAS. The 2019 PAS samples were blank adjusted by multiplying the field blank concentration with each sample AC mass and substracting the result from the mass of Hg sorbed on the respective AC.

FIGURE A.4. Mounting of mercury passive air samplers (PAS) at the crane ceiling above canopy (left) and at a tree at ground level (right) at the Hölstein research site.

A.8 Foliar Hg concentrations in Hölstein at peak season (August)

At the experimental mixed forest site Hölstein we sampled different types of foliage side by side allowing for comparison of foliar Hg concentrations between tree functional groups (deciduous leaves vs. coniferous needles). Deciduous beech and oak leaves exhibited higher Hg concentrations than coniferous pine and spruce needles of the same age (current season, Table A.4). However, average Hg concentrations in multi-year old needles (one to three year old) approached average Hg concentrations of leaves because needles accumulate Hg over their whole life cycle (see 2.3.1).

TABLE A.4. Mean ± sd (n = number of sampled trees) of foliar Hg concentration (ng Hg $g_{d.w.}^{-1}$) in four types of foliage at Hölstein in August. Foliage was sampled at top of canopy.

Foliage type	Current season (y_0)	One-year old (y_1)	Two-year old (y_2)	Tree-year old (y_3)
beech leaves	21.6 ± 2.9 (n = 3)	-	-	-
oak leaves	22.7 ± 4.1 (n = 4)	-	-	-
pine needles	6.5 ± 0.6 (n = 2)	13.2 ± 3.1 (n = 3)	not sampled	-
spruce needles	8.1 ± 2.2 (n = 3)	12.8 ± 1.3 (n = 3)	20.2 ± 5.5 (n = 2)	26.6 ± 7.4 (n = 2)

A.9 Foliar Hg pool calculation for coniferous trees

When assessing the foliar Hg pool of coniferous trees, Hg levels in needles of all age classes present at coniferous trees have to be taken into account. Consequently, Hg levels in each needle age class (weighted by their respective relative biomass RB) have to be added up. As an example calculation, we determined the spruce needle Hg pool of the boreal forest at Pallasjärvi in Northern Finland which is part of the atmosphere-ecosystem research site Pallas. To this end, we used the Hg concentration of current season (y_0) spruce needles sampled in Pallas in August 2018 which was 10.4 ± 1.5 ng Hg $g_{d.w.}^{-1}$ (mean ± sd; n = 5 sampled spruce trees). By multiplying the mean Hg concentration of y_0 needles by the Hg relative accumulation rate (RAR; see A.6 Table A.3) of each spruce needle age class y_1 to y_6 respectively, we derived theoretic Hg concentration gains (that is, quantities of Hg accumulated from the start of the growing season 2018 until sampling in August 2018) for each needle age class. These gains are 9.9 ng Hg $g_{d.w.}^{-1}$ for spruce needles y_1, 9.4 ng Hg $g_{d.w.}^{-1}$ for spruce needles y_2, 8.8 ng Hg $g_{d.w.}^{-1}$ for spruce needles y_3, 5.7 ng Hg $g_{d.w.}^{-1}$ for spruce needles y_4, 4.7 ng Hg $g_{d.w.}^{-1}$ for spruce needles y_5 and 1.4 ng Hg $g_{d.w.}^{-1}$. for spruce needles y_6. Using these gains, we estimated total Hg concentrations in each needle age class y_i by incrementally summing up the Hg concentration gains of needles y_i with Hg concentration gains of needles y_{i-1}. This results in a total Hg concentration of 10.4 ng Hg $g_{d.w.}^{-1}$ for needles y_0, 20.6 ng Hg $g_{d.w.}^{-1}$ for needles y_1, 29.8 ng Hg $g_{d.w.}^{-1}$ for needles y_2, 38.6 ng Hg $g_{d.w.}^{-1}$ for needles y_3, 44.3 ng Hg $g_{d.w.}^{-1}$ for needles y_4, 49.0 ng Hg $g_{d.w.}^{-1}$ for needles y_5 and 50.3 ng Hg $g_{d.w.}^{-1}$ for needles y_6. To calculate the Hg concentration pool representive for all spruce needles present, we weighted total Hg concentrations of each needle age class with their respective relative biomass (A.6 Table A.3) and summed up all resulting values. This resulted in a spruce needle concentration pool of 30.4 ng Hg $g_{d.w.}^{-1}$ which is close to the range of Hg concentrations in deciduous leaves (see for example A.8, Table A.4). In a final step, we obtained a foliar Hg

pool normalized to m^2 ground area by multiplying the concentration pool with an LMA value of 227 $g_{d.w.}$ $m^{-2}_{needle\ area}$ (median LMA value used for Pallas, see A.4.3) and an LAI value of 3 m^2_{leaf} m^{-2}_{ground} (retrieved from PROBA-V satellite LAI product for Pallasjärvi in August 2017). The final spruce needle Hg pool equals 20.7 μg Hg m^{-2}_{ground}.

A.10 Hg content per leaf area at various tree heights of beech and oak at Hölstein

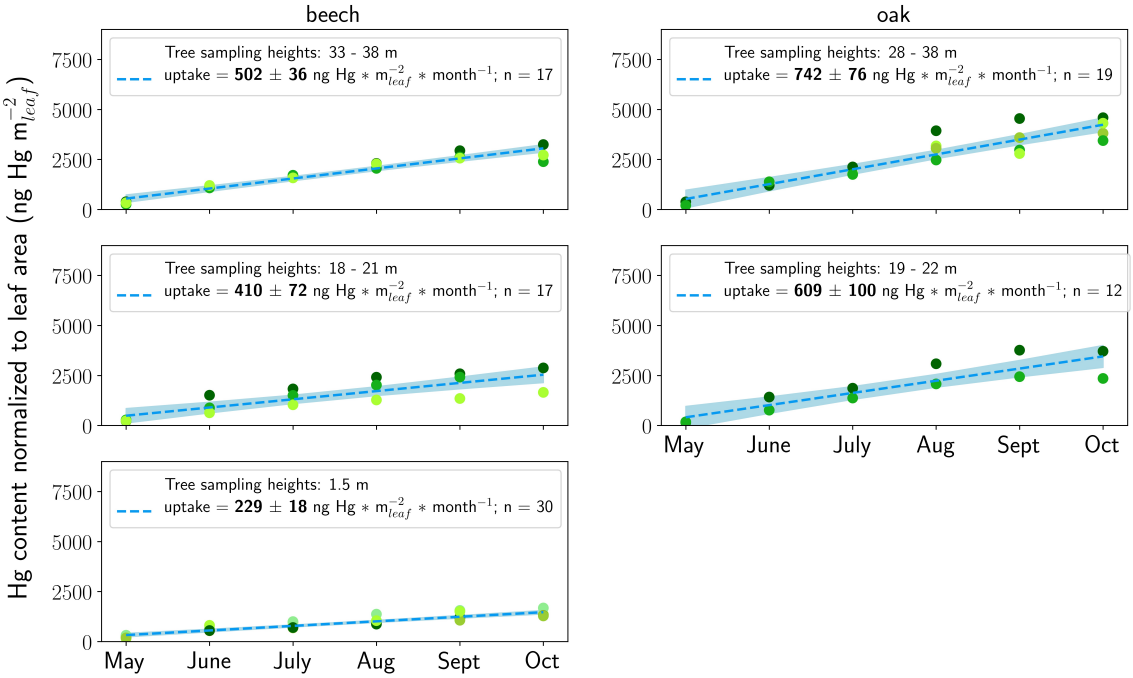

FIGURE A.5. Increasing Hg content normalized to leaf surface area (ng Hg $m^{-2}_{leaf\ area}$ $month^{-1}$) in leaves of beech trees (left column) and oak trees (right column) at Hölstein over the 2018 growing season. Trees were sampled vertically from top canopy height (top row; 28 – 38 m above ground level) to mid canopy height (middle row; 18 – 22 m above ground level) to ground level (bottom row; chest height of approximately 1.5 m above ground level).

A.11 Details on analysis of tree height correction factors (cf_{height})

We determined a crown height correction factor (cf_{height}) in order to scale up the foliar Hg uptake flux at canopy level to whole tree foliage. Cf_{height} equals the multiplication of the ratio $r_{conc.coeff.}$ and r_{LMA} (Eq. 2.5). In Hölstein $r_{conc.coeff.}$ was 1.31 ± 0.10 (ratio ± se) for beech, 1.11 ± 0.12 (ratio ± se) for oak and 1.13 ± 0.10 (ratio ± se) for spruce (Table A.4). The ratio r_{LMA} equals the average LMA values of foliage samples growing at ground/mid canopy level to

corresponding LMA values at top canopy level. We determined r_{LMA} two times with different data by using i) LMA values measured at different tree heights in Hölstein and ii) LMA values from literature [139, 290]. R_{LMA} calculated by using LMA values from Hölstein was 0.36 ± 0.06 (ratio ± se) for beech, 0.78 ± 0.08 (ratio ± se) for oak and 0.63 ± 0.07 (ratio ± se) for spruce (Table A.4). Changing LMA values with tree height are the result of changing foliage morphology with tree height which in turn is a function of changing sun light availability with tree height (Section 2.3.3). Consequently, LMA (or its inverse specific leaf area, SLA) may be conceived as an indirect function of available sun light. Stancioiu and O'Hara [139] determined SLA values as a function of percentage of above canopy light (PACL) for beech, spruce and fir. Under the assumption that light at ground level equals 10% and light at canopy level equals 90% of ambient light, r_{LMA} derived from Stancioiu and O'Hara [139] is 0.43 ± 0.18 (ratio ± se) for beech and 0.61 ± 0.24 (ratio ± se) for spruce. For oak trees we calculated an r_{LMA} of 0.62 from data by Eriksson et al. [290]. Thus, r_{LMA} values derived from Stancioiu and O'Hara [139], Eriksson et al. [290] are in the same range as average r_{LMA} values determined in Hölstein. As functions of inverse LMA with PACL by Stancioiu and O'Hara [139] were more generically determined for a range of trees of various heights, diameters and ages we used values from Stancioiu and O'Hara [139], Eriksson et al. [290] for all sites where foliage samples were taken at crown level (Hyltemossa, Norunda and Svartberget) except Hölstein. Pine was excluded from the analysis as pine trees in Hölstein exclusively grew needles in the canopy and pine on average exhibit LAI values < 3 (Table A.2). Standard errors of $r_{conc.coeff.}$, r_{LMA} and cf_{height} were determined by error propagation, see Section S13.

TABLE A.5. Species-specific factors (cf_{height}; Eq. 2.5) correcting foliar Hg uptake fluxes (Eq. 2.6) for tree height effects originating from changes in linear regression coefficients of foliar Hg concentration over time with tree height (represented by the ratio $r_{conc.coeff.}$) and changes of LMA with tree height (represented by the ratio r_{LMA}). R_{LMA} was calculated two times by using data from Hölstein (Hölstein r_{LMA}) and by using a function of inverse LMA with available sun light from literature (lit. r_{LMA}).

Tree species	**$r_{conc.coeff.}$ (ratio ± se)**	**Hölstein r_{LMA} (ratio ± se)**	**lit. r_{LMA} (ratio ± se)**	**Hölstein cf_{height} (ratio ± se)**	**lit. cf_{height} (ratio ± se)**
Beech	1.31 ± 0.10	0.36 ± 0.06	0.43 ± 0.18	0.47 ± 0.12	0.56 ± 0.20
Oak	1.13 ± 0.10	0.78 ± 0.08	0.62	0.88 ± 0.13	0.70
Spruce	1.11 ± 0.12	0.63 ± 0.07	0.61 ± 0.24	0.70 ± 0.14	0.68 ± 0.27

A.12 Tree species abundance at canopy sampling sites

TABLE A.6. Approximate abundance of tree species to each other at Hölstein and three Swedish ICOS sites where foliage samples were obtained from top canopies.

Site	Tree species	Tree species abundance to each other
Hölstein	beech	0.53
	oak	0.05
	pine	0.11
	spruce	0.31
Hyltemossa	spruce	1.0
Norunda	pine	0.47
	spruce	0.53
Svartberget	pine	0.60
	spruce	0.40

A.13 Foliar Hg uptake fluxes of Hg at the ten research sites

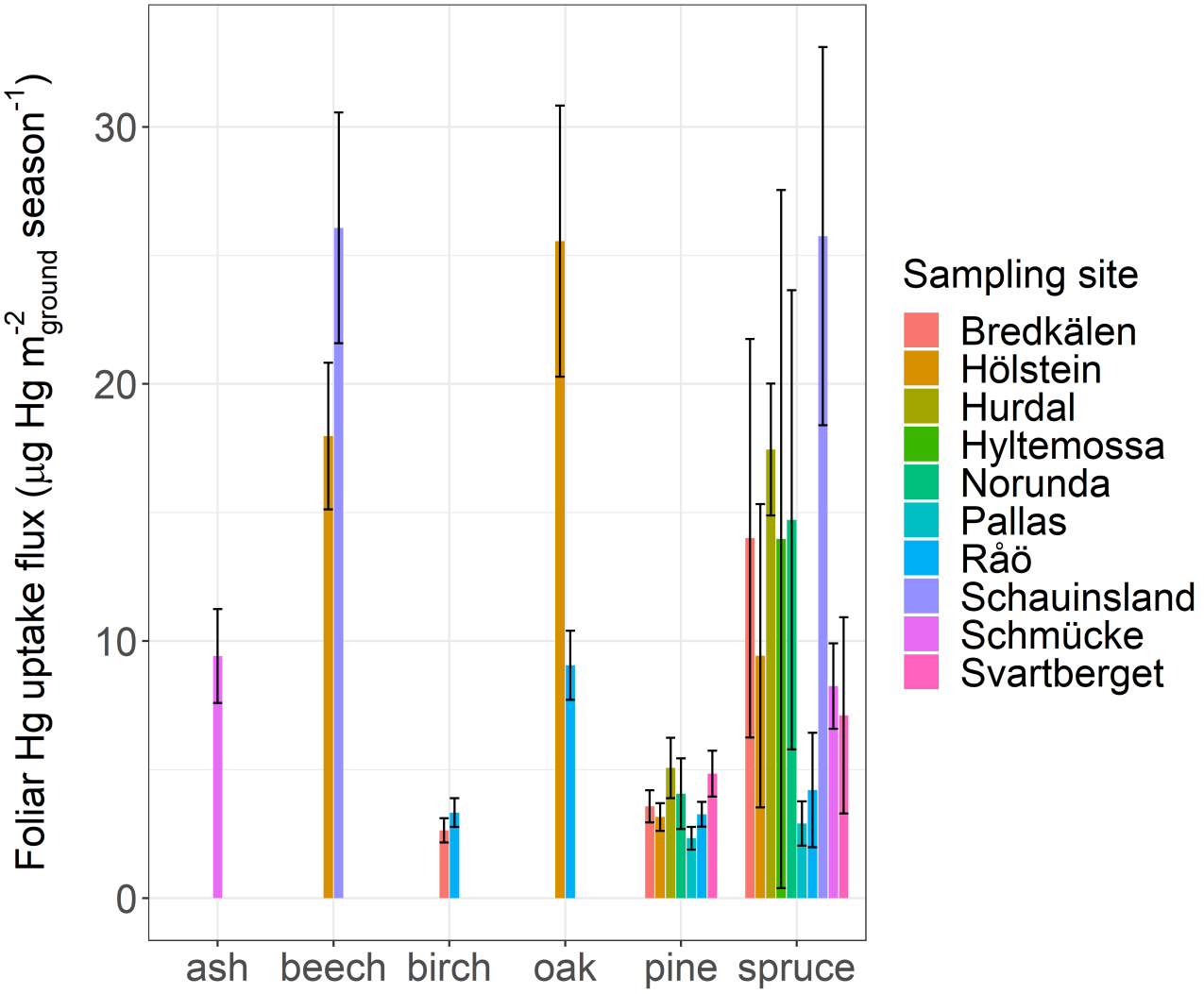

FIGURE A.6. Foliar Hg uptake fluxes (μg Hg m^{-2} during the 2018 growing season) of 6 tree species at 10 forested research sites in Europe.

A.14 Details on extrapolation of foliar Hg uptake fluxes to Europe and global temperate forests

We extrapolated foliar Hg uptake fluxes from this study to the forested land area of Europe and globally to the area of temperate forests. This was performed by 1) weighting average Hg uptake fluxes of each tree species (beech, oak, spruce, pine) at Hölstein, Hyltemossa, Norunda and Svartberget with the respective relative abundance of tree species in Europe and 2) multiplying the resulting average Hg uptake flux with the forested land area of Europe or the land area of global temperate forests respectively. The relative proportion of tree species to each other

in Europe was derived from Brus et al. [153] who analyzed the spatial distribution of 20 tree species in Europe by combining national forest inventories with ICP Forests Level I plot data. Derived from Brus et al. [153] the relative proportion is 0.11 for beech, 0.10 for oak, 0.36 for spruce and 0.44 for pine. We evaluated the total forested area of Europe to amount to 192.672 · 106 hectares (ha) which is the sum of the forested area reported for the EU28 (160.931 · 10^6 ha; comprising the EU countries as in 2015 including the United Kingdom) [291], Norway (12.141 · 10^6 ha) [292], Ukraine (9.657 · 10^6 ha) [293], Belarus (8.633 · 10^6 ha) [294] and Switzerland (1.31 · 10^6 ha) [295]. The global land area of temperate forests is approximately 1.04 · 10^9 ha [154].

A.15 Uncertainty assessment of foliar Hg uptake fluxes and of flux extrapolation

We calculated the relative standard error of foliar Hg uptake fluxes per site and tree species (rel.se$_{flux}$) by error propagation of i) the relative standard error of the regression slope of Hg content in foliage of all sampled trees (per site and tree species) normalized to leaf area over sampling time (rel.se$_{uptake}$) and ii) the relative standard error of mean LAI values (per tree species) from literature (rel.se$_{LAI}$). For coniferous tree species and for sampling sites where foliage samples had been obtained from top canopy (Hölstein, Hyltemossa, Norunda, Svartberget) we additionally propagated the relative standard error of mean needle age correction factor (rel.se$_{age}$) and the relative standard error of mean tree height correction factor (per tree species) (rel.se$_{height}$).
Uncertainty assessment for deciduous (tree species at sites where foliage samples where not strictly taken from top canopy is calculated according to error propagation rule [261, 262]:

$$rel.se_{flux;\,deciduous} = \sqrt{(rel.se_{uptake})^2 + (rel.se_{LAI})^2}$$

The foliar Hg uptake flux coniferous tree species is corrected for the presence of various needle age classes and thus the error propagation is extended to

$$rel.se_{flux;\,conifer} = \sqrt{(rel.se_{uptake})^2 + (rel.se_{LAI})^2 + (rel.se_{age})^2}$$

Foliar Hg uptake fluxes for tree species exhibiting a mean LAI values > 3 and at sites were foliage samples were taken from top canopy calculate according to Eq. 2.6:

$$uptakeF[ng\ Hg\ m^{-2}_{ground}\ months^{-1}] = uptakeR_{topcanopy;leafarea} \cdot (3 + cf_{height} \cdot (LAI - 3))$$

The corresponding error propagation of the flux (Eq. 2.3) is calculated as:

$$rel.se_{top\ canopy\ flux;\ deciduous} = \sqrt{(rel.se_{uptake})^2 + \sqrt{(rel.se_{uptake})^2 + (rel.se_{LAI})^2 + (rel.se_{height})^2}}$$

In case of top canopy sampled spruce with a mean LAI > 3 the standard error of the age correction rel.se$_{age}$ has to be taken into account:

$$rel.se_{top\ canopy\ flux;\ spruce} = \sqrt{\sqrt{(rel.se_{uptake})^2 + (rel.se_{age})^2} + \sqrt{(rel.se_{uptake})^2 + (rel.se_{LAI})^2 + (rel.se_{height})^2 + (rel.se_{age})^2}}$$

The relative standard error of cf$_{age}$ (rel.se$_{age}$) is calculated by error propagation of the relative standard errors of Hg accumulation rates (rel.se$_{RAR}$) and the relative biomass of n needle age classes (y_0, y_1,..., y_n) (Sect. A.6):

$$rel.se_{age} = \sqrt{(RB_{y0})^2 \cdot (se_{RAR;y0})^2 + (RB_{y1})^2 \cdot (se_{RAR;y1})^2 + ... + (RB_{yn})^2 \cdot (se_{RAR;yn})^2}$$

The relative standard error of cf$_{height}$ (rel.se$_{height}$) is calculated by error propagation of the relative standard errors of the regression slopes of Hg concentrations (mass Hg per dry weight) over sampling time (rel.se$_{conc.reg.}$) in top canopy and ground foliage and the relative standard errors of mean leaf mass per area (LMA) (rel.se$_{LMA}$) of respective top canopy and ground foliage:

$$rel.se_{height} = \sqrt{\sqrt{(rel.se_{conc.reg.\ ground})^2 + (rel.se_{conc.reg.\ canopy})^2} + \sqrt{(rel.se_{LMA\ ground})^2 + (rel.se_{LMA\ canopy})^2}}$$

Both relative standard errors rel.se$_{conc.reg.}$ and rel.se$_{LMA}$ were calculated per tree species by using data from Hölstein. Additionally, we derived rel.se$_{LMA}$ from LMA data by Stancioiu and O'Hara (2006) [139] for spruce at Hyltemossa, Norunda and Svartberget because LMA values by Stancioiu and O'Hara (2006) [139] were more generically determined for a range of trees of various height, diameter and age. Stancioiu and O'Hara (2006) [139] fitted a curve to their LMA data reading:

$$LMA^{-1} = a + b \cdot ln(PACL)$$

with PACL denoting the percentage of above canopy light (for top canopy foliage samples we generically set PACL = 90% and for ground samples PACL = 10%). Using the standard error of the intercept a and the standard error of the slope b rel.se$_{LMA}$ reads:

$$rel.se_{LMA} = \sqrt{(rel.se_a)^2 + ln(PACL)^2 \cdot (rel.se_b)^2}$$

Mean foliar Hg uptake fluxes per tree species were obtained by averaging species-specific foliar Hg uptake fluxes over multiple sites. For sites where foliage samples were taken from the tree canopy averaging over multiple sites per tree species was only possible for pine and spruce as beech and oak were exclusively sampled at one site (Hölstein). The standard error of mean foliar Hg uptake flux per species (pine/spruce) calculates as

$$se_{flux\ per\ species} = \sqrt{(se_{uptake;\ site\ 1})^2 + (se_{uptake;\ site\ 2})^2 + ... + (se_{uptake;\ site\ n})^2}$$

with n being the number of sites.
The average foliar Hg uptake flux per unit ground area for Europe was determined as the average foliar Hg uptake flux of different tree species weighted with the relative proportion (rel.prop.) of the respective tree species in Europe. The corresponding standard error of the flux calculates as

$$se_{average\ flux\ Europe} = \sqrt{(se_{species\ 1})^2 \cdot (rel.prop_{species\ 1})^2 + (se_{species\ 2})^2 \cdot (rel.prop_{species\ 2})^2 + ... + (se_{species\ m})^2 \cdot (rel.prop_{species\ m})^2}$$

with m being the number of species.
In a final step the average foliar Hg uptake flux for Europe is extrapolated to Europe by multiplication with the forested land area of Europe. Thus the standard error of this extrapolated value is equally multiplied with the forested land area of Europe.
Sources of error that we could not be quantified in this study was the uncertainty of the proportion of tree species in Europe which was taken from Brus et al. [153] and possible unknown biases during sampling. Additionally, it is currently not quantified to which extend the physiological status of trees e.g. regarding drought stress impacts foliar Hg uptake rates.

Appendix B

Supporting Information: Physiological and climate controls on foliar mercury uptake by European tree species

This Supporting Information is associated with the research article with the title “Physiological and climate controls on foliar mercury uptake by European tree species” (DOI: 10.5194/bg-2021-239)

B.1 Description of tree species groups

TABLE B.1. Classification of samples from different tree species within the processed dataset (i.e. after outlier correction) into groups of tree species and respective total number of samples within the processed dataset, including samples from all needle age classes.

Tree species group	Tree species	n samples
ash	*Fraxinus excelsior*	10
beech	*Fagus sylvatica*	372
birch	*Betula pendula*	1
Douglas fir	*Pseudotsuga menziesii*	55
fir	*Abies alba*	162
	Abies borisii regis	3
hornbeam	*Carpinus betulus*	10
larch	*Larix decidua*	3
oak	*Quercus petraea*	133
	Quercus robur	101
	Quercus (mix: *Quercus petraea* and *Quercus robur*)	42
	Quercus cerris	4
	Quercus ilex	4
	Quercus frainetto	2
	Quercus pubescens	1
pine	*Pinus sylvestris*	413
	Pinus nigra	125
	Pinus pinaster	19
	Pinus cembra	13
	Pinus mugo arborea	10
	Pinus nigra subsp. laricio	3
spruce	*Picea abies*	2073
	Picea sitchensis	10

B.2 Overview of forests plots in 2015

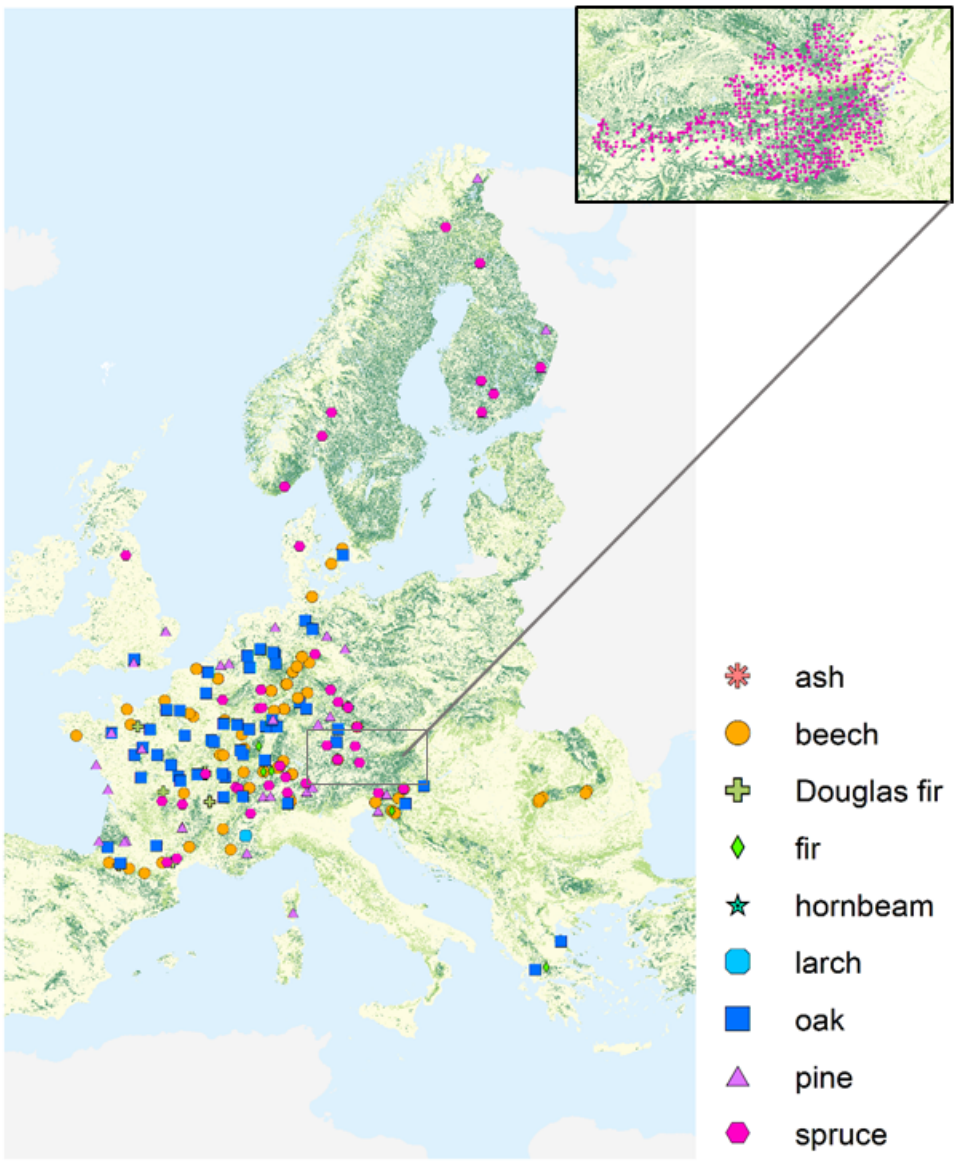

FIGURE B.1. Overview of forest plots, at which Hg foliage samples were harvested from different tree species groups during the sampling year 2015. The enlarged map view at the top right depicts sampling locations of the Bio-Indicator Grid in Austria. Use of base map authorized under European Commission reuse policy [107].

B.3 Determination of the beginning of the growing season

B.3.1 Matching of observations from the PEP725 database to forest plots

We matched observations on the beginning of the growing season of coniferous trees (flushing of current-season needles) from the Pan European Phenological database PEP725 [179] to the corresponding closest forest plot of the respective sampling year (2015 or 2017) within our database. It was necessary to complement start-of-season modelling (Sect. B.3.2) with conifer data from an external database, because the utilized PROBA-V LAI modelling method by Bórnez et al. [183] (see Sect. B.3.2) is validated with observations of deciduous tree species (beech, oak, birch, maple) only. Phenological observations of PEP725 sites are classified by BBCH (Biologische Bundesanstalt, Bundessortenamt and chemical industry) phenological scale. We used data for the beginning of the season (needle age class: y_0) of BBCH codes 10, 11, 13, 31, 60, 61 and 223. These BBCH codes correspond to the following growth stages: first leaves separated (BBCH 10); first true leaf, leaf pair or whorl unfolded, first leaves unfolded (BBCH 11); 3 true leaves, leaf pairs or whorls unfolded (BBCH 13); leaf unfolding (>= 50%) (BBCH 223); rosette 10% of final length (BBCH 31); first flowers open (BBCH 60); beginning of flowering (BBCH 61). Matching was performed using the nearest neighbor function *matchpt* from the R Biobase package [180] on coordinates of forest plots and PEP725 observation sites. We executed the nearest neighbor matching twice. In the first round, we gave latitude, longitude and altitude as input to the matching function. In a second round, we exclusively matched latitude and altitude of forest plots with a difference between plot and PEP725 observation point larger than three degrees of latitude or 30 m of altitude (12% of plots). As a result, spatial distances between forest plots and PEP725 observation points are less than three degrees of latitude and 30 m of altitude, with an exception of around 6% of forest plots for which no such close PEP725 observation points were available. A lack of close PEP725 observation points was the case for forest plots in Norway (10 degrees of latitude), Greece (9 degrees of latitude), a few sites in Southern France/Corsica, Southern Switzerland and Austria, and one site in England and Romania respectively (3 – 6 degrees of latitude). Exceedances of a distance of 30 m of altitude between forest plots and PEP725 observations emerged for only 1% of sites with the maximum altitude distance being 350 m. As a result, the average beginning of the season DOY (needle age class: y_0) for conifers (86% spruce plots, 13% pine plots, 1% other conifers) is 127 $\pm$ 14 d which is one day earlier than the average start-of-season PEP725 observations for spruce from 1970 – 2009 [296].

B.3.2 PROBA-V LAI modelling of the beginning of the growing season

We utilized the leaf area index (LAI) product by Copernicus Global Land Service based on PROBA-V satellite imagery at a resolution of 300 m and 10 days [182] to model the start of the growing season for deciduous trees as validated by Bórnez et al. [183]. This approach is part of the threshold based methods for growing season modelling. Figure B.2 gives an exemplary temporal sequence of PROBA-V LAIs from a forest plot in Switzerland. We defined the start of the growing season as the point in time when the LAI exceeds the 30% percentile threshold of the amplitude between minimum LAI at the beginning of the growing season and maximum LAI at peak season. Bórnez et al. [183] found a 30 % percentile amplitude threshold to perform best (root mean squared error of 12.5 days; $R^2 = 0.62$) for PROBA-V LAI modelling when modelling results for the beginning of the growing season were compared to 359 ground phenological observations of deciduous tree species in Europe. In the present ICP Forests database there were three forest plots for which PROBA-V LAI modelling yielded unrealistic results, as the beginning of the growing season was either too early (forest plot Gontrode in 2017) or too late (forest plots Ehrhorn and Maron in 2015) in the season given their respective latitude and altitude. We replaced the beginning of the growing season DOY (day of year) at these three plots with 119 (April 29th) which equals the average beginning of the growing season DOY of deciduous tree species of the present dataset. Figure B.3 presents an overview of the modelling results for beginning of the growing season DOYs at each deciduous forest plot per latitude. The coefficient of correlation of linear regression between beginning of growing season DOYs and latitude was positive and significant ($p < 0.01$), so as a tendency, the beginning of the growing season DOYs modelled here correspond to expected latitudinal differences. The average beginning of the growing season DOY (mean $\pm$ s.d. in days) is 120 ± 10 d for beech and 111 ± 11 d for oak. This average beginning of the growing season DOY for beech is consistent within an accuracy of 2 days with 7840 PEP725 observations from Central Europe between the years 1970 – 2009 [296]. For oak, the modelled beginning of the growing season is 13 days earlier than the respective average DOY from 6400 PEP725 observations between 1970 – 2009 [296]. This 13 d discrepancy could be due to the fact that the PEP725 oak beginning of season data evaluated by Basler [296] comprise observations mainly from Germany, while 26% of oak samples in the current data set originated from more southern latitudes < 48°.

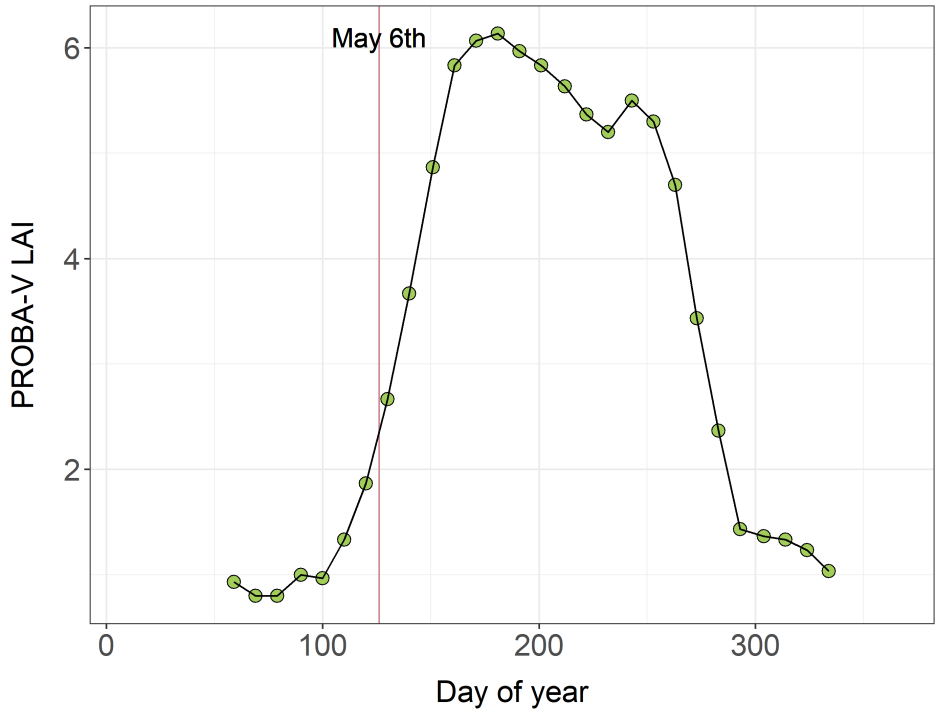

FIGURE B.2. Temporal development of the Copernicus LAI (leaf area index) values derived from PROBA-V satellite images [182] at the Swiss forest research site Bettlachstock in 2017. The beginning of the growing season is defined as the date, at which the LAI value exceeds the 30 percentile threshold of the amplitude between minimum LAI early in the year and maximum LAI at peak season following a modelling approach by Bórnez et al. [183]. Here the beginning of the growing season corresponds to May 6th 2017. This date is one week later than the average beginning of the growing season of this dataset for beech, which represents the main tree species at Bettlachstock. Given that Bettlachstock is located at 1101 m - 1196 m above sea level, however, May 6th is a plausible beginning of the growing season for beech at this site.

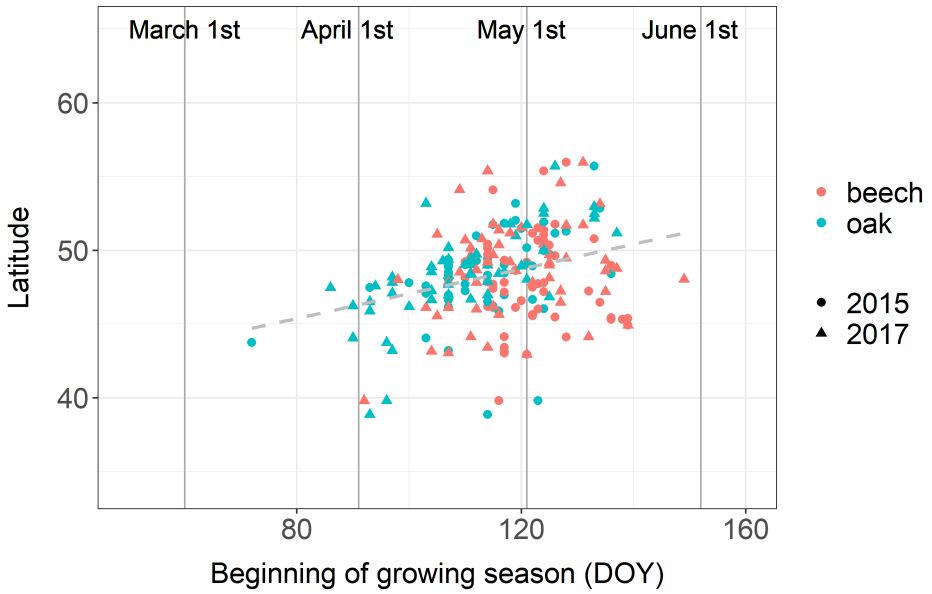

FIGURE B.3. Start-of-season DOY (day of year) at ICP Forests Level II plots resulting from growing season modelling approach after Bórnez et al. [183]

B.4 Foliar Hg concentration over the growing season

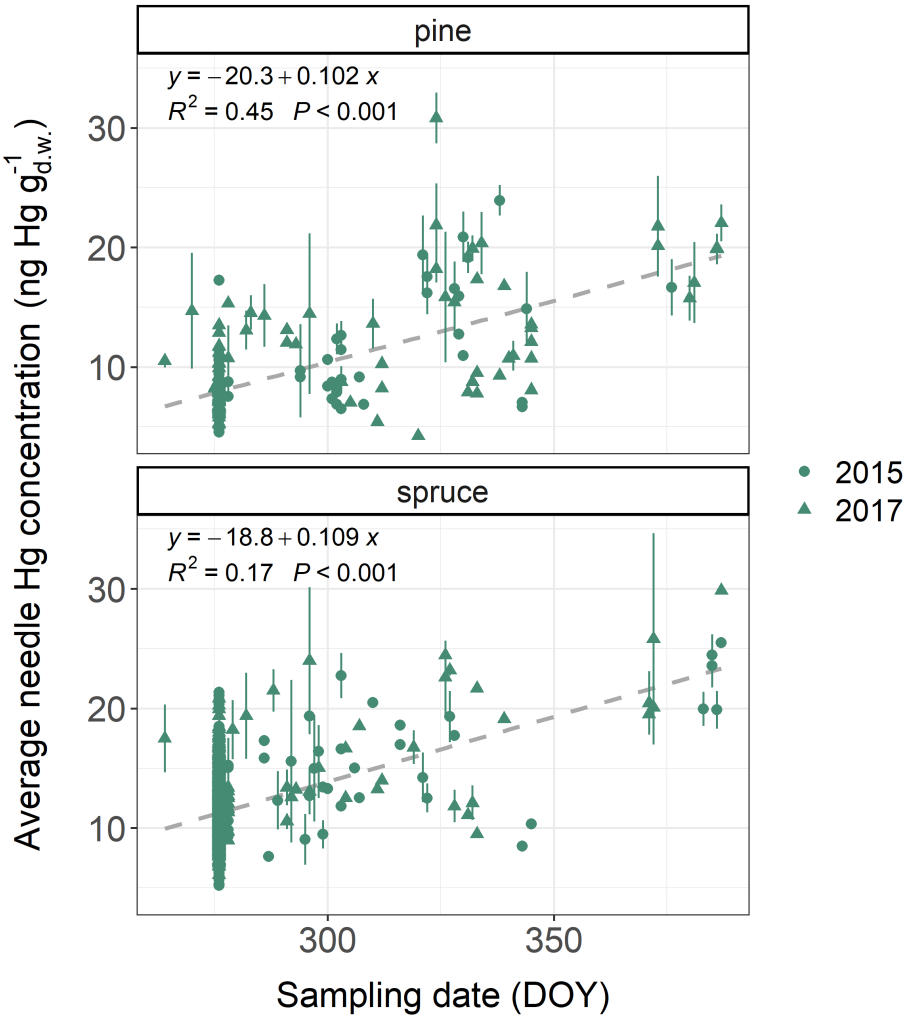

FIGURE B.4. Average foliar Hg concentrations (ng Hg $g_{d.w.}^{-1}$) per forest plot of pine and spruce samples versus respective sampling date (day-of-year of both 2015 and 2017). At some pine and spruce forest plots sampling took place in winter after 31st of December, such that day-of-year > 365. Error bars denote ± one standard deviation between multiple foliage samples at one forest plot. All samples represent current-season values.

B.5 Foliar Hg uptake per tree species

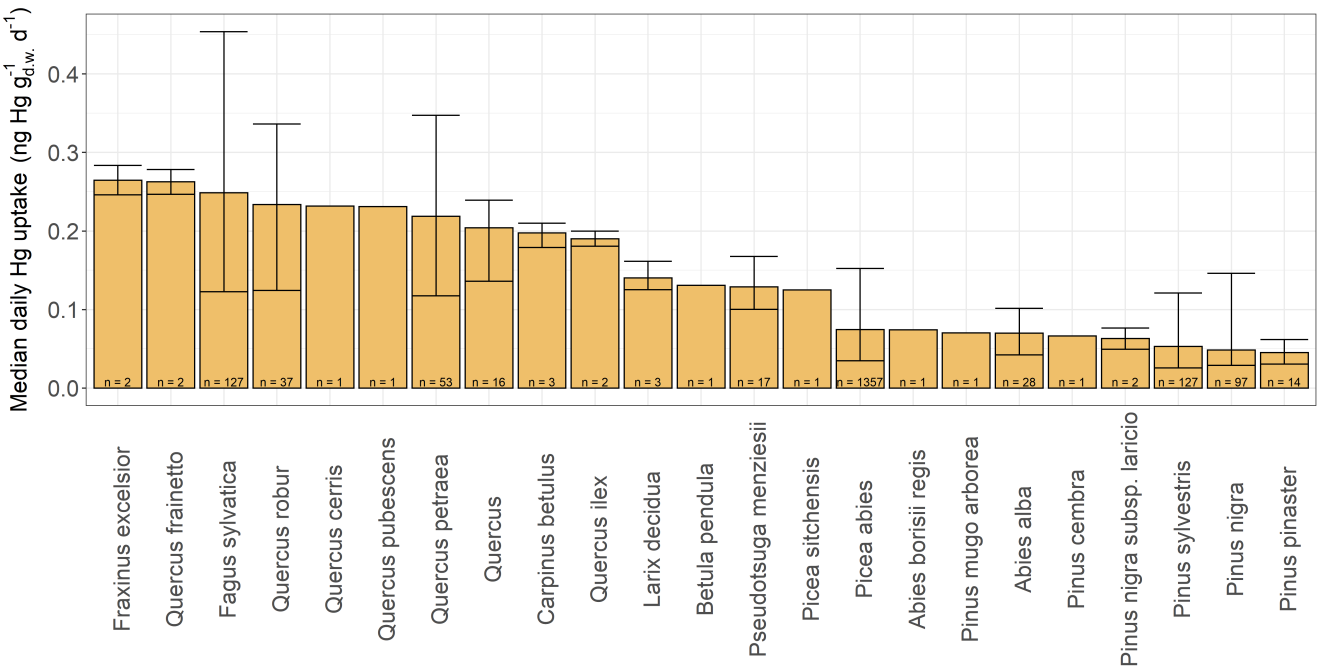

FIGURE B.5. Median daily foliar Hg uptake (ng Hg $g^{-1}_{d.w.}$ d^{-1}) of different tree species arranged from highest to lowest value. Error bars give the value range within each tree species and n indicates the number of sites at which the respective tree species were sampled in sum in the years 2015 and 2017. Foliar samples of evergreen coniferous tree species consist of needles of the current season. *Quercus* represents a mix of samples from *Quercus petraea* and *Quercus robur*.

B.6 Atmospheric Hg(0) concentrations from EMEP stations

In order to get a better understanding of the variation in atmospheric Hg(0) in Europe during the growing seasons 2015 and 2017, we obtained air Hg data from the European Monitoring and Evaluation Programme (EMEP) [66, 111]. Air Hg measurements for 2015 and 2017 were available at 6 stations (Table B.2, Fig. B.6). Measurements from one station (Iskrba) between May - Sept. 2015 were excluded from the dataset due to abnormally low air Hg values (0.41 $\pm$ 0.13 ng m^{-3}; mean $\pm$ sd). Selection of stations was based on availability of measurements in Europe at the relevant time intervals. The temporal frequency of measurements (hourly to 6 days) and consequently the number of measurements varied between the different EMEP stations (Table B.2).

TABLE B.2. Details on air Hg measurements at 6 EMEP stations during the growing seasons 2015 and 2017.

Station name (EMEP code)	coordinates (lat, lon)	altitude (m)	freq.	time coverage	air Hg (ng m^{-3}) (mean ± sd)	n
Andøya (NO0090R)	69.28, 16.01	380	hourly	May - Sept. 2015	1.50 ± 0.09	3371
Auchencorth Moss (GB0048R)	55.79, -3.24	260	3hourly	May - Sept. 2015	1.33 ± 0.15	1384
			hourly	May - Sept. 2017	1.40 ± 0.12	2285
BirkenesII (NO0002R)	58.39, 8.25	219	hourly	May - Sept. 2015	1.49 ± 0.24	3402
Diabla Gora (PL0005R)	54.15, 22.07	157	6 days	May - Sept. 2015	1.26 ± 0.45	23
Iskrba (SI0008R)	45.57, 14.87	520	daily	May - Sept. 2017	1.33 ± 0.80	39
Laheema (EE0009R)	59.5, 25.9	32	hourly	May - July 2015	1.40 ± 0.38	1396

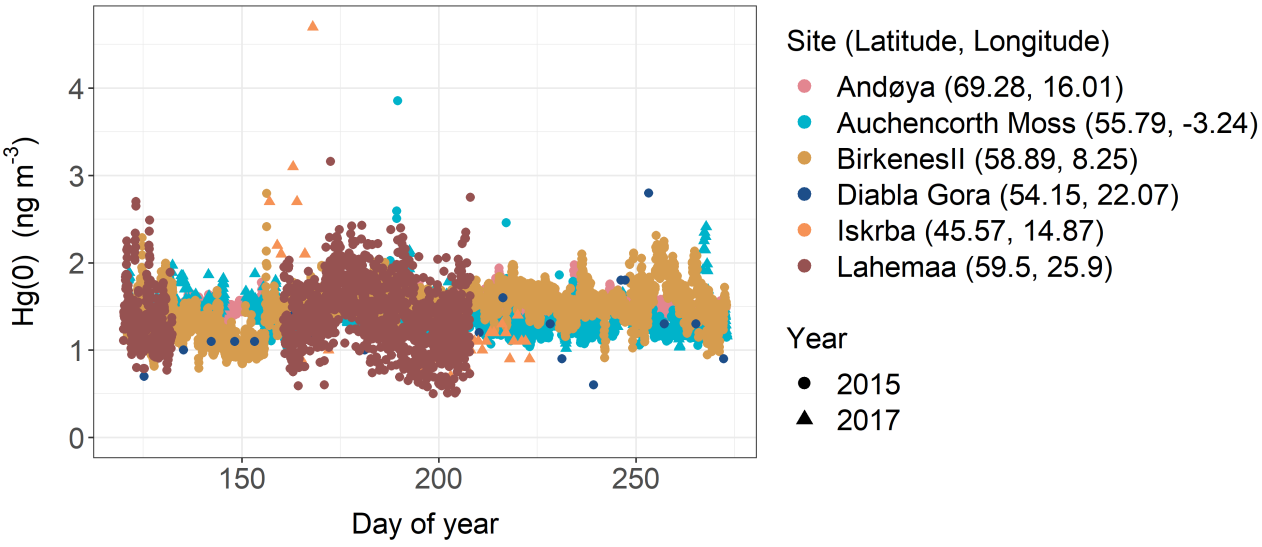

FIGURE B.6. Temporal resolution of air Hg at 6 EMEP stations during the growing seasons 2015 and 2017. For details on EMEP stations see Table B.2.

B.7 Calculation of median leaf stomatal conductance from data by Lin et al. [206]

We calculated median stomatal conductance values from a global database of leaf-level gas exchange parameters compiled by Lin et al. [206] from literature and unpublished sources. We exported stomatal conductance values of the following tree species from the database: beech (Fagus sylvatica), oak (Quercus petraea, Quercus robur), spruce (Picea abies) and pine (Pinus edulis, Pinus pinaster, Pinus sylvestris, Pinus taeda). All data were measured in Europe (Denmark, Finland, France, Germany, Sweden, UK) and North America. The following data contributors were named as data source for the data we used to calculate median stomatal conductance per tree species: Alexandre Bosc, D. Ellsworth, Jean-Marc Limousin, John Drake, Lasse Tarvainen, Maj-Lena Linderson, Mark Broadmeadow, Michael Freeman, Pasi Kolari, Reinhart Ceulemans and Mark Low. The database can be accessed at `https://figshare.com/articles/dataset/Optimal_stomatal_behaviour_around_the_world/1304289`.

B.8 Foliar Hg uptake and sample-specific nitrogen concentration

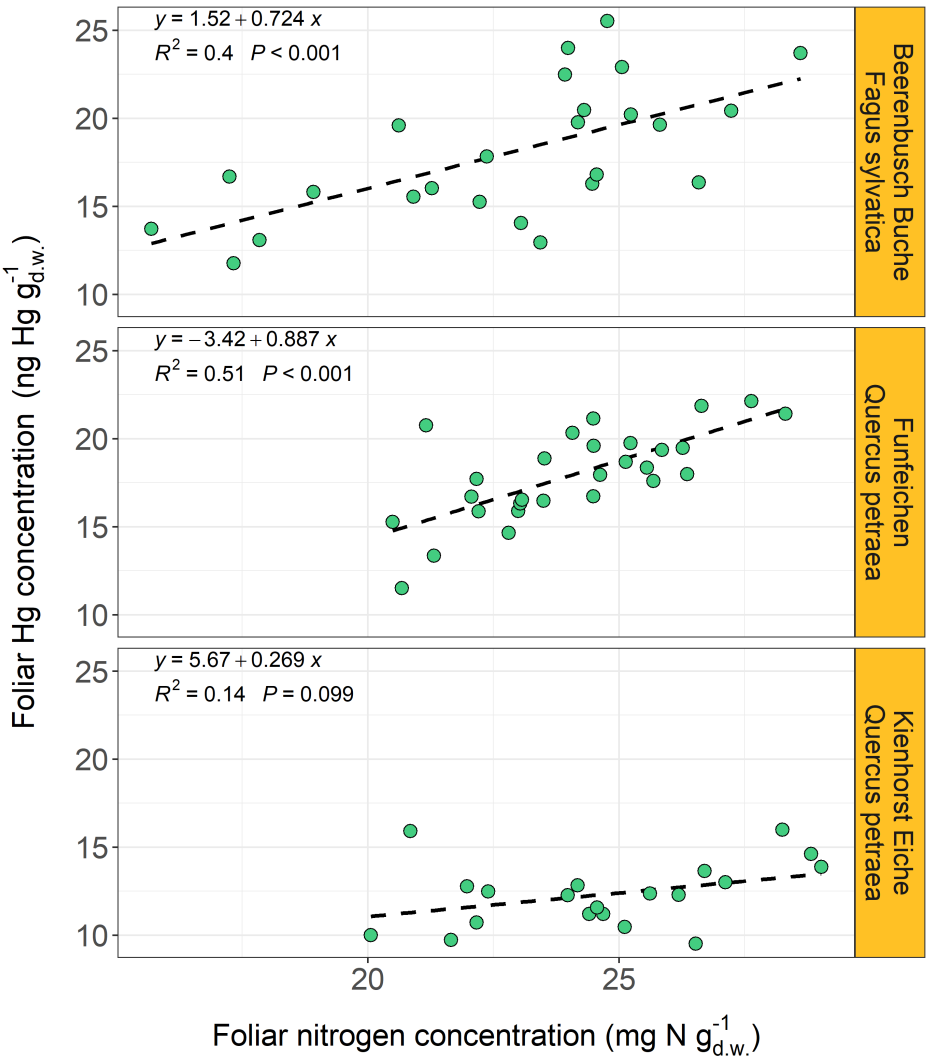

FIGURE B.7. Linear regression between foliar Hg concentrations (ng Hg $g^{-1}_{d.w.}$) and leaf nitrogen concentration (mg N $g^{-1}_{d.w.}$) in foliage samples from one beech (Fagus sylvatica, top) and two oak (Quercus petraea) forest plots in Brandenburg, Germany.

B.9 Foliar Hg uptake and Leaf Mass per Area

TABLE B.3. Daily Hg uptake rates, foliar N concentrations and leaf mass per area (LMA) values (mean ± sd) presented in Fig. 3.4.

Species group	daily Hg uptake ($ng\ Hg\ g_{d.w.}^{-1}$) (mean ± sd)	foliar N conc. ($mg\ N\ g_{d.w.}^{-1}$) (mean ± sd)	LMA ($g_{d.w.}\ m_{leaf}^{-2}$) (mean ± sd)	n
beech	0.26 ± 0.05	23.0 ± 2.8	68 ± 16	164
hornbeam	0.19 ± 0.04	18.9 ± 1.4	67 ± 11	9
pine	0.10 ± 0.02	16.1 ± 2.1	243 ± 84	35
Douglas fir	0.12 ± 6e-5	19.0 ± 2.2	284 ± 5	2
oak	0.22 ± 0.05	24.7 ± 2.7	100 ± 17	106
spruce	0.11 ± 0.02	14.5 ± 1.0	370 ± 67	33

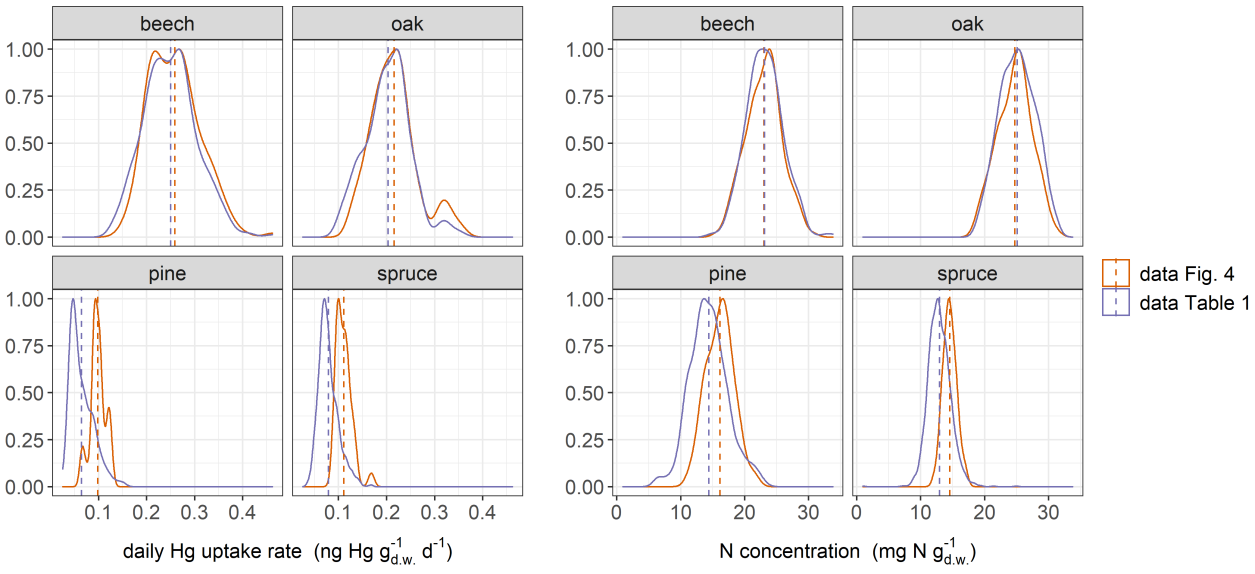

FIGURE B.8. Density (scaled to respective maximum value) within the datasets of daily Hg uptake rates (left) and foliar N concentrations (right) of beech leaves, oak leaves, current-season pine needles and current-season spruce needles presented in Table 3.1 and in Fig. 3.4. Data from Fig. 3.4 is a sub-dataset of the dataset from Table 3.1. The shift in daily needle Hg uptake rates of pine and spruce between the two datasets is possibly associated with a shift in needle N concentrations between the two datasets.

B.10 Foliar Hg uptake and proportion of VPD threshold hours

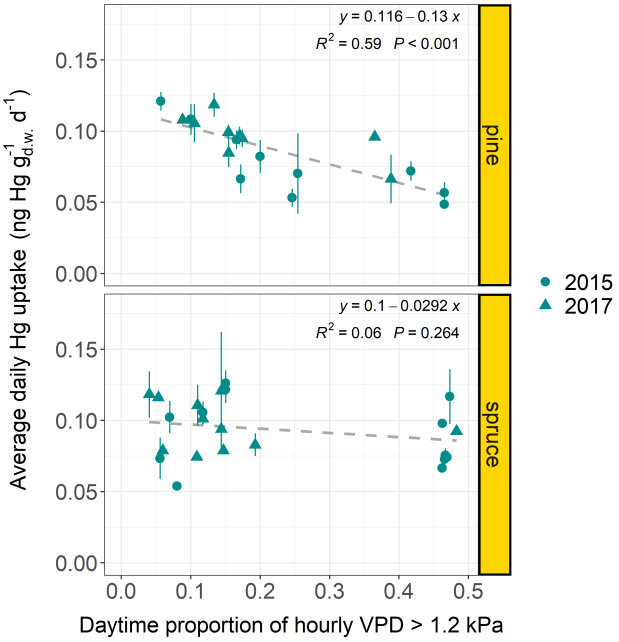

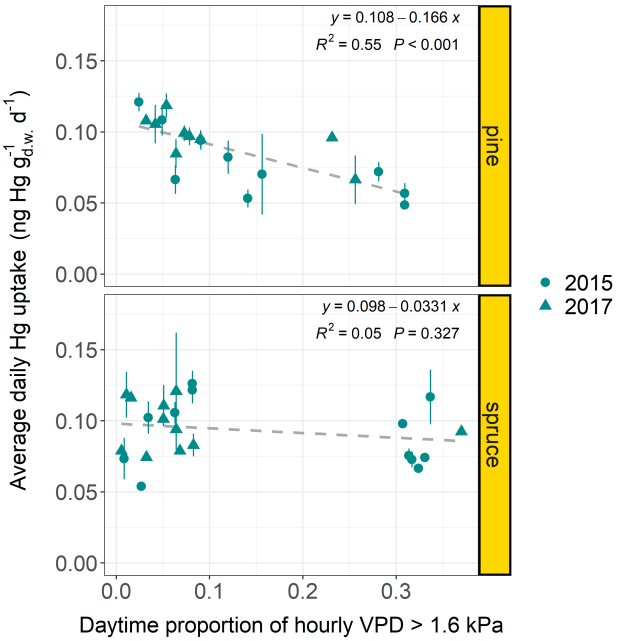

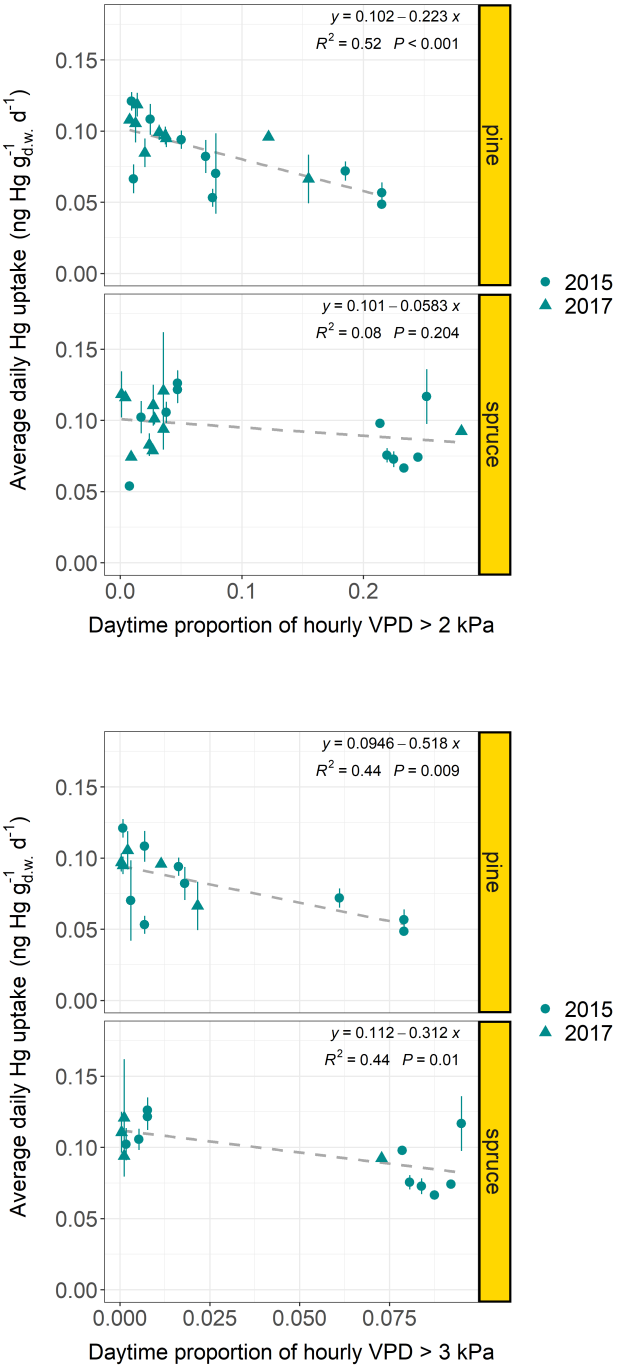

FIGURE B.9. Average daily foliar Hg uptake rates (ng Hg $g_{d.w.}^{-1}$ d^{-1}) of current-season pine and spruce needles per forest plot sampled in 2015 and 2017 versus the proportion of hours within an average day of the respective sample life periods, during which the average hourly daytime (06:00 - 18:00 LT) vapor pressure deficit (VPD) exceeded a threshold value of 1.2 kPa, 1.6 kPa, 2 kPa and 3 kPa respectively. Error bars denote ± one standard deviation between multiple samples at each forest plot.

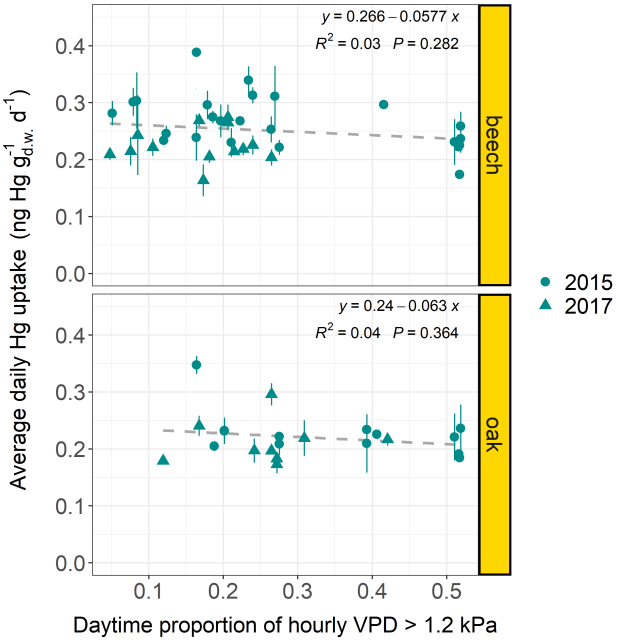
y = 0.266 – 0.0577 x
R² = 0.03 P = 0.282
beech
y = 0.24 – 0.063 x
R² = 0.04 P = 0.364
oak
2015
2017
Average daily Hg uptake (ng Hg g⁻¹d.w. d⁻¹)
Daytime proportion of hourly VPD > 1.2 kPa

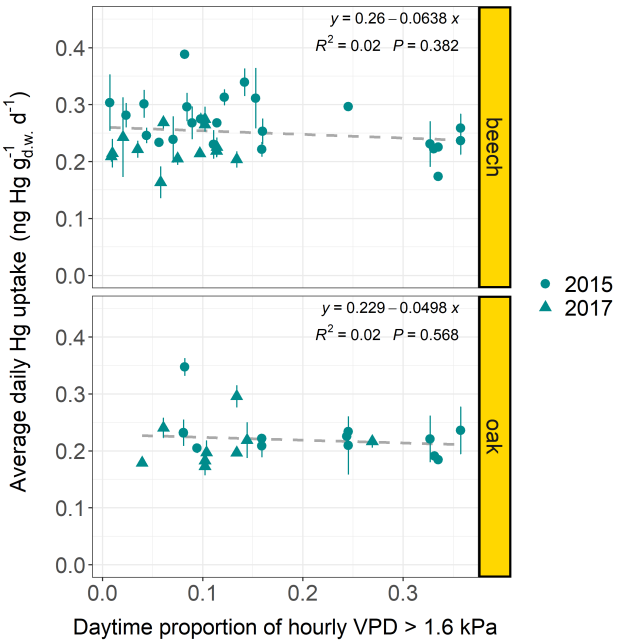
y = 0.26 – 0.0638 x
R² = 0.02 P = 0.382
beech
y = 0.229 – 0.0498 x
R² = 0.02 P = 0.568
oak
2015
2017
Average daily Hg uptake (ng Hg g⁻¹d.w. d⁻¹)
Daytime proportion of hourly VPD > 1.6 kPa

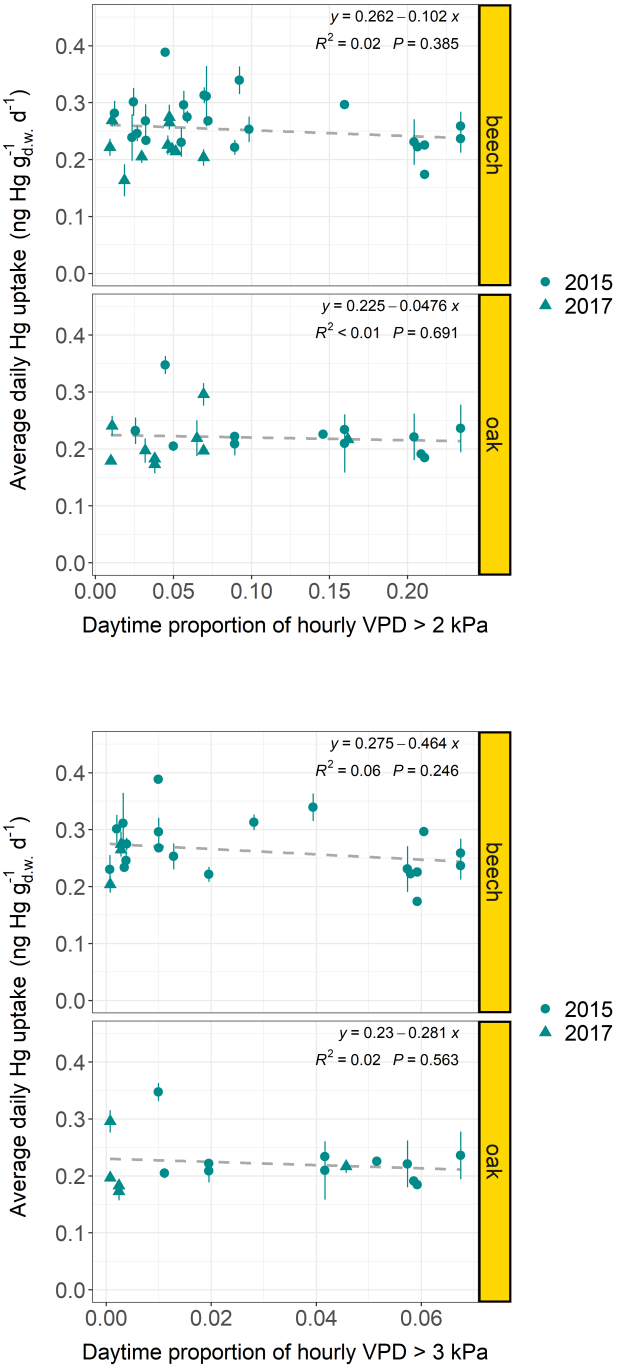

FIGURE B.10. Average daily foliar Hg uptake rates (ng Hg $g_{d.w.}^{-1}$ d^{-1}) of beech and oak leaves per forest plot sampled in 2015 and 2017 versus the proportion of hours within an average day of the respective sample life periods, during which the average hourly daytime (06:00 - 18:00 LT) vapor pressure deficit (VPD) exceeded a threshold value of 1.2 kPa, 1.6 kPa, 2 kPa and 3 kPa respectively. Error bars denote ± one standard deviation between multiple samples at each forest plot.

B.11 Soil hydraulic parameters for modelling of stomatal closure

TABLE B.4. Soil texture specific soil water at field capacity (SW_{FC}) and at the permanent wilting point (SW_{PWP}), plant available water (PAW), and critical PAW (PAW_{crit}), below which plants were modelled to start to close their stomata. PAW equals the difference between SW_{FC} and SW_{PWP} and $PAW_{crit} = 0.5 \cdot PAW + SW_{PWP}$. All values are taken from Saxton and Rawls [190] (Table 3 therein) and represent units of $\mathbf{m}^3\ \mathbf{m}^{-3}$.

Soil texture	$\mathbf{SW}_{FC}$	$\mathbf{SW}_{PWP}$	**PAW**	$\mathbf{PAW}_{crit}$
Sand	0.10	0.05	0.05	0.075
Loamy sand	0.12	0.05	0.07	0.085
Sandy loam	0.18	0.08	0.10	0.13
Sandy clay loam	0.27	0.17	0.10	0.22
Clay	0.42	0.30	0.12	0.36
Silty clay	0.41	0.27	0.14	0.34
Clay loam	0.36	0.22	0.14	0.29
Loam	0.28	0.14	0.14	0.21
Silty clay loam	0.38	0.22	0.16	0.30
Silt loam	0.31	0.11	0.20	0.21

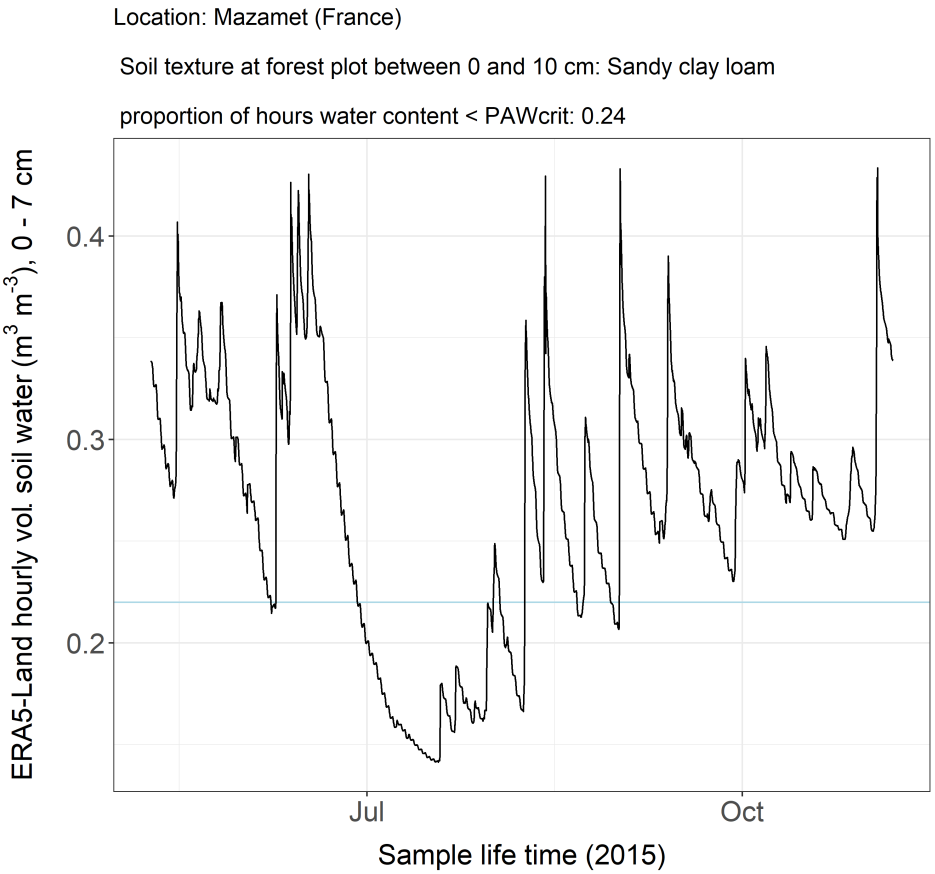

FIGURE B.11. Volumetric soil water (m^3 m^{-3}, layer 1) from the ERA5-Land hourly dataset [177] in the region of Mazamet (France) versus sample life period of the associated ICP Forests Level II Plot (plot code: 1-45). The lightblue line denotes the threshold value of plant available water (PAW_{crit}) of 0.22 m^3 m^{-3} for the soil texture (sandy clay loam) of this forest plot (compare Table B.4).

TABLE B.5. Species-specific daily foliar Hg uptake rates (mean ± sd; ng Hg $g_{d.w.}^{-1}$ d^{-1}; rounded to two decimals) resolved for the sampling years 2015 and 2017 and difference between respective average daily foliar Hg uptake rates of 2015 - average daily foliar Hg uptake rates of 2017.

Tree species group	year	Daily Hg uptake (mean ± sd) (ng Hg $g_{d.w.}^{-1}$ d^{-1})	Diff. daily Hg uptake (2015 - 2017)	n sites
beech	2015	0.27 ± 0.05	0.04	51
	2017	0.23 ± 0.04		
Douglas fir	2015	0.12 ± 0.02	- 0.02	7
	2017	0.14 ± 0.02		
fir	2015	0.07 ± 0.02	- 0.005	6
	2017	0.08 ± 0.02		
oak	2015	0.23 ± 0.04	0.004	49
	2017	0.22 ± 0.03		
pine	2015	0.05 ± 0.02	∼ 0	107
	2017	0.05 ± 0.02		
spruce	2015	0.07 ± 0.02	- 0.003	658
	2017	0.08 ± 0.02		

Appendix C

Supporting Information: A spatial assessment of current and future foliar Hg uptake fluxes across Europe

This Supporting Information is associated with the Chapter: A spatial assessment of current and future foliar Hg uptake fluxes across Europe

Text S1.

Zhou and Obrist [10] give an estimate of median global foliage Hg assimilation by evergreen needleleaf forests of 61 Mg Hg year^{-1} and by deciduous broadleaf forests of 28 Mg Hg year^{-1} (Zhou and Obrist [10], Table 1 therein). This estimate is based on global data on foliar Hg concentrations and net foliar biomass production. The global land area of evergreen needleleaf forests is given as 6.17 Mio km^2 and of deciduous broadleaf forests as 1.12 Mio km^2 [10]. Converted to the land area of coniferous (1.0 Mio km^2) and deciduous forests (0.73 Mio km^2) in Europe, we obtain a total Hg assimilation of 10.2 Mg Hg year^{-1} for European coniferous forests and of 18.4 Mg Hg year^{-1} for European deciduous forests.

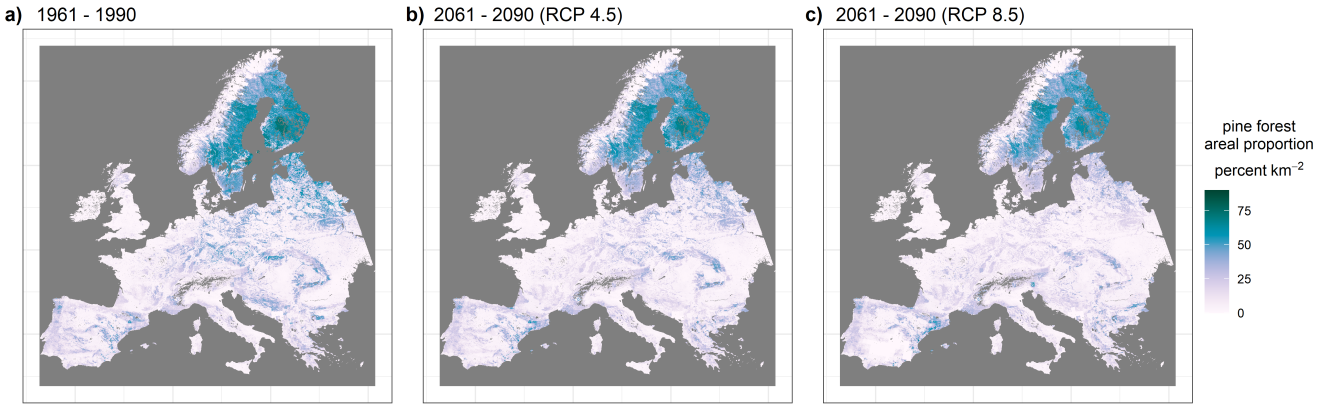

FIGURE C.1. Simulated areal cover (percent km^{-2}) of pine forests in Europe (a) historically, (b) for the time period 2061 - 2090 under the climate change scenario RCP 4.5, and (c) RCP 8.5. Geographic distribution was derived from statistic mapping from Brus et al. [153] and projected relative abundance probabilities under climate analogs Buras and Menzel [251] (see Sect. 4.2.1 for details).

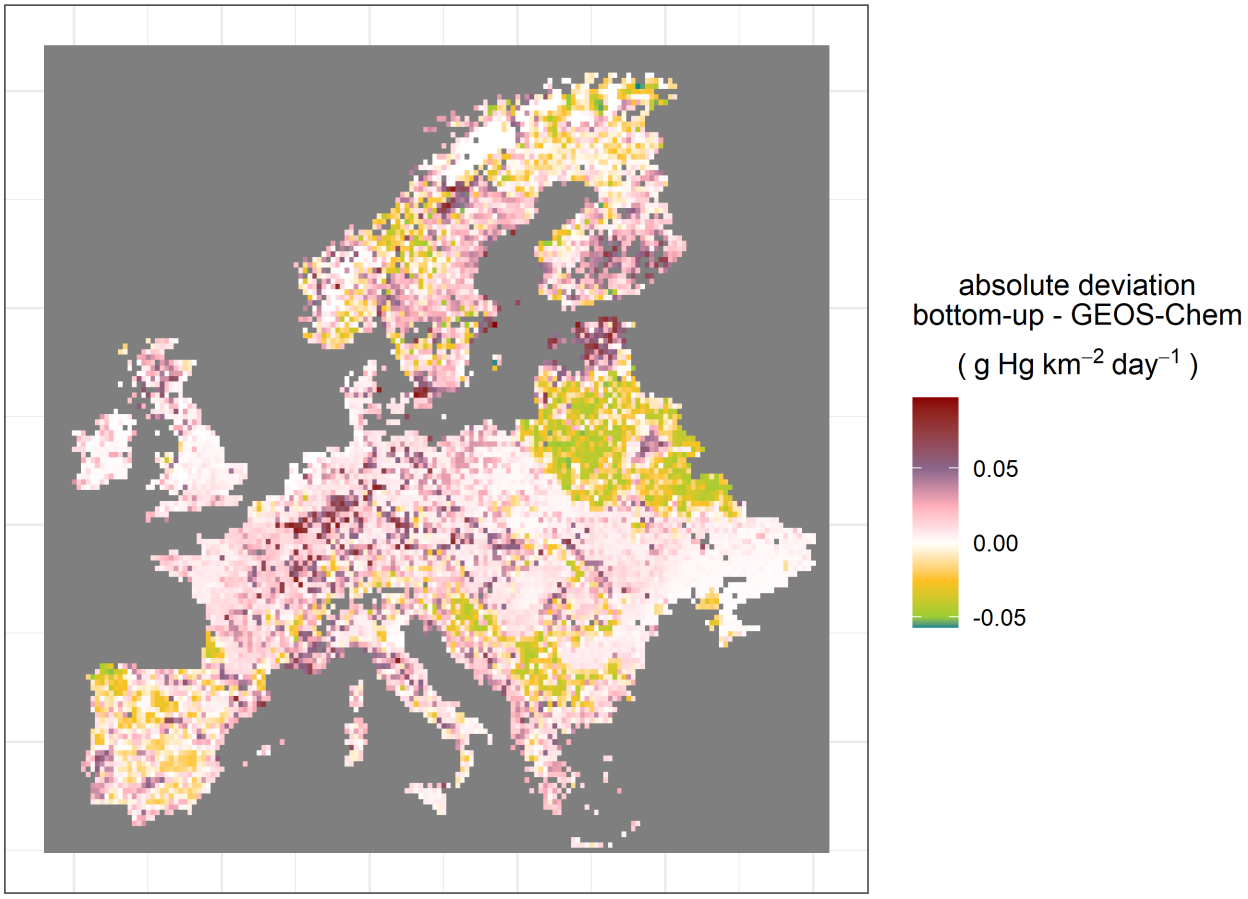

FIGURE C.2. Absolute difference map of model outputs of forest foliar Hg uptake fluxes (g Hg km^{-2} day^{-1}) from the bottom-up model - GEOS-Chem.

TABLE C.1. Overview of LAI correction factor for tree height (cf_{height}) and Hg uptake rate correction factor for needle age class (cf_{age}) obtained from Wohlgemuth et al. [165].

Tree species group	**cf_{height}**	**cf_{age}**
Abies alba	0.68	0.79
mix of all broadleaf values	0.63	-
Betula pendula	0.63	-
Carpinus betulus	0.63	-
mix of all conifer values	0.68	0.79
Fagus sylvatica	0.56	-
Fraxinus excelsior	0.63	-
Larix decidua	0.68	-
Pinus cembra; *Pinus mugo arborea*; *Pinus nigra* *Pinus nigra subsp. laricio*	0.68	0.86
Picea abies	0.68	0.79
Pinus pinaster	0.68	0.86
Pinus sylvestris	0.68	0.86
Pinus sylvestris	0.68	0.86
Pseudotsuga menziesii	0.68	0.86
Quercus cerris; *Quercus frainetto*; *Quercus ilex*; *Quercus pubescens*	0.7	-
Quercus robur; *Quercus petraea*	0.7	-

TABLE C.2. Dataset on proportion of tree species per land area matched to dataset on foliar Hg uptake rates by tree species groups.

Matched and aggregated tree species groups	
Dataset on tree species proportion of land area (Brus et al., 2012)	**Dataset on foliar Hg uptake per tree species (Wohlgemuth et al., 2022)**
Abies spp	*Abies alba*
Alnus spp; Broadleaved misc; Castanea spp; Eucalyptus spp; Populus spp; Robinia Spp	mix of all broadleaf values
Betula spp	*Betula pendula*
Carpinus spp	*Carpinus betulus*
Conifers misc	mix of all conifer values
Fagus spp	*Fagus sylvatica*
Fraxinus spp	*Fraxinus excelsior*
Larix spp	*Larix decidua*
Picea spp	*Picea abies*
Pinus misc	*Pinus cembra*; *Pinus mugo arborea*; *Pinus nigra* *Pinus nigra subsp. laricio*
Pinus pinaster	*Pinus pinaster*
Pinus sylvestris	*Pinus sylvestris*
Pseudotsuga menziesii	*Pseudotsuga menziesii*
Quercus misc	*Quercus cerris*; *Quercus frainetto*; *Quercus ilex*; *Quercus pubescens*
Quercus robur & Quercus petraea	*Quercus robur*; *Quercus petraea*

TABLE C.3. Overview of all combinations of Global Climate Models (GCMs) – Regional Climate Models (RCMs) and ensemble members used for downloading simulated data of 2m air temperature and 2m relative humidity from the Copernicus Climate Data Store in the framework of the Coordinated Regional Climate Downscaling Experiment (CORDEX) for the two climate scenarios of Representative Concentration Pathways (RCPs) 4.5 and 8.5. RCM data on a high regional resolution (here: European domain; 0.11° x 0.11°) depend on output from GCMs for lateral and lower boundary conditions. Temporal resolution of downloaded data was 3 hours and time period was 2068-2082.

Climate scenario	GCM	RCM	ensemble member
RCP 4.5	CNRM-CERFACS-CM5	KNMI-RACMO22E	r1i1p1
	ICHEC-EC-EARTH	DMI-HIRHAM5	r3i1p1
	ICHEC-EC-EARTH	GERICS-REMO2015	r12i1p1
	ICHEC-EC-EARTH	KNMI-RACMO22E	r1i1p1
	ICHEC-EC-EARTH	SMHI-RC4A	r12i1p1
	IPSL-CM5A-MR	SMHI-RC4A	r1i1p1
	MOHC-HadGEM2-ES	GERICS-REMO2015	r1i1p1
	MOHC-HadGEM2-ES	KNMI-RACMO22E	r1i1p1
	MOHC-HadGEM2-ES	SMHI-RC4A	r1i1p1
	MPI-M-MPI-ESM-LR	SMHI-RC4A	r1i1p1
	NCC-NorESM1-M	DMI-HIRHAM5	r1i1p1
	NCC-NorESM1-M	GERICS-REMO2015	r1i1p1
	NCC-NorESM1-M	SMHI-RC4A	r1i1p1
RCP 8.5	CCCma-CanESM2	CLMcom-CLM-CCLM4-8-17	r1i1p1
	CNRM-CERFACS-CM5	CLMcom-ETH-COSMO-crCLIM	r1i1p1
	CNRM-CERFACS-CM5	GERICS-REMO2015	r1i1p1
	ICHEC-EC-EARTH	CLMcom-ETH-COSMO-crCLIM	r12i1p1
	ICHEC-EC-EARTH	KNMI-RACMO22E	r12i1p1
	ICHEC-EC-EARTH	SMHI-RCA4	r12i1p1
	IPSL-CM5A-MR	DMI-HIRHAM5	r1i1p1
	MIROC-MIROC5	CLMcom-CLM-CCLM4-8-17	r1i1p1
	MOHC-HadGEM2-ES	SMHI-RCA4	r1i1p1
	MPI-M-MPI-ESM-LR	DMI-HIRHAM5	r1i1p1
	NCC-NorESM1-M	CLMcom-ETH-COSMO-crCLIM	r1i1p1
	NCC-NorESM1-M	GERICS-REMO2015	r1i1p1
	NCC-NorESM1-M	KNMI-RACMO22E	r1i1p1

TABLE C.4. Overview of relative uncertainty values for different parameters per forest tree species group propagated by error propagation principle for every spatial tile of the forest foliar Hg uptake flux map (Fig. 4.1).

Tree species group[a]	relative uncertainty (ru)						
	LMA[b]	DMA[c]	LAI[d]	Forest area[e]	cf_{age} [f]	pine[g]	**total**[h]
Abies spp	0.36				0.03	-	0.70
Betula spp	0.61				-	-	0.86
Broadleaved mixed	0.82				-	-	1.02
Carpinus spp	0.18				-	-	0.63
Fagus spp	0.47				-	-	0.77
Fraxinus spp	0.54	0.1	0.44	0.40	-	-	0.81
Larix spp	0.76				-	-	0.97
Picea spp	0.75				0.03	-	0.96
Pine	0.72				0.06	0.014	0.94
Pseudotsuga menziesii	0.69				0.06	-	0.92
Quercus misc	0.28				-	-	0.67
Quercus robur & Quercus petraea	0.52				-	-	0.80

a See Table C.2 for an overview of tree species aggregated into tree species groups. For the group of mixed conifer species (Table C.2), we calculated an average uncertainty value from total uncertainty values of coniferous needle tree species groups, which equals 0.90.

b Leaf mass per area (LMA) values per tree species group were obtained from Forrester et al. [252]. The relative uncertainty of LMA per tree species group was calculated including the range of all LMA values within each respective tree species group: (maximum LMA - minimum LMA)/(average LMA).

c Foliar Hg values were obtained from a dataset of Hg concentrations in foliage samples of the ICP Forests biomonitoring network and the Austrian Bio-Indicator Grid measured using a direct mercury analyzer (DMA) (see Sect. 4.2.1 and Wohlgemuth et al. [233]). A DMA measurement sequence of foliar Hg concentrations was accepted when primary liquid reference standards did not deviate by more than $\pm$ 10% from target value.

d Relative root mean square deviation (RMSD) of the leaf area index (LAI) product from PROBA-V from LAI ground observations evaluated by Fuster et al. [182].

e The uncertainty of the proportion of tree species per forest land area (spatial resolution: 1 km^2) was not evaluated by Brus et al. [153] and depends on the heterogenous availability of national forest inventories in Europe. From the overall accuracy given in Brus et al. [153], we estimated a relative uncertainty value of 0.4 per tree species and km^2.

f Uncertainty of the correction factor (cf_{age}) for upscaling Hg uptake rates of needles of different age classes to whole coniferous evergreen trees (see Wohlgemuth et al. [165]).

g Relative RMSD of the linear regression slope of the average daily pine needle Hg uptake rate vs. time proportion of VPD $>$ 1.2 kPa (see Wohlgemuth et al. [233]).

h Total species uncertainty = $\sqrt{ru^2_{LMA} + ru^2_{DMA} + ru^2_{LAI} + ru^2_{for.area} + ru^2_{cfage} + ru^2_{pine}}$

Bibliography

[1] Driscoll, C. T., Mason, R. P., Chan, H. M., Jacob, D. J., & Pirrone, N. (2013). Mercury as a global pollutant: sources, pathways, and effects. *Environmental Science & Technology*, *47*(10), 4967–4983.

[2] Bagnato, E., Tamburello, G., Avard, G., Martinez-Cruz, M., Enrico, M., Fu, X., Sprovieri, M., & Sonke, J. E. (2015). Mercury fluxes from volcanic and geothermal sources: an update. *Geological Society, London, Special Publications*, *410*(1), 263–285.

[3] Outridge, P. M., Mason, R. P., Wang, F., Guerrero, S., & Heimbürger-Boavida, L. E. (2018). Updated global and oceanic mercury budgets for the United Nations Global Mercury Assessment 2018. *Environmental Science & Technology*, *52*(20), 11466–11477.

[4] Environment, U. (2019). Global Mercury Assessment Report 2018. UN Environmental Programme, Chemicals and Health Branch Geneva, Switzerland.

[5] Fitzgerald, W. F., Lamborg, C. H., & Hammerschmidt, C. R. (2007). Marine Biogeochemical Cycling of Mercury. *Chemical Reviews*, *107*(2), 641–662.

[6] Sprovieri, F., Pirrone, N., Bencardino, M., D'Amore, F., Angot, H., Barbante, C., Brunke, E.-G., Arcega-Cabrera, F., Cairns, W., Comero, S., Diéguez, M. d. C., Dommergue, A., Ebinghaus, R., Feng, X. B., Fu, X., Garcia, P. E., Gawlik, B. M., Hageström, U., Hansson, K., Horvat, M., Kotnik, J., Labuschagne, C., Magand, O., Martin, L., Mashyanov, N., Mkololo, T., Munthe, J., Obolkin, V., Ramirez Islas, M., Sena, F., Somerset, V., Spandow, P., Vardè, M., Walters, C., Wängberg, I., Weigelt, A., Yang, X., & Zhang, H. (2017). Five-year records of mercury wet deposition flux at GMOS sites in the Northern and Southern hemispheres. *Atmospheric Chemistry and Physics*, *17*(4), 2689–2708.

[7] Shah, V., Jacob, D. J., Thackray, C. P., Wang, X., Sunderland, E. M., Dibble, T. S., Saiz-Lopez, A., Černušák, I., Kellö, V., Castro, P. J., Wu, R., & Wang, C. (2021). Improved Mechanistic Model of the Atmospheric Redox Chemistry of Mercury. *Environmental Science & Technology*.

[8] Horowitz, H. M., Jacob, D. J., Zhang, Y., Dibble, T. S., Slemr, F., Amos, H. M., Schmidt, J. A., Corbitt, E. S., Marais, E. A., & Sunderland, E. M. (2017). A new mechanism for atmospheric mercury redox chemistry: implications for the global mercury budget. *Atmospheric Chemistry and Physics*, *17*(10), 6353–6371.

[9] Zhou, J., Obrist, D., Dastoor, A., Jiskra, M., & Ryjkov, A. (2021). Vegetation uptake of mercury and impacts on global cycling. *Nature Reviews Earth & Environment*, (pp. 1–16).

[10] Zhou, J., & Obrist, D. (2021). Global mercury assimilation by vegetation. *Environmental Science & Technology*.

[11] Jiskra, M., Heimbürger-Boavida, L.-E., Desgranges, M.-M., Petrova, M. V., Dufour, A., Ferreira-Araujo, B., Masbou, J., Chmeleff, J., Thyssen, M., Point, D., & Sonke, J. E. (2021). Mercury stable isotopes constrain atmospheric sources to the ocean. *Nature*, *597*(7878), 678–682.

[12] Jiskra, M., Sonke, J. E., Obrist, D., Bieser, J., Ebinghaus, R., Myhre, C. L., Pfaffhuber, K. A., Wängberg, I., Kyllönen, K., Worthy, D., Martin, L. G., Labuschagne, C., Mkololo, T., Ramonet, M., Magand, O., & Dommergue, A. (2018). A vegetation control on seasonal variations in global atmospheric mercury concentrations. *Nature Geoscience*, (pp. 1–7).

[13] Zhang, L., Zhou, P., Cao, S., & Zhao, Y. (2019). Atmospheric mercury deposition over the land surfaces and the associated uncertainties in observations and simulations: a critical review. *Atmospheric Chemistry and Physics*, *19*(24), 15587–15608.

[14] Osterwalder, S., Eugster, W., Feigenwinter, I., & Jiskra, M. (2020). Eddy covariance flux measurements of gaseous elemental mercury over a grassland. *Atmospheric Measurement Techniques*, *13*(4), 2057–2074.

[15] Bishop, K., Shanley, J. B., Riscassi, A., de Wit, H. A., Eklöf, K., Meng, B., Mitchell, C., Osterwalder, S., Schuster, P. F., Webster, J., & Zhu, W. (2020). Recent advances in understanding and measurement of mercury in the environment: Terrestrial Hg cycling. *Science of The Total Environment*, *721*, 137647.

[16] Si, L., & Ariya, P. A. (2018). Recent Advances in Atmospheric Chemistry of Mercury. *Atmosphere*, *9*(2), 76.

[17] Jaffe, D. A., Lyman, S., Amos, H. M., Gustin, M. S., Huang, J., Selin, N. E., Levin, L., ter Schure, A., Mason, R. P., Talbot, R., Rutter, A., Finley, B., Jaeglé, L., Shah, V., McClure, C., Ambrose, J., Gratz, L., Lindberg, S., Weiss-Penzias, P., Sheu, G.-R., Feddersen, D., Horvat, M., Dastoor, A., Hynes, A. J., Mao, H., Sonke, J. E., Slemr, F., Fisher, J. A., Ebinghaus, R., Zhang, Y., & Edwards, G. (2014). Progress on understanding atmospheric mercury hampered by uncertain measurements. *Environmental Science & Technology*, *48*(13), 7204–7206.

[18] Lyman, S. N., Gratz, L. E., Dunham-Cheatham, S. M., Gustin, M. S., & Luippold, A. (2020). Improvements to the Accuracy of Atmospheric Oxidized Mercury Measurements. *Environmental Science & Technology*.

[19] Demers, J. D., Blum, J. D., & Zak, D. R. (2013). Mercury isotopes in a forested ecosystem: Implications for air-surface exchange dynamics and the global mercury cycle. *Global Biogeochemical Cycles*, *27*(1), 222–238.

[20] Jiskra, M., Wiederhold, J. G., Skyllberg, U., Kronberg, R.-M., Hajdas, I., & Kretzschmar, R. (2015). Mercury deposition and re-emission pathways in boreal forest soils investigated with Hg isotope signatures. *Environmental Science & Technology*, *49*(12), 7188–7196.

[21] Enrico, M., Roux, G. L., Marusczak, N., Heimbürger, L.-E., Claustres, A., Fu, X., Sun, R., & Sonke, J. E. (2016). Atmospheric mercury transfer to peat bogs dominated by gaseous elemental mercury dry deposition. *Environmental Science & Technology*, *50*(5), 2405–2412.

[22] Zheng, W., Obrist, D., Weis, D., & Bergquist, B. A. (2016). Mercury isotope compositions across North American forests. *Global Biogeochemical Cycles*, *30*(10), 1475–1492.

[23] Amos, H. M., Jacob, D. J., Kocman, D., Horowitz, H. M., Zhang, Y., Dutkiewicz, S., Horvat, M., Corbitt, E. S., Krabbenhoft, D. P., & Sunderland, E. M. (2014). Global Biogeochemical Implications of Mercury Discharges from Rivers and Sediment Burial. *Environmental Science & Technology*, *48*(16), 9514–9522.

[24] Liu, M., Zhang, Q., Maavara, T., Liu, S., Wang, X., & Raymond, P. A. (2021). Rivers as the largest source of mercury to coastal oceans worldwide. *Nature Geoscience*, (pp. 1–6).

[25] Fisher, J. A., Jacob, D. J., Soerensen, A. L., Amos, H. M., Steffen, A., & Sunderland, E. M. (2012). Riverine source of Arctic Ocean mercury inferred from atmospheric observations. *Nature Geoscience*, *5*(7), 499–504.

[26] Zhang, Y., Horowitz, H., Wang, J., Xie, Z., Kuss, J., & Soerensen, A. L. (2019). A Coupled Global Atmosphere-Ocean Model for Air-Sea Exchange of Mercury: Insights into Wet Deposition and Atmospheric Redox Chemistry. *Environmental Science & Technology*, *53*(9), 5052–5061.

[27] Convention, M. (2019). DRAFT Report on the work of the ad hoc technical group on effectiveness evaluation.

[28] Keeling, C. D., Bacastow, R. B., Bainbridge, A. E., Ekdahl, C. A., Guenther, P. R., Waterman, L. S., & Chin, J. F. S. (1976). Atmospheric carbon dioxide variations at Mauna Loa Observatory, Hawaii. *Tellus*, *28*(6), 538–551.

[29] Obrist, D., Pearson, C., Webster, J., Kane, T., Lin, C.-J., Aiken, G. R., & Alpers, C. N. (2016). A synthesis of terrestrial mercury in the western United States: Spatial distribution defined by land cover and plant productivity. *Science of The Total Environment*, *568*, 522–535.

[30] Wang, X., Bao, Z., Lin, C.-J., Yuan, W., & Feng, X. (2016). Assessment of global mercury deposition through litterfall. *Environmental Science & Technology*, *50*(16), 8548–8557.

[31] Fu, X., Zhu, W., Zhang, H., Sommar, J., Yu, B., Yang, X., Wang, X., Lin, C.-J., & Feng, X. (2016). Depletion of atmospheric gaseous elemental mercury by plant uptake at Mt. Changbai, Northeast China. *Atmospheric Chemistry and Physics*, *16*(20), 12861–12873.

[32] UNEP (2019). Technical background report to the Global Mercury Assessment 2018. *Arctic Monitoring and Assessment Programme*.

[33] Pan, Y., Birdsey, R. A., Phillips, O. L., & Jackson, R. B. (2013). The Structure, Distribution, and Biomass of the World's Forests. *Annual Review of Ecology, Evolution, and Systematics*, *44*(1), 593–622.

[34] Agnan, Y., Le Dantec, T., Moore, C. W., Edwards, G. C., & Obrist, D. (2016). New constraints on terrestrial surface–atmosphere fluxes of gaseous elemental mercury using a global database. *Environmental Science & Technology*, *50*(2), 507–524.

[35] Yuan, W., Sommar, J., Lin, C.-J., Wang, X., Li, K., Liu, Y., Zhang, H., Lu, Z., Wu, C., & Feng, X. (2019). Stable isotope evidence shows re-emission of elemental mercury vapor occurring after reductive loss from foliage. *Environmental Science & Technology*, *53*(2), 651–660.

[36] Drenner, R. W., Chumchal, M. M., Jones, C. M., Lehmann, C. M. B., Gay, D. A., & Donato, D. I. (2013). Effects of mercury deposition and coniferous forests on the mercury contamination of fish in the South Central United States. *Environmental Science & Technology*, *47*(3), 1274–1279.

[37] Jiskra, M., Wiederhold, J. G., Skyllberg, U., Kronberg, R.-M., & Kretzschmar, R. (2017). Source tracing of natural organic matter bound mercury in boreal forest runoff with mercury stable isotopes. *Environmental Science: Processes & Impacts*, *19*(10), 1235–1248.

[38] Laacouri, A., Nater, E. A., & Kolka, R. K. (2013). Distribution and uptake dynamics of mercury in leaves of common deciduous tree species in Minnesota, U.S.A. *Environmental Science & Technology*, *47*(18), 10462–10470.

[39] Buckley, T. N. (2019). How do stomata respond to water status? *New Phytologist*, *224*(1), 21–36.

[40] Rutter, A. P., Schauer, J. J., Shafer, M. M., Creswell, J., Olson, M. R., Clary, A., Robinson, M., Parman, A. M., & Katzman, T. L. (2011). Climate Sensitivity of Gaseous Elemental Mercury Dry Deposition to Plants: Impacts of Temperature, Light Intensity, and Plant Species. *Environmental Science & Technology*, *45*(2), 569–575.

[41] Rutter, A. P., Schauer, J. J., Shafer, M. M., Creswell, J. E., Olson, M. R., Robinson, M., Collins, R. M., Parman, A. M., Katzman, T. L., & Mallek, J. L. (2011). Dry deposition of gaseous elemental mercury to plants and soils using mercury stable isotopes in a controlled environment. *Atmospheric Environment*, *45*(4), 848–855.

[42] Teixeira, D. C., Lacerda, L. D., & Silva-Filho, E. V. (2018). Foliar mercury content from tropical trees and its correlation with physiological parameters in situ. *Environmental Pollution*, *242*, 1050–1057.

[43] Stamenkovic, J., & Gustin, M. S. (2009). Nonstomatal versus Stomatal Uptake of Atmospheric Mercury. *Environmental Science & Technology*, *43*(5), 1367–1372.

[44] Arnold, J., Gustin, M. S., & Weisberg, P. J. (2018). Evidence for Nonstomatal Uptake of Hg by Aspen and Translocation of Hg from Foliage to Tree Rings in Austrian Pine. *Environmental Science & Technology*, *52*(3), 1174–1182.

[45] Bishop, K. H., Lee, Y.-H., Munthe, J., & Dambrine, E. (1998). Xylem sap as a pathway for total mercury and methylmercury transport from soils to tree canopy in the boreal forest. *Biogeochemistry*, *40*(2), 101–113.

[46] Assad, M., Parelle, J., Cazaux, D., Gimbert, F., Chalot, M., & Tatin-Froux, F. (2016). Mercury uptake into poplar leaves. *Chemosphere*, *146*, 1–7.

[47] Fernández-Martínez, R., Larios, R., Gómez-Pinilla, I., Gómez-Mancebo, B., López-Andrés, S., Loredo, J., Ordóñez, A., & Rucandio, I. (2015). Mercury accumulation and speciation in plants and soils from abandoned cinnabar mines. *Geoderma*, *253-254*, 30–38.

[48] Cabrita, M. T., Duarte, B., Cesário, R., Mendes, R., Hintelmann, H., Eckey, K., Dimock, B., Caçador, I., & Canário, J. (2019). Mercury mobility and effects in the salt-marsh plant Halimione portulacoides: Uptake, transport, and toxicity and tolerance mechanisms. *Science of The Total Environment*, *650*, 111–120.

[49] Liu, Y., Liu, G., Wang, Z., Guo, Y., Yin, Y., Zhang, X., Cai, Y., & Jiang, G. (2021). Understanding foliar accumulation of atmospheric Hg in terrestrial vegetation: Progress and challenges. *Critical Reviews in Environmental Science and Technology*, *0*(0), 1–22.

[50] Manceau, A., Wang, J., Rovezzi, M., Glatzel, P., & Feng, X. (2018). Biogenesis of mercury–sulfur nanoparticles in plant leaves from atmospheric gaseous mercury. *Environmental Science & Technology*, *52*(7), 3935–3948.

[51] Pleijel, H., Klingberg, J., Nerentorp, M., Broberg, M. C., Nyirambangutse, B., Munthe, J., & Wallin, G. (2021). Mercury accumulation in leaves of different plant types – the significance of tissue age and specific leaf area. *Biogeosciences*, *18*(23), 6313–6328.

[52] Naharro, R., Esbri, J. M., Amoros, J. A., Garcia-Navarro, F. J., & Higueras, P. (2019). Assessment of mercury uptake routes at the soil-plant-atmosphere interface. *Geochemistry: Exploration, Environment, Analysis*, *19*(2), 146–154.

[53] Naharro, R., Esbri, J. M., Amoros, J. A., & Higueras, P. L. (2020). Experimental assessment of the daily exchange of atmospheric mercury in Epipremnum aureum. *Environmental Geochemistry and Health*, *42*(10), 3185–3198.

[54] Rea, A., Lindberg, S., Scherbatskoy, T., & Keeler, G. (2002). In *Mercury accumulation in foliage over time in two northern mixed-hardwood forests, Water Air Soil Poll., 133*, (pp. 49–67).

[55] Körner, C. (2013). Plant–Environment Interactions. In A. Bresinsky, C. Körner, J. W. Kadereit, G. Neuhaus, & U. Sonnewald (Eds.) *Strasburger's Plant Sciences: Including Prokaryotes and Fungi*, (pp. 1065–1166). Berlin, Heidelberg: Springer.

[56] Seibt, U., Kesselmeier, J., Sandoval-Soto, L., Kuhn, U., & Berry, J. A. (2010). A kinetic analysis of leaf uptake of COS and its relation to transpiration, photosynthesis and carbon isotope fractionation. *Biogeosciences*, *7*(1), 333–341.

[57] Körner, C., Scheel, J., & Bauer, H. (1979). Maximum leaf diffusive conductance in vascular plants. *Photosynthetica*, *13*, 45 – 82.

[58] Jarvis, P. G., Monteith, J. L., & Weatherley, P. E. (1976). The interpretation of the variations in leaf water potential and stomatal conductance found in canopies in the field. *Philosophical Transactions of the Royal Society of London. B, Biological Sciences*, *273*(927), 593–610.

[59] Pleijel, H., Danielsson, H., Emberson, L., Ashmore, M. R., & Mills, G. (2007). Ozone risk assessment for agricultural crops in Europe: Further development of stomatal flux and flux–response relationships for European wheat and potato. *Atmospheric Environment*, *41*(14), 3022–3040.

[60] Obrist, D., Roy, E. M., Harrison, J. L., Kwong, C. F., Munger, J. W., Moosmüller, H., Romero, C. D., Sun, S., Zhou, J., & Commane, R. (2021). Previously unaccounted atmospheric mercury deposition in a midlatitude deciduous forest. *Proceedings of the National Academy of Sciences*, *118*(29).

[61] IPCC (2021). Climate change 2021. The physical science basis. Working group I contribution to the Sixth Assessment Report of the Intergovernmental Panel on Climate Change.

[62] Zhang, H., Holmes, C., & Wu, S. (2016). Impacts of changes in climate, land use and land cover on atmospheric mercury. *Atmospheric Environment*, *141*, 230–244.

[63] Obrist, D., Kirk, J. L., Zhang, L., Sunderland, E. M., Jiskra, M., & Selin, N. E. (2018). A review of global environmental mercury processes in response to human and natural perturbations: Changes of emissions, climate, and land use. *Ambio*, *47*(2), 116–140.

[64] Ariya, P. A., Amyot, M., Dastoor, A., Deeds, D., Feinberg, A., Kos, G., Poulain, A., Ryjkov, A., Semeniuk, K., Subir, M., & Toyota, K. (2015). Mercury physicochemical and biogeochemical transformation in the atmosphere and at atmospheric interfaces: a review and future directions. *Chemical Reviews*, *115*(10), 3760–3802.

[65] Saiz-Lopez, A., Sitkiewicz, S. P., Roca-Sanjuán, D., Oliva-Enrich, J. M., Dávalos, J. Z., Notario, R., Jiskra, M., Xu, Y., Wang, F., Thackray, C. P., Sunderland, E. M., Jacob, D. J., Travnikov, O., Cuevas, C. A., Acuña, A. U., Rivero, D., Plane, J. M. C., Kinnison, D. E., & Sonke, J. E. (2018). Photoreduction of gaseous oxidized mercury changes global atmospheric mercury speciation, transport and deposition. *Nature Communications*, *9*(1), 1–9.

[66] EMEP (2016). Air pollution trends in the EMEP region between 1990 and 2012. *Joint Report*.

[67] Prestbo, E. M., & Gay, D. A. (2009). Wet deposition of mercury in the U.S. and Canada, 1996–2005: Results and analysis of the NADP mercury deposition network (MDN). *Atmospheric Environment*, *43*(27), 4223–4233.

[68] Wängberg, I., Nerentorp Mastromonaco, M. G., Munthe, J., & Gårdfeldt, K. (2016). Airborne mercury species at the Råö background monitoring site in Sweden: distribution of mercury as an effect of long-range transport. *Atmospheric Chemistry and Physics*, *16*(21), 13379–13387.

[69] Weiss-Penzias, P. S., Gay, D. A., Brigham, M. E., Parsons, M. T., Gustin, M. S., & ter Schure, A. (2016). Trends in mercury wet deposition and mercury air concentrations across the U.S. and Canada. *Science of The Total Environment*, *568*, 546–556.

[70] Zhang, L., Wright, L. P., & Blanchard, P. (2009). A review of current knowledge concerning dry deposition of atmospheric mercury. *Atmospheric Environment*, *43*(37), 5853–5864.

[71] Risch, M. R., DeWild, J. F., Gay, D. A., Zhang, L., Boyer, E. W., & Krabbenhoft, D. P. (2017). Atmospheric mercury deposition to forests in the eastern USA. *Environmental Pollution*, *228*, 8–18.

[72] Wright, L. P., Zhang, L., & Marsik, F. J. (2016). Overview of mercury dry deposition, litterfall, and throughfall studies. *Atmospheric Chemistry and Physics*, *16*(21), 13399–13416.

[73] Obrist, D., Pokharel, A. K., & Moore, C. (2014). Vertical profile measurements of soil air suggest immobilization of gaseous elemental mercury in mineral soil. *Environmental Science & Technology*, *48*(4), 2242–2252.

[74] Risch, M. R., DeWild, J. F., Krabbenhoft, D. P., Kolka, R. K., & Zhang, L. (2012). Litterfall mercury dry deposition in the eastern USA. *Environmental Pollution*, *161*, 284–290.

[75] Gencarelli, C. N., De Simone, F., Hedgecock, I. M., Sprovieri, F., Yang, X., & Pirrone, N. (2015). European and Mediterranean mercury modelling: Local and long-range contributions to the deposition flux. *Atmospheric Environment*, *117*, 162–168.

[76] Bushey, J. T., Nallana, A. G., Montesdeoca, M. R., & Driscoll, C. T. (2008). Mercury dynamics of a northern hardwood canopy. *Atmospheric Environment*, *42*(29), 6905–6914.

[77] Demers, J. D., Driscoll, C. T., Fahey, T. J., & Yavitt, J. B. (2007). Mercury cycling in litter and soil in different forest types in the Adirondack Region, New York, USA. *Ecological Applications*, *17*(5), 1341–1351.

[78] Graydon, J. A., St. Louis, V. L., Lindberg, S. E., Hintelmann, H., & Krabbenhoft, D. P. (2006). Investigation of mercury exchange between forest canopy vegetation and the atmosphere using a new dynamic chamber. *Environmental Science & Technology*, *40*(15), 4680–4688.

[79] Grigal, D. F. (2002). Inputs and outputs of mercury from terrestrial watersheds: a review. *Environmental Reviews*, *10*(1), 1–39.

[80] Rea, A. W., Lindberg, S. E., Scherbatskoy, T., & Keeler, G. J. (2002). Mercury accumulation in foliage over time in two northern mixed-hardwood forests. *Water, Air, and Soil Pollution*, *133*, 49–67.

[81] St. Louis, V. L., Rudd, J. W. M., Kelly, C. A., Hall, B. D., Rolfhus, K. R., Scott, K. J., Lindberg, S. E., & Dong, W. (2001). Importance of the forest canopy to fluxes of methyl mercury and total mercury to boreal ecosystems. *Environmental Science & Technology*, *35*(15), 3089–3098.

[82] Teixeira, D. C., Montezuma, R. C., Oliveira, R. R., & Silva-Filho, E. V. (2012). Litterfall mercury deposition in Atlantic forest ecosystem from SE – Brazil. *Environmental Pollution*, *164*, 11–15.

[83] Zhang, L., Wu, Z., Cheng, I., Wright, L. P., Olson, M. L., Gay, D. A., Risch, M. R., Brooks, S., Castro, M. S., Conley, G. D., Edgerton, E. S., Holsen, T. M., Luke, W., Tordon, R., & Weiss-Penzias, P. (2016). The estimated six-year mercury dry deposition across North America. *Environmental Science & Technology*, *50*(23), 12864–12873.

[84] Ericksen, J. A., & Gustin, M. S. (2004). Foliar exchange of mercury as a function of soil and air mercury concentrations. *Sci. Total Environ.*, *324*(1), 271–279.

[85] Fleck, J. A., Grigal, D. F., & Nater, E. A. (1999). Mercury uptake by trees: an observational experiment. *Water, Air, and Soil Pollution*, *115*(1), 513–523.

[86] Frescholtz, T. F., Gustin, M. S., Schorran, D. E., & Fernandez, G. C. J. (2003). Assessing the source of mercury in foliar tissue of quaking aspen. *Environmental Toxicology and Chemistry*, *22*(9), 2114–2119.

[87] Millhollen, A. G., Gustin, M. S., & Obrist, D. (2006). Foliar mercury accumulation and exchange for three tree species. *Environmental Science & Technology*, *40*(19), 6001–6006.

[88] Obrist, D. (2007). Atmospheric mercury pollution due to losses of terrestrial carbon pools? *Biogeochemistry*, *85*(2), 119–123.

[89] Blackwell, B. D., & Driscoll, C. T. (2015). Using foliar and forest floor mercury concentrations to assess spatial patterns of mercury deposition. *Environmental Pollution*, *202*, 126–134.

[90] Navrátil, T., Shanley, J. B., Rohovec, J., Oulehle, F., Šimeček, M., Houška, J., & Cudlín, P. (2016). Soil mercury distribution in adjacent coniferous and deciduous stands highly impacted by acid rain in the Ore Mountains, Czech Republic. *Applied Geochemistry*, *75*, 63–75.

[91] Obrist, D., Johnson, D. W., & Edmonds, R. L. (2012). Effects of vegetation type on mercury concentrations and pools in two adjacent coniferous and deciduous forests. *Journal of Plant Nutrition and Soil Science*, *175*(1), 68–77.

[92] Rasmussen, P. E., Mierle, G., & Nriagu, J. O. (1991). The analysis of vegetation for total mercury. *Water Air & Soil Pollution*, *56*(1), 379–390.

[93] Hall, B. D., & St. Louis, V. L. (2004). Methylmercury and Total Mercury in Plant Litter Decomposing in Upland Forests and Flooded Landscapes. *Environmental Science & Technology*, *38*(19), 5010–5021.

[94] Obrist, D., Johnson, D. W., Lindberg, S. E., Luo, Y., Hararuk, O., Bracho, R., Battles, J. J., Dail, D. B., Edmonds, R. L., Monson, R. K., Ollinger, S. V., Pallardy, S. G., Pregitzer, K. S., & Todd, D. E. (2011). Mercury distribution across 14 U.S. forests. Part I: spatial patterns of concentrations in biomass, litter, and soils. *Environmental Science & Technology*, *45*(9), 3974–3981.

[95] Hutnik, R. J., McClenahen, J. R., Long, R. P., & Davis, D. D. (2014). Mercury accumulation in Pinus nigra (Austrian Pine). *Northeastern Naturalist*, *21*(4), 529–540.

[96] Navrátil, T., Nováková, T., Roll, M., Shanley, J. B., Kopáček, J., Rohovec, J., Kaňa, J., & Cudlín, P. (2019). Decreasing litterfall mercury deposition in central European coniferous forests and effects of bark beetle infestation. *Science of The Total Environment*, *682*, 213–225.

[97] Ollerova, H., Maruskova, A., Kontrisova, O., & Pliestikova, L. (2010). Mercury accumulation in Picea abies (L.) Karst. needles with regard to needle age. *Polish Journal of Environmental Studies*, *19*(6), 1401–1404.

[98] Kahmen, A., Lustenberger, S., Zemp, E., & Erny, B. (2019). The Swiss Canopy Crane Experiment II and the botanical garden (University Basel). *DBG*.

[99] Schleyer, R., Bieber, E., & Wallasch, M. (2013). Das Luftmessnetz des Umweltbundesamtes (In German). *UBA German Federal Environment Agency*.

[100] Lindroth, A., Holst, J., Heliasz, M., Vestin, P., Lagergren, F., Biermann, T., Cai, Z., & Mölder, M. (2018). Effects of low thinning on carbon dioxide fluxes in a mixed hemiboreal forest. *Agricultural and Forest Meteorology*, *262*, 59–70.

[101] Lindroth, A., Heliasz, M., Klemedtsson, L., Friborg, T., Nilsson, M., Löfvenius, O., Rutgersson, A., & Stiegler, C. (2015). ICOS Sweden - a national infrastructure network for greenhouse gas research. *EGU Geophysical Research Abstracts*, *17*.

[102] Lohila, A., Penttilä, T., Jortikka, S., Aalto, T., Anttila, P., Asmi, E., Aurela, M., Hatakka, J., Hellén, H., Henttonen, H., Hänninen, P., Kilkki, J., Kyllönen, K., Laurila, T., Lepistö, A., Lihavainen, H., Makkonen, U., Paatero, J., Rask, M., Sutinen, R., Tuovinen, J.-P., Vuorenmaa, J., & Viisanen, Y. (2015). Preface to the special issue on integrated research of atmosphere, ecosystems and environment at Pallas. *Boreal Environment Research*, *20*, 431–454.

[103] Lange, H. (2017). Carbon exchange measurements at a flux tower in Hurdal. *SNS Efinord Growth and Yield Network Conference NIBIO Bok*, *3*.

[104] Wängberg, I., & Munthe, J. (2001). Atmospheric mercury in Sweden, Northern Finland and Northern Europe. Results from national monitoring and European research. *IVL Swedish Environmental Research Institute report*.

[105] JRC (2010). European Commission, Joint Research Centre (JRC): Forest Type Map 2006.

[106] Kempeneers, P., Sedano, F., Seebach, L., Strobl, P., & San-Miguel-Ayanz, J. (2011). Data fusion of different spatial resolution remote sensing images applied to forest-type mapping. *IEEE Transactions on Geoscience and Remote Sensing*, *49*(12), 4977–4986.

[107] EU (2011). European Commission, 2011/833/EU: Commission Decision of 12 December 2011 on the reuse of Commission documents.

[108] Rautio, P., Fürst, A., Stefan, K., Raitio, H., & Bartels, U. (2016). Part XII: Sampling and analysis of needles and leaves. In: UNECE ICP Forests, Programme Coordinating Centre (ed.): Manual on methods and criteria for harmonized sampling, assessment, monitoring and analysis of the effects of air pollution on forests. *Thünen Institute of Forest Ecosystems, Eberswalde, Germany*.

[109] Schuldt, B., Buras, A., Arend, M., Vitasse, Y., Beierkuhnlein, C., Damm, A., Gharun, M., Grams, T. E. E., Hauck, M., Hajek, P., Hartmann, H., Hiltbrunner, E., Hoch, G., Holloway-Phillips, M., Körner, C., Larysch, E., Lübbe, T., Nelson, D. B., Rammig, A., Rigling, A., Rose, L., Ruehr, N. K., Schumann, K., Weiser, F., Werner, C., Wohlgemuth, T., Zang, C. S., & Kahmen, A. (2020). A first assessment of the impact of the extreme 2018 summer drought on Central European forests. *Basic and Applied Ecology*, *45*, 86–103.

[110] NILU (2001). EMEP manual for sampling and chemical analysis.

[111] Torseth, K., Aas, W., Breivik, K., Fjæraa, A. M., Fiebig, M., Hjellbrekke, A. G., Lund Myhre, C., Solberg, S., & Yttri, K. E. (2012). Introduction to the European Monitoring and Evaluation Programme (EMEP) and observed atmospheric composition change during 1972 - 2009. *Atmospheric Chemistry and Physics*, *12*(12), 5447–5481.

[112] Loustau, D., Altimir, N., Barbaste, M., Gielen, B., Jiménez, S. M., Klumpp, K., Linder, S., Matteucci, G., Merbold, L., Op de Beeck, M., Soulé, P., Thimonier, A., Vincke, C., & Waldner, P. (2018). Sampling and collecting foliage elements for the determination of the foliar nutrients in ICOS ecosystem stations. *International Agrophysics*, *32*, 665–676.

[113] Yang, Y., Yanai, R. D., Montesdeoca, M., & Driscoll, C. T. (2017). Measuring mercury in wood: challenging but important. *International Journal of Environmental Analytical Chemistry*, *97*(5), 456–467.

[114] Lodenius, M., Tulisalo, E., & Soltanpour-Gargari, A. (2003). Exchange of mercury between atmosphere and vegetation under contaminated conditions. *Science of The Total Environment*, *304*(1), 169–174.

[115] Iio, A., & Ito, A. (2014). A global database of field-observed leaf area index in woody plant species, 1932 - 2011. Data set available online from Oak Ridge National Laboratory Distributed Active Archive Center, Oak Ridge, Tennessee, USA. *Oak Ridge*.

[116] Garonna, I., Jong, R. d., Wit, A. J. W. d., Mücher, C. A., Schmid, B., & Schaepman, M. E. (2014). Strong contribution of autumn phenology to changes in satellite-derived growing season length estimates across Europe (1982–2011). *Global Change Biology*, *20*(11), 3457–3470.

[117] Rötzer, T., & Chmielewski, F. (2001). Phenological maps of Europe. *Climate Research*, *18*, 249–257.

[118] Matyssek, R., Reich, P., Oren, R., & Winner, W. E. (1995). 9 - Response Mechanisms of Conifers to Air Pollutants. In W. K. Smith, & T. M. Hinckley (Eds.) *Ecophysiology of Coniferous Forests*, Physiological Ecology, (pp. 255–308). San Diego: Academic Press.

[119] Hirose, T. (2004). Development of the Monsi-Saeki Theory on Canopy Structure and Function. *Annals of Botany*, *95*(3), 483–494.

[120] Monsi, M., & Saeki, T. (2004). On the factor light in plant communities and its importance for matter production. *Annals of Botany*, *95*(3), 549–567.

[121] Fichtner, A., Sturm, K., Rickert, C., von Oheimb, G., & Härdtle, W. (2013). Crown size-growth relationships of European beech (Fagus sylvatica L.) are driven by the interplay of disturbance intensity and inter-specific competition. *Forest Ecol. Manag.*, *302*, 178–184.

[122] Hakkila, P. (1991). *Hakkuupoistuman latvusmassa =: Crown mass of trees at the harvesting phase*. No. 773 in Folia forestalia. Helsinki: Metsäntutkimuslaitos.

[123] Sharma, R. P., Vacek, Z., & Vacek, S. (2016). Individual tree crown width models for Norway spruce and European beech in Czech Republic. *Forest Ecology and Management*, *366*, 208–220.

[124] Tahvanainen, T., & Forss, E. (2008). Individual tree models for the crown biomass distribution of Scots pine, Norway spruce and birch in Finland. *Forest Ecology and Management*, *255*(3), 455–467.

[125] Temesgen, H., LeMay, V., & Mitchell, S. J. (2005). Tree crown ratio models for multi-species and multi-layered stands of southeastern British Columbia. *The Forestry Chronicle*, *81*(1), 133–141.

[126] Freeland, R. O. (1952). Effect of age of leaves upon the rate of photosynthesis in some conifers. *Plant Physiology*, *27*(4), 685–690.

[127] Jensen, A. M., Warren, J. M., Hanson, P. J., Childs, J., & Wullschleger, S. D. (2015). Needle age and season influence photosynthetic temperature response and total annual carbon uptake in mature Picea mariana trees. *Annals of Botany*, *116*(5), 821–832.

[128] Op de Beeck, M., Gielen, B., Jonckheere, I., Samson, R., Janssens, I. A., & Ceulemans, R. (2010). Needle age-related and seasonal photosynthetic capacity variation is negligible for modelling yearly gas exchange of a sparse temperate Scots pine forest. *Biogeosciences*, *7*(1), 199–215.

[129] Robakowski, P., & Bielinis, E. (2017). Needle age dependence of photosynthesis along a light gradient within an Abies alba crown. *Acta Physiologiae Plantarum*, *39*(3).

[130] Warren, C. R. (2006). Why does photosynthesis decrease with needle age in Pinus pinaster? *Trees*, *20*(2), 157–164.

[131] Wieser, G., Tausz, M., Kok, L. J. D., & Stulen, I. (Eds.) (2007). *Trees at their Upper Limit: Treelife Limitation at the Alpine Timberline*, vol. 5 of *Plant Ecophysiology*. Dordrecht: Springer Netherlands.

[132] Burkhardt, J., & Pariyar, S. (2014). Particulate pollutants are capable to 'degrade' epicuticular waxes and to decrease the drought tolerance of Scots pine (Pinus sylvestris L.). *Environmental Pollution*, *184*, 659–667.

[133] Güney, A., Zimmermann, R., Krupp, A., & Haas, K. (2016). Needle characteristics of Lebanon cedar (Cedrus libani A.Rich.): degradation of epicuticular waxes and decrease of photosynthetic rates with increasing needle age. *Turkish Journal of Agriculture and Forestry*, *40*, 386–396.

[134] Blackwell, B. D., Driscoll, C. T., Maxwell, J. A., & Holsen, T. M. (2014). Changing climate alters inputs and pathways of mercury deposition to forested ecosystems. *Biogeochemistry*, *119*(1-3), 215–228.

[135] Konôpka, B., Pajtík, J., Marušák, R., Bošeľa, M., & Lukac, M. (2016). Specific leaf area and leaf area index in developing stands of Fagus sylvatica L. and Picea abies Karst. *Forest Ecology and Management*, *364*, 52–59.

[136] Marshall, J. D., & Monserud, R. A. (2003). Foliage height influences specific leaf area of three conifer species. *Canadian Journal of Forest Research*, *33*(1), 164–170.

[137] Merilo, E., Tulva, I., Räim, O., Kükit, A., Sellin, A., & Kull, O. (2009). Changes in needle nitrogen partitioning and photosynthesis during 80 years of tree ontogeny in Picea abies. *Trees*, *23*(5), 951–958.

[138] Morecroft, M. D., & Roberts, J. M. (1999). Photosynthesis and stomatal conductance of mature canopy oak (Quercus robur) and sycamore (Acer pseudoplatanus) trees throughout the growing season. *Functional Ecology*, *13*(3), 332–342.

[139] Stancioiu, P. T., & O'Hara, K. L. (2006). Morphological plasticity of regeneration subject to different levels of canopy cover in mixed-species, multiaged forests of the Romanian Carpathians. *Trees*, *20*(2), 196–209.

[140] Xiao, C.-W., Janssens, I. A., Curiel Yuste, J., & Ceulemans, R. (2006). Variation of specific leaf area and upscaling to leaf area index in mature Scots pine. *Trees*, *20*(3), 304–310.

[141] Niinemets, U., Ellsworth, D. S., Lukjanova, A., & Tobias, M. (2001). Site fertility and the morphological and photosynthetic acclimation of Pinus sylvestris needles to light. *Tree Physiology*, *21*(17), 1231–1244.

[142] Sonnewald, U. (2013). Physiology of Metabolism. In A. Bresinsky, C. Körner, J. W. Kadereit, G. Neuhaus, & U. Sonnewald (Eds.) *Strasburger's Plant Sciences: Including Prokaryotes and Fungi*, (pp. 239–409). Berlin, Heidelberg: Springer.

[143] Poole, I., Weyers, J. D. B., Lawson, T., & Raven, J. A. (1996). Variations in stomatal density and index: implications for palaeoclimatic reconstructions. *Plant, Cell & Environment*, *19*(6), 705–712.

[144] Schulze, E. D. (1986). Carbon dioxide and water vapor exchange in response to drought in the atmosphere and in the soil. *Ann. Rev. Plant Physiol.*, *37*, 28.

[145] Jiskra, M., Sonke, J. E., Agnan, Y., Helmig, D., & Obrist, D. (2019). Insights from mercury stable isotopes on terrestrial–atmosphere exchange of Hg(0) in the Arctic tundra. *Biogeosciences*, *16*(20), 4051–4064.

[146] Reich, P. B., Walters, M. B., & Ellsworth, D. S. (1997). From tropics to tundra: Global convergence in plant functioning. *Proceedings of the National Academy of Sciences*, *94*(25), 13730–13734.

[147] Wright, I. J., Reich, P. B., Westoby, M., Ackerly, D. D., Baruch, Z., Bongers, F., Cavender-Bares, J., Chapin, T., Cornelissen, J. H. C., Diemer, M., Flexas, J., Garnier, E., Groom, P. K., Gulias, J., Hikosaka, K., Lamont, B. B., Lee, T., Lee, W., Lusk, C., Midgley, J. J., Navas, M.-L., Niinemets, U., Oleksyn, J., Osada, N., Poorter, H., Poot, P., Prior, L., Pyankov, V. I., Roumet, C., Thomas, S. C., Tjoelker, M. G., Veneklaas, E. J., & Villar, R. (2004). The worldwide leaf economics spectrum. *Nature*, *428*(6985), 821–827.

[148] Juillerat, J. I., Ross, D. S., & Bank, M. S. (2012). Mercury in litterfall and upper soil horizons in forested ecosystems in Vermont, USA. *Environmental Toxicology and Chemistry*, *31*(8), 1720–1729.

[149] Rea, A. W., Keeler, G. J., & Scherbatskoy, T. (1996). The deposition of mercury in throughfall and litterfall in the Lake Champlain Watershed: A short-term study. *Atmospheric Environment*, *30*(19), 3257–3263.

[150] Rea, A. W., Lindberg, S. E., & Keeler, G. J. (2001). Dry deposition and foliar leaching of mercury and selected trace elements in deciduous forest throughfall. *Atmospheric Environment*, *35*(20), 3453–3462.

[151] Obrist, D., Agnan, Y., Jiskra, M., Olson, C. L., Colegrove, D. P., Hueber, J., Moore, C. W., Sonke, J. E., & Helmig, D. (2017). Tundra uptake of atmospheric elemental mercury drives Arctic mercury pollution. *Nature*, *547*(7662), 201–204.

[152] Pokharel, A. K., & Obrist, D. (2011). Fate of mercury in tree litter during decomposition. *Biogeosciences*, *8*(9), 2507–2521.

[153] Brus, D. J., Hengeveld, G. M., Walvoort, D. J. J., Goedhart, P. W., Heidema, A. H., Nabuurs, G. J., & Gunia, K. (2012). Statistical mapping of tree species over Europe. *European Journal of Forest Research*, *131*(1), 145–157.

[154] Tyrrell, M. L., Ross, J., & Kelty, M. (2012). Carbon dynamics in the Temperate Forest. In M. S. Ashton, M. L. Tyrrell, D. Spalding, & B. Gentry (Eds.) *Managing Forest Carbon in a Changing Climate*, (pp. 77–107). Dordrecht: Springer Netherlands.

[155] Pacyna, J. M., Pacyna, E. G., & Aas, W. (2009). Changes of emissions and atmospheric deposition of mercury, lead, and cadmium. *Atmospheric Environment*, *43*(1), 117–127.

[156] Weiss-Penzias, P. S., Ortiz, C., Acosta, R. P., Heim, W., Ryan, J. P., Fernandez, D., Collett, J. L., & Flegal, A. R. (2012). Total and monomethyl mercury in fog water from the central California coast. *Geophysical Research Letters*, *39*(3).

[157] Grigal, D. F. (2003). Mercury sequestration in forests and peatlands. *Journal of Environment Quality*, *32*(2), 393.

[158] AMAP, & UNEP (2019). Technical background report to the global mercury assessment 2018. Arctic Monitoring and Assessment Programme, Oslo, Norway/UN Environment Programme, Chemicals and Health Branch, Geneva, Switzerland.

[159] Iverfeldt, A. (1991). Mercury in forest canopy throughfall water and its relation to atmospheric deposition. *Water Air & Soil Pollution*, *56*(1), 553–564.

[160] Schwesig, D., & Matzner, E. (2000). Pools and fluxes of mercury and methylmercury in two forested catchments in Germany. *Science of The Total Environment*, *260*(1), 213–223.

[161] Graydon, J. A., St. Louis, V. L., Hintelmann, H., Lindberg, S. E., Sandilands, K. A., Rudd, J. W. M., Kelly, C. A., Hall, B. D., & Mowat, L. D. (2008). Long-term wet and dry deposition of total and methyl mercury in the remote boreal ecoregion of Canada. *Environmental Science & Technology*, *42*(22), 8345–8351.

[162] Wang, X., Yuan, W., Lin, C.-J., Luo, J., Wang, F., Feng, X., Fu, X., & Liu, C. (2020). Underestimated sink of atmospheric mercury in a deglaciated forest chronosequence. *Environmental Science & Technology*, *54*(13), 8083–8093.

[163] Sonke, J. E., Teisserenc, R., Heimbürger-Boavida, L.-E., Petrova, M. V., Marusczak, N., Dantec, T. L., Chupakov, A. V., Li, C., Thackray, C. P., Sunderland, E. M., Tananaev, N., & Pokrovsky, O. S. (2018). Eurasian river spring flood observations support net Arctic Ocean mercury export to the atmosphere and Atlantic Ocean. *Proceedings of the National Academy of Sciences*, *115*(50), E11586–E11594.

[164] Yu, B., Fu, X., Yin, R., Zhang, H., Wang, X., Lin, C.-J., Wu, C., Zhang, Y., He, N., Fu, P., Wang, Z., Shang, L., Sommar, J., Sonke, J. E., Maurice, L., Guinot, B., & Feng, X. (2016). Isotopic composition of atmospheric mercury in china: new evidence for sources and transformation processes in air and in vegetation. *Environmental Science & Technology*, *50*(17), 9262–9269.

[165] Wohlgemuth, L., Osterwalder, S., Joseph, C., Kahmen, A., Hoch, G., Alewell, C., & Jiskra, M. (2020). A bottom-up quantification of foliar mercury uptake fluxes across Europe. *Biogeosciences*, *17*(24), 6441–6456.

[166] Travnikov, O., Angot, H., Artaxo, P., Bencardino, M., Bieser, J., D'Amore, F., Dastoor, A., De Simone, F., Diéguez, M. d. C., Dommergue, A., Ebinghaus, R., Feng, X. B., Gencarelli, C. N., Hedgecock, I. M., Magand, O., Martin, L., Matthias, V., Mashyanov, N., Pirrone, N., Ramachandran, R., Read, K. A., Ryjkov, A., Selin, N. E., Sena, F., Song, S., Sprovieri, F., Wip, D., Wängberg, I., & Yang, X. (2017). Multi-model study of mercury dispersion in the atmosphere: atmospheric processes and model evaluation. *Atmospheric Chemistry and Physics*, *17*(8), 5271–5295.

[167] Running, S. W., & Coughlan, J. C. (1988). A general model of forest ecosystem processes for regional applications I. Hydrologic balance, canopy gas exchange and primary production processes. *Ecological Modelling*, *42*(2), 125–154.

[168] Reich, P. B., Wright, I. J., Cavender-Bares, J., Craine, J. M., Oleksyn, J., Westoby, M., & Walters, M. B. (2003). The evolution of plant functional variation: traits, spectra, and strategies. *International Journal of Plant Sciences*, *164*(S3), S143–S164.

[169] Jonard, M., Fürst, A., Verstraeten, A., Thimonier, A., Timmermann, V., Potočić, N., Waldner, P., Benham, S., Hansen, K., Merilä, P., Ponette, Q., Cruz, A. C. d. l., Roskams, P., Nicolas, M., Croisé, L., Ingerslev, M., Matteucci, G., Decinti, B., Bascietto, M., & Rautio, P. (2015). Tree mineral nutrition is deteriorating in Europe. *Global Change Biology*, *21*(1), 418–430.

[170] Vilhar, U., Beuker, E., Mizunuma, T., Skudnik, M., Lebourgeois, F., Soudani, K., & Wilkinson, M. (2013). Chapter 9 - Tree Phenology. In M. Ferretti, & R. Fischer (Eds.) *Developments in Environmental Science*, vol. 12 of *Forest Monitoring*, (pp. 169–182). Elsevier.

[171] Dobbertin, M., & Neumann, M. (2016). Part V: Tree Growth. In: UNECE ICP Forests, Programme Coordinating Centre (ed.): Manual on methods and criteria for harmonized sampling, assessment, monitoring and analysis of the effects of air pollution on forests. *Thünen Institute of Forest Ecosystems, Eberswalde, Germany*.

[172] Fleck, S., Cools, N., De Vos, B., Meesenburg, H., & Fischer, R. (2016). The Level II aggregated forest soil condition database links soil physicochemical and hydraulic properties with long-term observations of forest condition in Europe. *Annals of Forest Science*, *73*(4), 945–957.

[173] Cools, N., & De Vos, B. (2020). Part X: Sampling and analysis of soil. In: UNECE ICP Forests, Programme Coordinating Centre (ed.): Manual on methods and criteria for harmonized sampling, assessment, monitoring and analysis of the effects of air pollution on forests. *Thünen Institute of Forest Ecosystems, Eberswalde, Germany*.

[174] Raspe, S., Bastrup-Birk, A., Fleck, S., Weis, W., Mayer, H., Meesenburg, H., Wagner, M., Schindler, D., & Gartner, K. (2013). Chapter 17 - Meteorology. In M. Ferretti, & R. Fischer (Eds.) *Developments in Environmental Science*, vol. 12 of *Forest Monitoring*, (pp. 319–336). Elsevier.

[175] Miralles, D. G., De Jeu, R. A. M., Gash, J. H., Holmes, T. R. H., & Dolman, A. J. (2011). Magnitude and variability of land evaporation and its components at the global scale. *Hydrology and Earth System Sciences*, *15*(3), 967–981.

[176] Martens, B., Miralles, D. G., Lievens, H., Schalie, R. v. d., Jeu, R. A. M. d., Fernández-Prieto, D., Beck, H. E., Dorigo, W. A., & Verhoest, N. E. C. (2017). GLEAM v3: satellite-based land evaporation and root-zone soil moisture. *Geoscientific Model Development*, *10*(5), 1903–1925.

[177] Muñoz Sabater, J. (2019). ERA5-Land hourly data from 1981 to present. Copernicus Climate Change Service (C3S) Climate Data Store (CDS).

[178] Iglewicz, B., & Hoaglin, D. C. (1993). *How to detect and handle outliers*. No. v. 16 in ASQC basic references in quality control. Milwaukee, Wis: ASQC Quality Press.

[179] Templ, B., Koch, E., Bolmgren, K., Ungersböck, M., Paul, A., Scheifinger, H., Rutishauser, T., Busto, M., Chmielewski, F.-M., Hájková, L., Hodzić, S., Kaspar, F., Pietragalla, B., Romero-Fresneda, R., Tolvanen, A., Vučetič, V., Zimmermann, K., & Zust, A. (2018). Pan European Phenological database (PEP725): a single point of access for European data. *International Journal of Biometeorology*, *62*(6), 1109–1113.

[180] Huber, W., Carey, V. J., Gentleman, R., Anders, S., Carlson, M., Carvalho, B. S., Bravo, H. C., Davis, S., Gatto, L., Girke, T., Gottardo, R., Hahne, F., Hansen, K. D., Irizarry, R. A., Lawrence, M., Love, M. I., MacDonald, J., Obenchain, V., Oleś, A. K., Pagès, H., Reyes, A., Shannon, P., Smyth, G. K., Tenenbaum, D., Waldron, L., & Morgan, M. (2015). Orchestrating high-throughput genomic analysis with Bioconductor. *Nature Methods*, *12*(2), 115–121.

[181] Dierckx, W., Sterckx, S., Benhadj, I., Livens, S., Duhoux, G., Van Achteren, T., Francois, M., Mellab, K., & Saint, G. (2014). PROBA-V mission for global vegetation monitoring: standard products and image quality. *International Journal of Remote Sensing*, *35*(7), 2589–2614.

[182] Fuster, B., Sánchez-Zapero, J., Camacho, F., García-Santos, V., Verger, A., Lacaze, R., Weiss, M., Baret, F., & Smets, B. (2020). Quality assessment of PROBA-V LAI, fAPAR and fCOVER collection 300 m products of Copernicus Global Land Service. *Remote Sensing*, *12*(6), 1017.

[183] Bórnez, K., Descals, A., Verger, A., & Peñuelas, J. (2020). Land surface phenology from VEGETATION and PROBA-V data. Assessment over deciduous forests. *International Journal of Applied Earth Observation and Geoinformation*, *84*, 101974.

[184] Yuan, W., Zheng, Y., Piao, S., Ciais, P., Lombardozzi, D., Wang, Y., Ryu, Y., Chen, G., Dong, W., Hu, Z., Jain, A. K., Jiang, C., Kato, E., Li, S., Lienert, S., Liu, S., Nabel, J. E. M. S., Qin, Z., Quine, T., Sitch, S., Smith, W. K., Wang, F., Wu, C., Xiao, Z., & Yang, S. (2019). Increased atmospheric vapor pressure deficit reduces global vegetation growth. *Science Advances*, *5*(8).

[185] CLRTAP (2017). Revised Chapter 3 of the Manual on Methodologies and Criteria for Modelling and Mapping Critical Loads and Levels and Air Pollution Effects, Risks and Trends: Mapping Critical Levels for Vegetation. *Umweltbundesamt*.

[186] Domec, J.-C., Noormets, A., King, J. S., Sun, G., Mcnulty, S. G., Gavazzi, M. J., Boggs, J. L., & Treasure, E. A. (2009). Decoupling the influence of leaf and root hydraulic conductances on stomatal conductance and its sensitivity to vapour pressure deficit as soil dries in a drained loblolly pine plantation. *Plant, Cell & Environment*, *32*(8), 980–991.

[187] Grünhage, L., Braden, H., Bender, J., Burkart, S., Lehmann, Y., & Schröder, M. (2011). Evaluation of the ozone-related risk for winter wheat at local scale with the CRO3PS model. *71*(3), 9.

[188] Grünhage, L., Pleijel, H., Mills, G., Bender, J., Danielsson, H., Lehmann, Y., Castell, J.-F., & Bethenod, O. (2012). Updated stomatal flux and flux-effect models for wheat for quantifying effects of ozone on grain yield, grain mass and protein yield. *Environmental Pollution*, *165*, 147–157.

[189] Büker, P., Morrissey, T., Briolat, A., Falk, R., Simpson, D., Tuovinen, J.-P., Alonso, R., Barth, S., Baumgarten, M., Grulke, N., Karlsson, P. E., King, J., Lagergren, F., Matyssek, R., Nunn, A., Ogaya, R., Peñuelas, J., Rhea, L., Schaub, M., Uddling, J., Werner, W., & Emberson, L. D. (2012). DO3SE modelling of soil moisture to determine ozone flux to forest trees. *Atmos. Chem. Phys.*, *12*(12), 5537–5562.

[190] Saxton, K. E., & Rawls, W. J. (2006). Soil water characteristic estimates by texture and organic matter for hydrologic solutions. *Soil Science Society of America Journal*, *70*(5), 1569–1578.

[191] Schwarz, P. A., Fahey, T. J., & Dawson, T. E. (1997). Seasonal air and soil temperature effects on photosynthesis in red spruce (Picea rubens) saplings. *Tree Physiology*, *17*(3), 187–194.

[192] Mellander, P.-E., Bishop, K., & Lundmark, T. (2004). The influence of soil temperature on transpiration: a plot scale manipulation in a young Scots pine stand. *Forest Ecology and Management*, *195*(1), 15–28.

[193] EMEP (2021). Present state of Hg(0) data.

[194] Reich, P. B., Walters, M. B., Ellsworth, D. S., Vose, J. M., Volin, J. C., Gresham, C., & Bowman, W. D. (1998). Relationships of leaf dark respiration to leaf nitrogen, specific leaf area and leaf life-span: a test across biomes and functional groups. *Oecologia*, *114*(4), 471–482.

[195] Evans, J. R. (1989). Photosynthesis and nitrogen relationships in leaves of C3 plants. *Oecologia*, *78*, 9–19.

[196] Loomis, R. S. (1997). On the utility of nitrogen in leaves. *Proceedings of the National Academy of Sciences*, *94*(25), 13378–13379.

[197] Bolton, J. K., & Brown, R. H. (1980). Photosynthesis of grass species differing in carbon dioxide fixation pathways: V. Response of Panicum maximum, Panicum milioides, and tall fescue (Festuca arundinacea) to nitrogen nutrition. *Plant Physiology*, *66*(1), 97–100.

[198] Schulze, E.-D., Kelliher, F. M., Körner, C., Lloyd, J., & Leuning, R. (1994). Relationships among maximum stomatal conductance, ecosystem surface conductance, carbon assimilation rate, and plant nitrogen nutrition: A global ecology scaling exercise. (p. 36).

[199] Reich, P. B., Ellsworth, D. S., Walters, M. B., Vose, J. M., Gresham, C., Volin, J. C., & Bowman, W. D. (1999). Generality of leaf trait relationships: a test across six biomes. *Ecology*, *80*(6), 1955–1969.

[200] Meziane, D., & Shipley, B. (2001). Direct and indirect relationships between specific leaf area, leaf nitrogen and leaf gas exchange. Effects of irradiance and nutrient supply. *Annals of Botany*, *88*(5), 915–927.

[201] Körner, C. (2018). Concepts in empirical plant ecology. *Plant Ecology & Diversity*, *11*(4), 405–428.

[202] Wilson, K. B., Baldocchi, D. D., & Hanson, P. J. (2000). Spatial and seasonal variability of photosynthetic parameters and their relationship to leaf nitrogen in a deciduous forest. *Tree Physiology*, *20*(9), 565–578.

[203] Mediavilla, S., & Escudero, A. (2003). Relative growth rate of leaf biomass and leaf nitrogen content in several mediterranean woody species. *Plant Ecology*, *168*(2), 321–332.

[204] Adams, M. B., Campbell, R. G., Allen, H. L., & Davey, C. B. (1987). Root and foliar nutrient concentrations in loblolly pine: effects of season, site, and fertilization. *Forest Science*, *33*(4), 984–996.

[205] Hatcher, P. E. (1990). Seasonal and age-related variation in the needle quality of five conifer species. *Oecologia*, *85*(2), 200–212.

[206] Lin, Y.-S., Medlyn, B. E., Duursma, R. A., Prentice, I. C., Wang, H., Baig, S., Eamus, D., de Dios, V. R., Mitchell, P., Ellsworth, D. S., de Beeck, M. O., Wallin, G., Uddling, J., Tarvainen, L., Linderson, M.-L., Cernusak, L. A., Nippert, J. B., Ocheltree, T. W., Tissue, D. T., Martin-StPaul, N. K., Rogers, A., Warren, J. M., De Angelis, P., Hikosaka, K., Han, Q., Onoda, Y., Gimeno, T. E., Barton, C. V. M., Bennie, J., Bonal, D., Bosc, A., Löw, M., Macinins-Ng, C., Rey, A., Rowland, L., Setterfield, S. A., Tausz-Posch, S., Zaragoza-Castells, J., Broadmeadow, M. S. J., Drake, J. E., Freeman, M., Ghannoum, O., Hutley, L. B., Kelly, J. W., Kikuzawa, K., Kolari, P., Koyama, K., Limousin, J.-M., Meir, P., Lola da Costa, A. C., Mikkelsen, T. N., Salinas, N., Sun, W., & Wingate, L. (2015). Optimal stomatal behaviour around the world. *Nature Climate Change*, *5*(5), 459–464.

[207] Blackwell, B. D., & Driscoll, C. T. (2015). Deposition of mercury in forests along a montane elevation gradient. *Environmental Science & Technology*, *49*(9), 5363–5370.

[208] Vesterdal, L., Schmidt, I. K., Callesen, I., Nilsson, L. O., & Gundersen, P. (2008). Carbon and nitrogen in forest floor and mineral soil under six common European tree species. *Forest Ecology and Management*, *255*(1), 35–48.

[209] Hikosaka, K. (2004). Interspecific difference in the photosynthesis–nitrogen relationship: patterns, physiological causes, and ecological importance. *Journal of Plant Research*, *117*(6), 481–494.

[210] Ellsworth, D. S., & Reich, P. B. (1993). Canopy structure and vertical patterns of photosynthesis and related leaf traits in a deciduous forest. *Oecologia*, *96*(2), 169–178.

[211] Niinemets, U., & Tenhunen, J. D. (1997). A model separating leaf structural and physiological effects on carbon gain along light gradients for the shade-tolerant species Acer saccharum. *Plant, Cell & Environment*, *20*(7), 845–866.

[212] Rosati, A., Esparza, G., DeJong, T. M., & Pearcy, R. W. (1999). Influence of canopy light environment and nitrogen availability on leaf photosynthetic characteristics and photosynthetic nitrogen-use efficiency of field-grown nectarine trees. *Tree Physiology*, *19*(3), 173–180.

[213] Evans, J. R., & Poorter, H. (2001). Photosynthetic acclimation of plants to growth irradiance: the relative importance of specific leaf area and nitrogen partitioning in maximizing carbon gain. *Plant, Cell & Environment*, *24*(8), 755–767.

[214] Franks, P. J., & Farquhar, G. D. (1999). A relationship between humidity response, growth form and photosynthetic operating point in C3 plants. *Plant, Cell & Environment*, *22*(11), 1337–1349.

[215] McAdam, S. A. M., & Brodribb, T. J. (2015). The evolution of mechanisms driving the stomatal response to vapor pressure deficit. *Plant Physiology*, *167*(3), 833–843.

[216] Grossiord, C., Buckley, T. N., Cernusak, L. A., Novick, K. A., Poulter, B., Siegwolf, R. T. W., Sperry, J. S., & McDowell, N. G. (2020). Plant responses to rising vapor pressure deficit. *New Phytologist*, *226*(6), 1550–1566.

[217] Emberson, L. D., Ashmore, M. R., Cambridge, H. M., Simpson, D., & Tuovinen, J. P. (2000). Modelling stomatal ozone flux across Europe. *Environmental Pollution*, *109*(3), 403–413.

[218] Zweifel, R., Rigling, A., & Dobbertin, M. (2009). Species-specific stomatal response of trees to drought – a link to vegetation dynamics? *Journal of Vegetation Science*, *20*(3), 442–454.

[219] Tsuji, S., Nakashizuka, T., Kuraji, K., Kume, A., & Hanba, Y. T. (2020). Sensitivity of stomatal conductance to vapor pressure deficit and its dependence on leaf water relations and wood anatomy in nine canopy tree species in a Malaysian wet tropical rainforest. *Trees*, *34*(5), 1299–1311.

[220] Martínez-Ferri, E., Balaguer, L., Valladares, F., Chico, J. M., & Manrique, E. (2000). Energy dissipation in drought-avoiding and drought-tolerant tree species at midday during the Mediterranean summer. *Tree Physiology*, *20*(2), 131–138.

[221] Zweifel, R., Steppe, K., & Sterck, F. J. (2007). Stomatal regulation by microclimate and tree water relations: interpreting ecophysiological field data with a hydraulic plant model. *Journal of Experimental Botany*, *58*(8), 2113–2131.

[222] Carnicer, J., Barbeta, A., Sperlich, D., Coll, M., & Penuelas, J. (2013). Contrasting trait syndromes in angiosperms and conifers are associated with different responses of tree growth to temperature on a large scale. *Frontiers in Plant Science*, *4*(409). Publisher: Frontiers.

[223] Coll, M., Peñuelas, J., Ninyerola, M., Pons, X., & Carnicer, J. (2013). Multivariate effect gradients driving forest demographic responses in the Iberian Peninsula. *Forest Ecology and Management*, *303*, 195–209.

[224] Cárcer, P. S. d., Vitasse, Y., Peñuelas, J., Jassey, V. E. J., Buttler, A., & Signarbieux, C. (2018). Vapor–pressure deficit and extreme climatic variables limit tree growth. *Global Change Biology*, *24*(3), 1108–1122.

[225] Lagergren, F., & Lindroth, A. (2002). Transpiration response to soil moisture in pine and spruce trees in Sweden. *Agricultural and Forest Meteorology*, *112*(2), 67–85.

[226] Panek, J. A., & Goldstein, A. H. (2001). Response of stomatal conductance to drought in ponderosa pine: implications for carbon and ozone uptake. *Tree Physiology*, *21*(5), 337–344.

[227] Simpson, D., Tuovinen, J.-P., Emberson, L., & Ashmore, M. R. (2003). Characteristics of an ozone deposition module II: Sensitivity analysis. *Water, Air, and Soil Pollution*, *143*(1), 123–137.

[228] Nunn, A. J., Kozovits, A. R., Reiter, I. M., Heerdt, C., Leuchner, M., Lütz, C., Liu, X., Lo¨w, M., Winkler, J. B., Grams, T. E. E., Häberle, K. H., Werner, H., Fabian, P., Rennenberg, H., & Matyssek, R. (2005). Comparison of ozone uptake and sensitivity between a phytotron study with young beech and a field experiment with adult beech (Fagus sylvatica). *Environmental Pollution*, *137*(3), 494–506.

[229] Emberson, L. D., Pleijel, H., Ainsworth, E. A., van den Berg, M., Ren, W., Osborne, S., Mills, G., Pandey, D., Dentener, F., Büker, P., Ewert, F., Koeble, R., & Van Dingenen, R. (2018). Ozone effects on crops and consideration in crop models. *European Journal of Agronomy*, *100*, 19–34.

[230] Feinberg, A., Dlamini, T., Jiskra, M., Shah, V., & E. Selin, N. (2022). Evaluating atmospheric mercury (Hg) uptake by vegetation in a chemistry-transport model. *Environmental Science: Processes & Impacts*.

[231] Sonke, J. E., Angot, H., Zhang, Y., Poulain, A., Björn, E., & Schartup, A. (2023). Global change effects on biogeochemical mercury cycling. *Ambio*, *52*(5), 853–876.

[232] Zhou, J., Bollen, S. W., Roy, E. M., Hollinger, D. Y., Wang, T., Lee, J. T., & Obrist, D. (2023). Comparing ecosystem gaseous elemental mercury fluxes over a deciduous and coniferous forest. *Nat Commun*, *14*(1), 2722. Number: 1 Publisher: Nature Publishing Group.

[233] Wohlgemuth, L., Rautio, P., Ahrends, B., Russ, A., Vesterdal, L., Waldner, P., Timmermann, V., Eickenscheidt, N., Fürst, A., Greve, M., Roskams, P., Thimonier, A., Nicolas, M., Kowalska, A., Ingerslev, M., Merilä, P., Benham, S., Iacoban, C., Hoch, G., Alewell, C., & Jiskra, M. (2022). Physiological and climate controls on foliar mercury uptake by European tree species. *Biogeosciences*, *19*(5), 1335–1353. Publisher: Copernicus GmbH.

[234] Berg, A., & Sheffield, J. (2018). Climate Change and Drought: the Soil Moisture Perspective. *Current Climate Change Reports*, *4*(2), 180–191.

[235] Stocker, B. D., Zscheischler, J., Keenan, T. F., Prentice, I. C., Seneviratne, S. I., & Peñuelas, J. (2019). Drought impacts on terrestrial primary production underestimated by satellite monitoring. *Nature Geoscience*, *12*(4), 264–270.

[236] Allen, C. D., Breshears, D. D., & McDowell, N. G. (2015). On underestimation of global vulnerability to tree mortality and forest die-off from hotter drought in the Anthropocene. *Ecosphere*, *6*(8), art129.

[237] Brando, P. M., Paolucci, L., Ummenhofer, C. C., Ordway, E. M., Hartmann, H., Cattau, M. E., Rattis, L., Medjibe, V., Coe, M. T., & Balch, J. (2019). Droughts, Wildfires, and Forest Carbon Cycling: A Pantropical Synthesis. *Annual Review of Earth and Planetary Sciences*, *47*(1), 555–581.

[238] Feinberg, A., Jiskra, M., Borrelli, P., Biswakarma, J., & Selin, N. E. (2023). Land use change as an anthropogenic driver of mercury pollution. Preprint. *Preprint*.

[239] Norby, R. J., & Zak, D. R. (2011). Ecological Lessons from Free-Air CO2 Enrichment (FACE) Experiments. *Annual Review of Ecology, Evolution, and Systematics*, *42*(1), 181–203.

[240] Hararuk, O., Obrist, D., & Luo, Y. (2013). Modelling the sensitivity of soil mercury storage to climate-induced changes in soil carbon pools. *Biogeosciences*, *10*(4), 2393–2407.

[241] Selin, N. E., Jacob, D. J., Yantosca, R. M., Strode, S., Jaeglé, L., & Sunderland, E. M. (2008). Global 3-D land-ocean-atmosphere model for mercury: Present-day versus preindustrial cycles and anthropogenic enrichment factors for deposition. *Global Biogeochemical Cycles*, *22*(2).

[242] Wesely, M. L. (2007). Parameterization of surface resistances to gaseous dry deposition in regional-scale numerical models. *Atmospheric Environment*, *41*, 52–63.

[243] Smith-Downey, N. V., Sunderland, E. M., & Jacob, D. J. (2010). Anthropogenic impacts on global storage and emissions of mercury from terrestrial soils: Insights from a new global model. *Journal of Geophysical Research: Biogeosciences*, *115*(G3).

[244] Wu, Z., Wang, X., Chen, F., Turnipseed, A. A., Guenther, A. B., Niyogi, D., Charusombat, U., Xia, B., William Munger, J., & Alapaty, K. (2011). Evaluating the calculated dry deposition velocities of reactive nitrogen oxides and ozone from two community models over a temperate deciduous forest. *Atmospheric Environment*, *45*(16), 2663–2674.

[245] Khan, T., Obrist, D., Agnan, Y., E. Selin, N., & A. Perlinger, J. (2019). Atmosphere-terrestrial exchange of gaseous elemental mercury: parameterization improvement through direct comparison with measured ecosystem fluxes. *Environmental Science: Processes & Impacts*, *21*(10), 1699–1712.

[246] Hersbach, H., Bell, B., Berrisford, P., Biavati, G., Horányi, A., Muñoz Sabater, J., Nicolas, J., Peubey, C., Radu, R., Rozum, I., Schepers, D., Simmons, A., Soci, C., Dee, D., & Thépaut, J.-N. (2018). ERA5 hourly data on pressure levels from 1979 to present. Copernicus Climate Change Service (C3S) Climate Data Store (CDS).

[247] IPCC (2021). Summary for Policymakers. Climate Change 2021: The Physical Science Basis. Contribution of Working Group I to the Sixth Assessment Report of the Intergovernmental Panel on Climate Change. *Cambride University Press*.

[248] Jacob, D., Teichmann, C., Sobolowski, S., Katragkou, E., Anders, I., Belda, M., Benestad, R., Boberg, F., Buonomo, E., Cardoso, R. M., Casanueva, A., Christensen, O. B., Christensen, J. H., Coppola,

E., De Cruz, L., Davin, E. L., Dobler, A., Domínguez, M., Fealy, R., Fernandez, J., Gaertner, M. A., García-Díez, M., Giorgi, F., Gobiet, A., Goergen, K., Gómez-Navarro, J. J., Alemán, J. J. G., Gutiérrez, C., Gutiérrez, J. M., Güttler, I., Haensler, A., Halenka, T., Jerez, S., Jiménez-Guerrero, P., Jones, R. G., Keuler, K., Kjellström, E., Knist, S., Kotlarski, S., Maraun, D., van Meijgaard, E., Mercogliano, P., Montávez, J. P., Navarra, A., Nikulin, G., de Noblet-Ducoudré, N., Panitz, H.-J., Pfeifer, S., Piazza, M., Pichelli, E., Pietikäinen, J.-P., Prein, A. F., Preuschmann, S., Rechid, D., Rockel, B., Romera, R., Sánchez, E., Sieck, K., Soares, P. M. M., Somot, S., Srnec, L., Sørland, S. L., Termonia, P., Truhetz, H., Vautard, R., Warrach-Sagi, K., & Wulfmeyer, V. (2020). Regional climate downscaling over Europe: perspectives from the EURO-CORDEX community. *Regional Environmental Change*, *20*(2), 51.

[249] C3S (2022). Copernicus Climate Change Service (C3S), Climate Data Store (CDS): CORDEX regional climate model data on single levels. *Copernicus*.

[250] Mauri, A., Strona, G., & San-Miguel-Ayanz, J. (2017). EU-Forest, a high-resolution tree occurrence dataset for Europe. *Scientific Data*, *4*.

[251] Buras, A., & Menzel, A. (2019). Projecting Tree Species Composition Changes of European Forests for 2061–2090 Under RCP 4.5 and RCP 8.5 Scenarios. *Frontiers in Plant Science*, *9*, 1986.

[252] Forrester, D. I., Tachauer, I. H. H., Annighoefer, P., Barbeito, I., Pretzsch, H., Ruiz-Peinado, R., Stark, H., Vacchiano, G., Zlatanov, T., Chakraborty, T., Saha, S., & Sileshi, G. W. (2017). Generalized biomass and leaf area allometric equations for European tree species incorporating stand structure, tree age and climate. *Forest Ecology and Management*, *396*, 160–175.

[253] Wang, R., Chen, J. M., Liu, Z., & Arain, A. (2017). Evaluation of seasonal variations of remotely sensed leaf area index over five evergreen coniferous forests. *ISPRS Journal of Photogrammetry and Remote Sensing*, *130*, 187–201.

[254] Wang, Q., Tenhunen, J., Dinh, N., Reichstein, M., Otieno, D., Granier, A., & Pilegarrd, K. (2005). Evaluation of seasonal variation of MODIS derived leaf area index at two European deciduous broadleaf forest sites. *Remote Sensing of Environment*, *96*(3-4), 475–484.

[255] Jeong, S.-J., Ho, C.-H., Gim, H.-J., & Brown, M. E. (2011). Phenology shifts at start vs. end of growing season in temperate vegetation over the Northern Hemisphere for the period 1982–2008. *Global Change Biology*, *17*(7), 2385–2399.

[256] Gibbs, H. K. (2006). Olson's Major World Ecosystem Complexes Ranked by Carbon in Live Vegetation: an Updated Database Using the GLC2000 Land Cover Product (NDP-017b). *OSTI*.

[257] Yuan, H., Dai, Y., Xiao, Z., Ji, D., & Shangguan, W. (2011). Reprocessing the MODIS Leaf Area Index products for land surface and climate modelling. *Remote Sensing of Environment*, *115*(5), 1171–1187.

[258] Lucchesi, R. (2018). File Specification for GEOS FP. GMAO Office Note No. 4 (Version 1.2). *GMAO*.

[259] Feinberg, A. (2022). Code reference: arifein/offline-drydep: Offline dry deposition model from GEOS-Chem v1.0 (v1.0). *Zenodo*.

[260] Wang, Y., Jacob, D. J., & Logan, J. A. (1998). Global simulation of tropospheric O3-NO x -hydrocarbon chemistry: 1. Model formulation. *Journal of Geophysical Research: Atmospheres*, *103*(D9), 10713–10725.

[261] Ku, H. (1966). Notes on the use of propagation of error formulas. *Journal of Research of the National Bureau of Standards*, *70C*(4).

[262] Papula, L. (2003). *Mathematische Formelsammlung für Ingenieure und Naturwissenschaftler*. Vieweg, 8 ed.

[263] Gharun, M., Hörtnagl, L., Paul-Limoges, E., Ghiasi, S., Feigenwinter, I., Burri, S., Marquardt, K., Etzold, S., Zweifel, R., Eugster, W., & Buchmann, N. (2020). Physiological response of Swiss ecosystems to 2018 drought across plant types and elevation. *Philosophical Transactions of the Royal Society B: Biological Sciences*, *375*(1810), 20190521. Publisher: Royal Society.

[264] Buras, A., Rammig, A., & Zang, C. S. (2020). Quantifying impacts of the 2018 drought on European ecosystems in comparison to 2003. *Biogeosciences*, *17*(6), 1655–1672.

[265] Naturvårdsverket (2023). Informative Inventory Report Sweden 2023. Submitted under the Convention on Long-Range Transboundary Air Pollution. *Swedish Environmental Protection Agency*.

[266] Forzieri, G., Feyen, L., Rojas, R., Flörke, M., Wimmer, F., & Bianchi, A. (2014). Ensemble projections of future streamflow droughts in Europe. *Hydrology and Earth System Sciences*, *18*(1), 85–108. Publisher: Copernicus GmbH.

[267] Samaniego, L., Thober, S., Kumar, R., Wanders, N., Rakovec, O., Pan, M., Zink, M., Sheffield, J., Wood, E. F., & Marx, A. (2018). Anthropogenic warming exacerbates European soil moisture droughts. *Nature Climate Change*, *8*(5), 421–426.

[268] Kellomäki, S., Strandman, H., Heinonen, T., Asikainen, A., Venäläinen, A., & Peltola, H. (2018). Temporal and Spatial Change in Diameter Growth of Boreal Scots Pine, Norway Spruce, and Birch under Recent-Generation (CMIP5) Global Climate Model Projections for the 21st Century. *Forests*, *9*(3), 118.

[269] Oksanen, E., Lihavainen, J., Keinänen, M., Keski-Saari, S., Kontunen-Soppela, S., Sellin, A., & Sõber, A. (2019). Northern Forest Trees Under Increasing Atmospheric Humidity. In F. M. Cánovas, U. Lüttge, R. Matyssek, & H. Pretzsch (Eds.) *Progress in Botany Vol. 80*, Progress in Botany, (pp. 317–336). Cham: Springer International Publishing.

[270] Panagos, P., Jiskra, M., Borrelli, P., Liakos, L., & Ballabio, C. (2021). Mercury in European topsoils: Anthropogenic sources, stocks and fluxes. *Environmental Research*, *201*, 111556.

[271] Zhang, H. H., Poissant, L., Xu, X., & Pilote, M. (2005). Explorative and innovative dynamic flux bag method development and testing for mercury air–vegetation gas exchange fluxes. *Atmospheric Environment*, *39*(39), 7481–7493.

[272] McDowell, N. G., Allen, C. D., Anderson-Teixeira, K., Aukema, B. H., Bond-Lamberty, B., Chini, L., Clark, J. S., Dietze, M., Grossiord, C., Hanbury-Brown, A., Hurtt, G. C., Jackson, R. B., Johnson, D. J., Kueppers, L., Lichstein, J. W., Ogle, K., Poulter, B., Pugh, T. A. M., Seidl, R., Turner, M. G., Uriarte, M., Walker, A. P., & Xu, C. (2020). Pervasive shifts in forest dynamics in a changing world. *Science*, *368*(6494).

[273] Kumar, A., Wu, S., Huang, Y., Liao, H., & Kaplan, J. O. (2018). Mercury from wildfires: Global emission inventories and sensitivity to 2000–2050 global change. *Atmospheric Environment*, *173*, 6–15.

[274] Friedlingstein, P., O'Sullivan, M., Jones, M. W., Andrew, R. M., Hauck, J., Olsen, A., Peters, G. P., Peters, W., Pongratz, J., Sitch, S., Le Quere, C., Canadell, J. G., Ciais, P., Jackson, R. B., Alin, S., Aragao, L. E. O. C., Arneth, A., Arora, V., Bates, N. R., Becker, M., Benoit-Cattin, A., Bittig, H. C., Bopp, L., Bultan, S., Chandra, N., Chevallier, F., Chini, L. P., Evans, W., Florentie, L., Forster, P. M., Gasser, T., Gehlen, M., Gilfillan, D., Gkritzalis, T., Gregor, L., Gruber, N., Harris, I., Hartung, K., Haverd, V., Houghton, R. A., Ilyina, T., Jain, A. K., Joetzjer, E., Kadono, K., Kato, E., Kitidis, V., Korsbakken, J. I., Landschützer, P., Lefevre, N., Lenton, A., Lienert, S., Liu, Z., Lombardozzi, D., Marland, G., Metzl, N., Munro, D. R., Nabel, J. E. M. S., Nakaoka, S.-I., Niwa, Y., O'Brien, K., Ono, T., Palmer, P. I., Pierrot, D., Poulter, B., Resplandy, L., Robertson, E., Rödenbeck, C., Schwinger, J., Seferian, R., Skjelvan, I., Smith, A. J. P., Sutton, A. J., Tanhua, T., Tans, P. P., Tian, H., Tilbrook, B., van der Werf, G., Vuichard, N., Walker, A. P., Wanninkhof, R., Watson, A. J., Willis, D., Wiltshire, A. J., Yuan, W., Yue, X., & Zaehle, S. (2020). Global Carbon Budget 2020. *Earth System Science Data*, *12*(4), 3269–3340.

[275] Friedlingstein, P., Jones, M. W., O'Sullivan, M., Andrew, R. M., Bakker, D. C. E., Hauck, J., Le Quere, C., Peters, G. P., Peters, W., Pongratz, J., Sitch, S., Canadell, J. G., Ciais, P., Jackson, R. B., Alin, S. R., Anthoni, P., Bates, N. R., Becker, M., Bellouin, N., Bopp, L., Chau, T. T. T., Chevallier, F., Chini, L. P., Cronin, M., Currie, K. I., Decharme, B., Djeutchouang, L., Dou, X., Evans, W., Feely, R. A., Feng, L., Gasser, T., Gilfillan, D., Gkritzalis, T., Grassi, G., Gregor, L., Gruber, N., Gürses, O., Harris, I., Houghton, R. A., Hurtt, G. C., Iida, Y., Ilyina, T., Luijkx, I. T., Jain, A. K., Jones, S. D., Kato, E., Kennedy, D., Klein Goldewijk, K., Knauer, J., Korsbakken, J. I., Körtzinger, A., Landschützer, P., Lauvset, S. K., Lefevre, N., Lienert, S., Liu, J., Marland, G., McGuire, P. C., Melton, J. R., Munro, D. R., Nabel, J. E. M. S., Nakaoka, S.-I., Niwa, Y., Ono, T., Pierrot, D., Poulter, B., Rehder, G., Resplandy, L., Robertson, E., Rödenbeck, C., Rosan, T. M., Schwinger, J., Schwingshackl, C., Seferian, R., Sutton, A. J., Sweeney, C., Tanhua, T., Tans, P. P., Tian, H., Tilbrook, B., Tubiello, F., van der Werf, G., Vuichard, N., Wada, C., Wanninkhof, R., Watson, A., Willis, D.,

Wiltshire, A. J., Yuan, W., Yue, C., Yue, X., Zaehle, S., & Zeng, J. (2021). Global Carbon Budget 2021. *Earth System Science Data Discussions*, (pp. 1–191).

[276] Ainsworth, E. A., & Long, S. P. (2005). What have we learned from 15 years of free-air CO2 enrichment (FACE)? A meta-analytic review of the responses of photosynthesis, canopy properties and plant production to rising CO2. *New Phytologist*, *165*(2), 351–372.

[277] Adams, M. A., Buckley, T. N., & Turnbull, T. L. (2020). Diminishing CO2-driven gains in water-use efficiency of global forests. *Nature Climate Change*, *10*(5), 466–471.

[278] Peñuelas, J., Ciais, P., Canadell, J. G., Janssens, I. A., Fernández-Martínez, M., Carnicer, J., Obersteiner, M., Piao, S., Vautard, R., & Sardans, J. (2017). Shifting from a fertilization-dominated to a warming-dominated period. *Nature Ecology & Evolution*, *1*(10), 1438–1445.

[279] Anav, A., Marco, A. D., Proietti, C., Alessandri, A., Dell'Aquila, A., Cionni, I., Friedlingstein, P., Khvorostyanov, D., Menut, L., Paoletti, E., Sicard, P., Sitch, S., & Vitale, M. (2016). Comparing concentration-based (AOT40) and stomatal uptake (PODY) metrics for ozone risk assessment to European forests. *Global Change Biology*, *22*(4), 1608–1627.

[280] Anav, A., Liu, Q., Marco, A. D., Proietti, C., Savi, F., Paoletti, E., & Piao, S. (2018). The role of plant phenology in stomatal ozone flux modeling. *Global Change Biology*, *24*(1), 235–248.

[281] Emberson, L. D., Ashmore, M., Simpson, D., Tuovinen, J.-P., & Cambridge, H. (2001). Modelling and mapping ozone deposition in Europe. *Water, Air, and Soil Pollution*, *130*(1), 577–582.

[282] Eghdami, H., Werner, W., Büker, P., & Sicard, P. (2022). Assessment of ozone risk to Central European forests: Time series indicates perennial exceedance of ozone critical levels. *Environmental Research*, *203*, 111798.

[283] Zhang, Q., Ficklin, D. L., Manzoni, S., Wang, L., Way, D., Phillips, R. P., & Novick, K. A. (2019). Response of ecosystem intrinsic water use efficiency and gross primary productivity to rising vapor pressure deficit. *Environmental Research Letters*, *14*(7), 074023.

[284] Pronger, J., Campbell, D. I., Clearwater, M. J., Mudge, P. L., Rutledge, S., Wall, A. M., & Schipper, L. A. (2019). Toward optimisation of water use efficiency in dryland pastures using carbon isotope discrimination as a tool to select plant species mixtures. *Science of The Total Environment*, *665*, 698–708.

[285] Poorter, H., Niinemets, U., Poorter, L., Wright, I. J., & Villar, R. (2009). Causes and consequences of variation in leaf mass per area (LMA): a meta-analysis. *New Phytologist*, *182*(3), 565–588.

[286] McLagan, D. S., Mitchell, C. P. J., Huang, H., Lei, Y. D., Cole, A. S., Steffen, A., Hung, H., & Wania, F. (2016). A high-precision passive air sampler for gaseous mercury. *Environmental Science & Technology Letters*, *3*(1), 24–29.

[287] McLagan, D. S., Mitchell, C. P. J., Huang, H., Abdul Hussain, B., Lei, Y. D., & Wania, F. (2017). The effects of meteorological parameters and diffusive barrier reuse on the sampling rate of a passive air sampler for gaseous mercury. *Atmospheric Measurement Techniques*, *10*(10), 3651–3660.

[288] McLagan, D., Steffen, A., Hung, H., Shin, C., Stupple, G. W., Olson, M. L., Luke, W. T., Kelley, P., Howard, D., Edwards, G. C., Nelson, P. F., Xiao, H., Sheu, G.-R., Dreyer, A., Huang, H., Abdul Hussain, B., Lei, Y. D., Tavshunsky, I., & Wania, F. (2018). Global evaluation and calibration of a passive air sampler for gaseous mercury. *Atmos. Chem. Phys.*, *18*(8), 5905–5919.

[289] McLagan, D. S., Huang, H., Lei, Y. D., Wania, F., & Mitchell, C. P. J. (2017). Application of sodium carbonate prevents sulphur poisoning of catalysts in automated total mercury analysis. *Spectrochimica Acta Part B: Atomic Spectroscopy*, *133*, 60–62.

[290] Eriksson, H., Eklundh, L., Hall, K., & Lindroth, A. (2005). Estimating LAI in deciduous forest stands. *Agricultural and Forest Meteorology*, *129*(1), 27–37.

[291] Eurostat (2015). European Commission forestry database: Area of wooded land (source: FAO - FE).

[292] NIBIO (2016). Landsskogtakseringen. Norway's National Forest Inventory Database. *Norwegian Institute of Bioeconomy Research*.

[293] FAO (2014). Global Forest Resources Assessment 2015. Country report, Ukraine. *Food and Agricultural Organization of the United Nations*.

[294] FAO (2014). Global Forest Resources Assessment 2015. Country Report, Belarus. Food and Agricultural Organization of the United Nations.

[295] Rigling, A., & Schaffer, H. P. (2015). Forest Report 2015. Condition and use of Swiss forests. *FOEN WSL*.

[296] Basler, D. (2016). Evaluating phenological models for the prediction of leaf-out dates in six temperate tree species across central Europe. *Agricultural and Forest Meteorology*, *217*, 10–21.